Small lesion detection with new PET technology

Daniëlle Koopman

Small lesion detection with new PET technology

Daniëlle Koopman

Graduation committee
Chairman and secretary
Prof. dr. J.N. Kok (University of Twente)

Supervisor
Prof. dr. ir. C.H. Slump (University of Twente)

Co-supervisors
Dr. P.L. Jager (Isala, Zwolle)
Dr. J.A. van Dalen (Isala, Zwolle)

Members
Prof. dr. L.F de Geus-Oei (University of Twente)
Prof. dr. J.J. Fütterer (University of Twente)
Prof. dr. R. Boellaard (University of Amsterdam / University of Groningen)
Prof. dr. H.J.M. Groen (University of Groningen)
Prof. dr. H.W.A.M. de Jong (University of Utrecht)
Dr. B.J. de Wit-van der Veen (NKI-AVL, Amsterdam)

Small lesion detection with new PET technology
PhD thesis

Cover design: Bregje Jaspers, STUDIO 0404, proefschriftontwerp.nl
Layout: Ferdinand van Nispen, Citroenvlinder DTP&Vormgeving, my-thesis.nl

Printed by: ProefschriftMaken
ISBN: 978-90-365-4870-0
DOI: 10.3990/1.9789036548700

Financial support by the foundation Nucleaire Geneeskunde, the University of Twente (department RAM-EWI) and the Zwolle Research foundation for publication of this thesis is gratefully acknowledged.

SMALL LESION DETECTION WITH NEW PET TECHNOLOGY

PROEFSCHRIFT

ter verkrijging van
de graad van doctor aan de Universiteit Twente,
op gezag van de rector magnificus,
prof. dr. T.T.M. Palstra,
volgens besluit van het College voor Promoties
in het openbaar te verdedigen
op vrijdag 22 november 2019 om 14.45 uur

door

Daniëlle Koopman

geboren op 20 januari 1990
te Hengelo (Overijssel)

Dit proefschrift is goedgekeurd door:

Promotor
Prof. dr. ir. C.H. Slump

Copromotoren
Dr. P.L. Jager
Dr. J.A. van Dalen

Paranimfen
ir. R.N. Kuin
A. Blaauwbroek, MSc

Table of contents

Chapter 1 Introduction 9

Part I **PET standardisation**

Chapter 2 Quantification, improvement, and harmonization of small lesion detection with state-of-the-art PET 29

Chapter 3 Technical note: how to determine the FDG activity for tumour PET imaging that satisfies European guidelines 57

Chapter 4 Digital PET compliance to EARL accreditation specifications 73

Chapter 5 SUV variability in EARL-accredited conventional and digital PET 85

Chapter 6 Multicentre quantitative ^{68}Ga PET/CT performance harmonisation 103

Part II **PET optimisation**

Chapter 7 Current generation time-of-flight ^{18}F-FDG PET/CT provides higher SUVs for normal adrenal glands, while maintaining an accurate characterization of benign and malignant glands 119

Chapter 8 Improving the detection of small lesions using a state-of-the-art time-of-flight PET/CT system and small-voxel reconstructions 137

Chapter 9 Diagnostic implications of a small-voxel reconstruction for loco-regional lymph node characterization in breast cancer patients using FDG-PET/CT 157

Chapter 10 Letter to the Editor: Small-voxel reconstructions significantly influence SUVs in PET imaging 179

Chapter 11 Performance of digital PET compared to high-resolution conventional PET in patients with cancer 185

Part III

Chapter 12 Summary and future perspectives 209

Chapter 13 Nederlandse samenvatting en toekomstperspectief 227

Appendices

I List of abbreviations 247

II List of publications 251

III Dankwoord 259

IV Over de auteur 264

CHAPTER 1

1

Introduction

Author

Daniëlle Koopman[1,2]

Author Affiliations
1: Department of Nuclear Medicine, Isala, Zwolle, the Netherlands
2: Technical Medicine Center, University of Twente, Enschede, the Netherlands

Unpublished

Cancer imaging

Cancer is the second-leading cause of death with more than 8.9 million deaths in 2016 worldwide [1]. In 2018 more than 115.000 people were diagnosed with cancer in the Netherlands [2]. The most common malignancies in men are prostate cancer (21%), skin cancer (18%), colon cancer (13%) and lung cancer (12%). In women the most common types are breast cancer (27%), skin cancer (19%), colon cancer (11%) and lung cancer (11%) [2].

Medical imaging plays an important role in the diagnostic evaluation of cancer, which is essential for appropriate treatment [3-6]. Twenty years ago whole-body positron emission tomography (PET) was introduced in clinical practice for oncology imaging [7]. PET scanners have the ability to visualise functional information of various tissues using positron-emitting radiopharmaceuticals. The most commonly used radiopharmaceutical for oncology imaging is fluor-18 (^{18}F) fluordeoxyglucose (FDG), a glucose analog that accumulates in cells with increased glucose metabolism such as tumour cells [8]. After intravenous FDG injection malignant tumours as well as regional and distant metastases can be visualised with PET. This enables accurate disease staging, which is crucial for diagnosis and treatment [9-12].

A few years after its introduction, PET was combined with computed tomography (CT). In this way functional and anatomical information became available in a single scan session with one device [13]. This further improved the diagnostic interpretation of PET/CT in patients with cancer and the results changed treatment plans and patient management [14-17]. Nowadays, FDG-PET/CT is one of the cornerstones of patient management in oncology [18].

In daily practice FDG-PET images are visually assessed together with semi-quantitative parameters. The most commonly used parameter for semi-quantitative PET is the standardized uptake value (SUV), which is defined as the ratio between the tracer activity concentration (in kBq/mL) in a certain region in a PET image and the administered tracer activity, normalised by a measure for distribution volume such as patient body weight [19]. Semi-quantitative parameters such as the SUV complement the visual interpretation and allow prediction of treatment response and prognosis [20-22]. However, SUV measurements are influenced by many biological and technical factors including patient preparation, data acquisition, image reconstruction and processing [23, 24].

To improve semi-quantitative comparisons of PET scans between patients, scanners and medical centres, there are ongoing efforts towards standardisation of PET imaging. In 2009 and 2015, the European Association of Nuclear Medicine (EANM) published procedure guidelines on FDG-PET/CT tumour imaging [8, 25] and they launched the EANM research ltd. (EARL) organisation to promote nuclear medicine (NM) research and support multi-centre trials. In 2010 EARL started an accreditation program for FDG-PET/CT tumour imaging. A recent evaluation among the first 200 EARL-accredited PET/CT systems showed that this accreditation program has reduced the variability in semi-quantitative FDG-PET performance [26].

PET limitations

Spatial resolution

A major limitation of PET is its low spatial resolution, which causes a limited detectability of small lesions (<20 mm), especially those with low metabolism [27, 28]. This impairs the diagnostic sensitivity of PET as compared to other imaging modalities like CT and magnetic resonance imaging (MRI) [29, 30]. However, PET often shows a higher specificity to distinguish benign from malignant lesions [31].

Many different factors contribute to the relatively low spatial resolution of PET images [28, 32]. Important factors are the positron range of the radionuclide, the scanner design (for example the size of the scintillation crystals) and the image reconstruction. Due to the finite spatial resolution of the imaging system, small lesions may be detected but they appear blurred in the PET image, resulting in an underestimation of lesion uptake combined with an overestimation of lesion size. This phenomenon is called the partial volume effect (PVE) and mostly affects lesions with sizes less than 3 times the image resolution [32, 33].

System sensitivity

Another major limitation of PET is its relatively low system sensitivity, resulting in a relatively low signal-to-noise Ratio (SNR) [34]. The sensitivity of a PET system is specifically influenced by the efficiency of the scintillation crystal and the scanner's geometric efficiency. A scintillator has four main properties that are crucial for its application in a PET detector: its stopping power for 511 keV photons, signal decay time, light output and intrinsic energy resolution [35]. There are many different PET scintillators, including sodium-iodine (NaI), bismuth-silicate (BSO), bismuth-germinate (BGO), lutetium-oxyorthosilicate (LSO) and lutetium-yttrium oxyorthosilicate (LYSO) that all have specific characteristics influencing these properties [35]. Regarding scanner geometry, the axial field-of-view (FOV) of a PET scanner is typically 15-25 cm and therefore about 10 bed positions are required to acquire a PET scan from head to groin (‘whole-body’). Moreover, to obtain a PET image with an acceptable noise level, millions of photon coincidences are required. Consequently, the acquisition of a whole-body PET scan typically takes 15 to 30 minutes.

Developments in PET imaging

Since the introduction of whole-body PET in clinical practice, several new hardware and software techniques were developed to improve the spatial resolution and system sensitivity of PET, potentially providing a better image quality and better diagnostic performance. This includes the introduction of time-of-flight (TOF) and digital PET technology as well as new image reconstruction techniques.

TOF

The incorporation of TOF information in the reconstruction algorithm improves PET image quality, because with TOF the SNR is improved while the same number of photon coincidences is obtained [36]. TOF means that the difference in detector arrival times between the two photons from an annihilation event is measured and subsequently used to estimate the annihilation point. In 2006 the first PET/CT scanner with TOF technology (Gemini TF, Philips Healthcare) was introduced in clinical practice [36]. The PET component of this system, consisting of LYSO crystals, had a coincidence timing resolution of 600 ps. Within a few years other vendors also introduced TOF-PET and many studies demonstrated that the incorporation of this technique resulted in a better image quality with improved small lesion detection, in particular in obese patients [37-39].

Digital PET

Since 2017 three vendors (GE Healthcare, Philips Healthcare and Siemens Healthineers) replaced the conventional photomultiplier tubes (PMTs) by silicon photomultipliers (SiPM) with digital readout [40-43]. Examples of these two photomultiplier types are shown in **Figure 1**. The main technical benefits of these digital SiPMs compared to PMTs are the better intrinsic timing resolution and improved photon detection efficiency [44, 45]. The clinical introduction of these digital SiPMs pushed the coincidence timing resolution forwards from typically 600 to 200-375 ps and improved the spatial resolution from typically 5 to 3.5 mm [41-43]. Consequently, digital PET systems can have a higher system sensitivity [44] and potentially provide images with higher SNR and better small lesion detection over PET systems with conventional PMTs.

Figure 1 Digital silicon photomultiplier (left) and conventional photomultiplier tube (right). The digital technique results in a better timing resolution and higher photon detection efficiency. Adapted from [44], images courtesy of Philips Healthcare

New image reconstruction techniques

Another development in PET imaging is the introduction of new image reconstruction techniques such as point spread function (PSF) modelling, metal artefact reduction, regularized reconstructions and the use of smaller voxels.

PSF modelling

The PSF describes the shape of a blur that is formed when a point source is imaged in each position within the FOV of a PET system [46]. The response of the imaging system to this point source can be modelled, thereby the blurring that surrounds the source can be partly removed and the true source is strengthened. PSF modelling (or resolution modelling) results in a better and more uniform spatial resolution across the transaxial FOV [39, 47].

Metal artefact reduction

In stand-alone CT systems, metal artefact reduction is a common tool [48] but in PET/CT imaging this method is relatively new. As CT images are used for photon attenuation correction in the PET image reconstruction, artefacts present on CT can influence PET images as well. Especially when the region of interest is located near an implant, the metal not only distorts the CT image but also influences semi-quantification with PET [49]. Recently, some vendors introduced iterative reconstructions for metal artefact reduction in PET/CT. It is expected that this can provide an improved quantification and interpretation of PET images near metal implants.

Regularised reconstructions

The most commonly used clinical PET reconstruction algorithm is the ordered subset expectation maximization (OSEM) algorithm. With this technique, a higher number of iterations (or subsets) results in an improved semi-quantitative accuracy for (small) lesions [50]. However with more iterations, image noise levels increase as well and therefore the iterative process is often stopped early to achieve acceptable noise levels. It is expected that by taking advantage of prior knowledge about the image quality using mathematical Bayesian methods, PET image quality can be further improved. Recently, GE Healthcare launched such a Bayesian penalized likelihood reconstruction algorithm (BSREM) for PET that allows effective convergence of the images using a penalty function, while the image noise is supressed [51].

Small voxels

New TOF-PET cameras provide the possibility to perform reconstructions with smaller voxels that may improve image quality. However in current practice the image voxel size for whole-body FDG-PET scans is typically 4x4x4 mm^3 [38, 52]. These relatively large voxels provide PET images with acceptable noise levels but they amplify the PVE, thereby limiting small lesion detection. The impact of reducing the PET voxel size from standard (4x4x4 mm^3) to small (2x2x2 mm^3) is illustrated in **Figure 2** for two spheres filled with FDG, with diameters of 37 mm (**Figure 2A**) and 10 mm (**Figure 2B**).

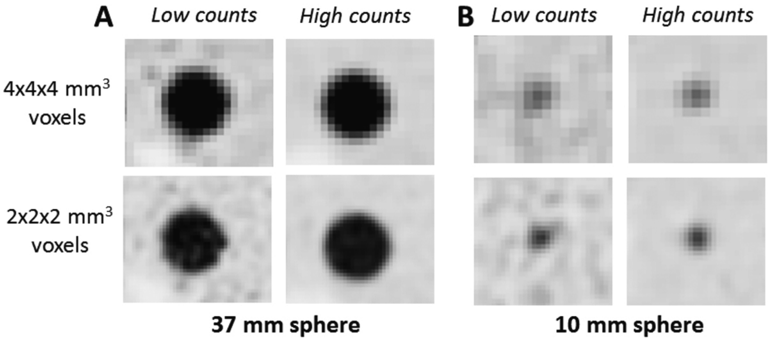

Figure 2 Impact of count statistics and voxel size on sphere visualisation with FDG-PET. In terms of FDG-uptake and sphere size, the 37 mm sphere (A) is properly visualised with both voxel reconstructions while the 10 mm sphere (B) is better visualised on small-voxel images than on standard-voxel images. On the latter, sphere intensity seems lower than is actually the case and lesion size is overestimated. A disadvantage of smaller voxels is the increase in image noise, which is visible in the image based on low counts

Thesis aim

The **aim** of this thesis is to evaluate the impact of these recent improvements in PET technology on the detection of small lesions (<20 mm) in cancer imaging. We studied the influence of *conventional TOF-PET* scanners and *small-voxel reconstructions* on small lesion detectability in lung and breast cancer. Furthermore, we studied *digital TOF-PET scanners* and determined their impact on semi-quantitative uptake measurements, image quality and lesion detectability in patients with cancer. Moreover, we evaluated the impact of conventional and digital PET scanners on European guidelines and especially on *EARL demands* for two different radionuclides.

Outline of this thesis

PART I – PET standardisation

In **Part I** of this thesis we investigated how recent developments in PET technology and scan protocols can be incorporated following European guidelines to further standardise PET oncology imaging.

In **Chapter 2** we described recent advances in PET/CT technology that may improve cancer imaging and we discussed the expectations towards incorporation of these developments in clinical practice, future EANM guidelines and EARL accreditation for FDG-PET imaging.

Previously, it has been demonstrated that administrating an FDG-activity that depends quadratically on patients' body weight can provide a constant image quality across patients [53]. However, a practical approach on how to implement this in clinical practice following European guidelines was lacking. In **Chapter 3** we used these guidelines as a standard to determine an FDG-activity formula for whole-body PET examinations that also fulfils recent insights on patient-specific administration of FDG-activity. In all patient studies that are described in this thesis, we applied an FDG-activity formula that depends quadratically on patients' body weight.

Current EANM guidelines on FDG-PET tumour imaging are based on conventional PET systems [8, 25]. Recently introduced PET systems with digital technology potentially provide an improved image quality compared to the conventional systems [42, 54, 55]. However, it was unknown if they can fulfil the EARL accreditation standards. Therefore in **Chapter 4** we aimed to evaluate the ability to accomplish these EARL standards for a recently introduced TOF-PET system with digital SiPMs.

Once different PET systems fulfil EARL specifications, it is expected that they provide PET scans with comparable semi-quantitative results. In **Chapter 5** we aimed to compare conventional and digital EARL-accredited PET systems by an evaluation of the SUV variation between those systems, using whole-body FDG-PET scans from patients with cancer.

In addition to the widely used ^{18}F radionuclides, gallium-68 (^{68}Ga) labelled peptides are increasingly used for PET imaging in both clinical practice and multi-centre trials [56]. However, EARL specifications for ^{68}Ga have not been determined yet. Therefore in **Chapter 6** we evaluated ^{68}Ga-PET semi-quantification variability in a multi-centre setting.

PART II – PET optimisation

In **Part II** of this thesis we investigated the value of three recent developments in PET technology: TOF, small-voxel reconstructions and digital SiPMs. We evaluated the effect of these technologies on PET image quality and small lesion detection in patients with cancer, focussed on lung cancer and breast cancer.

In non-small cell lung cancer (NSCLC), metastatic spread typically involves the brain, bone, liver, lymph node stations in mediastinum, hilum and supraclavicular regions, lung and adrenal glands [57]. An accurate evaluation of the adrenal glands is important for disease staging, specifically when the glands are enlarged on CT [58, 59]. The adrenal glands can be characterised with several imaging techniques like CT, MRI and PET. Especially FDG-PET/CT performs well and is often used for this purpose, as it is part of standard clinical practice in NSCLC. The new generation of conventional PET scanners, incorporating the TOF technique, may lead to a better detection of adrenal metastases. Moreover, this could change how NM specialists should evaluate adrenal glands on FDG-PET images to distinguish benign from malignant. Therefore in **Chapter 7** we aimed to analyse the impact of a conventional TOF-PET/CT scanner on adrenal gland SUV and adrenal-to-liver ratios in patients with suspected lung cancer. We compared our findings with results from literature based on non-TOF-PET and with commonly used SUV cut-off levels to distinguish benign from malignant adrenal glands.

In combination with new TOF-PET cameras, the use of image reconstructions with smaller voxels might improve the detection of small lesions [38]. However, the impact on semi-quantification and visual evaluation by NM specialists was unknown. In **Chapter 8** we determined the impact of a small-voxel image reconstruction on the detectability of small lesions in patients with lung cancer using a state-of-the-art conventional TOF-PET/CT system. Similarly in **Chapter 9** we aimed to evaluate the diagnostic implications, including sensitivity, specificity and accuracy, of this small-voxel reconstruction for lymph node characterisation in breast cancer patients using the same device.

Voxel sizes in PET image reconstructions influence image quality and this is an important aspect in PET comparison studies. In a recent paper of Fuentes-Ocampo et al.[60], conventional and digital PET were compared in 100 oncological patients and they found significant SUV increases which they attributed to the digital PET technology. However there was also a difference in image voxel size between the two PET scanners that they did not take into account. **Chapter 10** contains a Letter to the Editor with our reply to the paper of Fuentes-Ocampo et al.[60].

Finally, in **Chapter 11** we evaluated the impact of the digital SiPM technology on small lesion detection in patients with various types of cancer, by performing a prospective comparison study of optimised conventional TOF-PET with digital PET. For that purpose we compared the semi-quantitative and visual performance using small-voxel reconstructions for both PET systems and we investigated the effect on lesion detectability and disease staging.

PART III

In **Chapter 12** a summary of the key findings of this thesis is given, combined with a general discussion and future perspectives. **Chapter 13** contains a summary in Dutch.

References

1. Global Health Estimates 2016. Deaths by Cause, Age, Sex, by Country and by Region, 2000-2016. Geneva, World Health Organization. https://www.who.int/healthinfo/global_burden_disease/en. Accessed 03 Mar 2019.
2. Integraal kankercentrum Nederland. Nederlandse Kankerregistratie (NKR). https://www.cijfersoverkanker.nl/. Accessed 03 Mar 2019.
3. Labianca R, Nordlinger B, Beretta GD, Brouquet A, Cervantes A, ESMO Guidelines WG. Primary colon cancer: ESMO Clinical Practice Guidelines for diagnosis, adjuvant treatment and follow-up. Ann Oncol 2010;21:v70-7.
4. Ettinger DS, Akerley W, Borghaei H, Chang AC, Cheney RT, Chirieac LR, D'amico TA, Demmy TL, Govindan R, Grannis FW. Non–small cell lung cancer, version 2.2013. J Natl Compr Canc Netw 2013;11:645-53.
5. Senkus E, Kyriakides S, Ohno S, Penault-Llorca F, Poortmans P, Rutgers E, Zackrisson S, Cardoso F. Primary breast cancer: ESMO Clinical Practice Guidelines for diagnosis, treatment and follow-up. Ann Oncol 2015;26:v8-v30.
6. Mottet N, Bellmunt J, Bolla M, Briers E, Cumberbatch MG, De Santis M, Fossati N, Gross T, Henry AM, Joniau S. EAU-ESTRO-SIOG guidelines on prostate cancer. Part 1: screening, diagnosis, and local treatment with curative intent. Eur Urol 2017;71:618-29.
7. Bar-Shalom R, Valdivia AY, Blaufox MD. PET imaging in oncology. Semin Nucl Med 2000;30:150-85.
8. Boellaard R, O'Doherty M,J., Weber WA, Mottaghy FM, Lonsdale MN, Stroobants SG, Oyen WJG, Kotzerke J, Hoekstra OS, Pruim J. FDG PET and PET/CT: EANM procedure guidelines for tumour PET imaging: version 1.0. Eur J Nucl Med Mol Imaging 2010;37:181-200.
9. Pieterman RM, van Putten J,W.G., Meuzelaar JJ, Mooyaart EL, Vaalburg W, Koëter G,H., Fidler V, Pruim J, Groen HJM. Preoperative staging of non–small-cell lung cancer with positron-emission tomography. N Engl J Med 2000;343:254-61.
10. Flamen P, Lerut A, Van Cutsem E, Cambier JP, Maes A, De Wever W, Peeters M, De Leyn P, Van Raemdonck D, Mortelmans L. The utility of positron emission tomography for the diagnosis and staging of recurrent esophageal cancer. J Thorac Cardiovasc Surg 2000;120:1085-92.
11. Schrevens L, Lorent N, Dooms C, Vansteenkiste J. The role of PET scan in diagnosis, staging, and management of non-small cell lung cancer. Oncologist 2004;9:633-43.
12. Isasi CR, Moadel RM, Blaufox MD. A meta-analysis of FDG-PET for the evaluation of breast cancer recurrence and metastases. Breast Cancer Res Treat 2005;90:105-12.
13. Kapoor V, McCook BM, Torok FS. An introduction to PET-CT imaging. Radiographics 2004;24:523-43.

14. Bar-Shalom R, Yefremov N, Guralnik L, Gaitini D, Frenkel A, Kuten A, Altman H, Keidar Z, Israel O. Clinical performance of PET/CT in evaluation of cancer: additional value for diagnostic imaging and patient management. J Nucl Med 2003;44:1200-9.
15. Branstetter IV BF, Blodgett TM, Zimmer LA, Snyderman CH, Johnson JT, Raman S, Meltzer CC. Head and neck malignancy: is PET/CT more accurate than PET or CT alone?. Radiology 2005;235:580-6.
16. Rosen EL, Eubank WB, Mankoff DA. FDG PET, PET/CT, and breast cancer imaging. Radiographics 2007;27:S229.
17. Fischer B, Lassen U, Mortensen J, Larsen S, Loft A, Bertelsen A, Ravn J, Clementsen P, Høgholm A, Larsen K. Preoperative staging of lung cancer with combined PET–CT. N Engl J Med 2009;361:32-9.
18. Roland Hustinx and, Kristoff Muylle. European Nuclear Medicine Guide. EANM and UEMS/EBNM; 2018.
19. Tomasi G, Turkheimer F, Aboagye E. Importance of quantification for the analysis of PET data in oncology: review of current methods and trends for the future. Mol Imaging Biol 2012;14:131-46.
20. Lin C, Itti E, Haioun C, Petegnief Y, Luciani A, Dupuis J, Paone G, Talbot J, Rahmouni A, Meignan M. Early 18F-FDG PET for prediction of prognosis in patients with diffuse large B-cell lymphoma: SUV-based assessment versus visual analysis. J Nucl Med 2007;48:1626-32.
21. de Geus-Oei L, van der Heijden, Henricus FM, Corstens FH, Oyen WJG. Predictive and prognostic value of FDG-PET in nonsmall-cell lung cancer: a systematic review. Cancer 2007;110:1654-64.
22. Huang W, Zhou T, Ma L, Sun H, Gong H, Wang J, Yu J, Li B. Standard uptake value and metabolic tumor volume of 18 F-FDG PET/CT predict short-term outcome early in the course of chemoradiotherapy in advanced non-small cell lung cancer. Eur J Nucl Med Mol Imaging 2011;38:1628.
23. Vriens D, Visser EP, de Geus-Oei L, Oyen WJG. Methodological considerations in quantification of oncological FDG PET studies. Eur J Nucl Med Mol Imaging 2010;37:1408-25.
24. Adams MC, Turkington TG, Wilson JM, Wong TZ. A systematic review of the factors affecting accuracy of SUV measurements. Am J Roentgenol 2010;195:310-20.
25. Boellaard R, Delgado-Bolton R, Oyen WJG, Giammarile F, Tatsch K, Eschner W, Verzijlbergen FJ, Barrington SF, Pike LC, Weber WA. FDG PET/CT: EANM procedure guidelines for tumour imaging: version 2.0. Eur J Nucl Med Mol Imaging 2015;42:328-54.
26. Kaalep A, Sera T, Oyen WJG, Krause BJ, Chiti A, Liu Y, Boellaard R. EANM/EARL FDG-PET/CT accreditation - summary results from the first 200 accredited imaging systems. Eur J Nucl Med Mol Imaging 2018;45:412-22.

27. Takamochi K, Yoshida J, Murakami K, Niho S, Ishii G, Nishimura M, Nishiwaki Y, Suzuki K, Nagai K. Pitfalls in lymph node staging with positron emission tomography in non-small cell lung cancer patients. Lung Cancer 2005;47:235-42.
28. Berg E, Cherry SR. Innovations in instrumentation for positron emission tomography. Semin Nucl Med 2018;48:311-31.
29. Kim HS, Lee KS, Ohno Y, van Beek EJ, Biederer J. PET/CT versus MRI for diagnosis, staging, and follow-up of lung cancer. J Magn Reson Imaging 2015;42:247-60.
30. Ulzheimer S, Bongers M, Flohr T. Multi-slice CT: Current technology and future developments Medical Radiology. Berlin, Heidelberg: Springer; 2018.
31. Shim SS, Lee KS, Kim B, Chung MJ, Lee EJ, Han J, Choi JY, Kwon OJ, Shim YM, Kim S. Non–small cell lung cancer: prospective comparison of integrated FDG PET/CT and CT alone for preoperative staging. Radiology 2005;236:1011-9.
32. Mawlawi O, Townsend DW. Multimodality imaging: an update on PET/CT technology. Eur J Nucl Med Mol Imaging 2009;36:15-29.
33. Soret M, Bacharach SL, Buvat I. Partial-volume effect in PET tumor imaging. J Nucl Med 2007;48:932-45.
34. Budinger TF. PET instrumentation: what are the limits?. Semin Nucl Med 1998;28:247-67.
35. Positron Emission Tomography, Basic Sciences. Springer; 2005.
36. Surti S, Kuhn A, Werner ME, Perkins AE, Kolthammer J, Karp JS. Performance of Philips Gemini TF PET/CT scanner with special consideration for its time-of-flight imaging capabilities. J Nucl Med 2007;48:471-80.
37. Kadrmas DJ, Casey ME, Conti M, Jakoby BW, Lois C, Townsend DW. Impact of time-of-flight on PET tumor detection. J Nucl Med 2009;50:1315-23.
38. Conti M. Focus on time-of-flight PET: the benefits of improved time resolution. Eur J Nucl Med Mol Imaging 2011;38:1147-57.
39. Akamatsu G, Ishikawa K, Mitsumoto K, Taniguchi T, Ohya N, Baba S, Abe K, Sasaki M. Improvement in PET/CT image quality with a combination of point-spread function and time-of-flight in relation to reconstruction parameters. J Nucl Med 2012;53:1716-22.
40. Frach T, Prescher G, Degenhardt C, de Gruyter R, Schmitz A, Ballizany R. The digital silicon photomultiplier—Principle of operation and intrinsic detector performance. IEEE Nucl Sci Symp Conf Rec 2009:1959-65.
41. Hsu DF, Ilan E, Peterson WT, Uribe J, Lubberink M, Levin CS. Studies of a next-generation silicon-photomultiplier–based time-of-flight PET/CT system. J Nucl Med 2017;58:1511-8.
42. van Sluis JJ, de Jong J, Schaar J, Noordzij W, van Snick P, Dierckx R, Borra R, Willemsen A, Boellaard R. Performance characteristics of the digital Biograph Vision PET/CT system. J Nucl Med 2019;60:1031-6.

43. Rausch I, Ruiz A, Valverde-Pascual I, Cal-González J, Beyer T, Carrio I. Performance evaluation of the Vereos PET/CT system according to the NEMA NU2-2012 standard. J Nucl Med 2019;60:561-7.
44. Slomka PJ, Pan T, Germano G. Recent advances and future progress in PET instrumentation. Semin Nucl Med 2016;46:5-19.
45. Conti M, Bendriem B. The new opportunities for high time resolution clinical TOF PET. Clin Transl Imaging 2019;7:139-47.
46. Rapisarda E, Bettinardi V, Thielemans K, Gilardi MC. Image-based point spread function implementation in a fully 3D OSEM reconstruction algorithm for PET. Phys Med Biol 2010;55:4131-51.
47. Rogasch JM, Steffen IG, Hofheinz F, Großer OS, Furth C, Mohnike K, Hass P, Walke M, Apostolova I, Amthauer H. The association of tumor-to-background ratios and SUVmax deviations related to point spread function and time-of-flight F18-FDG-PET/CT reconstruction in colorectal liver metastases. EJNMMI Res 2015;5:31-8.
48. Gjesteby L, De Man B, Jin Y, Paganetti H, Verburg J, Giantsoudi D, Wang G. Metal artifact reduction in CT: where are we after four decades?. IEEE Access 2016;4:5826-49.
49. Van Der Vos, Charlotte S, Arens AI, Hamill JJ, Hofmann C, Panin VY, Meeuwis AP, Visser EP, de Geus-Oei L. Metal artifact reduction of CT scans to improve PET/CT. J Nucl Med 2017;58:1867-72.
50. Jaskowiak CJ, Bianco JA, Perlman SB, Fine JP. Influence of reconstruction iterations on 18F-FDG PET/CT standardized uptake values. J Nucl Med 2005;46:424-8.
51. Teoh EJ, McGowan DR, Macpherson RE, Bradley KM, Gleeson FV. Phantom and clinical evaluation of the Bayesian penalized likelihood reconstruction algorithm Q. Clear on an LYSO PET/CT system. J Nucl Med 2015;56:1447-52.
52. Kolthammer JA, Su K, Grover A, Narayanan M, Jordan DW, Muzic RF. Performance evaluation of the Ingenuity TF PET/CT scanner with a focus on high count-rate conditions. Phys Med Biol 2014;59:3843-59.
53. de Groot E,H., Post N, Boellaard R, Wagenaar NRL, Willemsen ATM, van Dalen J,A. Optimized dose regimen for whole-body FDG-PET imaging. EJNMMI Res 2013;3:63-72.
54. Wright CL, Binzel K, Zhang J, Knopp MV. Advanced functional tumor imaging and precision nuclear medicine enabled by digital PET technologies. Contrast Media Mol I 2017;2017:1-7.
55. Baratto L, Park SY, Hatami N, Davidzon G, Srinivas S, Gambhir SS, Iagaru A. 18F-FDG silicon photomultiplier PET/CT: A pilot study comparing semi-quantitative measurements with standard PET/CT. PloS one 2017;12:e0178936.
56. Perera M, Papa N, Christidis D, Wetherell D, Hofman MS, Murphy DG, Bolton D, Lawrentschuk N. Sensitivity, specificity, and predictors of positive 68Ga–prostate-specific membrane antigen positron emission tomography in advanced prostate cancer: a systematic review and meta-analysis. Eur Urol 2016;70:926-37.

57. Quint LE, Tummala S, Brisson LJ, Francis IR, Krupnick AS, Kazerooni EA, Iannettoni MD, Whyte RI, Orringer MB. Distribution of distant metastases from newly diagnosed non-small cell lung cancer. Ann Thorac Surg 1996;62:246-50.
58. Kumar R, Xiu Y, Jian QY, Takalkar A, El-Haddad G, Potenta S, Kung J, Zhuang H, Alavi A. 18F-FDG PET in evaluation of adrenal lesions in patients with lung cancer. J Nucl Med 2004;45:2058-62.
59. Park SY, Park BK, Kim CK. The value of adding 18F-FDG PET/CT to adrenal protocol CT for characterizing adrenal metastasis (≥ 10 mm) in oncologic patients. Am J Roentgenol 2014;202:W153-60.
60. Fuentes-Ocampo F, López-Mora DA, Flotats A, Paillahueque G, Camacho V, Duch J, Fernández A, Domènech A, Estorch M, Carrió I. Digital vs. analog PET/CT: intra-subject comparison of the SUVmax in target lesions and reference regions. Eur J Nucl Med Mol Imaging 2019;46:1745-50.

PART I

PET standardisation

CHAPTER 2

2

Quantification, improvement, and harmonization of small lesion detection with state-of-the-art PET

Authors

Charlotte S. van der Vos[1,2] | Daniëlle Koopman[2,3] | Sjoerd Rijnsdorp[4]
Albert J. Arends[4] | Ronald Boellaard[5,6] | Jorn A. van Dalen[3,7] | Mark Lubberink[8,9]
Antoon T. M. Willemsen[5] | Eric P. Visser[1]

Author Affiliations
1: Department of Radiology and Nuclear Medicine, Radboud University Medical Centre, Nijmegen, the Netherlands
2: MIRA Institute for Biomedical Technology and Technical Medicine, University of Twente, Enschede, the Netherlands
3. Department of Nuclear Medicine, Isala, Zwolle, the Netherlands
4: Department of Medical Physics, Catharina Hospital, Eindhoven, the Netherlands
5: Department of Nuclear Medicine and Molecular Imaging, University of Groningen, University Medical Centre Groningen, Groningen, the Netherlands
6: Department of Radiology and Nuclear Medicine, VU University Medical Center, Amsterdam, the Netherlands
7: Department of Medical Physics, Isala, Zwolle, the Netherlands
8: Department of Surgical Sciences, Uppsala University, Uppsala, Sweden
9: Department of Medical Physics, Uppsala, University Hospital, Uppsala, Sweden

Published in
European Journal of Nuclear Medicine and Molecular Imaging 2017;44:4-16

Abstract

In recent years, there have been multiple advances in positron emission tomography/computed tomography (PET/CT) that improve cancer imaging. The present generation of PET/CT scanners introduces new hardware, software, and acquisition methods. This review describes these new developments, which include time-of-flight (TOF), point-spread-function (PSF), maximum-a-posteriori (MAP) based reconstruction, smaller voxels, respiratory gating, metal artefact reduction, and administration of quadratic weight-dependent ^{18}F–fluorodeoxyglucose (FDG) activity. Also, hardware developments such as continuous bed motion (CBM), (digital) solid-state photodetectors and combined PET and magnetic resonance (MR) systems are explained. These novel techniques have a significant impact on cancer imaging, as they result in better image quality, improved small lesion detectability, and more accurate quantification of radiopharmaceutical uptake. This influences cancer diagnosis and staging, as well as therapy response monitoring and radiotherapy planning. Finally, the possible impact of these developments on the European Association of Nuclear Medicine (EANM) guidelines and EANM Research Ltd. (EARL) accreditation for FDG-PET/CT tumor imaging is discussed.

Keywords

Time-of-flight; Point-spread-function, Digital PET; PET/MR; Lesion detectability; EARL

Introduction

PET/CT is nowadays widely used in oncology and has become an essential multimodality imaging method that provides both anatomic and metabolic information [1, 2]. PET/CT imaging is important for the detection, localization, characterization, and staging of cancer [2]. However, the two main limitations of PET are the relatively low spatial resolution, which results in a partial-volume effect (PVE) affecting images both visually and quantitatively [3], and the generally low signal-to-noise ratio (SNR). The PVE limits the detection of small, low-contrast lesions (typically <2 cm), since they appear to be larger while their radiopharmaceutical uptake appears to be lower than the actual value, due to spill out of activity [4]. In addition, this also decreases the detection sensitivity itself when the signal-to-noise ratio of these lesions becomes too small. These effects are especially important when accurate quantification is needed. In recent years, there have been multiple advances in PET/CT that potentially improve cancer imaging and small lesion detection. In this article, these recent advances in PET/CT technology are explained. Also, the potential consequences of these developments for the EANM guidelines and EARL accreditation for FDG-PET imaging are discussed.

New PET technologies and image reconstruction methods

In this section, an overview of several PET technological developments that took place during the last decade will be given, as well as a short description of their underlying principles. In particular, this review addresses TOF [5], PSF modeling [6], MAP-based reconstruction [7], smaller voxels [8], respiratory gating [9], metal artefact reduction [10], as well as hardware improvements like CBM [11], the development of solid-state photodetectors using digital photon counting technology [12] and the introduction of combined PET/MR imaging [13].

Our descriptions will be limited to those features that are currently available in commercial, clinical whole-body PET/CT, and PET/MR systems. Nevertheless, still newer developments are under way, and might enter the market within the coming years. Among these, the most important ones in our opinion, could be the following. New PET reconstruction methods for which PET attenuation correction by CT is not necessary [14]. This can reduce or avoid several artefacts (motion, metal) in the PET images, and leads to lowering of the radiation dose. Further, a substantial improvement of the TOF timing resolution (see next section) can be expected [5], thus improving image quality, reducing scan time, or reducing administered activity. Finally, scanners with very large axial FOV, such as the total body system proposed by Cherry et al.[15] could provide an even larger improvement of these parameters.

Time-of-flight

PET imaging is based on the detection of annihilation photons along a line-of-response (LOR). When the difference in arrival time between two annihilation photons is known, the location from which these photons originated can be determined. If this difference equals Δt, the location of the annihilation event, with respect to the midpoint between the two detectors, is given by $\Delta x = c\,\Delta t/2$, where c is the speed of light (3×10^8 m/s). This technique is called time-of-flight PET.

In 2006, the first commercial whole-body TOF-PET scanners were introduced. These PET scanners use lutetium oxyorthosilicate (LSO) or lutetium-yttrium oxyorthosilicate (LYSO) scintillators, which provide a timing accuracy of 350–550 ps, resulting in a localization accuracy of 5.3–8.3 cm. **Table 1** shows vendor-specific timing and localization accuracy information. The spatial resolution of PET without TOF is already in the order of several millimeters. This indicates that TOF information will not directly lead to a higher spatial resolution. However, the incorporation of TOF information in the PET image reconstruction algorithm does provide images with a higher SNR, which improves the detection of small lesions with relatively low activity that would otherwise have been indistinguishable due to background noise. The SNR is approximated by $\mathrm{SNR}_{\mathrm{TOF}} \approx \sqrt{(D/\Delta x)} \times \mathrm{SNR}_{\text{non-TOF}}$ where D is the effective patient diameter [25]. Therefore, the effect of TOF is most pronounced in obese patients [5, 25, 26]. It has been shown that the SNR (as a property of the image) is proportional to the square root of the noise equivalent counts (NEC) [27], which is a property of the PET scanner. The increase in SNR is sometimes regarded as a gain in counts: a TOF image is equivalent to a non-TOF image obtained with a larger number of counts, where $D/\Delta x$ is called the gain factor. The sensitivity times this gain factor is sometimes called the effective sensitivity. In other words, the incorporation of TOF information increases the effective sensitivity. This can be used to provide better image quality and improved lesion detection, or to shorten the scan time while keeping the same image quality with better clinical workflow and added comfort for the patient, or finally to reduce radionuclide costs and reduce radiation dose to the patient and hospital personnel with the same scan time and image quality.

Table 1 PET/CT and PET/MR system specifications, including the availability and performance of recent developments such as TOF, PSF, respiratory gating, and metal artefact reduction. *Data from peer-reviewed publications. **Data from vendor. ***Data determined by authors (typical values measured during acceptance testing). Note about effective sensitivity: As explained in the section about time-of-flight, the gain factor by which the sensitivity is effectively increased by using TOF can be approximated as $D/\Delta x$. However, most manufacturers (except Toshiba) do not exactly specify how they have calculated their effective sensitivity. When the effective sensitivity was not known, the authors calculated this by using the NEMA sensitivity and the TOF information with D = 20 cm.

	Philips Vereos [16, 17]	Philips Ingenuity TF [18]	GE Discovery PET/CT 710 [12, 19]	GE Discovery IQ (five-ring system) [12, 20]	GE Discovery MI (four-ring system)	Siemens Biograph mCT Flow (TrueV) [11]	Toshiba Celesteion [21]	Mediso Anyscan	GE Signa [12, 22]	Siemens mMR [23, 24]
Patient port (cm)	70	70 Open view	70	70	70	78	88	70	60	60
MR	N/A	N/A	N/A	N/A	N/A	N/A	N/A	N/A	3 T	3 T
Patient scan range (cm)	190	190	200	200	200	198 FlowMotion: 195	179	235	188	200
Maximum patient weight (kg)	195	195	226	226	226	226	205	229	226	200
Crystal size (mm^3)	4 × 4 × 22	4 × 4 × 22	4.2 × 6.3 × 25	6.3 × 6.3 × 30	3.95 × 5.3 × 25	4 × 4 × 20	4 × 4 × 12	3.9 × 3.9 × 20	4.0 × 5.3 × 25	4 × 4 × 20
Photodetector	SiPM	PMT	PMT	PMT	SiPM	PMT	PMT	PMT	SiPM	APD
Axial FOV (cm)	16.4	18	15.7	26	20	22.1	19.6	23	25	25.8
Scintillation detector material	LYSO	LYSO	LYSO	BGO	LYSO	LSO	LYSO	LYSO	LYSO	LSO
NEMA system sensitivity at center (kcps/MBq)	5.7*	7.4*	7.1***	22.8*	13.5**	9.6*	>3.6**	9.1**	22.9*	13.3*
Effective sensitivity (kcps/MBq)	24.1*	>18.8**	17.3*	22.8*	46.6**	25.5**	≥10.8**	?	76.3*	13.3*

Table 1 Continued

	Philips Vereos [16, 17]	Philips Ingenuity TF [18]	GE Discovery PET/CT 710 [12, 19]	GE Discovery IQ (five-ring system) [12, 20]	GE Discovery MI (four-ring system)	Siemens Biograph mCT Flow (TrueV) [11]	Toshiba Celesteion [21]	Mediso Anyscan	GE Signa [12, 22]	Siemens mMR [23, 24]
NEMA radial resolution (FWHM) @ 10 cm	4.6*	5.3*	5.1* (average radial and tangential)	5.6*	4.5** (average radial and tangential)	5.2*	<5.1** (average radial and tangential)	4.9** (average radial and tangential)	5.8*	5.2*
NEMA tangential resolution (FWHM) @ 10 cm	4.2*	5.0*	5.1* (average radial and tangential)	5.1*	4.5** (average radial and tangential)	4.7*	<5.1** (average radial and tangential)	4.9** (average radial and tangential)	4.4*	4.8*
NEMA axial resolution (FWHM) @ 1 cm and 10 cm	3.8/4.0*	4.7/5.2*	4.8/5.6*	4.8/4.8*	4.8/4.7**	4.3/5.9*	<5.0/<5.4**	4.2/5.1**	5.4/6.8*	4.3/6.6*
Peak NECR (kcps) @ kBq/ml	171@50*	124@20*	144@29***	124@9*	180@20**	185@29*	61 +/- 10**	150**	215@18*	196@24*
TOF timing resolution (ps)	345**	495**	544*	N/A	385**	540**	<450**	?	<400*	N/A
TOF localization accuracy (cm)	5.2**	7.4**	8.2*	N/A	5.8**	8.1**	<6.8**	?	6.0*	N/A
PSF	y (PSF)	y (PSF)	y (SharpIR)	y (SharpIR)	y (SharpIR)	y (HD)	y	?	y (SharpIR)	y (HD)
Respiratory gating	Phase-based	Phase-based	Phase-based (Q.Static/Q. Freeze)	Phase-based (Q.Static)	Phase-based (Q.Static/Q. Freeze)	Amplitude-based (HD•Chest)	Phase-based	?	Phase-based (Q.Static/Q. Freeze)	Amplitude-based (HD•Chest)
Metal artefact reduction	O-MAR	O-MAR	Smart MAR		Smart MAR	iMAR	SEMAR	?		WARP

Point-spread-function modeling

Iterative image reconstruction methods use a system matrix that couples the coincidence counts along each LOR to the activity in the different voxels. In principle, this matrix takes into account all processes that influence the measured counts along each LOR. Among these are resolution degrading effects such as positron range, photon non-colinearity, and detector-related effects, including crystal widths, inter-crystal scattering, and inter-crystal penetration (depth of interaction effects). Resolution modeling or PSF modeling takes into account these effects during image reconstruction [6]. However, PSF modeling can also be applied as a post-reconstruction deconvolution [28]. The first method has been implemented by Siemens (HD) and GE (SharpIR), while the second method is used by Philips, as can be seen in **Table 1**.

It has been demonstrated that PSF modeling in PET reconstructions leads to higher and more uniform spatial resolution over the transaxial FOV [29-31]. Special attention should be given to some pitfalls, noise and Gibbs artefacts can be amplified [32]. However, for noise, this depends on its definition. As explained by Alessio et al.[33], PSF modeling can reduce noise when it is defined as intensity variation on a voxel-to-voxel basis, but may increase the ensemble standard deviation of mean lesion uptake. Also, spatially correlated noisy patterns can be introduced, especially for low count statistics [34].

An example of a clinical PET scan demonstrating the impact of TOF and PSF is shown in **Figure 1**. It is interesting to note that although PSF modeling was developed and tested mainly for ^{18}F–FDG imaging, it clearly also enhances small lesion detectability using ^{68}Ga-based tracers. Apparently, this is not hampered by the higher positron energy and larger range for ^{68}Ga versus ^{18}F.

Bayesian penalized likelihood

When using conventional iterative reconstruction algorithms based on maximum likelihood estimation maximization (MLEM) such as ordered subset expectation maximization (OSEM), the quantitative accuracy of the resulting images improves (the standardized uptake values (SUVs) of lesions increase) when the number of iterations is increased. However, image noise levels also increase with each iteration, hampering visual small lesion detection. As a compromise, some bias (underestimation of SUV in smaller lesions) is allowed in the reconstructed images in return for reduced noise levels, by stopping the iterative process after a limited number of iterations, or by applying post reconstruction spatial smoothing [35].

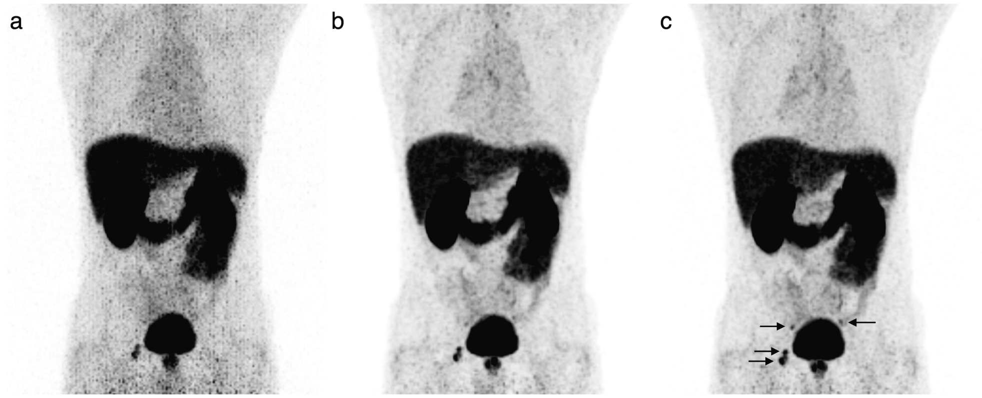

Figure 1 ^{68}Ga-labeled prostate-specific membrane antigen (PSMA) maximum intensity projection PET images (mCT, Siemens) of a patient with metastasized prostate cancer. PSMA uptake is visible in the prostate and four metastases (two lesions in the acetabulum (right), and two para-iliac lymph nodes (left and right)). All images were reconstructed with a transaxial matrix size of 256×256, pixel size of 3.1×3.1 mm^2. (**a**) PET reconstruction without PSF modeling and without TOF, (**b**) PET reconstruction with PSF modeling and without TOF, and (**c**) a PET reconstruction with both PSF modeling and TOF (data are from Radboudumc, Nijmegen, The Netherlands)

Bayesian methods are applied in PET image reconstructions to further improve the quality of reconstructed images by taking advantage of prior knowledge of the image, e.g., non-negativity of the tracer concentration, limited variation between neighboring voxels (while preserving real edges), or anatomical information for example from CT. The Bayesian penalized likelihood technique (BPL) or MAP algorithm (for instance as incorporated in Q.Clear (GE) [7]) allows effective convergence of image accuracy while suppressing noise, by using a penalty function [7, 36]. With every iteration, the outcomes with lower variation between neighboring voxels are slightly favored over noisier ones. The strength of this penalty term is chosen to match the procedure type. A substantial number of iterations (typically 25) warrants convergence without amplifying noise, resulting in improved image quality and increased SUV, particularly in small lesions when compared with reconstruction techniques without using MAP [7, 35, 37]. An example is given in **Figure 2**.

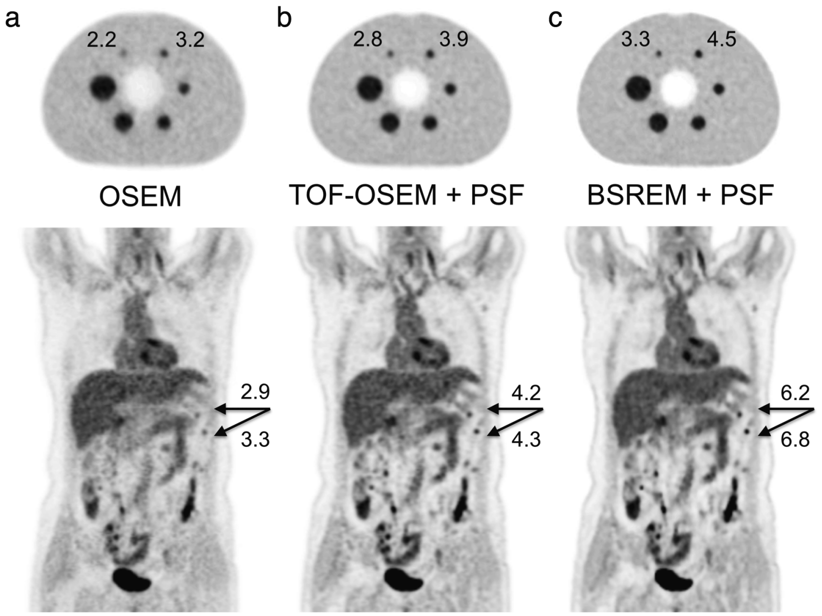

Figure 2 Top row: images of a 100 Mcounts acquisition of the NEMA image quality phantom (sphere-to-background activity concentration ratio 4:1). Measured sphere-to-background ratios (hottest pixel) are given for the two smallest spheres. Bottom row: ^{18}F–FDG PET images (four-ring Discovery MI, GE) of a patient with ovarian cancer with peritoneal carcinomatosis, (**a**) reconstructed using OSEM, (**b**) TOF-OSEM with PSF modeling, and (**c**) block-sequential regularized expectation maximization (BSREM; Q.clear) with PSF modeling and a beta-value of 400. SUV_{max} [g/cm^3] is given for the two lesions. Note the much better recovery in the small lesions when adding TOF and PSF, with further improvement for BSREM, optimized for BPL. The beta value in the BSREM reconstruction was chosen to result in similar background variability in the BSREM and TOF-OSEM images of the NEMA phantom (data are from Uppsala University Hospital, Uppsala, Sweden)

Small voxel reconstruction

In current practice, the image voxel size for whole-body FDG-PET scans is typically around 4×4×4 mm^3 [18, 38, 39], which is in the order of the NEMA spatial resolution of the PET scanner [40], defined as the full width at half and tenth maximum (FWHM/FWTM) of a point source when reconstructed using filtered back-projection without any corrections. Recent studies demonstrated that the use of smaller voxels and corresponding larger matrices, in combination with TOF-PET/CT systems, improves the detection of small lesions [8, 41-43]. Li et al.[41] demonstrated that using a 400×400 matrix (2×2 mm^2) resulted in more detected lymph nodes and a better visual image quality, as compared to a 200×200 matrix (4.1×4.1 mm^2). Furthermore, Koopman et al.[8] showed that the use of 2×2×2 mm^3 instead of 4×4×4 mm^3 voxels was preferred by physicians, based on rankings including lesion sharpness, lesion contrast, and diagnostic confidence. Moreover, the use of 2×2×2 mm^3 voxels resulted in an increase in SUV$_{mean}$, SUV$_{max}$, and SNR for small lesions (<11 mm) in patients. This is also demonstrated in **Figure 3**. Additionally, they found that the contrast recovery coefficients (as defined in their paper) for phantom spheres were more accurate using 2×2×2 mm^3 voxels [8].

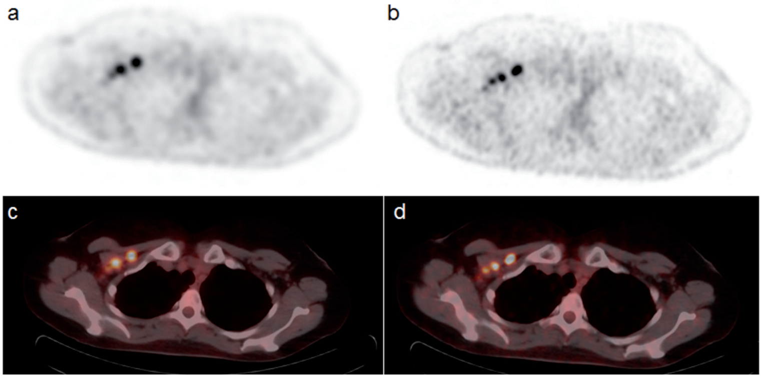

Figure 3 ^{18}F–FDG PET/CT images (Ingenuity TF, Philips) of a patient with metastasized breast cancer. The reconstructions were made without PSF modeling, but with TOF. (**a**, **c**) A standard 4×4×4 mm^3 voxel reconstruction and (**b**, **d**) a small 2×2×2 mm^3 voxel reconstruction. On the small-voxel images, there is an improved visualization of axillary lymph nodes, with an increase of SUV$_{max}$ of more than 65% for the small lymph nodes (data are from Isala Hospital, Zwolle, The Netherlands)

A drawback of the use of small voxels is an increase of noise in the PET images as smaller voxels imply fewer counts per voxel [8]. These higher noise levels may result in more false-positive findings [44].

Respiratory gating

Respiratory motion causes blurring of lesions in the thorax and upper abdomen, and can cause additional artefacts because of an inaccurate attenuation correction due to a mismatch between PET and CT [45]. This results in a lower detectability of tumors, inaccurate SUVs, and sub-optimal radiotherapy treatment planning [46, 47]. Respiratory gating can be used to create an essentially motion-free PET image. There are two methods that are most common. For the first method, the respiration of the patient is tracked and only a part of the PET data is used to reconstruct a motion-free image. For the second method, the respiration is also tracked, but all PET data is used to reconstruct a motion-free image by translating gated images of the different respiratory phases. In recent years, several respiratory gating methods have been developed for PET imaging [46, 48]. For the first method, to maintain image quality, respiratory gating requires a longer scan time and/or a higher injected activity. Therefore, respiratory gating is nowadays not routinely used for diagnostic imaging [49, 50]. However, it is more commonly applied for radiotherapy planning, where an accurate delineation and quantification is even more important [51-53].

Different vendors offer different respiratory gating methods. Philips, GE, and Toshiba use a phase-based gating method [54]. Siemens also allows phase-based gating, but in addition offers an amplitude-based optimal gating method, called HD•Chest. With this method only PET data collected from the respiratory amplitude range with the least amount of motion are used [9, 46]. GE also introduced Q.Freeze, which should only be used for diagnostic purposes. Q.Freeze is a phase-based gating method in combination with a non-rigid translation of the other phases, so all collected data are used for the final motion free image [48]. An example of the impact of respiratory gating on a PET image is shown in **Figure 4**.

Metal artefact reduction

Metal artefact reduction is a standard tool in stand-alone CT systems and different methods are well described in the literature [55]. However in PET/CT, reduction of metal artefacts is relatively new, not commonly implemented, and little research has been performed on the impact of CT metal artefacts on PET imaging. Artefacts on CT images can influence the PET reconstruction, as CT data are used for PET attenuation correction. If the region of interest is located near the implant, the metal not only distorts the CT image but also influences the quantification of radiotracer uptake and can reduce the image quality and interpreter confidence [10, 56]. Metal artefact reduction is important for diagnosis [57] and therapy planning [58] in head and neck cancer, and it can improve the image quality of ^{68}Ga-PSMA PET studies for metastasis detection in patients with one or two hip prostheses [10, 59].

Recently, iterative metal artefact reduction was introduced for some PET/CT scanners. Siemens introduced the iMAR algorithm [10], Philips introduced O-MAR and Toshiba SEMAR. It is expected that these algorithms result in an improved quantification and interpretation of the PET image near metal implants. An example is shown in **Figure 5**.

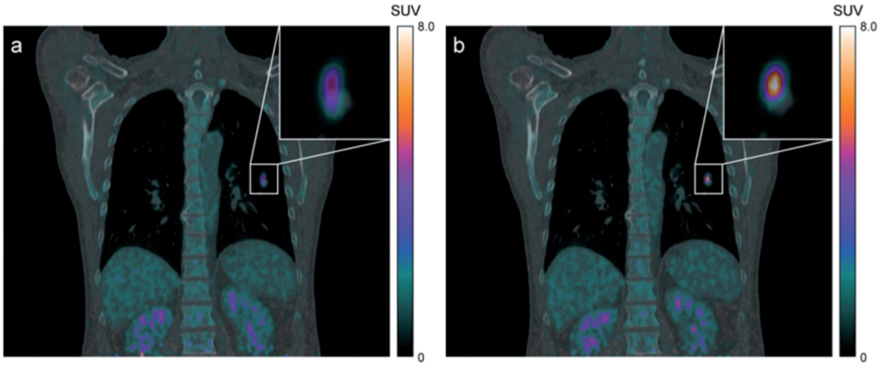

Figure 4 ^{18}F–FDG PET/CT images (mCT, Siemens) of a patient with a non-small cell lung cancer lesion in the left lower lobe. (**a**) Non-gated and (**b**) an essentially motion-free image (HD•Chest). Both PET images have been reconstructed with a matrix size of 400×400, pixel size of 2×2 mm^2, with PSF modeling and TOF. For the non-gated images, the first 35% (126 s) of the acquired data was used for image reconstruction, resulting in an equal number of acquired true coincidences as the gated image. There is a considerable increase in SUV$_{mean}$ of 70% and a decrease in volume of 80%. Images have been reproduced from [46]

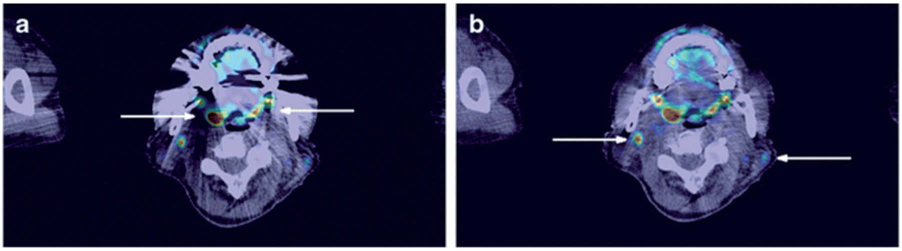

Figure 5 ^{18}F–FDG PET/CT images (mCT, Siemens) of a patient with uptake in the palatine tonsils (arrows in a) and ^{18}F–FDG-avid lymph nodes (arrows in b). Both PET images have been reconstructed with a matrix size of 200×200, pixel size of 4×4 mm^2, with PSF modeling and TOF. The metal artefact is visible on the (**a**) standard PET/CT reconstruction, while the (**b**) PET/CT reconstruction with metal artefact reduction (iMAR) shows fewer CT artefacts. There is an SUV$_{mean}$ increase from 2.5 to 2.8 g/cm^3 when iMAR is used for the tonsil. Images have been reproduced from [10]

Continuous bed motion

Due to the limited axial FOV of PET scanners, more than one bed position is generally needed to cover the section of the body that needs to be imaged. Since the sensitivity decreases toward the edges of the axial FOV, these bed positions are chosen to partly overlap to improve the uniformity in sensitivity along the axial direction [60]. Recently, CBM acquisition was introduced by Siemens (FlowMotion). The PET scanner shows similar performance compared to its predecessor system with discrete bed positions. The image quality was also similar for both techniques, with the exception of slightly increased noise levels for the planes at the edges of the outer bed positions in the standard acquisition [11, 61].

However, an advantage of the CBM technology is that the scan range can be selected without being restricted to a discrete number of bed positions, thus on average saving scan time by using a shorter scan range [62]. CBM could result in less CT radiation exposure due to this shorter range [62]. Finally, it has been stated that patients prefer the more fluent scanning of the CBM method over the more abrupt movements using discrete bed positions [61, 62].

Solid-state and digital PET

Recently, three vendors introduced PET scanners based on solid-state photodetectors, replacing the conventional photomultiplier tubes (PMTs). Siemens introduced their mMR PET/MR scanner that uses avalanche photodiodes (APD), which can operate in a magnetic field, thus offering the possibility of constructing an integrated PET/MR scanner. GE introduced their Signa PET/MR scanner using silicon photomultipliers (SiPM), which can also operate in a magnetic field. Philips introduced the Vereos PET/CT scanner based on SiPMs with digital readout, and GE released their Discovery MI PET/CT scanner, also based on SiPMs with digital readout.

In case of the digital PET scanner from Philips, the digital SiPMs are capable of detecting and processing single scintillation photons because their elements match the size of the scintillator crystal elements and they incorporate electronics to achieve a one-to-one relation between the scintillator crystal elements and the digital photomultipliers [63-65]. In terms of system performance, this design results in an improved spatial and timing resolution and relatively high maximum count rates. In case of the Discovery MI scanner (GE), 12 crystals (4×3) are coupled to an array of SiPMs (3×2), much like the block design of analogue PMT-based scanners. This reduces count-rate capability and spatial resolution compared to one-to-one coupling of crystals and SiPMs, but improves sensitivity.

Based on phantom and patient studies that were recently performed on a digital PET system [16, 66, 67], it is expected that digital PET can provide a higher image quality and/or allow for a lower radiopharmaceutical dose and improved small lesion detection for oncology scans, as compared to an analogue PET system with PMTs. **Figure 6** shows PET images of an analogue, PMT-based system and a digital PET system, of a NEMA image quality phantom (sphere diameters 10–37 mm) and a micro hollow sphere phantom (sphere diameters 4–8 mm). The reconstructed images demonstrate that image quality and small object detection improve using reconstruction settings with small voxels, on both the analogue and the digital PET. Furthermore, there is a higher contrast of the smallest spheres on the digital PET images as compared to the analogue PMT-based PET. Nguyen et al.[68] reported their initial experience in cancer patients with a prototype digital PET scanner compared to an analogue PET system with PMTs. They found a better image quality, diagnostic confidence, and accuracy with their digital PET.

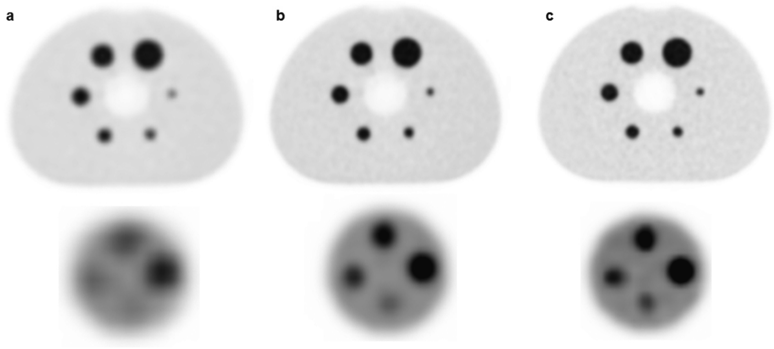

Figure 6 PET images of a NEMA phantom (sphere diameters 10–37 mm) and micro phantom (sphere diameters 4-8 mm), filled with 20 and 2 kBq/ml FDG in the spheres and the background, respectively. Data were acquired on an analogue, PMT-based PET (Ingenuity TF, Philips) and a digital SiPM-based PET (Vereos, Philips). (**a**) Images of the analogue PET that fulfils EARL requirements. (**b**) Images of the analogue PET using 2×2×2 mm^3 voxel reconstruction. (**c**) Images of a digital PET using a 2×2×2 mm^3 voxel reconstruction (data are from Isala Hospital, Zwolle, The Netherlands)

Hybrid PET/MR imaging

During the development of hybrid PET/MR systems, two major challenges needed to be overcome. First of all, conventional PET photodetectors are based on PMTs that cannot be operated in the high magnetic field of an MR scanner and are too large to allow placement inside an MR body coil whilst still leaving a sufficiently large patient opening. Integrated PET/MR was achieved using (analogue) APDs or SiPMs for conversion of the light produced by the scintillator crystals. In addition to their ability to function properly in a magnetic field, both APDs and SiPMs are much smaller than traditional PMTs, allowing for detector rings of about 5 cm thickness inside a 70-cm MR bore, leaving a 60-cm patient port diameter. An advantage of SiPMs compared to APDs is that SiPMs allow for TOF, whereas APDs, due to their timing resolution of about 2000 ps, do not. Specifications of the PET components for two fully integrated PET/MR systems are given in **Table 1**.

The second major challenge of quantitative PET with PET/MR, is that the PET attenuation correction needs to be derived from MR images, which essentially provide proton density rather than attenuation coefficients. Most PET/MR systems employ a dedicated (fast) MR sequence, followed by segmentations or tissue classification of the resulting MR image and assigning a priori known attenuation coefficients to a limited number of segmentation or tissue classes. This approach has several limitations. First of all, bone tissue is typically not included in this process and its attenuation is assumed to be equivalent to soft tissue attenuation. Secondly, lungs are segmented and assigned a uniform attenuation coefficient. Thirdly, the patient couch, fixation devices, and the coils used for MR image acquisition are not detected by the MR scanner and dedicated predefined attenuation templates need to be added to the attenuation image to compensate for them. Fourthly, the MR FOV is typically smaller than that of the PET scanner and truncation of the MR image in the transaxial direction is often observed, resulting in incomplete attenuation coefficient images and thus incorrect attenuation correction of the PET data. For most of the limitations indicated above, solutions have been proposed but not all of them are yet routinely available on all systems. For example ultra-short echo time (UTE) or zero echo time (ZTE) MR can be used to visualize bone and has only recently been introduced for brain PET/MR [69]. Another approach would be the use of CT-based templates which are registered onto the patients MR images and finally combined and processed to generate patient-specific attenuation images [69]. MR truncation artefacts in the attenuation images can be solved by first performing a PET reconstruction without attenuation, then derive the outer contour of the patient from this image and assign soft tissue attenuation to the tissues missed in the MR image [69]. However, advanced reconstruction methods, such as maximum likelihood of activity and attenuation (MLAA), might also be used to correct for MR truncation or otherwise incorrect attenuation maps [70-72]. A more complete overview of current PET/MR technologies, opportunities and challenges can be found in a review by Quick and Boellaard [73].

Possible future implications of technological developments on imaging guidelines and applications

To date, most of the new technologies that were discussed in this paper are not yet widely spread in clinical practice. However, several of these, such as digital photodetector technology, PET/MR and novel PET reconstruction methods will become more available. We expect that they will be increasingly clinically used in the next decade and will have a large impact on image quality, lesion detection, and quantification in cancer PET imaging. These new technological developments thus provide a technology push for the evolution of new standards and imaging guidelines.

Imaging guidelines and quantitative standards

The EANM guidelines for FDG-PET/CT tumor imaging and the associated PET/CT system accreditation program run by EARL aim to harmonize the use of FDG-PET/CT in oncology as a quantitative imaging biomarker in multicenter studies [39]. To date, the EANM/EARL standard is based on the technological status for the majority of the installed PET/CT systems. In order to allow sites to benefit from the advantages of the new technologies described, two different PET reconstructions could be made: one optimized for visual interpretation and another meeting international quantitative standards [39, 74-76]. With the introduction of new acquisition and reconstruction techniques in the latest scanners from multiple vendors, and assuming that the availability and presence of PET scanners using older technology will decrease, it is expected that these technologies will become widely spread during the next 5 to 10 years. Consequently, EARL standards will need to be updated over time and the implication of new technologies on harmonized quantitative performance is presently being explored by EARL as discussed in more detail elsewhere in this supplement issue [77].

New applications facilitated by new technologies

The improved image quality can be used to adjust administered activity and/or scan duration. In 2013, de Groot et al.[78] published an optimized FDG-activity regimen, which is based on a quadratic relation between FDG-activity and patient's body weight. They demonstrated that when using a quadratic administration regimen, the image quality (in terms of SNR in the liver) remains constant for patients with various body masses. This FDG-activity regimen has been mentioned as an alternative to the linear regimen in the second version of the EANM guidelines for FDG-PET tumor imaging [39]. Recently, a technical note was published by Koopman et al.[79] describing how to derive an FDG-activity formula, taking into account both EANM guidelines [39, 80] and a quadratic relation between FDG-activity and patient's body weight. Their equation can be applied for all PET/CT systems, regardless of their technological status. A drawback of the quadratic administration of FDG-activity is that it requires a high amount of FDG-activity in obese patients. Alternatively, a quadratic-dependent duration of the PET scan could be implemented in these cases.

An example of a new application of PET/CT that has been facilitated by the recent developments in PET/CT technology is the use of ^{90}Y–PET/CT imaging in patients with liver metastasis who were treated by selective internal radiation therapy

(SIRT). ^{90}Y is a radionuclide with a very small positron fraction (31.9 × 10^{-6}) and therefore it is challenging to use it for PET imaging [81]. However, several studies have recently compared Bremstrahlung ^{90}Y–single-photon emission computed tomography (SPECT)/CT with ^{90}Y–PET/CT and demonstrated that ^{90}Y–PET/CT scans using state-of-the-art TOF-PET systems provide a higher image quality with improved lesion detection and more accurate quantification and dosimetry [82-86].

Furthermore, the recent developments in PET/CT technology facilitate the use of low-count-rate PET studies such as imaging with ^{124}I, which is performed in the follow-up of thyroid cancer. In general, the image quality for the ^{124}I–PET scan is poor due to the complex decay scheme and especially the emission of prompt gamma rays with an energy of 602.7 keV, well within the standard energy window of a PET scanner. Furthermore, even higher energy gammas are present, which can downscatter into the energy window, or increase the dead time. For such a radionuclide, TOF results in a better SNR for the same number of counts [5, 87]. It is expected that recent developments in PET/CT technology, combined with a careful application of correction methods for the prompt gammas [88], further facilitate the use of ^{124}I–PET/ CT [89] (or tracers labeled with other radionuclides such as ^{89}Zr [90]) with an improved image quality and a more accurate quantification [91].

Conclusions

In recent years, the development of PET/CT scanners has mainly focused on improved small lesion detection. The introduction of TOF, PSF modeling, and smaller voxels were the main reasons for this improvement. Also, an increased axial length increased the sensitivity of the scanner [60], while the spatial resolution was improved by reducing the size of the scintillator crystal element and by using smaller voxels [60]. Other reconstruction techniques have been developed for specific problems, such as respiratory gating and metal artefact reduction. Together, all these advancements made it possible to improve the quality and quantification of PET/CT images and optimize radiation dose and scan time.

The increase in effective sensitivity and improved spatial resolution led to an improved visibility of small lesions, which is not only important for detection of lesions and metastases in ^{18}F–FDG-PET/CT scans, but also for other tracers, for instance the use of ^{68}Ga-PSMA for the detection of (lymph node) metastases in patients with prostate cancer, ^{89}Zr-MAb immunoPET studies, ^{90}Y imaging for patients who are treated for liver metastasis, or ^{124}I imaging for follow-up of thyroid cancer.

This implies that PET/CT is nowadays not only used for detection and identification of lesions but has also been increasingly implemented for radiotherapy planning and therapy response monitoring [39]. For these applications, an accurate quantification and repeatability/reproducibility is of the utmost importance. The ongoing improvements discussed in this paper can contribute to this.

Declarations

Compliance with ethical standards

Charlotte van der Vos and Eric Visser received a research grant from Siemens, and Isala has a research cooperation with Philips. Mark Lubberink has received speaking fees and research support from GE Healthcare. The other authors declare that they have no conflicts of interest. This article does not contain any studies with human participants or animals performed by any of the authors. Since this study does not contain any human participants, no informed consent was signed.

References

1. Schöder H, Erdi YE, Larson SM, Yeung HW. PET/CT: a new imaging technology in nuclear medicine. Eur J Nucl Med Mol Imaging 2003;30:1419-37.
2. Townsend DW. Dual-modality imaging: combining anatomy and function. J Nucl Med 2008;49:938-55.
3. Takamochi K, Yoshida J, Murakami K, Niho S, Ishii G, Nishimura M, Nishiwaki Y, Suzuki K, Nagai K. Pitfalls in lymph node staging with positron emission tomography in non-small cell lung cancer patients. Lung Cancer 2005;47:235-42.
4. Soret M, Bacharach SL, Buvat I. Partial-volume effect in PET tumor imaging. J Nucl Med 2007;48:932-45.
5. Vandenberghe S, Mikhaylova E, D'Hoe E, Mollet P, Karp JS. Recent developments in time-of-flight PET. EJNMMI Phys 2016;3:3-32.
6. Panin VY, Kehren F, Michel C, Casey M. Fully 3-D PET reconstruction with system matrix derived from point source measurements. IEEE Trans Med Imaging 2006;25:907-21.
7. Teoh EJ, McGowan DR, Macpherson RE, Bradley KM, Gleeson FV. Phantom and clinical evaluation of the Bayesian penalized likelihood reconstruction algorithm Q. Clear on an LYSO PET/CT system. J Nucl Med 2015;56:1447-52.
8. Koopman D, van Dalen J,A., Lagerweij MCM, Arkies H, de Boer J, Oostdijk AHJ, Slump CH, Jager PL. Improving the detection of small lesions using a state-of-the-art time-of-flight PET/CT system and small-voxel reconstructions. J Nucl Med Technol 2015;43:21-7.
9. van Elmpt W, Hamill J, Jones J, De Ruysscher D, Lambin P, Öllers M. Optimal gating compared to 3D and 4D PET reconstruction for characterization of lung tumours. Eur J Nucl Med Mol Imaging 2011;38:843-55.
10. Van Der Vos, Charlotte S, Arens AI, Hamill JJ, Hofmann C, Panin VY, Meeuwis AP, Visser EP, de Geus-Oei L. Metal artifact reduction of CT scans to improve PET/CT. J Nucl Med 2017;58:1867-72.
11. Rausch I, Cal-González J, Dapra D, Gallowitsch HJ, Lind P, Beyer T, Minear G. Performance evaluation of the Biograph mCT Flow PET/CT system according to the NEMA NU2-2012 standard. EJNMMI Phys 2015;2:26-42.
12. Slomka PJ, Pan T, Germano G. Recent advances and future progress in PET instrumentation. Semin Nucl Med 2016;46:5-19.
13. Wehrl HF, Sauter AW, Divine MR, Pichler BJ. Combined PET/MR: a technology becomes mature. J Nucl Med 2015;56:165-8.
14. Berker Y, Li Y. Attenuation correction in emission tomography using the emission data—a review. Med Phys 2016;43:807-32.
15. Cherry SR, Badawi RD, Karp JS, Moses WW, Price P, Jones T. Total-body imaging: transforming the role of positron emission tomography. Sci Transl Med 2017;9:1-7.

16. Miller M, Zhang J, Binzel K, Griesmer J, Laurence T, Narayanan M, Natarajamani D, Wang S, Knopp M. Characterization of the vereos digital photon counting PET system. J Nucl Med 2015;56:434.
17. Nguyen NC, Vercher-Conejero J, Sattar A, Miller MA, Maniawski PJ, Jordan DW, Muzic RF, Su K, O'Donnell J,K., Faulhaber PF. Image quality and diagnostic performance of a digital PET prototype in patients with oncologic diseases: Initial experience and comparison with analog PET. J Nucl Med 2015;56:1378-85.
18. Kolthammer JA, Su K, Grover A, Narayanan M, Jordan DW, Muzic RF. Performance evaluation of the Ingenuity TF PET/CT scanner with a focus on high count-rate conditions. Phys Med Biol 2014;59:3843-59.
19. Yoon HJ, Jeong YJ, Son HJ, Kang D, Hyun K, Lee M. Optimization of the spatial resolution for the GE Discovery PET/CT 710 by using NEMA NU 2-2007 standards. J Korean Phys Soc 2015;66:287-94.
20. Reynés-Llompart G, Gámez-Cenzano C, Romero-Zayas I, Rodríguez-Bel L, Vercher-Conejero JL, Martí-Climent JM. Performance characteristics of the whole-body Discovery IQ PET/CT system. J Nucl Med 2017;58:1155-61.
21. Burr KC, Wang G, Du H, Mann G, Balakrishnan K, Wang J, Li X, Rollet C, Kundro E, Buhin M. A new modular and scalable detector for a time-of-flight PET scanner. IEEE Nucl Sci Symp Conf Rec 2012:2830-4.
22. Grant AM, Deller TW, Khalighi MM, Maramraju SH, Delso G, Levin CS. NEMA NU 2-2012 performance studies for the SiPM-based ToF-PET component of the GE SIGNA PET/MR system. Med Phys 2016;43:2334-43.
23. Karlberg AM, Sæther O, Eikenes L, Goa PE. Quantitative comparison of PET performance—Siemens Biograph mCT and mMR. EJNMMI Phys 2016;3:5-18.
24. Delso G, Fürst S, Jakoby B, Ladebeck R, Ganter C, Nekolla SG, Schwaiger M, Ziegler SI. Performance measurements of the Siemens mMR integrated whole-body PET/MR scanner. J Nucl Med 2011;52:1914-22.
25. Conti M. Focus on time-of-flight PET: the benefits of improved time resolution. Eur J Nucl Med Mol Imaging 2011;38:1147-57.
26. Lois C, Jakoby BW, Long MJ, Hubner KF, Barker DW, Casey ME, Conti M, Panin VY, Kadrmas DJ, Townsend DW. An assessment of the impact of incorporating time-of-flight information into clinical PET/CT imaging. J Nucl Med 2010;51:237-45.
27. Strother SC, Casey ME, Hoffman EJ. Measuring PET scanner sensitivity: relating countrates to image signal-to-noise ratios using noise equivalents counts. IEEE Trans Nucl Sci 1990;37:783-8.
28. Perkins A, Narayanan M, Zhang B, Scheuermann J, Karp J, Shao L. Influence of a post-reconstruction resolution recovery algorithm on quantitation. J Nucl Med 2013;54:2128.

29. Rogasch JM, Steffen IG, Hofheinz F, Großer OS, Furth C, Mohnike K, Hass P, Walke M, Apostolova I, Amthauer H. The association of tumor-to-background ratios and SUVmax deviations related to point spread function and time-of-flight F18-FDG-PET/CT reconstruction in colorectal liver metastases. EJNMMI Res 2015;5:31-8.
30. Akamatsu G, Ishikawa K, Mitsumoto K, Taniguchi T, Ohya N, Baba S, Abe K, Sasaki M. Improvement in PET/CT image quality with a combination of point-spread function and time-of-flight in relation to reconstruction parameters. J Nucl Med 2012;53:1716-22.
31. Bellevre D, Fournier C, Switsers O, Dugué AE, Levy C, Allouache D, Desmonts C, Crouet H, Guilloit J, Grellard J. Staging the axilla in breast cancer patients with 18F-FDG PET: how small are the metastases that we can detect with new generation clinical PET systems?. Eur J Nucl Med Mol Imaging 2014;41:1103-12.
32. Lee YS, Kim JS, Kim KM, Kang JH, Lim SM, Kim H. Performance measurement of PSF modeling reconstruction (true X) on Siemens Biograph TruePoint TrueV PET/CT. Ann Nucl Med 2014;28:340-8.
33. Alessio AM, Rahmim A, Orton CG. Resolution modeling enhances PET imaging. Med Phys 2013;40.
34. Grootjans W, Meeuwis AP, Slump CH, de Geus-Oei L, Gotthardt M, Visser EP. Performance of 3DOSEM and MAP algorithms for reconstructing low count SPECT acquisitions. Z Med Phys 2016;26:311-22.
35. Teoh EJ, McGowan DR, Bradley KM, Belcher E, Black E, Gleeson FV. Novel penalised likelihood reconstruction of PET in the assessment of histologically verified small pulmonary nodules. Eur Radiol 2016;26:576-84.
36. Parvizi N, Franklin JM, McGowan DR, Teoh EJ, Bradley KM, Gleeson FV. Does a novel penalized likelihood reconstruction of 18F-FDG PET-CT improve signal-to-background in colorectal liver metastases?. Eur J Radiol 2015;84:1873-8.
37. Rowley LM, Bradley KM, Boardman P, Hallam A, McGowan DR. Optimization of image reconstruction for 90Y selective internal radiotherapy on a lutetium yttrium orthosilicate PET/CT system using a Bayesian penalized likelihood reconstruction algorithm. J Nucl Med 2017;58:658-64.
38. Conti M. Focus on time-of-flight PET: the benefits of improved time resolution. Eur J Nucl Med Mol Imaging 2011;38:1147-57.
39. Boellaard R, Delgado-Bolton R, Oyen WJG, Giammarile F, Tatsch K, Eschner W, Verzijlbergen FJ, Barrington SF, Pike LC, Weber WA. FDG PET/CT: EANM procedure guidelines for tumour imaging: version 2.0. Eur J Nucl Med Mol Imaging 2015;42:328-54.
40. Performance measurements of positron emission tomographs. NEMA Standards Publication NU 2-2012.

41. Li C, Klohr S, Sadick H, Weiss C, Hoermann K, Schoenberg SO, Sadick M. Effect of time-of-flight technique on the diagnostic performance of 18F-FDG PET/CT for assessment of lymph node metastases in head and neck squamous cell carcinoma. J Nucl Med Technol 2014;42:181-7.
42. Zhang J, Wright C, Binzel K, Siva A, Saif T, Nagar V, Tung C, Knopp M. High Definition (HD) and Ultra-High Definition (UHD) PET reconstructions improves lesion detectability in digital 18F-FDG PET/CT. J Nucl Med 2016;57:1980.
43. Morey AM, Noo F, Kadrmas DJ. Effect of using 2 mm voxels on observer performance for PET lesion detection. IEEE Trans Nucl Sci 2016;63:1359-66.
44. Sadick M, Molina F, Frey S, Piniol R, Sadick H, Brade J, Fink C, Schoenberg SO, He Y. Effect of reconstruction parameters in high-definition PET/CT on assessment of lymph node metastases in head and neck squamous cell carcinoma. J Nucl Med Technol 2013;41:19-25.
45. Van Der Vos, Charlotte S, Grootjans W, Osborne DR, Meeuwis AP, Hamill JJ, Acuff S, de Geus-Oei L, Visser EP. Improving the spatial alignment in PET/CT using amplitude-based respiration-gated PET and respiration-triggered CT. J Nucl Med 2015;56:1817-22.
46. Grootjans W, de Geus-Oei L, Meeuwis AP, van der Vos, Charlotte S, Gotthardt M, Oyen WJG, Visser EP. Amplitude-based optimal respiratory gating in positron emission tomography in patients with primary lung cancer. Eur Radiol 2014;24:3242-50.
47. Nehmeh SA, Erdi YE. Respiratory motion in positron emission tomography/computed tomography: a review. Semin Nucl Med 2008;38:167-76.
48. Minamimoto R, Mitsumoto T, Miyata Y, Sunaoka F, Morooka M, Okasaki M, Iagaru A, Kubota K. Evaluation of a new motion correction algorithm in PET/CT: combining the entire acquired PET data to create a single three-dimensional motion-corrected PET/CT image. Nucl Med Commun 2016;37:162-70.
49. Grootjans W, Hermsen R, van der Heijden, Erik HFM, Schuurbiers-Siebers OC, Visser EP, Oyen WJG, de Geus-Oei L. The impact of respiratory gated positron emission tomography on clinical staging and management of patients with lung cancer. Lung Cancer 2015;90:217-23.
50. Callahan J, Kron T, Schneider ME, Hicks RJ. A prospective investigation into the clinical impact of 4D-PET/CT in the characterisation of solitary pulmonary nodules. Cancer Imaging 2014;14:24.
51. Wijsman R, Grootjans W, Troost EG, van der Heijden, Erik H, Visser EP, de Geus-Oei L, Bussink J. Evaluating the use of optimally respiratory gated 18F-FDG-PET in target volume delineation and its influence on radiation doses to the organs at risk in non-small-cell lung cancer patients. Nucl Med Commun 2016;37:66-73.
52. Callahan J, Kron T, Siva S, Simoens N, Edgar A, Everitt S, Schneider ME, Hicks RJ. Geographic miss of lung tumours due to respiratory motion: a comparison of 3D vs 4D PET/CT defined target volumes. Radiat Oncol 2014;9:291.

53. Guerra L, Meregalli S, Zorz A, Niespolo R, De Ponti E, Elisei F, Morzenti S, Brenna S, Crespi A, Gardani G. Comparative evaluation of CT-based and respiratory-gated PET/CT-based planning target volume (PTV) in the definition of radiation treatment planning in lung cancer: preliminary results. Eur J Nucl Med Mol Imaging 2014;41:702-10.
54. Chirindel A, Adebahr S, Schuster D, Schimek-Jasch T, Schanne DH, Nemer U, Mix M, Meyer P, Grosu A, Brunner T. Impact of 4D-18FDG-PET/CT imaging on target volume delineation in SBRT patients with central versus peripheral lung tumors. Multi-reader comparative study. Radiother Oncol 2015;115:335-41.
55. Gjesteby L, De Man B, Jin Y, Paganetti H, Verburg J, Giantsoudi D, Wang G. Metal artifact reduction in CT: where are we after four decades?. IEEE Access 2016;4:5826-49.
56. Kamel EM, Burger C, Buck A, von Schulthess GK, Goerres GW. Impact of metallic dental implants on CT-based attenuation correction in a combined PET/CT scanner. Eur Radiol 2003;13:724-8.
57. Shimamoto H, Kakimoto N, Fujino K, Hamada S, Shimosegawa E, Murakami S, Furukawa S, Hatazawa J. Metallic artifacts caused by dental metal prostheses on PET images: a PET/CT phantom study using different PET/CT scanners. Ann Nucl Med 2009;23:443-9.
58. Awan MJ, Siddiqui F, Schwartz D, Yuan J, Machtay M, Yao M. Application of positron emission tomography/computed tomography in radiation treatment planning for head and neck cancers. World J Radiol 2015;7:382-93.
59. Abdoli M, Dierckx RA, Zaidi H. Metal artifact reduction strategies for improved attenuation correction in hybrid PET/CT imaging. Med Phys 2012;39:3343-60.
60. Cherry SR, Sorenson JA, Phelps ME. Physics in nuclear medicine. 4th edition ed. Philadelphia: Elsevier/Saunders; 2012.
61. Schatka I, Weiberg D, Reichelt S, Owsianski-Hille N, Derlin T, Berding G, Bengel FM. A randomized, double-blind, crossover comparison of novel continuous bed motion versus traditional bed position whole-body PET/CT imaging. Eur J Nucl Med Mol Imaging 2016;43:711-7.
62. Acuff SN, Osborne D. Clinical workflow considerations for implementation of continuous-bed-motion PET/CT. J Nucl Med Technol 2016;44:55-8.
63. Frach T, Prescher G, Degenhardt C, de Gruyter R, Schmitz A, Ballizany R. The digital silicon photomultiplier—Principle of operation and intrinsic detector performance. IEEE Nucl Sci Symp Conf Rec 2009:1959-65.
64. Degenhardt C, Prescher G, Frach T, Thon A, de Gruyter R, Schmitz A, Ballizany R. The digital silicon photomultiplier—A novel sensor for the detection of scintillation light. IEEE Nucl Sci Symp Conf Rec 2009:2383-6.
65. Degenhardt C, Rodrigues P, Trindade A, Zwaans B, Mülhens O, Dorscheid R, Thon A, Salomon A, Frach T. Performance evaluation of a prototype positron emission tomography scanner using digital photon counters (DPC). IEEE Nucl Sci Symp Conf Rec 2012.

66. Narayanan M, Andreyev A, Bai C, Miller M, Hu Z. TOF-benefits on the Philips digital PET/CT scanner: evaluation of faster convergence and reduced scan times. J Nucl Med 2016;57:201.
67. Zhang J, Binzel K, Bardos P, Nagar V, Knopp M, Zhang B, Hu Z, Maniawski P, Knopp M. FDG dose reduction potential of a next generation digital detector PET/CT system: initial clinical demonstration in wholebody imaging. J Nucl Med 2015;56:1823.
68. Nguyen NC, Vercher-Conejero JL, Sattar A, Miller MA, Maniawski PJ, Jordan DW, Muzic RF, Su K, O'Donnell JK, Faulhaber PF. Image quality and diagnostic performance of a digital PET prototype in patients with oncologic diseases: initial experience and comparison with analog PET. J Nucl Med 2015;56:1378-85.
69. Hofmann M, Pichler B, Schölkopf B, Beyer T. Towards quantitative PET/MRI: a review of MR-based attenuation correction techniques. Eur J Nucl Med Mol Imaging 2009;36:93-104.
70. Mehranian A, Zaidi H. Emission-based estimation of lung attenuation coefficients for attenuation correction in time-of-flight PET/MR. Phys Med Biol 2015;60:4813-33.
71. Benoit D, Ladefoged CN, Rezaei A, Keller SH, Andersen FL, Højgaard L, Hansen AE, Holm S, Nuyts J. Optimized MLAA for quantitative non-TOF PET/MR of the brain. Phys Med Biol 2016;61:8854-74.
72. Cheng J, Salomon A, Yaqub M, Boellaard R. Investigation of practical initial attenuation image estimates in TOF-MLAA reconstruction for PET/MR. Med Phys 2016;43:4163-73.
73. Boellaard R, Quick HH. Current image acquisition options in PET/MR. Semin Nucl Med 2015;45:192-200.
74. Lasnon C, Salomon T, Desmonts C, Dô P, Oulkhouir Y, Madelaine J, Aide N. Generating harmonized SUV within the EANM EARL accreditation program: software approach versus EARL-compliant reconstruction. Ann Nucl Med 2017;31:125-34.
75. Quak E, Le Roux P, Hofman MS, Robin P, Bourhis D, Callahan J, Binns D, Desmonts C, Salaun P, Hicks RJ. Harmonizing FDG PET quantification while maintaining optimal lesion detection: prospective multicentre validation in 517 oncology patients. Eur J Nucl Med Mol Imaging 2015;42:2072-82.
76. Lasnon C, Desmonts C, Quak E, Gervais R, Do P, Dubos-Arvis C, Aide N. Harmonizing SUVs in multicentre trials when using different generation PET systems: prospective validation in non-small cell lung cancer patients. Eur J Nucl Med Mol Imaging 2013;40:985-96.
77. Aide N, Lasnon C, Veit-Haibach P, Sera T, Sattler B, Boellaard R. EANM/EARL harmonization strategies in PET quantification: from daily practice to multicentre oncological studies. Eur J Nucl Med Mol Imaging 2017;44:17-31.
78. de Groot E,H., Post N, Boellaard R, Wagenaar NRL, Willemsen ATM, van Dalen J,A. Optimized dose regimen for whole-body FDG-PET imaging. EJNMMI Res 2013;3:63-72.

79. Koopman D, van Osch J,A.C., Jager PL, Tenbergen CJA, Knollema S, Slump CH, van Dalen J,A. Technical note: how to determine the FDG activity for tumour PET imaging that satisfies European guidelines. EJNMMI Phys 2016;3:22-31.
80. Boellaard R, O'Doherty M,J., Weber WA, Mottaghy FM, Lonsdale MN, Stroobants SG, Oyen WJG, Kotzerke J, Hoekstra OS, Pruim J. FDG PET and PET/CT: EANM procedure guidelines for tumour PET imaging: version 1.0. Eur J Nucl Med Mol Imaging 2010;37:181-200.
81. Selwyn RG, Nickles RJ, Thomadsen BR, DeWerd LA, Micka JA. A new internal pair production branching ratio of 90Y: the development of a non-destructive assay for 90Y and 90Sr. Appl Radiat Isot 2007;65:318-27.
82. Zade AA, Rangarajan V, Purandare NC, Shah SA, Agrawal AR, Kulkarni SS, Shetty N. 90Y microsphere therapy: does 90Y PET/CT imaging obviate the need for 90Y Bremsstrahlung SPECT/CT imaging?. Nucl Med Commun 2013;34:1090-6.
83. Pasciak AS, Bourgeois AC, Bradley YC. A comparison of techniques for 90Y PET/CT image-based dosimetry following radioembolization with resin microspheres. Front Oncol 2014;4:121.
84. Willowson KP, Tapner M, Bailey DL. A multicentre comparison of quantitative 90 Y PET/CT for dosimetric purposes after radioembolization with resin microspheres. Eur J Nucl Med Mol Imaging 2015;42:1202-22.
85. Braat AJ, Smits ML, Braat MN, van den Hoven, Andor F, Prince JF, de Jong HW, van den Bosch, Maurice AAJ, Lam MG. 90Y hepatic radioembolization: an update on current practice and recent developments. J Nucl Med 2015;56:1079-87.
86. Wright C, Binzel K, Zhang J, Wuthrick E, Tung C, Knopp M. Post-radioembolization assessment of intrahepatic yttrium-90 microsphere biodistribution using next-generation digital PET/CT and comparison to current pre/post-radioembolization SPECT/CT methodologies. J Nucl Med 2016;57:197.
87. Preylowski V, Schlögl S, Schoenahl F, Jörg G, Samnick S, Buck AK, Lassmann M. Is the image quality of I-124-PET impaired by an automatic correction of prompt gammas?. PLoS One 2013;8:e71729.
88. Lubberink M, Herzog H. Quantitative imaging of 124I and 86Y with PET. Eur J Nucl Med Mol Imaging 2011;38:10.
89. Surti S, Scheuermann R, Karp JS. Correction technique for cascade gammas in I-124 imaging on a fully-3D, time-of-flight PET scanner. IEEE Trans Nucl Sci 2009;56:653-60.
90. Makris NE, Boellaard R, Visser EP, de Jong JR, Vanderlinden B, Wierts R, van der Veen, Berlinda J, Greuter HJ, Vugts DJ, van Dongen GA. Multicenter harmonization of 89Zr PET/CT performance. J Nucl Med 2014;55:264-7.
91. Conti M, Eriksson L. Physics of pure and non-pure positron emitters for PET: a review and a discussion. EJNMMI Phys 2016;3:8-24.

CHAPTER 3

3

Technical note: how to determine the FDG activity for tumour PET imaging that satisfies European guidelines

Authors

Daniëlle Koopman[1,2] | Jochen A. C. van Osch[3] | Pieter L. Jager[1]
Carlijn J.A. Tenbergen[1,2] | Siert Knollema[1] | Cornelis H. Slump[2]
Jorn A. van Dalen[3]

Author Affiliations
1: Department of Nuclear Medicine, Isala, Zwolle, the Netherlands
2: MIRA Institute for Biomedical Technology and Technical Medicine, University of Twente, Enschede, the Netherlands
3: Department of Medical Physics, Isala, Zwolle, the Netherlands

Published in
EJNMMI Physics 2016;3:22-31

Abstract

Background

For tumour imaging with PET, the literature proposes to administer a patient-specific FDG activity that depends quadratically on a patient's body weight. However, a practical approach on how to implement such a protocol in clinical practice is currently lacking. We aimed to provide a practical method to determine a FDG activity formula for whole-body PET examinations that satisfies both the EANM guidelines and this quadratic relation.

Results

We have developed a methodology that results in a formula describing the patient-specific FDG activity to administer. A PET study using the NEMA NU-2001 image quality phantom forms the basis of our method. This phantom needs to be filled with 2.0 and 20.0 kBq FDG/mL in the background and spheres, respectively. After a PET acquisition of 10 min, a reconstruction has to be performed that results in sphere recovery coefficients (RCs) that are within the specifications as defined by the EANM Research Ltd (EARL). By performing reconstructions based on shorter scan durations, the minimal scan time per bed position (T_{min}) needs to be extracted using an image coefficient of variation (COV) of 15 %. At T_{min}, the RCs should be within EARL specifications as well. Finally, the FDG activity (in MBq) to administer can be described by $\mathrm{A} = \mathrm{c} \cdot \mathrm{w}^2 \cdot \frac{T_{\min}}{t}$ with c a constant that is typically 0.0533 (MBq/kg^2), w the patient's body weight (in kg), and t the scan time per bed position that is chosen in a clinical setting (in seconds). We successfully demonstrated this methodology using a state-of-the-art PET/CT scanner.

Conclusions

We provide a practical method that results in a formula describing the FDG activity to administer to individual patients for whole-body PET examinations, taking into account both the EANM guidelines and a quadratic relation between FDG activity and patient's body weight. This formula is generally applicable to any PET system, using a specified image reconstruction and scan time per bed position.

Keywords

FDG-PET; scan time protocol; tumour imaging; EANM guidelines

Background

Positron emission tomography/computed tomography (PET/CT) scanning, using the radioactive tracer fluor-18 fluordeoxyglucose (FDG), has an important role in tumour imaging for patients with cancer. There is a trend towards standardization and harmonization in FDG-PET scanning to allow comparisons of FDG uptake parameters across patients, scanners and medical centres [1]. Recently, version 2.0 of the European Association of Nuclear Medicine (EANM) procedure guidelines for FDG-PET tumour imaging was published. This guideline contains recommendations for tumour imaging with PET/CT by prescribing FDG activity as a function of a patient's body weight, type of scanner, reconstruction method and scan duration [2].

It is widely known that PET image quality is influenced by a patient's body weight. Heavier patients show more photon attenuation and higher scatter fractions, resulting in lower PET image quality for these patients when using a fixed tracer activity and scan time. This effect can be compensated by increasing the scan time and/or tracer activity in heavier patients [3-6]. De Groot et al.[7] demonstrated that the use of a dedicated FDG activity protocol, depending quadratically on a patient's body weight, delivers a constant image quality across patients in several weight categories. Thereby, it provided an improved radiation exposure justification. This protocol has been included as an alternative in version 2.0 of the EANM procedure guidelines [2].

However, a practical approach on how to implement such a protocol in clinical practice is currently lacking. First, it is not clear how to translate minimum requirements for image quality into a quadratic formula that describes a patient-specific FDG activity for a given scanner, reconstruction method and scan duration. Second, when using a particular patient-specific FDG activity, it needs to be verified that the applied PET reconstruction meets the harmonizing specifications for recovery coefficients (RCs), as described on the EANM Research Ltd (EARL) website [8].

Our aim was to provide an easy applicable method that results in a formula describing the FDG activity to administer to a patient, that is quadratically related to a patient's body weight and satisfies EANM procedure guidelines [2]. We intended to obtain a formula that is applicable to any PET system, using a specified image reconstruction and scan time per bed position.

Methods

The formula to be derived has to fulfil two demands. First, the product of FDG activity and scan time per bed position should depend quadratically on a patient's body weight. Second, specifications of RCs as described by EARL should be satisfied [8].

In eight steps, we describe the method to derive this formula. **Figure 1** shows a flow chart presenting all steps. A FDG-PET/CT phantom study using a NEMA NU2-2001 image quality phantom (IQ phantom) [9] forms the basis of our method.

Step 1: phantom preparation

Prior to the phantom scan, the following materials should be available:

- A NEMA NU2-2001 IQ Phantom
- A bottle filled with 1000 mL water
- Two syringes, both with 20 MBq FDG activity (volume between 2 and 5 mL), specified at the expected phantom acquisition time T_a (hh:mm:ss).
- A dose calibrator

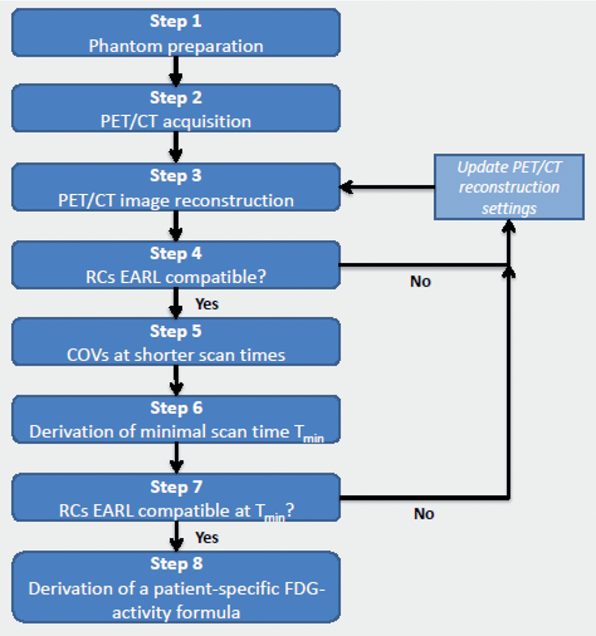

Figure 1 Flowchart demonstrating the eight steps to obtain a patient-specific FDG activity formula

Filling of the spheres

- Measure the amount of FDG activity (in kBq) present in one syringe using the dose calibrator. Record the time of measurement $T_{m,1}$ (hh:mm:ss) and record the volume of FDG activity present in the syringe (in mL).
- Add the FDG activity from this syringe to the bottle with water. Make sure all activity is entered into the bottle.
- Homogenize the solution in the bottle by shaking the phantom. Fill all phantom spheres with this solution [1].
- Calculate the true FDG activity concentration at the time of measurement in the spheres, $[S_{true}]$ at $T_{m,1}$ (in kBq/mL), by dividing the FDG activity from the syringe at $T_{m,1}$ as measured with the dose calibrator to the volume of the total solution of bottle and syringe [1].

Output
$[S_{true}]$ at $T_{m,1}$ (in kBq/mL).

Filling of the background compartment

- Fill the background compartment of the IQ phantom completely with water.
- Remove 30 mL water from the background compartment.
- Measure the amount of FDG activity (in kBq) in the second syringe using the dose calibrator and record the time of measurement $T_{m,2}$ (hh:mm:ss).
- Add the FDG activity from this syringe to the phantom background compartment. Make sure all activity is entered into the phantom. Homogenize the solution by shaking the phantom.
- Calculate the true FDG activity concentration in the phantom background compartment, $[B_{true}]$ at $T_{m,2}$ (in kBq/mL), by dividing the FDG activity (in kBq) of the second syringe at $T_{m,2}$ to the volume of the phantom background compartment [1].

Output
$[B_{true}]$ at $T_{m,2}$ (in kBq/mL).

Step 2: PET/CT acquisition

- Position the IQ phantom on the scanner bed such that the centre of each sphere is located in a single transverse plane and at the centre of the axial field of view.
- Acquire a routine list-mode PET scan based on one bed position for at least 10 min, using a whole-body FDG-PET/CT protocol. Include a CT scan for attenuation correction purposes.

- Record the start time of the PET acquisition T_a and calculate the FDG activity concentrations in the spheres $[S_{true}]$ and the background compartment $[B_{true}]$ at T_a. This can be done by correcting for FDG activity decay during the time between the FDG activity measurements $T_{m,1}$ and $T_{m,2}$ (step 1), and T_a [1].

Output
$[S_{true}]$ at T_a (in kBq/mL) and $[B_{true}]$ at T_a (in kBq/mL)

Step 3: PET/CT image reconstruction
Apply an image reconstruction that corrects for geometrical response and detector efficiency (normalization), system dead time, random coincidences, scatter and attenuation. In version 1.0 of the EANM procedure guidelines for tumour PET imaging, a number of indicative reconstruction settings are given for different system types [1].

Step 4: EARL compatibility check
Based on the reconstructed image, measure the maximum and mean recovery coefficients (RCs) of the spheres, using the following definitions:

- The maximum activity concentration recovery coefficient (RC_{max}) of a sphere is defined as the maximum pixel value within a sphere as measured on the reconstructed PET image, divided by the true FDG activity in the sphere $[S_{true}]$ at T_a [1].
- The mean activity concentration recovery coefficient (RC_{mean}) of a sphere is determined by creating a volume of interest (VOI) at 50 % of the maximum pixel value, corrected for background uptake [1]. To obtain RC_{mean}, the mean pixel value within this VOI is divided by the true FDG activity in the sphere $[S_{true}]$ at T_a.

Check whether the measured RCs for all spheres are within the minimal and maximal RCs as defined by EARL [8]. If this is the case, continue to step 5. If not, go back to step 3 and revise the reconstruction settings, within the recommendations indicated in the EANM FDG-PET/CT procedure guidelines version 2 [2]. In general, by including or adapting a post-processing smoothing filter in the reconstruction, RCs can be reduced (by more filtering) or amplified (by less filtering) in such a way that they satisfy EARL requirements.

Step 5: image coefficient of variation measurements at shorter scan times

- Perform additional reconstructions, using list-mode data and identical settings as determined at step 3, for shorter scan times at 75, 50, 25, 12.5, 6.25 and 3.13 % of the original scan duration of 10 min. Each reconstruction should be based on data with start time T_a. In case re-reconstruction of data using list-mode acquisition is not possible, an alternative is to acquire multiple acquisitions, for example as described in the EARL procedure [10]. In that case, the scan time for each additional acquisition needs to be corrected for radioactive decay between the start time of the first acquisition T_a and the time of each next acquisition T_x, using correction factor $C = 2^{(T_x - T_a)/T_{1/2}}$ with $T_{1/2}$ is the half-life of fluor-18 (110 min).
- Create three rectangular regions of interest (ROIs), each of 900 mm^2, in three axial planes within the phantom background compartment of the reconstructed images. For each ROI, the image coefficient of variation (COV) was determined by dividing the standard deviation to the mean pixel value within this ROI.
- The COV for a reconstructed image is obtained by taking the average of the nine measured COVs.

Output

COVs for images based on different scan times.

Step 6: derivation of the minimal scan time T $_{\min}$

Create a graph comparing the COV on the *y*-axis with the scan time per bed position *T* (in seconds) on the *x*-axis. Include a power-law fit: COV = $a\,T^{-b}$, with *a* and *b* as fit parameters. The minimal scan time per bed position ($T_{\min}$) can be derived using formula 1:

$$T_{min} = \left(\frac{a}{COV_{max}}\right)^{\frac{1}{b}} \cdot \frac{[B_{true}]}{2.0} \qquad (1)$$

In this formula, $[B_{true}]$ at T_a (in kBq/mL) is the true FDG activity concentration in the background compartment of the phantom at the start of the PET scan, as determined in step 2. In case $[B_{true}]$ deviates from 2.0 kBq/mL, the ratio $[B_{true}]/2.0$ in formula 1 is necessary as in the EARL procedure [10], it is assumed that the background of the IQ phantom is filled with 2.0 kBq/mL FDG activity. An activity concentration of 2.0 kBq/mL would represent a patient with a reference body weight (w_{ref}) of 75 kg, who received a reference FDG activity (A_{ref}) of 300 MBq, 60 min prior to the scan time T_a [10]. Furthermore, a maximum COV (COV_{max}) of 0.15 is proposed as a cut-off to set the minimal scan time [10].

Output

T_{min} at a predefined COV_{max}.

Step 7: EARL compatibility check at T_{min}

- Check whether the RCs are still within EARL specifications at T_{min}.
- If this is the case, continue to step 8.
- If this is not the case, go back to step 3 and update the PET reconstruction settings, within the recommendations indicated in the EANM FDG-PET/CT procedure guidelines version 2.0 [2].

Step 8: derivation of a patient-specific FDG activity formula

To determine the final FDG activity formula, the following input parameters are required:

- T_{min} (in seconds): the minimal scan time to reach COV_{max}, as derived in step 6.
- A_{ref} and w_{ref}: a reference FDG activity and reference body weight.

Formula 2 shows the formula for the product of FDG activity (*A* in MBq) to administer and the scan time *t* (in seconds) per bed position as applied in a clinical setting.

$$A \cdot t = \frac{w^2}{w_{ref}^2} \cdot A_{ref} \cdot T_{min} \tag{2}$$

The product $A \cdot t$ depends quadratically on a patient's body weight and satisfies the EANM guideline in terms of RCs and COV.

Using $w_{ref} = 75$ kg and $A_{ref} = 300$ MBq as suggested by [10], formula 2 simplifies to:

$$A \cdot t = 0.0533 \cdot w^2 \cdot T_{min} \tag{3}$$

Results

We have tested the methodology described above using a state-of-the-art PET/CT scanner (Ingenuity TF, Philips Healthcare).

Step 1: phantom preparation

We filled the IQ phantom with FDG activity. At $T_{m,1} = 16{:}24{:}00$, the concentration in the phantom spheres $[S_{true}]$ was 30.2 kBq/mL. Furthermore, the phantom background concentration $[B_{true}]$ was 2.4 kBq/mL at $T_{m,2} = 16{:}58{:}00$.

Step 2: PET/CT acquisition

We performed a PET/CT scan which started at $T_a = 17{:}38{:}00$. Consequently, $[S_{true}]$ and $[B_{true}]$ at T_a were 18.9 and 1.84 kBq/mL, respectively.

Step 3: PET/CT image reconstruction

We made a PET reconstruction using a default 3D ordered-subset iterative TOF reconstruction technique with 144 × 144 matrices (voxel size $4 \times 4 \times 4$ mm^3), 3 iterations, 43 subsets and a relaxation parameter 1.0 (“normal” smoothing setting), consistent with the reconstruction setting suggestions in the EANM guideline [1]. The reconstruction method is based on blobs, to compensate for detector blurring. The blob had a 2.5 mm radius, with a blob shape parameter of 8.4 mm. **Figure 2** shows an axial PET and CT image of the IQ phantom filled with FDG.

Step 4: EARL compatibility check

Mean and maximum RCs at 10 min scan duration are shown in **Table 1**. All RCs were within the EARL specifications.

Table 1 RC_{mean} and RC_{max} ranges as defined by EARL [8], compared with RC results for all spheres at 10 min and 62 s scan duration. For all spheres, RCs were within EARL specifications

Sphere volume (mL)	EARL: RC_{mean} range	RC_{mean} at $t = 600$ s	RC_{mean} at $t = 62$ s	EARL: RC_{max} range	RC_{max} at $t = 600$ s	RC_{max} at $t = 62$ s
26.52	0.76–0.89	0.79	0.80	0.95–1.16	0.98	1.05
11.49	0.72–0.85	0.75	0.74	0.91–1.13	0.96	1.04
5.57	0.63–0.78	0.72	0.69	0.83–1.09	0.97	0.94
2.57	0.57–0.73	0.68	0.64	0.73–1.01	0.93	0.90
1.15	0.44–0.60	0.44	0.48	0.59–0.85	0.59	0.71
0.52	0.27–0.38	0.33	0.27	0.31–0.49	0.44	0.40

Step 5: image coefficient of variation measurements at shorter scan times

We used list-mode data with start time T_a to perform additional reconstructions with shorter scan durations and determined the COV from nine ROIs with three rectangular ROIs, as illustrated in **Figure 2**, in three planes each.

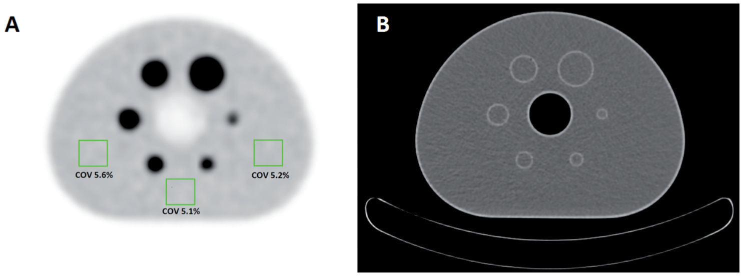

Figure 2 Phantom PET/CT images. Axial PET (A) and attenuation CT (B) images from the IQ phantom on the scanner bed. The phantom spheres and background were filled with FDG activity (ratio 10:1), and the scan duration was 10 min. The *squares* illustrate three ROIs in one axial plane that are used to determine the COV

Step 6: derivation of the minimal scan time T_{min}

In **Figure 3**, the measured COVs are presented as a function of the scan duration. The values of the power-law fit parameters were $a = 1.26$ and $b = 0.51$. Using formula 1 with $COV_{max} = 0.15$ and $[B_{true}] = 1.84$ kBq/mL, the minimal scan time T_{min} was found to be 62 s.

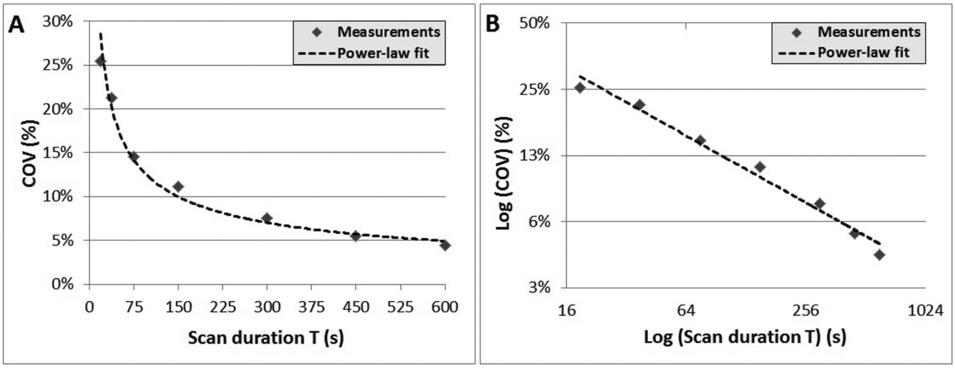

Figure 3 Comparing COV in the phantom background compartment measured at several scan durations, in graphs with standard scale (A) and log-log scale (B). A power-law fit resulted in $COV = 1.26T^{-0.51}$. The coefficient of determination r^2 was 0.98, which indicates a good fit of the trend line to the data. Using the fit result, $[B_{true}] = 1.84$ kBq/mL and $COV_{max} = 0.15$, formula 1 resulted in $T_{min} = 62$ s. The log-log scale graph can be described by $\log(COV) = \log(a) - b \cdot \log(T)$ in which the steepness of the curve is described by b

Step 7: EARL compatibility check at T_{min}

Mean and maximum RCs at $T_{min} = 62$ s scan duration are shown in **Table 1**. All RCs were within the EARL specifications.

Step 8: derivation of a patient-specific FDG activity formula

Using **formula 3** with $T_{min} = 62$ s, we derived the following body-weight-dependent formula for the product of FDG activity to administer and scan time per bed position:

$$A \cdot t = 3.29\, w^2 \tag{4}$$

Discussion

The FDG activity formula presented in this paper provides a constant and standardized PET image quality for all patients [7]. Changing the value of COV_{max} will impact image quality and quantification accuracy. Ideally, its value should be chosen in such way that it provides the highest diagnostic accuracy. Note, however, that according to [10], COV_{max} should remain below 15 %, to keep image quality and quantification accuracy within acceptable limits. A lower COV_{max} value can easily be implemented in formula 1 and will result in higher FDG activity per patient, compared to the result based on a COV_{max} of 0.15. Furthermore, we used the EARL prescription that a phantom background compartment filled with 2.0 kBq/mL FDG activity represents a patient of 75 kg who received 300 MBq FDG activity. However, these reference values can be easily modified using formulas 1 and 2.

Our method includes a RC verification step on PET data acquired with the minimal scan time T_{min}. This is important because it has been shown that an upward bias of (maximal) RCs can be expected at low scan statistics [11, 12]. In case RCs are above EARL requirements, it may therefore be helpful to apply an additional post-smoothing filter in the reconstruction that may compensate for this bias. It may also occur that an individual RC measurement does not fit EARL RC specifications due to statistical uncertainties at a shorter scan duration. When the difference between RCs and EARL requirements is relatively small, possibly after updating the reconstruction settings, it may also be useful to just repeat the reconstruction at a different time frame, e.g. starting at T_{min} and ending at $2 \cdot T_{min}$.

Our suggested FDG activity formula provides an image quality that is achievable with multiple scanners at multiple PET centres. However, the reconstruction settings within this protocol are not necessarily optimized for optimal image quality. The latest generation PET scanners can provide an improved image quality. For example, the use of smaller voxels or point-spread function modelling, may improve the detection of small lesions [13, 14]. However, such reconstructions may also increase the image coefficient of variation and could therefore require a higher dose.

Furthermore, as already mentioned by de Groot et al.[7], the quadratic FDG activity regime results in very high levels of administered FDG activity for very heavy patients, when the scan time is not adapted. This may increase count rate losses of the system, and it increases the radiation burden for both the patient and the technician. Typically, it is recommended not to administer more than 530 MBq FDG activity for lutetium oxyorthosilicate systems [1, 6]. Using formula 4, with, e.g. an intrinsic scan time t of 90 s, this would imply that for patients with a body weight above 120 kg, it is advised not to further increase the administered FDG activity.

We derived the minimal scan time T_{min} by applying a power-law fit, to reduce the impact of single COV measurements at fixed time points. It can be discussed whether a power law is the best fit to describe the COV as a function of scan time. We assume that a power law can fit the data as noise properties in PET generally can be represented by a Poisson model, i.e. COV is generally inversely proportional to the square root of the measured counts. However, COV measurements, that are based on reconstructed data, may be influenced by detector dead time, normalization, attenuation correction or the reconstruction algorithm that is applied [4, 15]. Thereby, measured noise may not necessarily be represented by a Poisson model and hence a power-law fit may not be the best function to fit our COV data as a function of scan time. Furthermore, other techniques might be applied to estimate T_{min}, for example by connecting the data points and reading the graph at a given COV_{max}. In our study, the coefficient of determination r^2 of 0.98 indicates a good fit of the power-law trend line to our data.

Conclusion

This technical note provides a practical method that results in a formula describing the FDG activity to administer to individual patients for whole-body PET examinations, taking into account both the EANM guidelines and a quadric relation between FDG activity and a patient's body weight.

References

1. Boellaard R, O'Doherty M,J., Weber WA, Mottaghy FM, Lonsdale MN, Stroobants SG, Oyen WJG, Kotzerke J, Hoekstra OS, Pruim J. FDG PET and PET/CT: EANM procedure guidelines for tumour PET imaging: version 1.0. Eur J Nucl Med Mol Imaging 2010;37:181-200.
2. Boellaard R, Delgado-Bolton R, Oyen WJG, Giammarile F, Tatsch K, Eschner W, Verzijlbergen FJ, Barrington SF, Pike LC, Weber WA. FDG PET/CT: EANM procedure guidelines for tumour imaging: version 2.0. Eur J Nucl Med Mol Imaging 2015;42:328-54.
3. Everaert H, Vanhove C, Lahoutte T, Muylle K, Caveliers V, Bossuyt A, Franken PR. Optimal dose of 18F-FDG required for whole-body PET using an LSO PET camera. Eur J Nucl Med Mol Imaging 2003;30:1615-9.
4. Watson CC, Casey ME, Bendriem B, Carney JP, Townsend DW, Eberl S, Meikle S, DiFilippo FP. Optimizing injected dose in clinical PET by accurately modeling the counting-rate response functions specific to individual patient scans. J Nucl Med 2005;46:1825-34.
5. Halpern BS, Dahlbom M, Auerbach MA, Schiepers C, Fueger BJ, Weber WA, Silverman DHS, Ratib O, Czernin J. Optimizing imaging protocols for overweight and obese patients: a lutetium orthosilicate PET/CT study. J Nucl Med 2005;46:603-7.
6. Masuda Y, Kondo C, Matsuo Y, Uetani M, Kusakabe K. Comparison of imaging protocols for 18F-FDG PET/CT in overweight patients: optimizing scan duration versus administered dose. J Nucl Med 2009;50:844-8.
7. de Groot E,H., Post N, Boellaard R, Wagenaar NRL, Willemsen ATM, van Dalen J,A. Optimized dose regimen for whole-body FDG-PET imaging. EJNMMI Res 2013;3:63-72.
8. EARL. EANM FDG PET/CT accreditation specifications for SUV recovery coefficients. http://earl.eanm.org/cms/website.php. Accessed Jan 30, 2016.
9. Performance measurements of positron emission tomographs. NEMA Standards Publication NU 2-2012.
10. Boellaard R, Willemsen AT, Arends B, Visser EP. EARL procedure for assessing PET/CT system specific patient FDG activity preparations for quantitative FDG PET/CT studies. EANM research Ltd (EARL). http://earl.eanm.org/html/img/pool/EARL-procedure-for-optimizing-FDG-activity-for-quantitative-FDG-PET-studies_version_1_1.pdf.
11. Boellaard R, Krak NC, Hoekstra OS, Lammertsma AA. Effects of noise, image resolution, and ROI definition on the accuracy of standard uptake values: a simulation study. J Nucl Med 2004;45:1519-27.
12. Lodge MA, Chaudhry MA, Wahl RL. Noise considerations for PET quantification using maximum and peak standardized uptake value. J Nucl Med 2012;53:1041-7.
13. Koopman D, van Dalen J,A., Lagerweij MCM, Arkies H, de Boer J, Oostdijk AHJ, Slump CH, Jager PL. Improving the detection of small lesions using a state-of-the-art time-of-flight PET/CT system and small-voxel reconstructions. J Nucl Med Technol 2015;43:21-7.

14. Schaefferkoetter J, Casey M, Townsend D, El Fakhri G. Clinical impact of time-of-flight and point response modeling in PET reconstructions: a lesion detection study. Phys Med Biol 2013;58:1465-78.
15. Teymurazyan A, Riauka T, Jans H, Robinson D. Properties of noise in positron emission tomography images reconstructed with filtered-backprojection and row-action maximum likelihood algorithm. J Digital Imaging 2013;26:447-56.

CHAPTER 4

4

Digital PET compliance to EARL accreditation specifications

Authors

Daniëlle Koopman[1,2] | Maureen Groot Koerkamp[1,2] | Pieter L. Jager[1]
Hester Arkies[1] | Siert Knollema[1] | Cornelis H. Slump[2] | Pedro G. Sanches[3]
Jorn A. van Dalen[4]

Author Affiliations
1: Department of Nuclear Medicine, Isala, Zwolle, the Netherlands
2: MIRA Institute for Biomedical Technology and Technical Medicine, University of Twente, Enschede, the Netherlands
3: Health Systems, Philips Benelux, Eindhoven, the Netherlands
4: Department of Medical Physics, Isala, Zwolle, the Netherlands

Published in
EJNMMI Physics 2017;4:9-14

Abstract

Background
Our aim was to evaluate if a recently introduced TOF PET system with digital photon counting technology (Philips Healthcare), potentially providing an improved image quality over analogue systems, can fulfil EANM research Ltd (EARL) accreditation specifications for tumour imaging with FDG-PET/CT.

Findings
We have performed a phantom study on a digital TOF PET system using a NEMA NU2-2001 image quality phantom with six fillable spheres. Phantom preparation and PET/CT acquisition were performed according to the European Association of Nuclear Medicine (EANM) guidelines. We made list-mode ordered-subsets expectation maximization (OSEM) TOF PET reconstructions, with default settings, three voxel sizes (4×4×4 mm^3, 2×2×2 mm^3 and 1×1×1 mm^3) and with/without point spread function (PSF) modelling.

On each PET dataset, mean and maximum activity concentration recovery coefficients (RC_{mean} and RC_{max}) were calculated for all phantom spheres and compared to EARL accreditation specifications. The RCs of the 4×4×4 mm^3 voxel dataset without PSF modelling proved closest to EARL specifications. Next, we added a Gaussian post-smoothing filter with varying kernel widths of 1–7 mm. EARL specifications were fulfilled when using kernel widths of 2 to 4 mm.

Conclusions
TOF PET using digital photon counting technology fulfils EARL accreditation specifications for FDG-PET/CT tumour imaging when using an OSEM reconstruction with 4× 4×4 mm^3 voxels, no PSF modelling and including a Gaussian post-smoothing filter of 2 to 4 mm.

Keywords
Digital PET; EANM guidelines; EARL accreditation; FDG-PET Tumour imaging

Introduction

Recently, a time-of-flight (TOF) positron emission tomography (PET) system was introduced by Philips Healthcare, with digital photon counting technology using silicon photomultipliers. The replacement of conventional photomultipliers by digital detectors, including the implementation of single-photon avalanche photodiodes, provides true digital photon counting without the need of additional analogue-to-digital conversions [1-3]. Moreover, the detector elements and the scintillator crystals have equal sizes which enables one-to-one coupling. Acceptance tests on performance characteristics showed that this digital PET provides a higher timing resolution and improved spatial resolution, as compared to state-of-the-art analogue PET using conventional photomultipliers [4, 5]. In clinical practice, digital PET may provide a higher image quality and improved small lesion detection and quantification [6].

PET/computed tomography (CT) scanning, using fluor-18 fluordeoxyglucose (FDG), has an important role in tumour imaging for patients with cancer. There is a trend towards standardization in FDG-PET scanning to allow quantitative comparisons of FDG-uptake parameters across patients, scanners and medical centres [7]. To support standardization between scanners and medical centres, the European Association of Nuclear Medicine (EANM) has published guidelines on FDG-PET tumour imaging [7, 8]. Furthermore, the EANM launched the EANM research Ltd (EARL) to promote nuclear medicine research and multi-centre studies. EARL has developed an accreditation programme for tumour imaging with FDG-PET/CT [9].

In clinical practice, the EARL FDG-PET/CT accreditation specifications are widely implemented. These specifications, which are primarily about activity concentration recovery coefficient (RC) measurements on PET images, are based on analogue PET systems using conventional photomultipliers [7, 8]. Intrinsically, higher RCs may be expected using digital PET, due to improved spatial and time-of-flight resolution compared to other non-digital, but state-of-the-art systems [5]. Our aim was to evaluate if a recently introduced TOF PET/CT system with digital photon counting technology can fulfil EARL requirements as well.

Method

Phantom study

We have performed a phantom study using a NEMA IEC-61675-1 NU2-2001 image quality phantom (IQ phantom) with six fillable spheres (10, 13, 17, 22, 28 and 37 mm diameter). According to the EANM guidelines [7], the IQ phantom was filled with FDG-activity, with a sphere-to-background ratio of 10:1. Using a TOF PET/CT system with digital photon counting technology (Philips Healthcare) [6], we performed a PET scan of one bed position with a scan duration of 10 min. Additionally, a CT scan was acquired for attenuation correction. Prior to our measurements, the digital PET was calibrated with FDG and verified to be within an offset of 2%, using the method as described in [7].

PET reconstructions

We have performed six default TOF PET reconstructions, using blob-based ordered-subsets expectation maximization (OSEM) [10], with three voxel sizes and with/without point spread function (PSF) modelling, which corrects for partial-volume effects in PET images. When incorporating PSF modelling, we used a noise regularization kernel of 6 mm full-width at half-maximum and 1 PSF iteration. For each voxel size, we used a fixed number of iterations and subsets, as recommended by the manufacturer.

1. 4×4×4 mm^3, with 3 iterations and 15 subsets, without PSF
2. 4×4×4 mm^3, with 3 iterations and 15 subsets, with PSF
3. 2×2×2 mm^3, with 3 iterations and 17 subsets, without PSF
4. 2×2×2 mm^3, with 3 iterations and 17 subsets, with PSF
5. 1×1×1 mm^3, with 3 iterations and 9 subsets, without PSF
6. 1×1×1 mm^3, with 3 iterations and 9 subsets, with PSF

On each reconstructed PET dataset, we calculated mean and maximum activity concentration recovery coefficients (RC_{mean} and RC_{max}) for all phantom spheres, according to EANM guidelines [7]. Next, we compared our RC results with EARL accreditation specifications [9].

To evaluate reconstruction settings for digital PET that meet the requirements for EARL accreditation, we performed additional reconstructions. We selected the reconstructed PET dataset whose RCs fitted best to the EARL accreditation specifications and added a 3D Gaussian post-smoothing filter with varying kernel widths of 1–7 mm, using standard vendor software. Again, RC_{mean} and RC_{max} were measured for all phantom spheres and compared to EARL accreditation specifications.

Results

Figure 1 shows RC$_{\text{mean}}$ and RC$_{\text{max}}$ results for all spheres, for each of the six default PET reconstructions. For each reconstruction, at least one RC$_{\text{max}}$ value was above EARL accreditation specifications. The PET reconstruction without PSF modelling and using 4×4×4 mm^3 voxels showed RCs nearest to EARL requirements. For this specific reconstruction, only RC$_{\text{max}}$ for the 10-mm sphere was above the EARL limit.

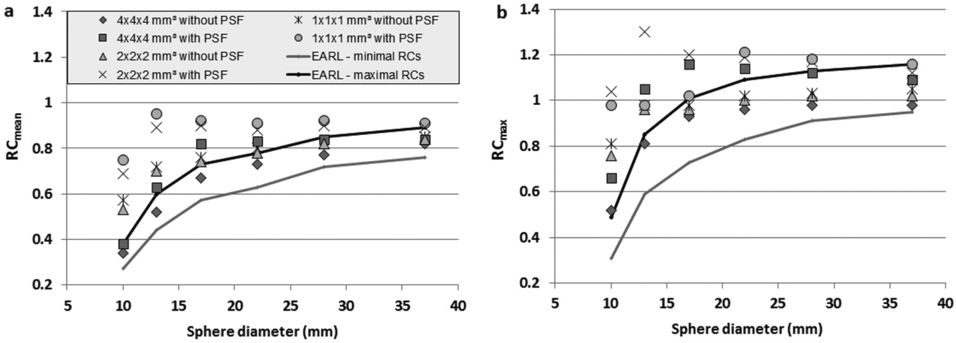

Figure 1 RC$_{\text{mean}}$ and RC$_{\text{max}}$ values for all phantom spheres, as compared to EARL minimal and maximal accreditation specifications. a. RC$_{\text{mean}}$ for six default TOF PET reconstructions. Only for a PET reconstruction using 4×4×4 mm^3 voxels without PSF modelling, RC$_{\text{mean}}$ values were all within accreditation specifications. **b.** RC$_{\text{max}}$ for six default TOF PET reconstructions. For all reconstructions, at least one RC$_{\text{max}}$ was above maximal accreditation specifications

Table 1 shows the impact of an additional Gaussian post-smoothing filter with 1 to 7 mm kernel widths, on RC$_{\text{mean}}$ and RC$_{\text{max}}$ in a PET reconstruction using 4 × 4 × 4 mm^3 voxels, without PSF modelling. As shown in **Figure 2**, EARL accreditation specifications for RC$_{\text{mean}}$ and RC$_{\text{max}}$ can be achieved with digital PET using filters with kernel widths of 2 to 4 mm.

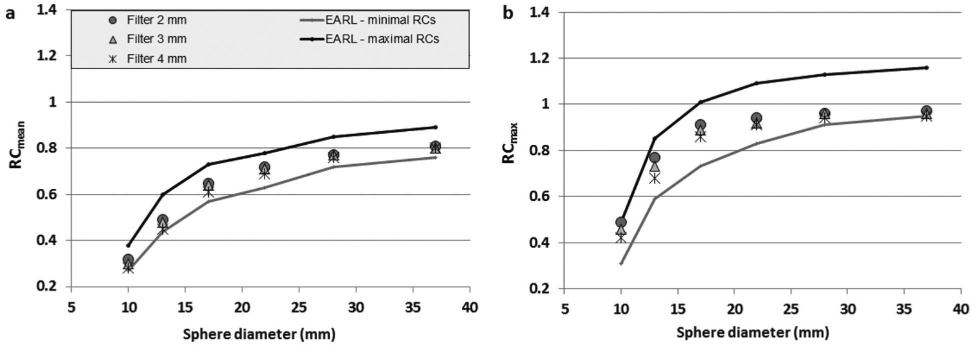

Figure 2 Impact of a Gaussian post-smoothing filter using a kernel width of 2, 3 and 4 mm on RC_{mean} (a) and RC_{max} (b) for a TOF PET reconstruction with 4×4×4 mm³ voxels without PSF modelling. For all phantom spheres, both RC_{mean} and RC_{max} fulfilled EARL accreditation specifications

Table 1 The impact of a Gaussian post-smoothing filter with a kernel width of 1–7 mm on RC_{mean} and RC_{max} for a TOF PET reconstruction with 4×4×4 mm³ voxels, without PSF modelling. RCs within EARL accreditation specifications are marked in italic style

Recon Sphere diameter (mm)	EARL minimum	EARL maximum	No filter	Filter 1 mm	Filter 2 mm	Filter 3 mm	Filter 4 mm	Filter 5 mm	Filter 6 mm	Filter 7 mm
	RC_{mean}									
10	0.27	0.38	*0.34*	*0.33*	*0.32*	*0.30*	*0.28*	0.26	0.24	0.22
13	0.44	0.60	*0.52*	*0.51*	*0.49*	*0.48*	*0.45*	0.42	0.39	0.35
17	0.57	0.73	*0.67*	*0.65*	*0.65*	*0.64*	*0.61*	*0.58*	0.55	0.52
22	0.63	0.78	*0.73*	*0.72*	*0.72*	*0.71*	*0.69*	*0.67*	*0.64*	0.62
28	0.72	0.85	*0.77*	*0.77*	*0.77*	*0.77*	*0.76*	*0.74*	*0.72*	0.71
37	0.76	0.89	*0.82*	*0.81*	*0.81*	*0.80*	*0.80*	*0.78*	*0.77*	0.76
	RC_{max}									
10	0.31	0.49	*0.52*	*0.51*	*0.49*	*0.46*	*0.42*	*0.38*	*0.34*	0.31
13	0.59	0.85	*0.81*	*0.80*	*0.77*	*0.73*	*0.68*	*0.63*	0.57	0.51
17	0.73	1.01	*0.93*	*0.92*	*0.91*	*0.89*	*0.86*	*0.82*	*0.77*	0.72
22	0.83	1.09	*0.96*	*0.96*	*0.94*	*0.92*	*0.91*	*0.90*	*0.89*	*0.87*
28	0.91	1.13	*0.98*	*0.98*	*0.96*	*0.96*	*0.94*	*0.93*	*0.92*	*0.91*
37	0.95	1.16	*0.98*	*0.98*	*0.97*	*0.96*	*0.95*	0.94	0.94	0.94

Conclusion

PET with digital photon counting technology typically shows an activity concentration recovery coefficient above EARL specifications, especially for small objects. To meet EARL standards, a TOF OSEM reconstruction without PSF modulation, with 3 iterations, 15 subsets, 4×4×4 mm^3 voxels and a Gaussian post-smoothing filter with a kernel width of 2 to 4 mm can be used.

Discussion

To meet EARL standards for PET with digital photon counting technology, the use of relatively large 4×4×4 mm^3 voxels and a post-smoothing filter is recommended. With smaller voxel sizes and/or PSF modelling, RCs in our study were above EARL specifications. This has been demonstrated for state-of-the-art analogue PET systems as well [11, 12]. With the introduction of advanced reconstruction algorithms (e.g. using small voxels or incorporating PSF modelling), eventually combined with new digital PET technologies, EARL specification updates may be needed in the future. Under the assumption that the availability and presence of PET scanners using older technology will decrease, a way to maintain the uniformity across modern PET cameras is to increase both lower- and upper RC EARL specifications, especially for small spheres. Furthermore, the use of smaller phantom spheres, for example as available in a micro phantom that we used in a previous study [11], may be warranted to be able to compare reconstruction algorithms for smaller sphere sizes and to harmonize the quantification of small lesions across scanners.

Besides, given the high RCs that can be achieved with digital photon counting technology combined with advanced reconstruction settings, it might be appropriate to perform multiple PET reconstructions for different purposes. Next to an EARL-approved reconstruction to perform quantitative analyses, a high-resolution small-voxel PET reconstruction could be made for visual evaluation and optimal small lesion detection [8, 11, 13].

This short communication focused on determing PET reconstruction settings to fulfil EARL RC specifications. However, to obtain the EARL accreditation, these reconstruction settings should be chosen to meet both RC requirements and specifications for the calibration QC [7], and EANM guidelines should be fully implemented in clinical practice [7, 8].

Declarations

Funding

This work was supported by a research exhibit with Philips Healthcare (Exhibit B: phantom based comparison of conventional and digital photon counting PET technology).

Competing interests

The Department of Nuclear Medicine, Isala, has established a research cooperation with Philips Healthcare regarding new PET technologies. Pedro G. Sanches is an employee of Philips Healthcare, in the position of clinical scientist. The content of the article was solely the responsibility of the authors. The other authors declare that they have no competing interests.

References

1. Frach T, Prescher G, Degenhardt C, de Gruyter R, Schmitz A, Ballizany R. The digital silicon photomultiplier—Principle of operation and intrinsic detector performance. IEEE Nucl Sci Symp Conf Rec 2009:1959-65.
2. Degenhardt C, Prescher G, Frach T, Thon A, de Gruyter R, Schmitz A, Ballizany R. The digital silicon photomultiplier—A novel sensor for the detection of scintillation light. IEEE Nucl Sci Symp Conf Rec 2009:2383-6.
3. Degenhardt C, Rodrigues P, Trindade A, Zwaans B, Mülhens O, Dorscheid R, Thon A, Salomon A, Frach T. Performance evaluation of a prototype positron emission tomography scanner using digital photon counters (DPC). IEEE Nucl Sci Symp Conf Rec 2012.
4. Miller M, Zhang J, Binzel K, Griesmer J, Laurence T, Narayanan M, Natarajamani D, Wang S, Knopp M. Characterization of the vereos digital photon counting PET system. J Nucl Med 2015;56:434.
5. Slomka PJ, Pan T, Germano G. Recent advances and future progress in PET instrumentation. Semin Nucl Med 2016;46:5-19.
6. Nguyen NC, Vercher-Conejero J, Sattar A, Miller MA, Maniawski PJ, Jordan DW, Muzic RF, Su K, O'Donnell J,K., Faulhaber PF. Image quality and diagnostic performance of a digital PET prototype in patients with oncologic diseases: Initial experience and comparison with analog PET. J Nucl Med 2015;56:1378-85.
7. Boellaard R, O'Doherty M,J., Weber WA, Mottaghy FM, Lonsdale MN, Stroobants SG, Oyen WJG, Kotzerke J, Hoekstra OS, Pruim J. FDG PET and PET/CT: EANM procedure guidelines for tumour PET imaging: version 1.0. Eur J Nucl Med Mol Imaging 2010;37:181-200.
8. Boellaard R, Delgado-Bolton R, Oyen WJG, Giammarile F, Tatsch K, Eschner W, Verzijlbergen FJ, Barrington SF, Pike LC, Weber WA. FDG PET/CT: EANM procedure guidelines for tumour imaging: version 2.0. Eur J Nucl Med Mol Imaging 2015;42:328-54.
9. EARL. EANM FDG PET/CT accreditation specifications for SUV recovery coefficients. Accessed June 1, 2016.
10. Wang W, Hu Z, Gualtieri EE, Parma MJ, Walsh ES, Sebok D, Hsieh Y, Tung C, Song X, Griesmer JJ. Systematic and distributed time-of-flight list mode PET reconstruction. IEEE Nucl Sci Symp Conf Rec 2006.
11. Koopman D, van Dalen J,A., Lagerweij MCM, Arkies H, de Boer J, Oostdijk AHJ, Slump CH, Jager PL. Improving the detection of small lesions using a state-of-the-art time-of-flight PET/CT system and small-voxel reconstructions. J Nucl Med Technol 2015;43:21-7.

12. Lasnon C, Salomon T, Desmonts C, Dô P, Oulkhouir Y, Madelaine J, Aide N. Generating harmonized SUV within the EANM EARL accreditation program: software approach versus EARL-compliant reconstruction. Ann Nucl Med 2017;31:125-34.
13. Lasnon C, Desmonts C, Quak E, Gervais R, Do P, Dubos-Arvis C, Aide N. Harmonizing SUVs in multicentre trials when using different generation PET systems: prospective validation in non-small cell lung cancer patients. Eur J Nucl Med Mol Imaging 2013;40:985-96.

CHAPTER 5

5

SUV variability in EARL-accredited conventional and digital PET

Authors

Daniëlle Koopman[1,2] | Pieter L. Jager[1] | Cornelis H. Slump[2]
Siert Knollema[1] | Jorn A. van Dalen[3]

Author Affiliations
1: Department of Nuclear Medicine, Isala, Zwolle, the Netherlands
2: Technical Medicine Center, University of Twente, Enschede, the Netherlands
3: Department of Medical Physics, Isala, Zwolle, the Netherlands

Submitted to
EJNMMI Research

Abstract

Background

A high SUV-reproducibility is crucial when different PET scanners are in use. We evaluated the SUV variability in whole-body FDG-PET scans of patients with suspected or proven cancer using an EARL-accredited conventional and digital PET scanner.

In a head-to-head comparison we studied images of 50 patients acquired on a conventional scanner (cPET, Ingenuity TF PET/CT, Philips) and compared them with images acquired on a digital scanner (dPET, Vereos PET/CT, Philips). The PET scanning order was randomised and EARL-compatible reconstructions were applied.

We measured SUV_{mean}, SUV_{peak} SUV_{max} and lesion diameter in up to 5 FDG-positive lesions per patient. The relative difference ΔSUV between cPET and dPET was calculated for each SUV-parameter. Furthermore, we calculated repeatability coefficients, reflecting the 95% confidence interval of ΔSUV.

Results

We included 128 lesions with an average size of 19±14 mm. Average ΔSUVs were 6-8% with dPET values being higher for all three SUV-parameters ($p<0.001$). ΔSUV_{max} was significantly higher than ΔSUV_{mean} (8% vs. 6%, $p=0.002$) and then ΔSUV_{peak} (8% vs. 7%, $p=0.03$). Repeatability coefficients across individual lesions were 27% (ΔSUV_{mean} and ΔSUV_{peak}) and 33% (ΔSUV_{max}) ($p<0.001$).

Conclusions

With EARL-accredited conventional and digital PET, we found a limited SUV variability with average differences up to 8%. Furthermore, only a limited number of lesions showed a SUV difference of more than 30%. These findings indicate that EARL standardisation works.

Keywords

FDG-PET; EARL-accreditation; Conventional PET; Digital PET, Cancer

Background

Positron emission tomography/computed tomography (PET/CT) using fluor-18 fluorodeoxyglucose (FDG) is widely used for tumour imaging in patients with cancer. There are ongoing efforts towards standardization of FDG-PET imaging to allow a quantitative comparison between patients, scanners and medical centres. In 2009 and 2015 the European Association of Nuclear Medicine (EANM) published procedure guidelines on FDG-PET/CT tumour imaging [1, 2]. Furthermore, the EANM launched the EANM Research Ltd. (EARL) to promote nuclear medicine research, including multi-centre trials. In 2010, EARL started an accreditation program for FDG-PET/CT tumour imaging. This includes EARL-accreditation requirements based on activity concentration recovery coefficients (CRCs) as measured in PET images of a NEMA NU2-2001 image quality phantom. A recent evaluation among the first 200 accredited systems from 150 sites worldwide showed that setting up a harmonizing accreditation program is feasible and achievable, and that the FDG-PET/CT program has reduced the variability in semi-quantitative PET performance [3].

Recently, time-of-flight (TOF) PET systems with silicon photomultipliers (SiPM) with digital readout were introduced in clinical practice [4-6]. Although these systems potentially improve image quality compared to PET systems using conventional photomultiplier technology, they can also fulfil EARL accreditation specifications for tumour imaging with FDG-PET/CT when appropriate reconstruction settings are used [6, 7]. Hence, independent of detector technology, PET systems should provide comparable semi-quantitative results once they fulfil EARL specifications. To our knowledge, this has not yet been explored in clinical practice in a substantial group of patients. Therefore, our aim was to investigate the variability in standardized uptake values (SUVs) on whole-body FDG-PET scans from patients with cancer, using both a conventional and digital EARL-accredited PET scanner.

Materials and methods

Inclusion

We performed a prospective single-centre side-by-side comparison study in 50 patients with suspected or proven cancer who were referred for whole-body FDG-PET/CT. Written informed consent was obtained from all participants included in this study. The Medical Ethical Committee of our institution (METC Isala, Zwolle, Netherlands) approved the study protocol (NL52329.075.15).

PET/CT acquisition

Patients fasted for at least 6h prior to the PET scan. Blood glucose levels were measured before intravenous injection of FDG, to ensure a value below 10 mmol/L. Patients were administered a FDG-activity based on $A = 6.2\, w^2\!/t$, where A is the FDG-activity administered in Megabecquerel (MBq), w is the patient's body weight in kilogram (kg) and t is the acquisition time per bed position in seconds (s) [8].

For each patient whole-body PET scans from head to groin were acquired in supine position using a state-of-the-art TOF PET/CT scanner with conventional photomultiplier technology (cPET, Ingenuity TF, Philips Healthcare) and a TOF PET/CT scanner with digital SIPMs and digital readout (dPET, Vereos, Philips Healthcare). Both systems were EARL-accredited. For both PET scanners the error in cross-calibration with the associated dose calibrator was less than 5%. The PET scanning order was randomized per patient. We included 25 patients who were first scanned on dPET and afterwards on cPET (*dPET-first group*) and we included 25 patients who were first scanned on cPET and afterwards on dPET (*dPET-second group*). Per patient and per scan we collected ΔT which was defined as the time between FDG-administration and the start of the PET scan.

PET acquisition times of the first scan were 72 s and 144 s per bed position for patients with body weight ≤80 kg and >80 kg, respectively. For the second scan the scan time per bed position was equal to the scan time of the first scan plus a compensation for the radioactive decay of fluor-18. The resulting average scan time of the second PET scan was 85 s (range 72-91 s) for patients ≤80 kg and 180 s (range 147-205 s) for patients >80 kg.

Prior to each PET scan a CT scan was acquired for attenuation correction. The CT scan parameters were 120 kV, 64 mAs (range 39-136 mAs), 64×0.625 mm slice collimation, a pitch of 0.83 and a rotation time of 0.5 s.

PET/CT reconstruction

For both systems we used EARL-compatible reconstructions. For cPET an Ordered Subset Expectation Maximization (OSEM) TOF PET reconstruction was applied with 4x4x4 mm^3 voxels and a relaxation parameter of 1.0, without point spread function (PSF) modelling, as previously described [9]. For dPET we performed an OSEM TOF PET reconstruction with 4x4x4 mm^3 voxels and a 3 mm Gaussian post-smoothing filter, without PSF modelling, as previously described [7]. For both cPET and dPET attenuation correction was applied using iteratively reconstructed CT data with iDose level 4 and a slice thickness of 3 mm.

Semi-quantitative evaluation

Semi-quantitative analyses were performed using the quAntitative onCology moleCUlar Analysis suiTE (ACCURATE) tool [10]. For each patient we included a maximum of 5 FDG-positive lesions, to prevent a possible bias from patients with many lesions. In case a patient had more than 5 eligible lesions, we selected the 5 lesions with the shortest diameter on the CT scan and which were measurable on both PET scans using the ACCURATE tool.

For each lesion we measured the mean, peak and maximum standardized uptake value (SUV_{mean}, SUV_{peak} and SUV_{max}) on cPET and dPET images. SUV_{mean} was based on the 3D isocontour derived at 50% of the maximum pixel value. SUV_{peak} was defined as the average SUV of a spherical 1 cm^3 volume-of-interest in the tumour-region with the highest uptake [11]. Furthermore, we measured the short-axis diameter on the axial slice of the CT scan.

Following the paper by Lodge [12] we calculated the relative difference ΔSUV per lesion between cPET and dPET for SUV_{mean}, SUV_{peak} and SUV_{max} using **formula 1**.

$$\Delta SUV = \frac{SUV_{dPET} - SUV_{cPET}}{(SUV_{dPET} + SUV_{cPET}) \cdot 0.5} \tag{1}$$

In addition, we derived the standard deviation (SD) of ΔSUV and we calculated the repeatability coefficient (RC) using **formula 2**.

$$RC = 1.96 \times SD(\Delta SUV) \tag{2}$$

The RC reflects the 95% confidence interval of ΔSUV. Moreover, we counted the number of lesions with an absolute ΔSUV ≥30% for all three SUV-parameters as this cut-off value is considered by PERCIST to indicate a switch from “stable” disease to either “progression” or “response” [13].

Statistical analysis

The statistical analysis was performed using SPSS Version 24. Quantitative results were presented as mean ± SD. Data distribution normality was evaluated using the Shapiro-Wilk test. For data that were not normally distributed the median was included as well. We performed an independent-samples t-test to compare patient and scan characteristics (age, body weight, administered FDG-activity and ΔT) between patients in both scanning groups. Furthermore, we performed the Mann-Whitney U-test to compare lesion diameters between lesions in both scanning groups. Differences in average SUV_{mean}, SUV_{peak} and SUV_{max} between cPET and dPET were evaluated with the Wilcoxon signed-rank test. To test whether average ΔSUV differences between the two PET systems were similar for the three SUV-parameters, we pairwise compared ΔSUV_{mean}, ΔSUV_{peak} and ΔSUV_{max} using a paired 2-samples t-test. Furthermore, we performed the Pitman-Morgan test (using R studio, package PairedData) to pairwise compare the RCs of the three SUV-parameters. Moreover, we performed a linear regression analysis (Pearson's correlation coefficient and F-test) to determine correlations between ΔSUV and the time between FDG-administration and the start of the dPET scan (ΔT_{dPET}), and between ΔSUV and lesion diameter. A p-value less than 0.05 was considered to indicate statistical significance.

Results

Patient characteristics

We included 50 patients (27 males, 23 females) with suspected or proven lung cancer (n=35), breast cancer (n=8), lymphoma (n=3), oesophageal cancer (n=3) or gastric cancer (n=1). Patient and scan characteristics per scanning group are presented in **Table 1**. The characteristics of both groups were comparable (p≥0.16). In total we evaluated 128 FDG-positive lesions, among which 66 lesions were part of the dPET-first group and 62 lesions of the dPET-second group. The average lesion diameter was 19±14 mm (median 15 mm, range 4–90 mm) with comparable sizes across both scanning groups (p=0.36). The number of included lesions per patient was 1 in 17 patients, 2 in 11 patients, 3 in 7 patients, 4 in 7 patients and 5 in 8 patients.

Table 1 Patient (n=50) and scan characteristics

	dPET-first group (n=25)	dPET-second group (n=25)	p-value
Age (in years)[a]	64±10	67±12	*0.23*
Body weight (in kg)[a]	83±19	76±16	*0.16*
Glucose level (in mmol/L)[a]	5.7±0.8	6.0±1.0	*0.25*
Administered FDG-activity (in MBq)[a]	413±105	397±97	*0.60*
ΔT from FDG administration			
until first PET scan (in min)[a]	64±10	66±10	*0.51*
until second PET scan (in min)[a]	96±11	97±13	*0.79*

[a] Continuous variables are described as mean ± SD

Semi-quantitative evaluation

SUV_{mean}, SUV_{peak} and SUV_{max} over all 128 lesions are shown in **Table 2** and **Figure 1** for cPET and dPET separately. Average dPET values were higher than cPET values for all three SUV-parameters ($p<0.001$).

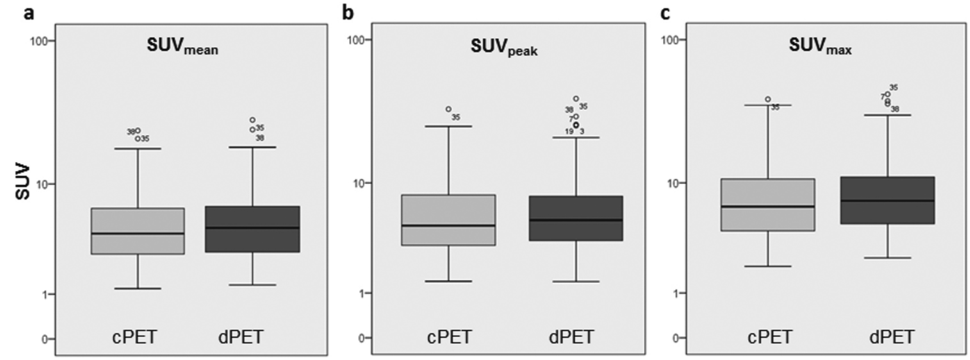

Figure 1 SUV_{mean} (a), SUV_{peak} (b) and SUV_{max} (c) as measured on cPET and dPET across all lesions (n=128). The y-axis is shown on a log scale. Average dPET values were significantly higher than cPET values for all three parameters ($p<0.001$)

Table 2 Average SUV_{mean}, SUV_{peak} and SUV_{max} across all lesions (n=128), the relative difference ΔSUV between both systems and the RC per SUV-parameter. dPET SUVs were higher than cPET SUVs ($p<0.001$) with average ΔSUVs of 6-8%

	cPET[a]	dPET[a]	ΔSUV (%)[a]	*RC*	*p-value*
SUV_{mean}	5.3 ± 3.8 (4.1)	5.6 ± 4.3 (4.6)	6% ± 14%	*27%*	*<0.001*
SUV_{peak}	6.4 ± 5.2 (4.7)	6.8 ± 5.9 (5.2)	7% ± 14%	*27%*	*<0.001*
SUV_{max}	8.4 ± 6.3 (6.6)	9.1 ± 7.0 (7.3)	8% ± 17%	*33%*	*<0.001*

[a] Continuous variables are described as mean ± SD (and median if not normally distributed)

Furthermore, relative SUV differences (ΔSUV) between cPET and dPET are shown in **Table 2** and **Figure 2**. The average variability in SUV_{max} was significantly higher than in SUV_{mean} (8% vs. 6%, $p=0.002$) and in SUV_{peak} (8% vs. 7%, $p=0.03$), while ΔSUV_{mean} and ΔSUV_{peak} were similar across all lesions (6% vs. 7%, $p=0.08$). Furthermore, corresponding RCs were 27% (ΔSUV_{mean} and ΔSUV_{peak}) and 33% (ΔSUV_{max}), with the RC of SUV_{max} being higher than the RCs of SUV_{mean} and SUV_{peak} ($p<0.001$). SUV_{mean} and SUV_{peak} RCs were similar ($p=0.35$).

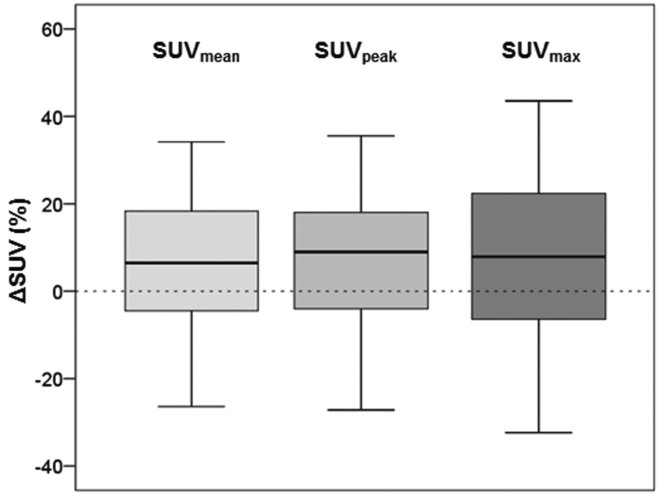

Figure 2 ΔSUV variability for SUV_{mean}, SUV_{peak} and SUV_{max} between cPET and dPET across all lesions (n=128). The average variability in ΔSUV_{max} was larger than the variability in ΔSUV_{mean} (p=0.002) and ΔSUV_{peak} (p=0.03). Furthermore, ΔSUV_{max} had a higher variance as compared to ΔSUV_{mean} and ΔSUV_{peak} ($p<0.001$)

The number of lesions with an absolute ΔSUV ≥30% was 3 (2%) for SUV_{mean}, 4 (3%) for SUV_{peak} and 15 (12%) for SUV_{max}. All lesions but one with a ΔSUV variability of ≥30% were part of the dPET-second group.

Correlations between ΔSUV and ΔT_{dPET} are presented in **Figure 3** for all three SUV-parameters. It shows that ΔSUV_{mean}, ΔSUV_{peak} and ΔSUV_{max} increased at prolonged ΔT_{dPET} ($p<0.001$) with correlation coefficients of 0.54, 0.55 and 0.59, respectively. Furthermore, the average ΔSUV of lesions in the dPET-second group was significantly higher as compared to lesions in the dPET-first group, with ΔSUV_{mean} of 16% and -3%, respectively ($p<0.001$), ΔSUV_{peak} of 16% and -2%, respectively ($p<0.001$), and ΔSUV_{max} of 21% and -4%, respectively ($p<0.001$). In **Figure 4** we compared ΔSUV for each lesion with its diameter. We found no correlation between these two parameters ($R<0.09$, $p>0.33$).

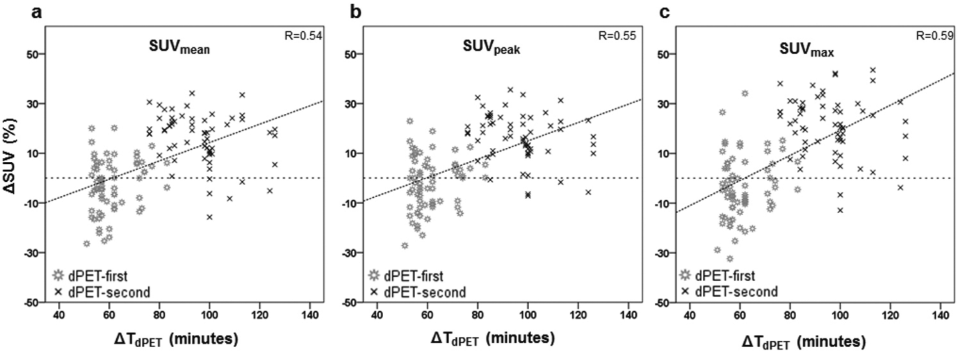

Figure 3 Scatterplot comparing the relative change in SUV$_{mean}$ (a), SUV$_{peak}$ (b) and SUV$_{max}$ (c) with ΔT$_{dPET}$, defined as the time between FDG-administration and start of the dPET scan. ΔSUV$_{mean}$, ΔSUV$_{peak}$ and ΔSUV$_{max}$ increased with prolonged ΔT$_{dPET}$ (p<0.001)

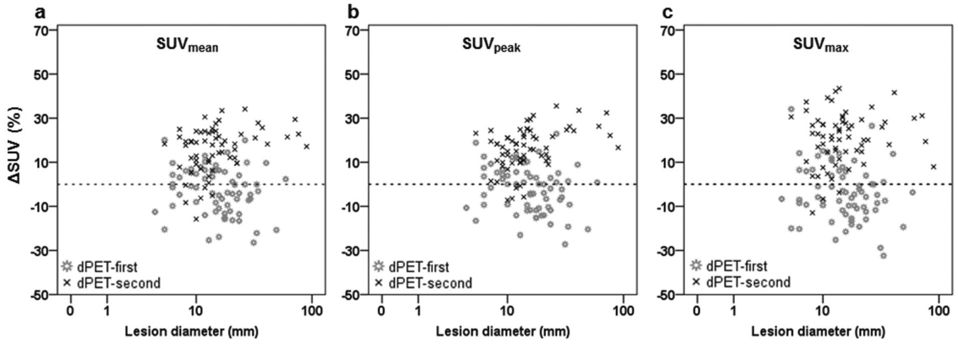

Figure 4 Scatterplot comparing the relative change in SUV$_{mean}$ (a), SUV$_{peak}$ (b) and SUV$_{max}$ (c) with lesion diameter. The x-axis is shown on a log scale. There were no significant correlations between ΔSUV and lesion diameter with R=0.09 for ΔSUV$_{mean}$ and ΔSUV$_{peak}$ (p=0.32), and R=0.01 for ΔSUV$_{max}$ (p=0.96)

Clinical example

In **Figure 5,** FDG-PET/CT images are shown from a patient with suspected lung cancer in the dPET-second group. Both PET scans showed bilateral adrenal gland metastases with higher SUVs (ΔSUV 7-15%) on the second dPET scan that was acquired 24 minutes after the cPET scan.

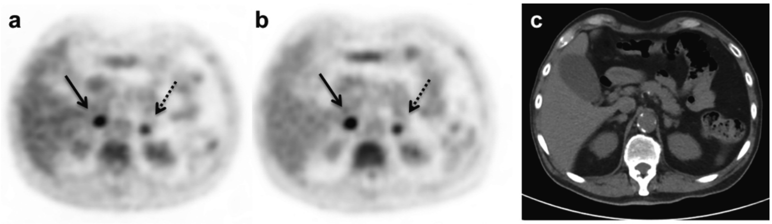

cPET scan
ΔT=62 min

dPET scan
ΔT=86 min

Attenuation CT scan

Figure 5 Axial FDG-PET/CT images from a lung cancer patient with bilateral adrenal gland metastases showing higher SUVs on the dPET scan (b) that was acquired 24 min after the cPET scan. The left-gland metastasis (diameter 11 mm) showed ΔSUVs of 7% (SUV_{mean}), 10% (SUV_{peak}) and 15% (SUV_{max}). ΔSUVs of the right-gland metastasis (diameter 14 mm) were 13% (SUV_{mean}) and 11% (SUV_{peak} and SUV_{max}). In this case the impact of the digital scanner cannot be separated from the SUV rise caused by the prolonged FDG-uptake. Meanwhile, the visual image quality of both PET scans appeared comparable in terms of image noise, texture and FDG-uptake as intended with an EARL-compatible protocol

Discussion

We evaluated the SUV variability in whole-body FDG-PET scans from 50 patients with cancer by comparing conventional and digital EARL-accredited PET. The average SUV variability across 128 FDG-positive lesions was limited with ΔSUVs of 6-8%. Furthermore, only a limited number of lesions showed a SUV difference of more than 30%. These findings indicate that EARL standardisation works.

We compared the variability of three SUV-parameters in a pairwise fashion and as expected we found the variability in SUV_{max} to be higher than in SUV_{mean} and SUV_{peak} ($p \leq 0.03$), although the average differences were relatively small (8% vs. 6-7%). We used automated software to identify the tumour region with the highest uptake within the lesion and it has been suggested that this method provides a lower variability for SUV_{peak} as compared to SUV_{max} [12]. Recently, EARL adopted SUV_{peak} as an additional metric in the updated EARL accreditation standards [14], as it appeared to be less sensitive to changes in reconstruction parameters and acquisition durations than SUV_{mean} or SUV_{max} [15]. However, a drawback of common SUV_{peak} definitions that its volume of 1 cm^3 is not suitable for (sub)centimeter lesions [15].

We found repeatability coefficients of 27% (SUV_{mean} and SUV_{peak}) and 33% (SUV_{max}). This variability is likely caused by a combination of three factors: a difference in EARL CRCs between our cPET and dPET system, the impact of prolonged FDG-uptake and the SUV test-retest variability. These 3 factors are discussed in the next 3 paragraphs.

Concerning CRC differences, the EARL protocol for our dPET system was based on relatively high CRCs for sub-15 mm small spheres [7] as compared to the CRCs of our cPET EARL protocol [9], with 10-20% higher CRCs on dPET. This explains why we found average ΔSUVs of 6-8% with dPET SUVs being higher than cPET values ($p<0.001$) in most cases. Larger variations can be expected at other PET sites or in clinical trials that use multiple EARL-accredited PET systems with divergent CRCs. This is possible because current EARL accreditation specifications [16] accept relatively large differences in CRCs, especially for small spheres (**Table 3**). To further harmonize the semi-quantitative results of EARL-accredited PET scanners, PET reconstruction settings could be further aligned to provide more similar CRCs. Naturally, SUV variability could also be reduced by using the same system and therefore this should be applied in longitudinal PET comparisons of the same patient [17].

Table 3 $\mathbf{CRC_{mean}}$ and $\mathbf{CRC_{max}}$ limits for the six phantom spheres as defined by EARL [16]. For each sphere, relative differences between the upper and lower CRC limits were calculated using $CRC_{dif}\,(\%) = \frac{\text{maximumCRC} - \text{minimumCRC}}{(\text{maximumCRC}+\text{minimumCRC})*0.5} \cdot 100$

Limits / Sphere diameter	CRC_{mean}		CRC_{max}	
	min-max	CRC_{dif} (%)	min-max	CRC_{dif} (%)
10 mm	0.27 – 0.43	46%	0.34 – 0.57	51%
13 mm	0.44 – 0.60	31%	0.59 – 0.85	36%
17 mm	0.57 – 0.73	25%	0.73 – 1.01	32%
22 mm	0.63 – 0.78	21%	0.83 – 1.09	27%
28 mm	0.72 – 0.85	17%	0.91 – 1.13	22%
37 mm	0.76 – 0.89	16%	0.95 – 1.16	20%

Concerning the time-interval between the first and the second scan, it is known that SUVs generally increase with prolonged FDG-uptake [18, 19]. We corrected for this effect by randomizing the PET scanning order. Consequently, the average ΔSUV across all lesions is likely not influenced by this effect. However, ΔSUVs of individual lesions were higher after the longer interval as shown in **Figure 3**. It is likely that the higher average ΔSUV for lesions in the *dPET-second group* is both caused by an increase in SUV due to prolonged FDG-uptake as well as the effect of the digital scanner with its higher CRCs. Conversely, in the *dPET-first* *group* an increase in SUV on the second scan caused by prolonged FDG-uptake is partly being compensated as cPET images were based on a reconstruction with lower CRCs as compared to dPET. For example, the average ΔSUV_{max} in the dPET-first group was -4% whereas the average ΔSUV_{max} in dPET-second group was 21%. Based on these averages, we expect that about (21%+4%)/2=13% of the higher SUV_{max} on the second scan can be attributed to the prolonged FDG-uptake time. If this theoretical correction of 13% is applied to all individual ΔSUVs, only 1 lesion (1%) remains with a ΔSUV_{max} ≥30%.

Concerning the SUV test-retest variability, it is known that biological, technical and methodological factors [12, 19] play a role. Several studies have evaluated this in different types of cancer [12, 20-22]. In a recent review, Lodge [12] stated that with a strict protocol, lesion-SUV has a within-subject coefficient of variation (wCV) of 10% (SUV_{mean} and SUV_{peak}) and 11% (SUV_{max}). In our study, we found RCs of 27-33%, representing wCVs of 10% (SUV_{mean} and SUV_{peak}) and 12% (SUV_{max}) when using $wCV = RC/(\sqrt{2} * 1.96)$. This indicates that the average ΔSUV in our study is comparable with values reported by Lodge [12]. However, our study includes two aspects that make it difficult to compare our wCVs with the data reported by Lodge. First, we performed both PET scans on the same day after a single FDG-administration while Lodge [12] only included results based on two separate FDG-administrations. Second, the lesions that we included were relatively small (median size 15 mm) while Lodge [12] described that most repeatability studies included lesions with a minimum diameter of 20 to 30 mm.

Our conclusion that EARL standardisation works is in agreement with findings from a recently published paper by van Sluis et al.[23]. They performed a cPET versus dPET comparison study, using scanners from another vendor, in a small group of patients with cancer (n=20). Although they did not calculate relative differences or repeatability coefficients, they observed a good agreement in SUV measurements between both PET/CT systems, in particular when using EARL compliant reconstructions on both systems [23].

The present study has some limitations. We included 128 lesions across 50 patients where the included number of lesions varied between 1 and 5 lesions per patient, but we did not take a possible intra-patient correlation between lesions into account in the statistical analysis. Yet, the number of lesions in both scanning groups was almost similar (66 vs. 62 lesions). Furthermore, our study was not a full test-retest study since for each patient both PET scans were acquired on the same day and with just a single FDG-injection. Therefore, variability associated with patient preparation, biological factors and FDG-administration was not fully taken into account in our study. However, other factors such as patient motion, breathing and potential CT-PET mismatches could still have influenced the ΔSUV in this intra-individual comparison of EARL-accredited cPET and dPET scans. Still, given that the impacts of the PET systems, biological effect and test-retest are intricate and that biological effects are not negligible, it would be useful to repeat this semi-quantitative comparison of EARL-accredited PET scans in a full test-retest setting to confirm our results. Another limitation is the wide range in ΔT for the second scan as shown in **Figure 3**, which influences individual ΔSUVs. Fortunately, the average FDG-uptake time per scan between both scanning groups was similar.

While the present study is based on current EARL accreditation specifications [16], an update of those specifications has been proposed because in recent years different vendors launched new PET/CT systems equipped with novel techniques such as TOF, resolution modelling/PSF technologies and digital detectors. These modern systems can deliver PET images with higher CRCs, especially for small spheres and therefore an update of the EARL accreditation specifications is desirable. Kaalep et al.[15] evaluated the feasibility of harmonising performance for novel PET/CT systems and they also proposed new EARL criteria. In these newly proposed CRCs the relative difference (%) between upper and lower limits is similar to current EARL specifications [16]. Therefore, it is expected that the potential variability in semi-quantitative FDG-PET with such updated EARL-compatible protocols will remain similar.

Conclusion

With EARL-accredited conventional and digital PET, we found a limited SUV variability with average differences up to 8%. Furthermore, only a limited number of lesions showed a SUV difference of more than 30%. These findings indicate that EARL standardisation works. When EARL-accredited systems with divergent CRCs are used, larger SUV differences can be expected.

Competing interests

This work was supported by a research agreement between the Department of Nuclear Medicine, Isala, and Philips Healthcare regarding new PET technologies. The content of the article was solely the responsibility of the authors. The authors declare that they have no conflict of interest.

Funding

This work was supported by a research agreement between the Department of Nuclear Medicine, Isala, and Philips Healthcare regarding new PET technologies.

References

1. Boellaard R, O'Doherty M,J., Weber WA, Mottaghy FM, Lonsdale MN, Stroobants SG, Oyen WJG, Kotzerke J, Hoekstra OS, Pruim J. FDG PET and PET/CT: EANM procedure guidelines for tumour PET imaging: version 1.0. Eur J Nucl Med Mol Imaging 2010;37:181-200.
2. Boellaard R, Delgado-Bolton R, Oyen WJG, Giammarile F, Tatsch K, Eschner W, Verzijlbergen FJ, Barrington SF, Pike LC, Weber WA. FDG PET/CT: EANM procedure guidelines for tumour imaging: version 2.0. Eur J Nucl Med Mol Imaging 2015;42:328-54.
3. Kaalep A, Sera T, Oyen WJG, Krause BJ, Chiti A, Liu Y, Boellaard R. EANM/EARL FDG-PET/CT accreditation - summary results from the first 200 accredited imaging systems. Eur J Nucl Med Mol Imaging 2018;45:412-22.
4. Miller M, Zhang J, Binzel K, Griesmer J, Laurence T, Narayanan M, Natarajamani D, Wang S, Knopp M. Characterization of the vereos digital photon counting PET system. J Nucl Med 2015;56:434.
5. Hsu DF, Ilan E, Peterson WT, Uribe J, Lubberink M, Levin CS. Studies of a next-generation silicon-photomultiplier–based time-of-flight PET/CT system. J Nucl Med 2017;58:1511-8.
6. van Sluis JJ, de Jong J, Schaar J, Noordzij W, van Snick P, Dierckx R, Borra R, Willemsen A, Boellaard R. Performance characteristics of the digital Biograph Vision PET/CT system. J Nucl Med 2019;60:1031-6.
7. Koopman D, Koerkamp MG, Jager PL, Arkies H, Knollema S, Slump CH, Sanches PG, van Dalen JA. Digital PET compliance to EARL accreditation specifications. EJNMMI Phys 2017;4:9-14.
8. de Groot E,H., Post N, Boellaard R, Wagenaar NRL, Willemsen ATM, van Dalen J,A. Optimized dose regimen for whole-body FDG-PET imaging. EJNMMI Res 2013;3:63-72.
9. Koopman D, van Dalen J,A., Lagerweij MCM, Arkies H, de Boer J, Oostdijk AHJ, Slump CH, Jager PL. Improving the detection of small lesions using a state-of-the-art time-of-flight PET/CT system and small-voxel reconstructions. J Nucl Med Technol 2015;43:21-7.
10. Boellaard R. Quantitative oncology molecular analysis suite: ACCURATE. J Nucl Med 2018;59:1753.
11. Sher A, Lacoeuille F, Fosse P, Vervueren L, Cahouet-Vannier A, Dabli D, Bouchet F, Couturier O. For avid glucose tumors, the SUV peak is the most reliable parameter for 18 F] FDG-PET/CT quantification, regardless of acquisition time. EJNMMI Res 2016;6:21-6.
12. Lodge MA. Repeatability of SUV in Oncologic 18F-FDG PET. J Nucl Med 2017;58:523-32.
13. Wahl RL, Jacene H, Kasamon Y, Lodge MA. From RECIST to PERCIST: evolving considerations for PET response criteria in solid tumors. J Nucl Med 2009;50:122S.

14. EARL. Updated EANM FDG PET/CT accreditation specifications for SUV recovery coefficients [2019]. 2019. http://earl.eanm.org/cms/website.php. Accessed 01-08-2019.
15. Kaalep A, Sera T, Rijnsdorp S, Yaqub M, Talsma A, Lodge MA, Boellaard R. Feasibility of state of the art PET/CT systems performance harmonisation. Eur J Nucl Med Mol Imaging 2018;45:1344-61.
16. EARL. EANM FDG PET/CT accreditation specifications for SUV recovery coefficients. 2017. http://earl.eanm.org/cms/website.php. Accessed 01-10- 2018.
17. Boellaard R, Delgado-Bolton R, Oyen WJG, Giammarile F, Tatsch K, Eschner W, Verzijlbergen FJ, Barrington SF, Pike LC, Weber WA. FDG PET/CT: EANM procedure guidelines for tumour imaging: version 2.0. Eur J Nucl Med Mol Imaging 2015;42:328-54.
18. Shankar LK, Hoffman JM, Bacharach S, Graham MM, Karp J, Lammertsma AA, Larson S, Mankoff DA, Siegel BA, Van den Abbeele A. Consensus recommendations for the use of 18F-FDG PET as an indicator of therapeutic response in patients in National Cancer Institute Trials. J Nucl Med 2006;47:1059-66.
19. Vriens D, Visser EP, de Geus-Oei L, Oyen WJG. Methodological considerations in quantification of oncological FDG PET studies. Eur J Nucl Med Mol Imaging 2010;37:1408-25.
20. de Langen AJ, Vincent A, Velasquez LM, van Tinteren H, Boellaard R, Shankar LK, Boers M, Smit EF, Stroobants S, Weber WA. Repeatability of 18F-FDG uptake measurements in tumors: a metaanalysis. J Nucl Med 2012;53:701.
21. Rockall AG, Avril N, Lam R, Iannone R, Mozley PD, Parkinson C, Bergstrom DA, Sala E, Sarker S, McNeish IA. Repeatability of quantitative FDG-PET/CT and contrast enhanced CT in recurrent ovarian carcinoma: test retest measurements for tumor FDG uptake, diameter and volume. Clin Cancer Res 2014;20:2751-60.
22. Weber WA, Gatsonis CA, Mozley PD, Hanna LG, Shields AF, Aberle DR, Govindan R, Torigian DA, Karp JS, Yu JQM. Repeatability of 18F-FDG PET/CT in advanced non–small cell lung cancer: prospective assessment in 2 multicenter trials. J Nucl Med 2015;56:1137-43.
23. van Sluis J, Boellaard R, Somasundaram A, van Snick P, Borra R, Dierckx R, Stormezand G, Glaudemans A, Noordzij W. Image quality and semi-quantitative measurements of the Siemens Biograph Vision PET/CT: Initial experiences and comparison with Siemens Biograph mCT PET/CT. J Nucl Med 2019.

CHAPTER 6

6

Multicentre quantitative ^{68}Ga PET/CT performance harmonisation

Authors

Daphne M.V. Huizing[1] | Daniëlle Koopman[2] | Jorn A. van Dalen[3]
Martin Gotthardt[4] | Ronald Boellaard[5,6,7] | Terez Sera[7] | Michiel Sinaasappel[8]
Marcel P.M. Stokkel[1] | Berlinda J. de Wit – van der Veen[1]

Author Affiliations

1: Department of Nuclear Medicine, Netherlands Cancer Institute, Amsterdam, the Netherlands
2: Department of Nuclear Medicine, Isala, Zwolle, the Netherlands
3: Department of Medical Physics, Isala, Zwolle, the Netherlands
4: Department of Radiology and Nuclear Medicine, Radboud University Medical Center, Nijmegen, the Netherlands
5: Department of Radiology & Nuclear Medicine, Amsterdam University Medical Centres, location VU University Medical Center, Amsterdam, the Netherlands
6: Department of Nuclear Medicine and Molecular Imaging, University of Groningen, University Medical Center Groningen, Groningen, the Netherlands
7: EANM Research Limited (EARL), Vienna, Austria
8: Department of Physics, Netherlands Cancer Institute, Amsterdam, the Netherlands

Accepted for publication in EJNMMI Physics

Abstract

Purpose

Performance standards for quantitative ^{18}F-FDG PET/CT studies are provided by the EANM Research Ltd (EARL) to enable comparability of quantitative PET in multicentre studies. Yet such specifications are not available for ^{68}Ga. Therefore our aim was to evaluate ^{68}Ga-PET/CT quantification variability in a multicentre setting.

Methods

A survey across Dutch hospitals was performed to evaluate differences in clinical ^{68}Ga PET/CT study protocols. ^{68}Ga and ^{18}F phantom acquisitions were performed by eight centres with thirteen different PET/CT systems according to EARL protocol. The cylindrical phantom and NEMA image quality (IQ) phantom were used to assess image noise and to identify recovery coefficients (RCs) for quantitative analysis. Both phantoms were used to evaluate cross-calibration between the PET/CT system and local dose calibrator.

Results

The survey across Dutch hospitals showed a large variation in clinical ^{68}Ga PET/CT acquisition and reconstruction protocols. ^{68}Ga PET/CT image noise was below 10%. Cross-calibration was within 10% deviation, except for one system to overestimate ^{18}F and two systems to underestimate the ^{68}Ga activity concentration. RC-curves for ^{18}F and ^{68}Ga were within and on the lower limit of current EARL standards, respectively. After correction for local ^{68}Ga/^{18}F cross-calibration, mean ^{68}Ga performance was 5% below mean EARL performance specifications.

Conclusions

^{68}Ga PET/CT quantification performs on the lower limits of the current EARL RC standards for ^{18}F. Correction for local ^{68}Ga/^{18}F cross-calibration mismatch is advised, while maintaining the EARL reconstruction protocol thereby avoiding multiple EARL protocols.

Keywords

Quantification; ^{68}Gallium PET/CT; Image Quality; Harmonisation

Introduction

The use of ^{68}Gallium (^{68}Ga)-labelled peptides for PET imaging has increased in the past years with the market authorisation for ^{68}Ga/^{68}Ge-generators. The main applications include imaging of neuroendocrine tumours using somatostatin analogues and prostate cancer imaging using the prostate specific membrane antigen [1, 2]. Though interpretation of ^{68}Ga-PET/CT is mainly based on visual assessment, quantitative measures should be used to evaluate or predict therapy response.

Previous experience with ^{18}Fluorine (^{18}F) expressed the need for standardization of acquisition and reconstruction protocols in order to retrieve comparable quantitative imaging data. The EANM Research Ltd (EARL) provides an accreditation program to ensure PET/CT system harmonisation in multicentre ^{18}F-FDG PET/CT studies [3]. This approach is based on standardizing the recovery coefficient (RC) for six phantom sphere with different sizes, thereby minimizing inter- and intra-institute variability. For other isotopes, quantification should be evaluated separately as isotope characteristics can result in different image quality and quantification accuracy. For example, Makris et al. studied ^{89}Zirconium (^{89}Zr) PET and showed the need for a specific harmonisation step including post-reconstruction smoothing to enable comparable quantitative measures among PET/CT systems [4]. In contrast, a recent ^{18}F performance study showed that post-reconstruction filtering is not required for state-of-the-art PET/CT systems in relation to this isotope [5]. However, for ^{68}Ga such studies are not yet available.

In general, PET quantification accuracy depends on reconstructions, noise and spatial resolution [6]. For ^{68}Ga, the lower positron yield (89%), long positron range due to high initial positron energy (max 1.90 MeV, mean 0.84 MeV), short physical half-life (68 minutes) and small prompt gamma branching (3.2%, 1.077 MeV) may result in an inferior image quality compared to ^{18}F [7]. Therefore, the aim of this study was to assess ^{68}Ga-PET/CT quantification accuracy and reproducibility in a multicentre setting based on EARL standards.

Materials and Methods

Clinical protocol evaluation

A survey among eight Dutch hospitals was performed to evaluate factors that affect quantification and to assess variability in clinical ^{68}Ga-PET/CT acquisition protocols. Questions focussed on administered activity, PET/CT system, and acquisition- and reconstruction settings.

^{18}F and ^{68}Ga PET/CT phantom acquisitions

Eight European hospitals with thirteen PET/CT systems performed phantom acquisitions, of which eleven systems were EARL accredited, but all had recoveries within the published EARL specifications. Six Biograph mCT systems (Siemens Healthineers, Erlangen, Germany), three Discovery systems (GE Healthcare, Milwaukee, WI, USA) and four Philips systems (Philips Healthcare, Eindhoven, The Netherlands) were included.

^{18}F and ^{68}Ga acquisitions were performed in the end of 2017 and beginning of 2018 with two phantoms which were prepared using a standardized procedure by experienced staff from each centre. First, the NEMA PET cylindrical phantom was filled with 6-13 kBq/ml of ^{18}F and ^{68}Ga. Second, the NEMA NU-2 Image Quality (IQ) phantom was imaged using a 1:10 ratio with 2.0 and 20.0 kBq/ml of ^{18}F and ^{68}Ga in background compartment and spheres (37, 28, 21, 17, 13 and 10 mm diameter), respectively. Acquisitions of both phantoms were performed with minimal 2 bed positions and at least 5 minutes per bed position. Images were reconstructed according to local settings, including corrections for decay, randoms, dead time, CT-based attenuation and scatter.

Data analysis

Image noise was characterized for ^{68}Ga only using the coefficient of variation (CoV) along a 30×30×160 mm bar in the centre of the cylindrical phantom. Image quality was based on the RC of all six spheres, analysed by the EARL semi-automatic tool [5, 8]. The RC_{max}, RC_{peak} and RC_{mean} were determined as a function of sphere size based on the maximum voxel value (RC_{max}), the 1.0 cm^3 volume with the maximized average value (RC_{peak}) and the mean value of 50% isocontour of the maximum voxel value (RC_{mean}) with contrast correction, respectively. A spherical volume-of-interest (VOI) of ~300 ml in the centre of the cylindrical phantom and ten VOIs in the background of the IQ phantom were used for local PET and dose calibrator cross-calibration. IQ phantom background volume was 9400ml, unless specified otherwise by the institute.

Results

Eight Dutch hospitals provided their clinical acquisition- and reconstruction protocols (**Table 1**), which showed to be different. An overview of all PET/CT systems and reconstruction settings is provided in **Table 2**. For local cross-calibration, most systems performed within 10% deviation of the dose calibrator (**Figure 1**). The median [IQR] ratio was 0.93 [0.91 – 0.98] and

Table 1 Acquisition and reconstruction settings of clinical ^{68}Ga PET/CT imaging for prostate cancer and neuroendocrine tumours. One hospital per row is presented

Site	PET/CT system	Reconstruction settings	Prostate cancer			Neuroendocrine tumours		
			Minutes per bed position		Injected activity	Minutes per bed position		Injected activity
A	Philips Gemini TOF 64	BLOB-OS-TF 4mm , 3i33ss	Pelvis: 4	Body: 3	1.5 MBq/kg (range 50-250 MBq)	<90kg: 2.5	> 90 kg: 3.5	2.6 MBq/kg (range 100-160 MBq)
B	Philips Gemini TF and XL	Astonish iterative reconstruction	4		2.0 MBq/kg	4		2.6 MBq/kg
C	Siemens mCT Flow	TrueX + TOF , 2i21ss, Gaussian 5mm filter	1.5mm/sec CTM		2.0 MBq/kg	2.5		100 MBq
D	Philips Ingenuity TF	BLOB-OS-TF 4mm, 3i33ss, 2mm smooth B filter	NA			4		<90 kg: 150 MBq >90 kg: 200 MBq
E	Siemens mCT TrueV	OSEM3D, TOF + PSF 2i21ss, Gaussian 5mm	4		1.5 MBq/kg (min 80 MBq)	NA		
F	Philips Gemini TOF	BLOB-OS-TF 4mm 3i33ss	Pelvis: 3	Body: 2	100 MBq	2.5		100 MBq
G	Siemens mCT	TrueX + TOF, 4i21ss Gaussian 5mm filter	3		1.5 MBq/kg	3		1.5 MBq/kg
H	Siemens mCT40 and mCT128	TrueX + TOF, 3i21ss Gaussian 3mm filter	<70 kg: 1.5 MBq/kg: 3 1.13 MBq/ml: 4 0.9 MBq/ml: 5	>70 kg: 1.5 MBq/kg: 4 1.2 MBq/ml: 5 1 MBq/ml: 6	1.5 MBq/kg	<70 kg: 1.5 MBq/kg: 3 1.13 MBq/ml: 4 0.9 MBq/ml: 5	>70 kg: 1.5 MBq/kg: 4 1.2 MBq/ml: 5 1 MBq/ml: 6	1.5 MBq/kg

NA = not applicable, i = iteration, ss = subsets, TOF = time-of-flight, PSF = point-spread-function, CTM = continuous table motion

Table 2 PET/CT reconstruction settings for phantom measurements

No	Manufacturer	PET/CT system	Reconstruction	Iterations	Subsets	Filter size (mm)	Matrix	Voxel size (mm)	Slice thickness (mm)
1	Siemens	Biograph mCT 40 (1)	PFS + TOF	3	21	7.00	256×256	3.18	3
2	Siemens	Biograph mCT 40 (2)	PFS + TOF	3	21	7.00	256×256	3.18	3
3	Siemens	mCT 123 X3R	Backprojection	-	-	5.00	200×200	4.07	5
4	Siemens	Biograph mCT Flow 20	PFS + TOF	2	21	5.00	200×200	4.07	2.027
5	GE	VCT	3D IR[a]	N7S	NS	NS	128×128	5.47	3.27
6	GE	Discovery D690	VPFXS[b]	4	8	NS	192×192	3.65	3.27
7	Philips	Gemini TOF	BLOB-OS-TF	3	31	NS	144×144	4	4
8	Philips	Gemini TOF BigBore	BLOB-OS-TF	3	31	NS	144×144	4	4
9	Philips	Ingenuity TF	BLOB-OS-TF	3	31	NS	169×169	4	4
10	Philips	Vereos	BLOB-OS-TF	3	15	3.00	144×144	4	4
11	GE	Discovery 710	VPFX[c]	NS	NS	NS	256×256	2.73	3.27
12	Siemens	mCT 40	PFS + TOF	3	21	6.50	256×256	3.18	2
13	Siemens	mCT 64	PFS + TOF	3	21	6.50	256×256	3.18	2

a: 3D OSEM, b: 3D OSEM with TOF and PSF, c: 3D OSEM with TOF. TOF or TF = time-of-flight, PSF = point-spread-function, NS = not specified.

0.99 [0.97 – 1.01] for ^{68}Ga and ^{18}F, respectively. Two systems showed identical calibration accuracy for both isotopes (system 2 and 11, all other show a consistent underestimation for ^{68}Ga. The ^{68}Ga CoV in the centre of the cylindrical phantom was below 10% (**Figure 2**).

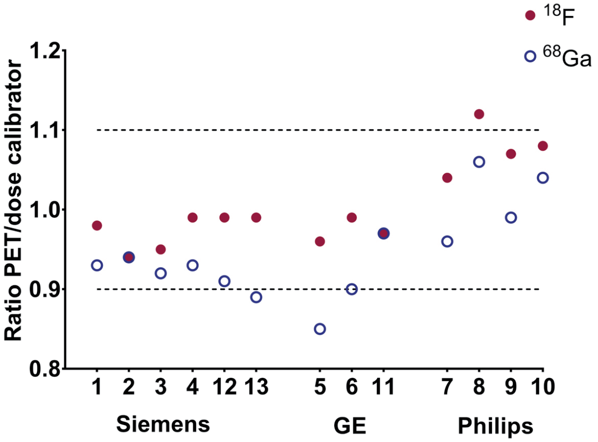

Figure 1 Accuracy of the measured activity by the PET/CT system and local dose calibrator, based on the average between the cylindrical and IQ phantom. Numbers correspond to Table 2

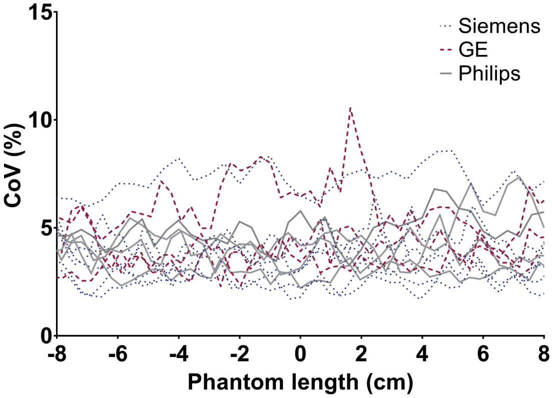

Figure 2 Noise across the cylindrical phantom filled with ^{68}Ga, visualized as coefficient of variation (CoV)

The ^{18}F RC-curves of all PET/CT systems satisfied the current EARL specifications (**Figure 3A-C**). However, for ^{68}Ga the RC-curves were located around the lower limit of the EARL specifications (**Figure 3D-F**). In addition, ^{68}Ga showed a reduced mean recovery and larger variation between PET/CT systems compared to the ^{18}F. The variation for all spheres of the RC$_{mean}$, RC$_{max}$ and RC$_{peak}$ for ^{18}F was 6%, 6% and 8%, respectively. For ^{68}Ga, the mean range was 11%, 11% and 15% (largest variation was 19%). Furthermore, the mean RC$_{max}$ and RC$_{mean}$ were both 11% lower compared to the mean EARL specifications for ^{18}F. The mean ^{68}Ga/^{18}F calibration difference within one scanner was 7% (range 1-13%).

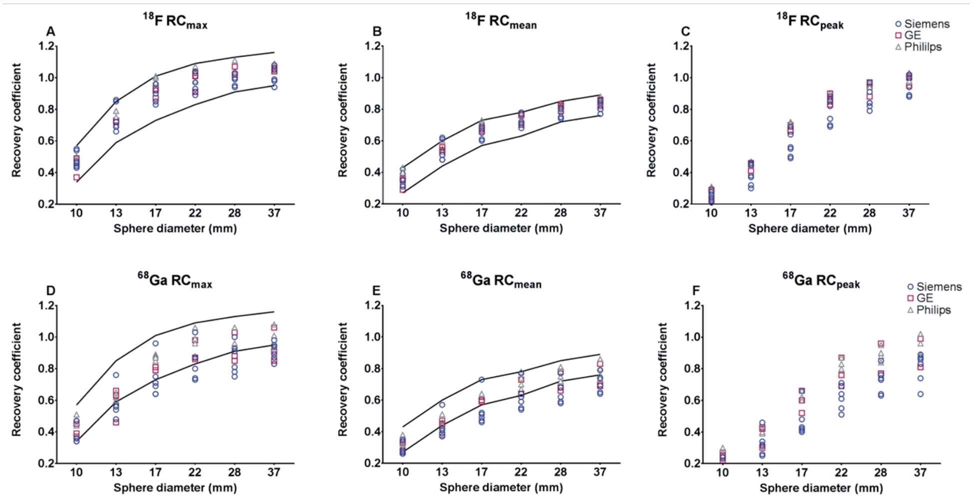

Figure 3 RC for ^{18}F with the current EARL standards and RC of ^{68}Ga. Solid lines: maximum and minimum values according to EARL limits as applicable before 2019

After correction for the local difference between ^{68}Ga/^{18}F cross-calibration (**Figure 1**), the ^{68}Ga RC-curve was within EARL limits for all but two scanners (**Figure 4**). The mean ^{68}Ga RC$_{max}$ and RC$_{mean}$ were accordingly 5% lower compared to mean EARL standards.

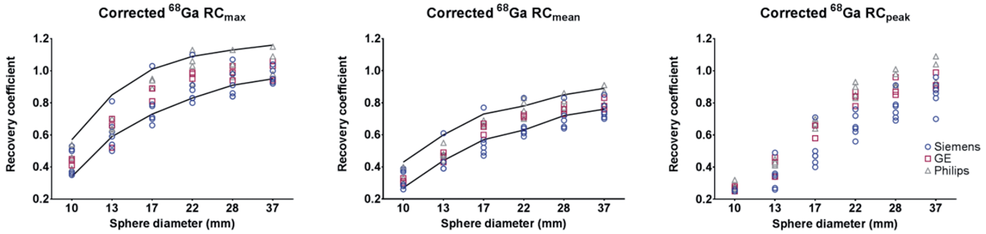

Figure 4 ^{68}Ga RC-curves corrected for the ^{18}F/^{68}Ga calibration mismatch according to local cross-calibration. Solid lines: maximum and minimum values according to EARL limits as applicable before 2019

Discussion

In this study, quantitative ^{68}Ga PET/CT performance was evaluated in a multicentre setting. In a survey across Dutch hospitals, differences in clinical acquisition and reconstruction protocols were observed, underlining the need for clinical harmonisation. Although eleven out of the thirteen PET/CT systems were EARL accredited, all systems showed ^{18}F recovery performance within EARL standards. For this reason, all systems were included for ^{68}Ga evaluation.

The absence of local and central dose calibrator cross-calibration for ^{68}Ga is a limitation in this study. This would increase local calibrator harmonisation and improves PET/CT comparability across sites. Most institutes use a long-lived (Ceasium-137) source to assess constancy and accuracy of the dose calibrator on a daily basis, and perform actual cross-calibration with the PET/CT system at least once a year using ^{18}F. Still, in all but three PET/CT systems the measured ^{18}F and ^{68}Ga activity concentrations were within 10% deviation from the local dose calibrator. High energy prompt gammas emitted by ^{68}Ga are likely detected by the dose calibrator causing a disconcordance, yet in fewer extent by the PET system. Because of this, the dose calibrator overestimates ^{68}Ga-activity, and a persistent underestimation for ^{68}Ga compared to ^{18}F is seen in **Figure 1**. A recent study by Bailey et al. also showed an underestimation of ±15% for ^{68}Ga, which was primary related to an inaccurate scaling factor for the dose calibrator of a specific vendor [9]. To avoid these issues, they calibrated the dose calibrator towards the PET, after verifying that the scanner has a good response for ^{18}F. These results are also supported by the fact that on specific Siemens scanners (scanner 1 and 2) a traceable ^{68}Germanium (^{68}Ge) source was used to verify absolute PET response independent of a dose calibrator. When imaging the ^{68}Ge-source, the PET/CT system did not show the same offset as was observed when imaging the ^{68}Ga cross-calibration phantom (roughly a deviation of <1% vs. 6% and 7%, respectively). For sake of simplicity we would suggest to correct the RC-curve for the local ^{68}Ga/^{18}F discrepancy, as after correction for this ^{68}Ga/^{18}F difference in our group (**Figure 4**) all but two scanners were within EARL specifications. This correction has to be performed off line in multicentre quantitative studies. The ^{68}Ga used for this study was produced either locally or by a pharmaceutical institution and was therefore not traceable to a central dose calibrator. We expect that the response between the dose calibrator and the PET-system could be uniform in future clinical ^{68}Ga-PET/CT studies if a traceable (NIST) source is used to harmonise protocols between centres.

^{68}Ga image noise was below 10% for all PET/CT systems which is in concordance with the EANM/EARL guidelines [3, 8]. The RC variation is larger for ^{68}Ga compared to ^{18}F (**Figure 3**). However, ^{68}Ga performance nearly reached EARL performance specifications after correction for the local ^{68}Ga/^{18}F ratio. Surprisingly, the RC_{peak} variation (8% and 15%) is larger in contrast to RC_{max} and RC_{mean} (both 6% and 11%) for both ^{18}F and ^{68}Ga, respectively. The study of Kaalep et al. showed the opposite result in RC_{peak} variation [5]. The RC_{peak} is expected to be less prone to noise compared to RC_{max}; therefore, it was expected to be more comparable over all PET-systems. The difference could be explained by the fact that the standard deviation of RC_{max} and RC_{peak} are similar: 8.4% and 8.6% for ^{68}Ga and 4.8% and 5.0% for ^{18}F, respectively. Yet the mean RC_{peak} value is lower, therefore resulting in a higher CoV. Next to that, the larger ^{68}Ga variation in the RC-curves compared to ^{18}F is likely related to the higher positron energy of ^{68}Ga and thereby revealing a lower signal-to-noise ratio. This effect is enhanced by post-reconstruction filtering. Finally, previous single centre studies show ^{68}Ga RC-curves similar [10] or somewhat better due to point spread function reconstruction [11] as observed in the current study. The EARL limits as applicable before 2019 (EARL1) are shown in Figure 3 and 4, as all acquisitions were acquired before 2019 and therefore site-specific acquisition and reconstruction protocols are designed to meet the EARL1 limits. RC_{peak} specifications are not available for EARL1 and are therefore not shown in Figure 3 and 4. EARL2 limits (applicable from 2019) for RC_{max} and RC_{mean} increased with ~25% in comparison to EARL1. We expect that the gap between ^{18}F and ^{68}Ga recoveries will further increase with this new limits, as already for EARL1 not all scanners agreed to EARL1 limits after ^{68}Ga/^{18}F correction (**Figure 4**).

Based on the results we propose to correct ^{68}Ga recovery towards ^{18}F recovery to correct for the current dose calibrator deviation. We suggest, therefore, to apply the EARL acquisition and reconstruction protocol and to correct for ^{68}Ga/^{18}F cross-calibration mismatch. One can assume that ^{68}Ga recovery is steady if ^{18}F specifications of a PET-system are stable during regular yearly assessment. Unless the acquisition and reconstruction protocol is changed or major maintenance is performed to the PET/CT-system, we recommend to perform additional ^{68}Ga IQ acquisitions only when regular ^{18}F evaluations are deviating. An EARL accreditation program for ^{68}Ga can thus be based on the ^{18}F accreditation but extended with a cross-calibration verification between ^{68}Ga measured by the dose calibrator and PET/CT system only, similarly as proposed by Kaalep et al. for ^{89}Zr [12]. In addition, frequent ^{18}F cross-calibration acquisitions using the cylindrical phantom are advised, especially after PET/CT system maintenance.

Conclusion

This evaluation of multicentre ^{68}Ga PET/CT performance showed that ^{68}Ga RCs perform at the lower limits of current ^{18}F EARL standards. For practical reasons we recommend to use the ^{18}F EARL approved reconstruction settings and to correct for ^{68}Ga/^{18}F calibration mismatch based on local cross-calibration. Finally, we suggest to evaluate ^{68}Ga PET/CT recovery performance once and repeat only when ^{18}F specifications are changed.

Declarations

Funding

The research leading to these results have received funding from the European Community's Seventh Framework Programme (FP7/2007-2013) under grant agreement n° 602812 (BetaCure study).

Conflicts of interest

RB is scientific advisor and chair of the EARL accreditation program. TS is an associate of the EARL program. The other authors declare that they have no conflict of interest.

References

1. Singh S, Poon R, Wong R, Metser U. 68Ga PET Imaging in Patients With Neuroendocrine Tumors: A Systematic Review and Meta-analysis. Clin Nucl Med 2018;43:802-10.
2. Lütje S, Heskamp S, Cornelissen AS, Poeppel TD, van den Broek, Sebastiaan AMW, Rosenbaum-Krumme S, Bockisch A, Gotthardt M, Rijpkema M, Boerman OC. PSMA ligands for radionuclide imaging and therapy of prostate cancer: clinical status. Theranostics 2015;5:1388-401.
3. Boellaard R, Willemsen AT, Arends B, Visser EP. EARL procedure for assessing PET/CT system specific patient FDG activity preparations for quantitative FDG PET/CT studies. EANM research Ltd (EARL). http://earl.eanm.org/html/img/pool/EARL-procedure-for-optimizing-FDG-activity-for-quantitative-FDG-PET-studies_version_1_1.pdf.
4. Makris NE, Boellaard R, Visser EP, de Jong JR, Vanderlinden B, Wierts R, van der Veen, Berlinda J, Greuter HJ, Vugts DJ, van Dongen GA. Multicenter harmonization of 89Zr PET/CT performance. J Nucl Med 2014;55:264-7.
5. Kaalep A, Sera T, Rijnsdorp S, Yaqub M, Talsma A, Lodge MA, Boellaard R. Feasibility of state of the art PET/CT systems performance harmonisation. Eur J Nucl Med Mol Imaging 2018;45:1344-61.
6. Boellaard R, Krak NC, Hoekstra OS, Lammertsma AA. Effects of noise, image resolution, and ROI definition on the accuracy of standard uptake values: a simulation study. J Nucl Med 2004;45:1519-27.
7. Sanchez-Crespo A. Comparison of Gallium-68 and Fluorine-18 imaging characteristics in positron emission tomography. Appl Radiat Isot 2013;76:55-62.
8. Boellaard R, Delgado-Bolton R, Oyen WJG, Giammarile F, Tatsch K, Eschner W, Verzijlbergen FJ, Barrington SF, Pike LC, Weber WA. FDG PET/CT: EANM procedure guidelines for tumour imaging: version 2.0. Eur J Nucl Med Mol Imaging 2015;42:328-54.
9. Bailey DL, Hofman MS, Forwood NJ, O'Keefe GJ, Scott AM, van Wyngaardt WM, Howe B, Kovacev O, Francis RJ, ProPSMA Trial Investigators. Accuracy of dose calibrators for 68Ga PET imaging: unexpected findings in a multicenter clinical pretrial assessment. J Nucl Med 2018;59:636-8.
10. Preylowski V, Schlögl S, Schoenahl F, Jörg G, Samnick S, Buck AK, Lassmann M. Is the image quality of I-124-PET impaired by an automatic correction of prompt gammas?. PLoS One 2013;8:e71729.
11. Jönsson L, Stenvall A, Mattsson E, Larsson E, Sundlöv A, Ohlsson T, Hindorf C. Quantitative analysis of phantom studies of 111 In and 68 Ga imaging of neuroendocrine tumours. EJNMMI Phys 2018;5:5-17.
12. Kaalep A, Huisman M, Sera T, Vugts D, Boellaard R, TRISTAN Consortium. Feasibility of PET/CT system performance harmonisation for quantitative multicentre 89 Zr studies. EJNMMI Phys 2018;5:26-33.

PART II

PET optimisation

CHAPTER 7

7

Current generation time-of-flight ^{18}F-FDG PET/CT provides higher SUVs for normal adrenal glands, while maintaining an accurate characterization of benign and malignant glands

Authors

Daniëlle Koopman[1,2] | Jorn A. van Dalen[3] | Jos A. Stigt[4]
Cornelis H. Slump[2] | Siert Knollema[1] | Pieter L. Jager[1]

Author affiliations
1: Department of Nuclear Medicine, Isala, Zwolle, the Netherlands
2: MIRA Institute for Biomedical Technology and Technical Medicine, University of Twente, Enschede, the Netherlands
3: Department of Medical Physics, Isala, Zwolle, the Netherlands
4: Department of Pulmonology, Isala, Zwolle, the Netherlands

Published in
Annals of Nuclear Medicine 2016;30:145–152

Abstract

Objective

Modern PET/CT scanners have significantly improved detectors and fast time-of-flight (TOF) performance and this may improve clinical performance. The aim of this study was to analyze the impact of a current generation TOF PET/CT scanner on standardized uptake values (SUV), lesion-background contrast and characterization of the adrenal glands in patients with suspected lung cancer, in comparison with literature data and commonly used SUV cut-off levels.

Methods

We included 149 adrenal glands from 88 patients with suspected lung cancer, who underwent ^{18}F-FDG PET/CT. We measured the SUV_{max} in the adrenal gland and compared this with liver SUV_{mean} to calculate the adrenal-to-liver ratio (AL ratio). Results were compared with literature derived with older scanners, with SUV_{max} values of 1.0 and 1.8 for normal glands [1, 2]. Final diagnosis was based on histological proof or follow-up imaging. We proposed cut-off values for optimal separation of benign from malignant glands.

Results

In 127 benign and 22 malignant adrenal glands, SUV_{max} values were 2.3 ± 0.7 (mean ± SD) and 7.8 ± 3.2 respectively ($p<0.01$). Corresponding AL ratios were 1.0 ± 0.3 and 3.5 ± 1.4 respectively ($p<0.01$). With a SUV_{max} cut-off value of 3.7, 96% sensitivity and 96% specificity was reached. An AL ratio cut-off value of 1.8 resulted in 91% sensitivity and 97% specificity. The ability of both SUV_{max} and AL ratio to separate benign from malignant glands was similar (AUC 0.989 vs. 0.993, $p=0.22$).

Conclusions

Compared with literature based on the previous generation of PET scanners, current generation TOF ^{18}F-FDG PET/CT imaging provides higher SUVs for benign adrenal glands, while it maintains a highly accurate distinction between benign and malignant glands. Clinical implementation of current generation TOF PET/CT requires not only the use of higher cut-off levels but also visual adaptation by PET readers.

Keywords

^{18}F-FDG; PET/CT; Adrenal glands; Lung cancer

Introduction

Metastatic spread in non-small cell lung cancer (NSCLC) typically involves the brain, bone, liver, contralateral lung and adrenal glands [3]. An accurate evaluation of the adrenal glands is important, especially when the glands are enlarged on computed tomography (CT) [4, 5].

The adrenal glands can be characterized with several imaging techniques, like CT, magnetic resonance imaging (MRI), positron emission tomography (PET) using the tracer fluorine-18 fluordeoxyglucose (^{18}F-FDG) and combined ^{18}F-FDG PET/CT. All these techniques are capable of distinguishing benign from malignant adrenal masses, although with different degrees of accuracy [6]. Especially ^{18}F-FDG PET/CT performs well and is often used for this purpose as it is part of standard clinical practice in NSCLC.

The combination of the small size of the normal adrenal gland with the low ^{18}F-FDG uptake make the glands usually invisible on older PET scanners because of relatively low resolution. In 2004, a paper about the appearance of the normal adrenal gland on ^{18}F-FDG PET was published, which reported an average maximum standardized uptake value (SUV_{max}) around 1.0 [1]. More recently, Kim et al.[2] reported an average SUV_{max} value around 1.8 for normal glands. The introduction of combined PET/CT made the evaluation of adrenal glands with ^{18}F-FDG PET easier because the location of tracer uptake could now be more accurately assigned to the adrenal gland as seen on CT [1]. The visual aid provided by CT therefore led to a larger proportion of gland visualization, although ^{18}F-FDG uptake was still similar to the PET/CT era. Furthermore, it was demonstrated that the use of combined PET/CT improved the distinction between benign and malignant adrenal masses [7, 8].

In the past decade, however, PET technology itself has been upgraded with new, faster scintillators like Lutetium-Orthosilicate (LSO) and Lutetium-Yttrium-Orthosilicate (LYSO). As a consequence, time-of-flight (TOF) PET became the new standard technology for PET manufacturers. Generally, incorporation of the TOF technique leads to a more accurate determination of the origin of the annihilation event [9], resulting in improved measurements of ^{18}F-FDG uptake.

Even more recently, TOF performance is steadily improving in newer scanners. A recently introduced TOF PET/CT scanner (Ingenuity TF, Philips Healthcare) has a time-of-flight performance with a timing resolution of around 500 picoseconds [10], which translates to a location uncertainty of 7.5 cm on lines-of-response. The improved temporal resolution induces a higher signal-to-noise ratio, higher spatial resolution and improved PET image quality [11].

Therefore, the current generation of PET scanners may lead to a better detection of the adrenal glands as well as other small lesions. Therefore, the aim of this investigation was to analyze the impact of a current generation TOF PET/CT scanner on SUVs, lesion-to-background levels and characterization of adrenal glands in patients with clinically suspected lung cancer.

Materials and methods

Patients

We included 88 patients, referred for a whole-body ^{18}F-FDG PET/CT scan, to evaluate clinically suspected lung cancer. Only patients harboring at least one adrenal gland with a final diagnosis, based on histological proof or follow-up imaging, were selected for this study. For 27 patients who underwent a single adrenal gland biopsy, no follow-up imaging was available resulting in an unknown status for the contralateral gland that was not invasively evaluated. Consequently, in these patients, only the adrenal gland with histological proof was included.

We received a waiver from the Medical Ethical Committee of our institution to perform this partly retrospective and prospective study, as it only deals with additional evaluation of a clinical indicated scan. However, all patients agreed to the use of their data by signing an informed consent form.

PET/CT data acquisition

Patients fasted for at least 6 h prior to scanning. Before intravenous injection of ^{18}F-FDG, blood glucose levels were measured to ensure a value below 15 mmol/L. A dedicated dose protocol depending quadratically on patients' body weight, as recently proposed in the literature [12], was routinely used. It is described by the formula $A \times t = 3.8 \times w^2$, where A is the ^{18}F-FDG dose to administer (in MBq), t the time per bed position (in seconds) and w is the patients' body weight (in kilogram).

All PET/CT scans were acquired with a current generation PET/CT scanner (Ingenuity TF, Philips Healthcare, Cleveland, OH, USA). This fully three-dimensional TOF scanner is combined with a 128-slice CT scanner. The PET system contains 28,336 LYSO crystals (size 4×4×22 mm) divided across 44 detector rings. Regarding TOF performances, the timing resolution of the PET scanner is 495 picoseconds with a TOF localization-accuracy of 7.4 cm. The PET scan was performed using a whole-body PET/CT acquisition protocol with 50% bed-overlap. Acquisition times for the patient studies were 1 and 2 min per bed position for patients with body weight ≤80 and >80 kg, respectively. The average administered ^{18}F-FDG activity was 330 MBq (range 154–557 MBq).

Prior to PET imaging, a CT scan was acquired for attenuation correction. The CT scan parameters were: tube voltage 120 kV, average tube current 61 mA (range 36–140 mA), slice collimation 64 × 0.625 mm, pitch 0.83 and rotation time 0.5 s. The average CT dose-index was 4.1 mGy (range 2.5–9.3) with an average dose-length product of 438 mGy cm (range 250–930).

PET/CT data reconstruction

PET data were reconstructed using the default reconstruction algorithm “Blob-OS-TF”, a 3D ordered subset iterative TOF reconstruction technique [13, 14]. For all reconstructions, 3 iterations and 43 subsets were applied. PET images were reconstructed in 144×144 matrices with voxel size 4×4×4 mm^3 and relaxation parameter 1.0. The blob had a 2.5 mm radius with a blob shape parameter of 8.4 mm. Point-spread function modeling was not applied.

Raw CT data were reconstructed using an iterative reconstruction algorithm (iDose, Philips Healthcare, Cleveland, OH, USA) with iDose level 4 and a slice thickness of 3 mm. The acquisition- and reconstruction protocol were both compatible with the guidelines of the European Association of Nuclear Medicine (EANM) [15].

PET/CT data analysis

Integrated PET/CT data were reviewed on a dedicated workstation (IntelliSpace Portal 6, Philips Healthcare, Cleveland, OH, USA). The attenuation CT scan was used to identify the adrenal glands and to characterize the gland as normal sized or enlarged. The adrenal gland was regarded as enlarged when an adrenal mass of at least 1 cm was detected on an axial CT slice.

When histological evidence was not available, adrenal glands were considered benign when they were stable in size and had identical ^{18}F-FDG uptake on follow-up imaging. Adrenal glands were considered malignant when there was progression in size or ^{18}F-FDG uptake had increased as evaluated by experienced readers. Furthermore, in patients who received systemic treatment during the follow-up period, glands were considered malignant when they showed a decrease in size or ^{18}F-FDG uptake on follow-up imaging.

Quantitative PET measurements were performed by an experienced PET reader, blinded to histological and follow-up findings, who measured the uptake on the axial slice through the adrenal with the highest visual uptake. Around the adrenal, an elliptical 2D region-of-interest (ROI) was drawn that included at least two-thirds of the gland. After accurate placement of the adrenal ROI was confirmed on axial PET/CT images, the SUV_{max} within the ROI was determined.

Furthermore, we performed background measurements in a homogenous region in the liver. On the axial PET image containing the largest liver area, we drew a circular 2D ROI of 2000 mm^2 (5 cm diameter) in the right liver lobe and measured the mean standardized uptake value (SUV_{mean}) within this ROI. We made sure that this liver section was homogeneous on ^{18}F-FDG PET and free of any tumor or benign abnormality. For each adrenal gland, the adrenal-liver ratio (AL ratio) was derived by dividing adrenal gland SUV_{max} by liver SUV_{mean}.

Data analysis

We calculated average SUV_{max} and AL ratio values for benign and malignant adrenal glands, including a sub-analysis for normal-sized and enlarged glands. We determined the sensitivity and specificity of SUV_{max} and AL ratio for adrenal gland characterization at various cut-off levels, using the final diagnosis as a reference standard. For both parameters, the area under the curve (AUC) with the 95% confidence-interval (CI) was provided.

Statistical analysis

Results were presented as mean ± standard deviation (SD). Furthermore, ranges (minimum–maximum) in uptake values were included. We applied the Independent samples Mann–Whitney U test to compare the SUV_{max} and AL ratio between benign and malignant glands and normal-sized and enlarged glands, respectively. To evaluate differences in characterization performance between SUV_{max} and AL ratio, we compared the AUCs for both parameters using a Chi-square test. A p value less than 0.05 was considered to indicate statistical significance.

Results

Patient characteristics

Clinical data from 88 patients and 149 evaluated adrenal glands are presented in **Table 1**. All adrenal glands were identified on PET/CT images. There were 22 malignant and 127 benign glands. 91% (20/22) of the malignant glands were enlarged. Conversely, 40% (20/50) of the enlarged glands were malignant. For

76% of the adrenal glands (113/149) the final diagnosis was based on follow-up imaging. The average follow-up period was 6.1 months, which is fairly long in relation to the general rate of progression of lung cancer.

Average uptake values for benign and malignant glands

Table 2 contains average SUV_{max} and AL ratios for benign (n = 127) and malignant (n = 22) adrenal glands. For both parameters, we found significantly higher uptake values for malignant glands as compared to benign glands ($p < 0.001$), but with a wide range in uptake values for both groups as visualised in **Figure 1**.

Table 1 Summary of patient characteristics

Patients characteristics (n=88)	
Sex	
Male	56
Female	32
Age (years)	66 ± 11
Bodyweight (kg)	78 ± 15
Glucose (mmol/L)	6.1 ± 1.4
Follow-up period (months)	6.1 ± 2.4
Adrenal glands (n=149)	
Final diagnosis	
Benign	127
Malignant	22
Final diagnosis from	
Histological proof	36
Follow-up imaging	113
Gland characterization	
Normal-sized	99
Enlarged	50
Enlarged glands (n=50)	
Benign	30
Malignant	20

Table 2 SUV_{max} and AL ratios for benign and malignant adrenal glands

	Benign glands (n=127)	Malignant glands (n=22)	p value
	SUV_{max}		
Mean ± SD	2.3 ± 0.7	7.8 ± 3.2	p<0.001
Range	1.4–5.2	3.0–16.1	
	AL ratio		
Mean ± SD	1.0 ± 0.3	3.5 ± 1.4	p<0.001
Range	0.5–2.3	1.6–6.7	

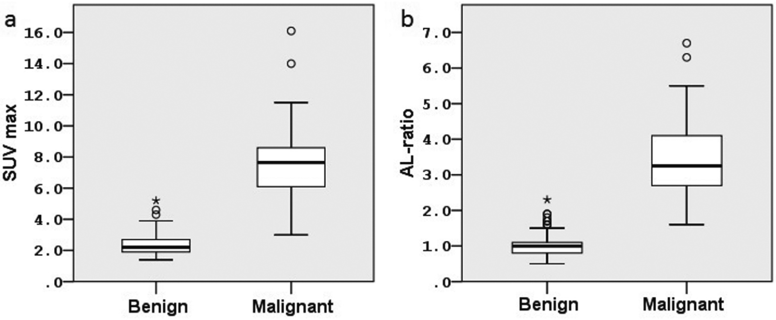

Figure 1 Box plots of the adrenal gland SUV$_{max}$ (a) and AL ratios (b) for benign and malignant adrenal glands. *Significant difference (p<0.001) in SUV$_{max}$ and AL ratio between benign and malignant glands. *Circle o* values that are between 1.5 and 3.0 box length from the percentile borders. Asterisk values that fall more than 3.0 box length outside the box borders

Normal-sized and enlarged adrenal glands

In **Table 3**, average SUV$_{max}$ and AL ratios for normal-sized (n=99) and enlarged (n=50) glands are presented. In enlarged glands, we found significantly higher uptake values when they were malignant (p<0.001). In normal-sized malignant glands, we also observed higher uptake values as compared to normal-sized benign glands, although the number of normal-sized malignant glands was limited (n=2).

Table 3 SUV$_{max}$ and AL ratios for normal-sized and enlarged, benign and malignant glands

	Normal-sized glands		p value	Enlarged glands		p value
	Benign (n=97)	Malignant (n=2)		Benign (n=30)	Malignant (n=20)	
			SUV$_{max}$			
Mean ± SD	2.3 ± 0.6	5.5 ± 0.8	p<0.001	2.6 ± 0.7	8.0 ± 3.3	p<0.001
Range	1.4–4.6	4.9–6.1		1.4–5.2	3.0–16.1	
			AL ratio			
Mean ± SD	1.0 ± 0.3	2.8 ± 0.6	p<0.001	1.3 ± 0.3	3.6 ± 1.4	p<0.001
Range	0.5–1.9	2.4–3.3		0.8–2.3	1.6–6.7	

Furthermore, for enlarged benign glands there were slightly higher uptake values as compared to normal-sized benign glands (p=0.01 for SUV$_{max}$ and p<0.001 for AL ratio, respectively). For both groups of benign glands, there was a wide range in uptake values as visualised in **Figure 2**.

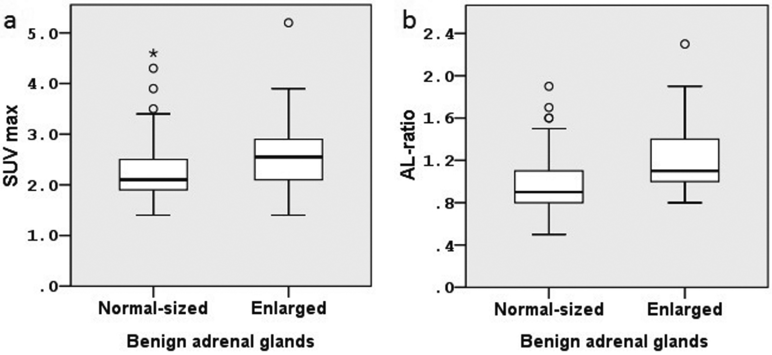

Figure 2 Box plots of the adrenal gland SUV$_{max}$ (a) and AL ratios (b) for normal-sized and enlarged benign adrenal glands. *Significant difference in SUV$_{max}$ (p=0.01) and AL ratio (p<0.001) between normal-sized and enlarged benign glands. *Circle o* values that are between 1.5 and 3.0 box length from the percentile borders. Asterisk values that fall more than 3.0 box length outside the box borders

Adrenal gland visualization with ^{18}F-FDG PET/CT

Figure 3 contains ^{18}F-FDG PET/CT images of three patients with benign normal-sized, benign enlarged and malignant adrenal glands. These examples present the typical visualization of adrenal glands as visualised on ^{18}F-FDG TOF PET/CT imaging.

Adrenal gland characterization

Both the SUV$_{max}$ and the AL ratio provided an accurate separation of benign from malignant glands. For the SUV$_{max}$, a cut-off value of 3.7 resulted in both 96% sensitivity and specificity. Using a lower SUV$_{max}$ of 3.0, 100% sensitivity was reached. However, this resulted in only 84% specificity. Furthermore, a higher SUV$_{max}$ of 5.7 resulted in 100% specificity with 77% sensitivity.

For the AL ratio, a cut-off value of 1.8 resulted in 91% sensitivity and 97% specificity. Using a lower AL ratio of 1.6, 100% sensitivity was reached with 92% specificity. Furthermore at AL ratio 2.4, 100% specificity was reached with 86% sensitivity.

The Chi-square test showed that the ability of both SUV$_{max}$ and AL ratio to separate benign from malignant glands was similar (p=0.22) with AUC values 0.989 (CI 0.974–1.000) and 0.993 (CI 0.983–1.000), respectively.

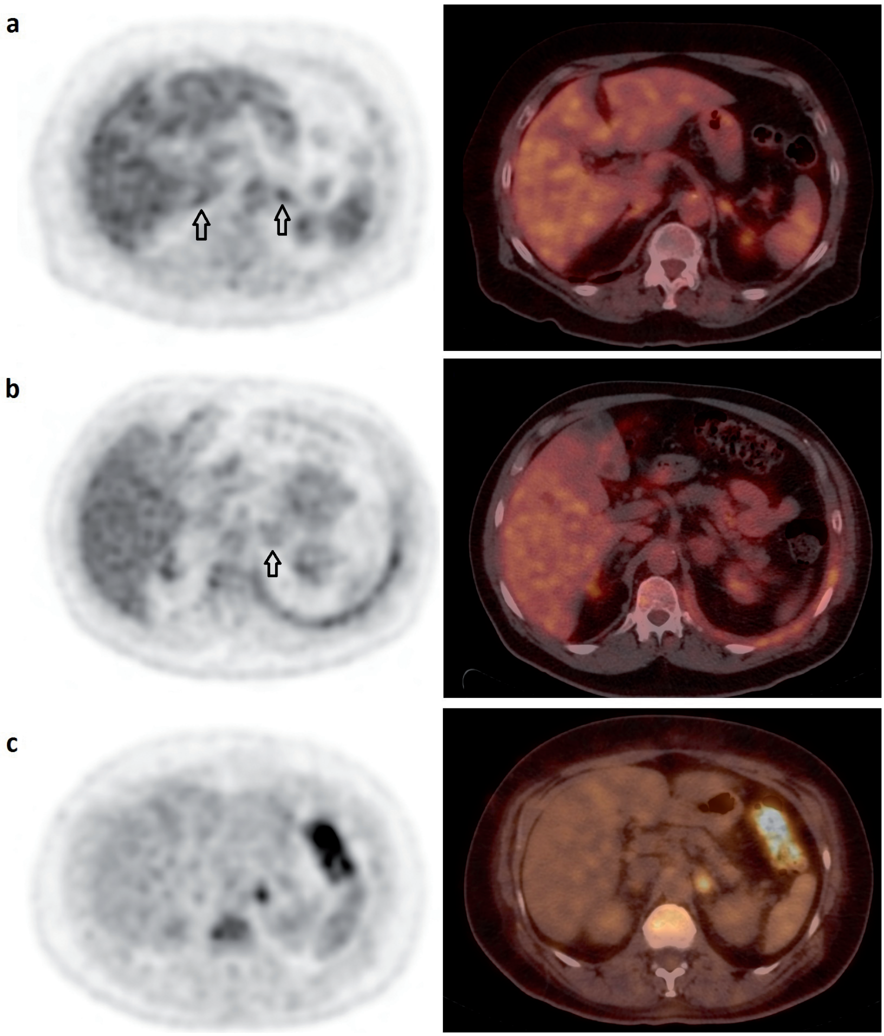

Figure 3 Single ^{18}F-FDG PET (left) and fused ^{18}F-FDG PET/CT (right) images of three patients. a. Two normal-sized adrenal glands (arrows) are visualised. Uptake values for the left adrenal gland were 3.4 (SUV_{max}) and 1.2 (AL ratio). For the right adrenal gland, the SUV_{max} and AL ratio were 3.2 and 1.1 respectively. A 6-months follow-up ^{18}F-FDG PET/CT scan did not reveal any changes in adrenal gland size, shape and ^{18}F-FDG uptake for both adrenal glands. **b.** Patient with an enlarged left adrenal gland (arrow), axial diameter 32 mm. Average uptake values were 2.6 (SUV_{max}) and 1.0 (AL ratio). A biopsy performed during endoscopic ultrasound was negative for tumor cells. Furthermore, 3-month follow-up ^{18}F-FDG PET/CT imaging did not reveal metastatic disease in this enlarged adrenal gland. **c.** Patient with a metastatic lesion in the left adrenal gland. On ^{18}F-FDG PET images, we measured a SUV_{max} of 4.9 and an AL ratio of 3.3 for this adrenal gland. A biopsy performed during endoscopic ultrasound-guided fine-needle aspiration (EUS-FNA) confirmed the presence of an adrenal metastasis, originating from a lung tumor.

Discussion

The present study shows that the use of current generation TOF PET/CT imaging yields higher SUVs in benign adrenal glands, as compared to values described in the literature based on the previous generation of PET scanners. Consequently, the visualization of normal glands on current generation TOF PET/CT has improved. Although theoretically the improved visualization of benign glands may lead to confusion, it appeared that the ability of ^{18}F-FDG PET to distinguish between benign and malignant nature of the adrenal lesions remains very high, as SUVs in malignant glands is also significantly higher than before. Using appropriate cut-off values, 96% sensitivity and 96% specificity can be reached, which leads to an accurate detection of metastatic adrenal gland lesions with modern PET/CT.

This study can be regarded as an update of published results in adrenal glands based on older PET/CT technology. Results from the present study differ in many aspects from previous investigations described in literature. For example, we found statistically different SUVs between normal-sized and enlarged benign glands ($p = 0.01$) which has been described before; however, in our study the mean difference in SUV between these groups was relatively small (SUV 2.3 vs. SUV 2.6). For enlarged adrenal glands (also mentioned adrenal lesions, nodules or masses), it is known that they may show an increased ^{18}F-FDG uptake when benign [16, 17] and our results are comparable with values reported in the literature. However, for normal-sized glands, an average SUV_{max} of 2.3 as found in our study is considerably higher than values of 1.0 and 1.8 as reported in the literature [1, 2]. In other words, with current generation TOF PET/CT there is an increase in measured SUV, especially for normal-sized benign glands. Their SUVs get closer to the commonly reported uptake values for enlarged benign glands.

Furthermore, our study revealed a broad range (1.4–5.2) in SUV_{max} for benign adrenal glands. The presence of a wide range in uptake values has been mentioned before [1, 2], but with much smaller ranges (0.95–2.46 and 1.0–3.3, respectively). Higher SUVs in normal-sized benign adrenal glands, as found in the present study, are likely caused by the improved resolution of current PET cameras with fast TOF providing a better image quality for more accurate SUV measurements [18]. Also the reduced partial volume effect contributes to the more accurate evaluation of small organs such as the adrenals.

In simplified terms, using older generation of PET scanners a clearly visualized adrenal could often times safely and correctly be reported as malignant. With the modern scanners, however, this is no longer the case. PET readers should be aware of higher SUVs as well as wider ranges in benign adrenal glands when evaluating scans acquired with current generation TOF PET/CT. Readers should also update their cut-off levels if they decide to use SUV measurements to assist the visual diagnosis. It is expected that this new particular knowledge improves the diagnostic confidence of PET readers and prevents unnecessary adrenal gland biopsies when implementing current generation TOF PET/CT.

The main advantage of ^{18}F-FDG PET/CT in adrenal gland evaluation is the ability to detect and exclude metastatic disease. Therefore, our finding that normal adrenal glands show higher ^{18}F-FDG uptake values on TOF PET/CT may make interpretation more difficult, as it can be hypothesized that the presence of higher SUVs in normal adrenal glands makes the distinction between benign glands and (small) adrenal metastases more difficult. However, in our study uptake in malignant glands was also considerably higher and overall, we showed that ^{18}F-FDG PET/CT still has a great ability to detect metastatic disease in adrenal glands, with 96% sensitivity and 96% specificity at a SUV_{max} cut-off level of 3.7. Many studies described lower SUV_{max} cut-off values ranging between 2.5 and 3.4 [2, 7, 19-22]. Furthermore, one study reported an optimal SUV_{max} of 3.9 with a relative poor performance (sensitivity 96%, specificity 82%) [23] while another study recently found sensitivity and specificity values of 90% using SUV_{max} cut-off 5.2 [18].

Apart from the use of SUV_{max} in image interpretation, adrenal gland uptake is always visually or quantitatively compared with tracer intensity in the liver. In the present study, SUV_{max} and AL ratio performances for adrenal gland characterization were comparable. Nonetheless, some studies suggested that the AL ratio is the most accurate parameter for gland characterization [18, 23, 24]. In the past 15 years, many studies used a visual or quantitative AL ratio equal to or larger than 1.0 as cut-off value to separate benign from malignant adrenal glands [5, 8, 24, 25]. In contrast, our study indicates that an AL ratio of at least 1.6 should be used for accurate distinction while recently, two other studies reported AL ratios of 1.4 and 1.5 with sensitivity and specificity values above 90% [18, 23]. Hence, this demonstrates that clinical implementation of current generation TOF PET/CT requires higher AL ratio cut-offs than used to the past, which demands a change in both quantitative and visual adrenal gland assessment by PET readers.

In this study we demonstrated that the current generation TOF PET/CT scanner is highly accurate in adrenal gland characterization. However, we also found a wide range in benign gland SUVs with some overlap in malignant gland SUVs. Therefore, when a gland with a SUV ranging between 3 and 6 is suspected to be the only metastatic location in a patient, the status is still often verified by biopsy (for leftsided glands) or short term follow-up imaging (for right-sided glands), despite the very high detection performance of PET.

The present study has some limitations. With an average follow-up of 6 months, the follow-up period in this study may be short, potentially biasing the results. However, on average NSCLC rapidly progresses even after chemotherapy. It seems unlikely that a normal sized metastatic gland remains unchained in this period, although we cannot completely exclude this possible small error. Furthermore, the diagnostic performance might be further improved if we would take additional information such as adrenal gland Hounsfield measurements and contrast washout into account [5, 7, 21]. Moreover, we focused on quantitative assessment of the adrenal glands, while visual adrenal-to-background evaluation on ^{18}F-FDG PET remains important and sensitive in clinical practice [19, 26]. Finally, adrenal gland uptake may differ depending on the populations studied [2].

Conclusion

Current generation TOF ^{18}F-FDG PET/CT imaging results in higher SUVs and adrenal-to-liver ratios in benign adrenal glands, as compared to literature based on older scanners. This leads to an improved visualization of both benign and malignant glands and requires adaptation of PET readers when evaluating current generation TOF PET/CT images. However, this study indicates that the quantitative differentiation between benign and malignant glands in patients with suspected lung cancer remains highly accurate, when appropriate cut-off levels are used.

References

1. Bagheri B, Maurer AH, Cone L, Doss M, Adler L. Characterization of the normal adrenal gland with 18F-FDG PET/CT. J Nucl Med 2004;45:1340-3.
2. Kim BS, Lee JD, Kang WJ. Differentiation of an adrenal mass in patients with non-small cell lung cancer by means of a normal range of adrenal standardized uptake values on FDG PET/CT. Ann Nucl Med 2015;29:276-83.
3. Quint LE, Tummala S, Brisson LJ, Francis IR, Krupnick AS, Kazerooni EA, Iannettoni MD, Whyte RI, Orringer MB. Distribution of distant metastases from newly diagnosed non-small cell lung cancer. Ann Thorac Surg 1996;62:246-50.
4. Kumar R, Xiu Y, Jian QY, Takalkar A, El-Haddad G, Potenta S, Kung J, Zhuang H, Alavi A. 18F-FDG PET in evaluation of adrenal lesions in patients with lung cancer. J Nucl Med 2004;45:2058-62.
5. Park SY, Park BK, Kim CK. The value of adding 18F-FDG PET/CT to adrenal protocol CT for characterizing adrenal metastasis (≥ 10 mm) in oncologic patients. Am J Roentgenol 2014;202:W153-60.
6. Blake MA, Cronin CG, Boland GW. Adrenal imaging. Am J Roentgenol 2010;194:1450-60.
7. Metser U, Miller E, Lerman H, Lievshitz G, Avital S, Even-Sapir E. 18F-FDG PET/CT in the evaluation of adrenal masses. J Nucl Med 2006;47:32-7.
8. Kim Y, Cheon GJ, Paeng JC, Cho JY, Kang KW, Chung J, Kim EE, Lee DS. Total lesion glycolysis as the best 18F-FDG PET/CT parameter in differentiating intermediate–high risk adrenal incidentaloma. Nucl Med Commun 2014;35:606-12.
9. Kadrmas DJ, Casey ME, Conti M, Jakoby BW, Lois C, Townsend DW. Impact of time-of-flight on PET tumor detection. J Nucl Med 2009;50:1315-23.
10. Kolthammer JA, Su K, Grover A, Narayanan M, Jordan DW, Muzic RF. Performance evaluation of the Ingenuity TF PET/CT scanner with a focus on high count-rate conditions. Phys Med Biol 2014;59:3843-59.
11. Conti M. Focus on time-of-flight PET: the benefits of improved time resolution. Eur J Nucl Med Mol Imaging 2011;38:1147-57.
12. de Groot E,H., Post N, Boellaard R, Wagenaar NRL, Willemsen ATM, van Dalen J,A. Optimized dose regimen for whole-body FDG-PET imaging. EJNMMI Res 2013;3:63-72.
13. Lewitt RM. Multidimensional digital image representations using generalized Kaiser–Bessel window functions. J Opt Soc Am 1990;7:1834-46.
14. Matej S, Lewitt RM. Practical considerations for 3-D image reconstruction using spherically symmetric volume elements. IEEE Trans Med Imaging 1996;15:68-78.
15. Boellaard R, Delgado-Bolton R, Oyen WJG, Giammarile F, Tatsch K, Eschner W, Verzijlbergen FJ, Barrington SF, Pike LC, Weber WA. FDG PET/CT: EANM procedure guidelines for tumour imaging: version 2.0. Eur J Nucl Med Mol Imaging 2015;42:328-54.

16. Erasmus JJ, Patz Jr EF, McAdams HP, Murray JG, Herndon J, Coleman RE, Goodman PC. Evaluation of adrenal masses in patients with bronchogenic carcinoma using 18F-fluorodeoxyglucose positron emission tomography. AJR Am J Roentgenol 1997;168:1357-60.
17. Chong S, Lee KS, Kim HY, Kim YK, Kim B, Chung MJ, Yi CA, Kwon GY. Integrated PET-CT for the characterization of adrenal gland lesions in cancer patients: diagnostic efficacy and interpretation pitfalls 1. Radiographics 2006;26:1811-24.
18. Kunikowska J, Matyskiel R, Toutounchi S, Grabowska-Derlatka L, Koperski Ł, Królicki L. What parameters from 18F-FDG PET/CT are useful in evaluation of adrenal lesions?. Eur J Nucl Med Mol Imaging 2014;41:2273-80.
19. Jana S, Zhang T, Milstein DM, Isasi CR, Blaufox MD. FDG-PET and CT characterization of adrenal lesions in cancer patients. Eur J Nucl Med Mol Imaging 2006;33:29-35.
20. Okada M, Shimono T, Komeya Y, Ando R, Kagawa Y, Katsube T, Kuwabara M, Yagyu Y, Kumano S, Imaoka I. Adrenal masses: the value of additional fluorodeoxyglucose-positron emission tomography/computed tomography (FDG-PET/CT) in differentiating between benign and malignant lesions. Ann Nucl Med 2009;23:349-54.
21. Brady MJ, Thomas J, Wong TZ, Franklin KM, Ho LM, Paulson EK. Adrenal nodules at FDG PET/CT in patients known to have or suspected of having lung cancer: a proposal for an efficient diagnostic algorithm 1. Radiology 2009;250:523-30.
22. Ansquer C, Scigliano S, Mirallié E, Taïeb D, Brunaud L, Sebag F, Leux C, Drui D, Dupas B, Renaudin K. 18F-FDG PET/CT in the characterization and surgical decision concerning adrenal masses: a prospective multicentre evaluation. Eur J Nucl Med Mol Imaging 2010;37:1669-78.
23. Watanabe H, Kanematsu M, Goshima S, Kondo H, Kawada H, Noda Y, Moriyama N. Adrenal-to-liver SUV ratio is the best parameter for differentiation of adrenal metastases from adenomas using 18F-FDG PET/CT. Ann Nucl Med 2013;27:648-53.
24. Caoili EM, Korobkin M, Brown RKJ, Mackie G, Shulkin BL. Differentiating adrenal adenomas from nonadenomas using 18F-FDG PET/CT: quantitative and qualitative evaluation. Acad Radiol 2007;14:468-75.
25. Evans PD, Miller CM, Marin D, Stinnett SS, Wong TZ, Paulson EK, Ho LM. FDG-PET/CT characterization of adrenal nodules: diagnostic accuracy and interreader agreement using quantitative and qualitative methods. Acad Radiol 2013;20:923-9.
26. Boland GWL, Blake MA, Holalkere NS, Hahn PF. PET/CT for the characterization of adrenal masses in patients with cancer: qualitative versus quantitative accuracy in 150 consecutive patients. Am J Roentgenol 2009;192:956-62.

CHAPTER 8

8

Improving the detection of small lesions using a state-of-the-art time-of-flight PET/CT system and small-voxel reconstructions

Authors

Daniëlle Koopman[1,2] | Jorn A. van Dalen[3] | Martine C. M. Lagerweij[3]
Hester Arkies[1] | Jaep de Boer[1] | Ad H. J. Oostdijk[1]
Cornelis H. Slump[2] | Pieter L. Jager[1]

Author Affiliations
1: Department of Nuclear Medicine, Isala, Zwolle, the Netherlands
2: MIRA Institute for Biomedical Technology and Technical Medicine, University of Twente, Enschede, the Netherlands
3: Department of Medical Physics, Isala, Zwolle, the Netherlands

Published in
Journal of Nuclear Medicine Technology 2015;43:21-27

Abstract

A major disadvantage of ^{18}F-FDG PET involves poor detection of small lesions and lesions with low metabolism, caused by limited spatial resolution and relatively large image voxel size. As spatial resolution and sensitivity are better in new PET systems, it is expected that small-lesion detection could be improved using smaller voxels. The aim of this study was to test this hypothesis using a state-of-the-art time-of-flight PET/CT device.

Methods

^{18}F-FDG PET scans of 2 image-quality phantoms (sphere sizes, 4–37 mm) and 39 consecutive patients with lung cancer were analyzed on a time-of-flight PET/CT system. Images were iteratively reconstructed with standard 4×4×4 mm voxels and smaller 2×2×2 mm^3 voxels. For the phantom study, we determined contrast-recovery coefficients and signal-to-noise ratios (SNRs). For the patient study, ^{18}F-FDG PET–positive lesions in the chest and upper abdomen with a volume less than 3.0 mL (diameter, <18 mm) were included. Lesion mean and maximum standardized uptake values (SUV$_{mean}$ and SUV$_{max}$, respectively) were determined in both image sets. SNRs were determined by comparing SUV$_{max}$ and SUV$_{mean}$ with background noise levels. A subanalysis was performed for lesions less than 0.75 mL (diameter, <11 mm). For qualitative analysis of patient data, 3 experienced nuclear medicine physicians gave their preference after visual side-by-side analysis.

Results

For phantom spheres 13 mm or less, we found higher contrast-recovery coefficients and SNRs using small-voxel reconstructions. For 66 included ^{18}F-FDG PET–positive lesions, the average increase in SUV$_{mean}$ and SUV$_{max}$ using the small-voxel images was 17% and 32%, respectively ($p<0.01$). For lesions less than 0.75 mL (21 in total), the average increase was 21% and 44%, respectively. Moreover, averaged over all lesions, the mean and maximum SNR increased by 20% and 27%, respectively ($p<0.01$). For lesions less than 0.75 mL, these values increased up to 23% and 46%, respectively. The physicians preferred the small-voxel reconstructions in 76% of cases.

Conclusion

Supported by a phantom study, there was a visual preference toward ^{18}F-FDG PET images reconstructed with 2×2×2 mm^3 voxels and a profound increase in standardized uptake value and SNR for small lesions. Hence, it is expected that small-lesion detection improves using small-voxel reconstructions.

Keywords

18F-FDG PET; time-of-flight small-voxel reconstruction; lung cancer; small lesions

Introduction

Whole-body ^{18}F-FDG PET integrated with CT is widely used for primary tumor analysis and mediastinal lymph node staging in patients with non–small cell and small cell lung cancer [1, 2]. For these patients, accurate lymph node staging is of high importance because both prognosis and therapeutic management depend on the tumor stage [3]. A major disadvantage of ^{18}F-FDG PET involves poor detection of small lesions and lesions with low metabolism. With a sensitivity of 76% and specificity of 88% [4], PET/CT is less sensitive for nodal involvement of small nodes (diameter, <10 mm) [3, 5]. This poor detection is caused by limited spatial resolution and sensitivity [3, 6]. To improve work flow and patient comfort, relatively large image voxel sizes are generally preferred in clinical practice to effectively obtain more counts per voxel and subsequently a reduction in image noise [7]. However, the low spatial resolution introduces the partial-volume effect, which affects images both visually and quantitatively because small lesions may appear larger and their ^{18}F-FDG uptake may seem lower than is actually the case [8]. Consequently, the detection of small lesions is limited by the partial-volume effect.

In the literature, several ways to improve lesion detectability on PET/CT are described. With the introduction of scintillators such as lutetium orthosilicate and lutetium yttrium orthosilicate, time-of-flight (TOF) PET became the new standard technology for PET manufacturers. With the implementation of TOF PET, the increased signal-to-noise ratio (SNR) appeared to improve the detectability of small lesions [9-12]. Furthermore, the detection of small lesions can be improved by changing reconstruction settings, for example, by optimizing the number of iterations and subsets and by modeling of the point-spread function [13-15].

In current practice, the image voxel size for whole-body ^{18}F-FDG PET scans is typically around 4×4×4 mm^3 [7, 16]. Conti [7] suggested that in combination with new high sensitive TOF PET/CT cameras, the use of reconstructions with smaller voxels might further improve the detection of small lesions. However, it was not assessed before to which extent small lesion detectability is influenced by the reconstruction voxel size. Therefore, the aim of this study was to determine the impact of a small-voxel reconstruction on the detectability of small lesions using a state-of-the-art TOF PET/CT device.

Materials and methods

To study the impact of small-voxel reconstructions on lesion detectability using a state-of-the-art TOF PET/CT device, we first performed a phantom study and subsequently a patient study.

Phantom Study

We analyzed 2 image-quality phantoms consisting of spheres with varying sizes. The National Electrical Manufacturers Association (NEMA) International Electrotechnical Commission (IEC) Body Phantom Set (model PET/IEC-BODY-P) image-quality phantom (NEMA phantom) has an interior length of 18 cm and contains 6 fillable spheres with 10-, 13-, 17-, 22-, 28-, and 37-mm inner diameters. The large background compartment (with a volume of 9,300 mL) and the 6 spheres were filled with a solution of ^{18}F-FDG, 2.0 and 19.9 kBq/mL, respectively, resulting in a sphere-to-background ratio of 10.0. The sphere-to-background ratio was consistent with the guidelines of the European Association of Nuclear Medicine (EANM) [17]. The cylinder-shaped Micro Hollow Sphere Phantom (model ECT/HS/MMP) (microphantom) has an inside diameter of 40 mm, inside height of 82 mm, and volume of 103 mL. It contains 4 fillable spheres with 4-, 5-, 6-, and 8-mm inner diameters. The background compartment and 4 spheres were filled with a solution of ^{18}F-FDG, 1.9 and 17.4 kBq/mL, respectively, resulting in a sphere-to-background ratio of 9.4.

Patient Study

Thirty-nine consecutive patients with lung cancer, who underwent ^{18}F-FDG PET/CT, were analyzed. Patients signed a written informed consent form, and this study was approved by the local ethical committee of our institution. Patients fasted for at least 6 h before scanning. Before intravenous injection of ^{18}F-FDG, blood glucose levels were measured to ensure a value below 15 mmol/L. A dedicated dose protocol, depending quadratically on patients' body weight [18], was implemented using the formula $A \times t = 3.8 \times m^2$. In this formula, A is the ^{18}F-FDG dose to administer in MBq, t the time per bed position in seconds (s), and m the body weight in kilograms (kg). ^{18}F-FDG dose and acquisition time were consistent with EANM guidelines for tumor PET imaging [17].

Data Acquisition

All PET/CT scans were acquired with the Ingenuity TF PET/CT scanner (Philips Healthcare). This fully 3-dimensional (3D) TOF scanner is combined with a 128-slice CT scanner. The PET system contains 28,336 lutetium yttrium orthosilicate crystals (size, 4×4×22 mm) divided across 44 detector rings. Regarding TOF performance, the timing resolution of the PET scanner is 495 picoseconds, with a TOF localization accuracy of 7.43 cm. The scan duration for the NEMA phantom was 10 min per bed position, as proposed in the EANM guidelines [17]. Also for the microphantom, the duration of the PET scan was 10 min. Acquisition times for the patient studies were, respectively, 1 and 2 min per bed position for patients with a body weight 80 kg or less and more than 80 kg. The administered ^{18}F-FDG dose ranged from 185 to 500 MBq. The PET scan was followed by a CT scan, used for attenuation correction.

Data Reconstruction

PET data were reconstructed using a default 3D ordered-subset iterative TOF reconstruction technique. Images were reconstructed in 2 types of matrices: 144×144 matrices with a voxel size of 4×4×4 mm^3 (standard-voxel reconstruction) and 288×288 matrices with a voxel size of 2×2×2 mm^3 (small-voxel reconstruction). To compensate for detector blurring, a blob-based reconstruction was applied. These spheric symmetric image elements (blobs), originating from Kaiser–Bessel basis functions [19, 20], are used instead of voxels for image representation. In a blob reconstruction, there is blob overlap, enabling better contrast-to-noise performance without the need for postfiltering [20]. We used 2 types of blobs in this study. For the standard-voxel reconstruction, the blob had a 2.5-mm radius, with a blob shape parameter of 8.4 mm. The blob radius and shape parameter for the small-voxel reconstruction were 2.8 and 6.4 mm, respectively. Furthermore, the relaxation parameters for the standard- and small-voxel reconstruction were 1.0 and 0.5, respectively. For both types of voxel reconstructions, 3 iterations and 43 subsets were applied. All reconstruction parameters were default settings recommended by the manufacturer.

Data Analysis

Phantom Study

Quantitative measurements were performed on a dedicated workstation (IntelliSpace Portal 6; Philips Healthcare). For each sphere, we determined the mean and maximum ^{18}F-FDG concentration (kBq/mL) in both standard- and small-voxel reconstructed image sets. The mean ^{18}F-FDG concentration was calculated from a 3D isocontour created at 50% of the maximum pixel value. Furthermore, background measurements were performed in a circle-based region of interest (ROI) of approximately 2,000 mm^2 (NEMA phantom) and 400 mm^2 (microphantom) localized in a homogeneous region in a background part of the phantom. For the NEMA phantom, we performed background measurements on the most central axial slice, at least 20 mm away from both the phantom edge and the phantom spheres to prevent influence of the partial-volume effect. For the microphantom, we performed the background measurements in an axial slice 20 mm below the spheres. The mean ^{18}F-FDG concentration and SD in the ROI were determined. Using **Formula 1**, we calculated the noise in the phantom background compartment.

$$\mathbf{Noise} = \frac{SD_b}{C_{bg}} \tag{1}$$

In this formula, C_{bg} and SD_{bg} are, respectively, the mean and SD of the ^{18}F-FDG concentration as measured in the background of the reconstructed images. For each sphere, we determined the mean and maximum contrast recovery coefficients (CRC_{mean} and CRC_{max}, respectively) using **Formula 2**.

$$\mathbf{CRC} = \frac{C_{measured}}{C_{true}} \tag{2}$$

CRC is defined as the ratio between the measured (maximum or mean) ^{18}F-FDG concentration in the images ($C_{measured}$) and the true ^{18}F-FDG concentration in the sphere (C_{true}). $C_{measured}$ and C_{true} were both adapted for the background, to distinguish the uptake in the (small) spheres from background uptake. Hence, for the NEMA phantom spheres C_{true} was 17.9 kBq/mL, and for the microphantom spheres C_{true} was 15.5 kBq/mL. Furthermore, we calculated the mean and maximum SNR (SNR_{mean} and SNR_{max}, respectively) using **Formula 3**.

$$\mathbf{SNR} = \frac{C_{measured}}{SD_{bg}} \tag{3}$$

In this equation, SD_{bg} is the SD of the ^{18}F-FDG concentration as measured in the background of the images. For all parameters, we determined the relative changes between the standard- and small-voxel reconstructions.

Patient Study

For quantitative analysis of the patient data, the same workstation was used as for the phantom study. Lesion volume was determined by taking the average lesion volume (based on isocontours at 50% of the maximum pixel value) derived from both reconstructed PET images. Only ^{18}F-FDG PET–positive lesions in the chest and upper abdominal region with an average lesion volume of less than 3.0 mL (≈diameter, <18 mm) were included for analysis. Lesions were considered as ^{18}F-FDG PET–positive when there was an increased uptake (visually assessed), compared with the mediastinal blood pool [21-23] on the standard-voxel reconstruction. A maximum of 3 lesions per patient was incorporated to avoid the impact of some patients with many small lesions. In these cases, the 3 smallest lesions were selected. In total, we included sixty-six ^{18}F-FDG PET–positive lesions, located, respectively, in the mediastinum (n=30), lung (n=23), hilar region (n=8), axilla (n=3), and high abdominal region (n=2). A subanalysis was performed for lesions less than 0.75 mL (≈diameter, <11 mm).

For each lesion, we measured the mean and maximum standardized uptake values (SUV_{mean} and SUV_{max}, respectively), where the mean value was again based on the isocontour at 50% of the maximum pixel value. We performed background measurements in the mediastinal blood pool, by drawing an ROI of approximately 400 mm^2. This way, the SUV_{mean} ($SUV_{background}$) and SD in this background were determined. Subsequently, SNR_{mean}, SNR_{max} and background noise were calculated in a similar way as for the phantom study. For all parameters, we determined the relative changes between the standard- and small-voxel reconstructions.

For a visual analysis, 3 experienced nuclear medicine physicians, who were unaware of the study purpose, performed a side-by-side analysis of the standard- and small-voxel reconstructed images. For the 66 selected lesions, the physicians had to rank their preference based on lesion sharpness, lesion contrast, and diagnostic confidence.

Statistical Analysis

We used the Wilcoxon signed-rank test to compare SUV_{mean}, SUV_{max}, SNR_{mean} and SNR_{max} measurements between the standard- and small-voxel reconstructions. Furthermore, we performed linear regression analysis to determine correlations between lesion volume and relative changes in SUV_{mean}, SUV_{max}, SNR_{mean} and SNR_{max}. In this perspective, we performed the F test and calculated Pearson correlation coefficients. A p value of less than 0.05 was considered to indicate statistical significance.

Results

Phantom Study

Figure 1 shows illustrations of the NEMA phantom and microphantom that were reconstructed using standard and small voxels. When **Figures 1A and 1B** are compared, it is clearly visualized that the 2 smallest spheres of the NEMA phantom have an enhanced contrast on the small-voxel reconstruction (**Fig. 1B**). Furthermore, as can be seen in **Figure 1D**, the contrast of the small spheres in the microphantom is clearly increased on the small-voxel reconstruction, compared with the standard-voxel reconstruction (**Fig. 1C**). This particularly pertains for the smallest phantom sphere (4 mm) of the microphantom, which could not be distinguished from the background on the standard-voxel reconstruction, whereas it is clearly visualized on the small-voxel reconstruction. Background noise levels in the NEMA phantom were 5.1% and 7.5% for the standard- and small-voxel reconstruction, respectively. For the microphantom, noise levels for these reconstructions were 4.0% and 5.6%, respectively.

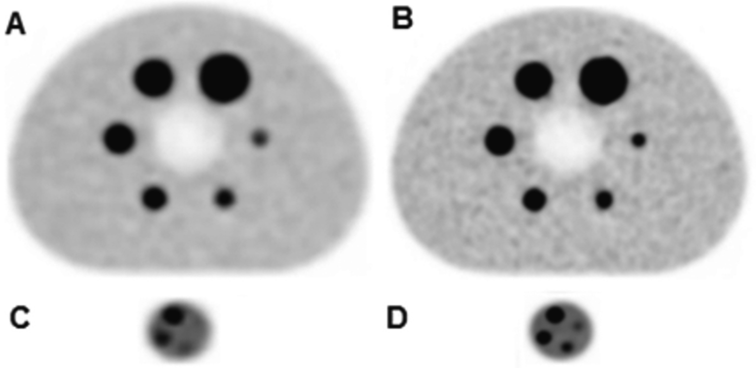

Figure 1 ^{18}F-FDG PET images of NEMA phantom (A and B) and microphantom (C and D) using standard-voxel reconstruction (A and C) and small-voxel reconstructions (B and D). Sphere sizes for NEMA phantom were 10, 13, 17, 22, 28, and 37 mm, inner diameter, and sphere sizes for microphantom were 4, 5, 6, and 8 mm, inner diameter. For all spheres with diameter of 13 mm or less, contrast is clearly increased using small-voxel reconstruction. Moreover, smallest microphantom sphere cannot be distinguished from background on standard-voxel reconstruction (C), yet it can be detected on small-voxel reconstruction (D)

The impact of the small-voxel reconstruction on CRC_{mean}, CRC_{max}, SNR_{mean} and SNR_{max} is summarized in **Table 1**. As presented in this table, for all parameters we found increases for the small spheres (≤13 mm) using the small-voxel reconstruction. The relative increases were the highest for the smallest spheres (≤6 mm). In particular for the 5- and 6-mm spheres, we found relative increases of more than 100% for CRC_{max} and SNR_{max}. The 4-mm microphantom sphere could not be distinguished from the background on the standard-voxel reconstruction (listed as not applicable). For the larger spheres (≥17 mm), decreases in SNR_{mean} and SNR_{max} were approximately 30%. These decreases were related to the increase of noise on the small-voxel reconstruction. However, the detection of these spheres on the small-voxel reconstruction was not compromised because the SNRs were still quite large (>60). Furthermore, the CRCs remained constant for the larger spheres as presented in **Table 1**.

Table 1 CRC$_{mean}$, CRC$_{max}$, SNR$_{mean}$ and SNR$_{max}$ for 10 phantom spheres for both voxel reconstructions, including relative changes (%)

	Microphantom sphere diameter (mm)				NEMA phantom sphere diameter (mm)					
Parameter	4	5	6	8	10	13	17	22	28	37
CRC$_{mean}$										
Standard	N/A	0.02	0.06	0.14	0.25	0.38	0.62	0.67	0.71	0.75
Small	0.03	0.04	0.12	0.25	0.37	0.45	0.65	0.69	0.73	0.71
%	N/A	84%	84%	79%	46%	19%	5%	3%	3%	−6%
CRC$_{max}$										
Standard	N/A	0.03	0.11	0.20	0.43	0.65	0.99	1.01	0.96	1.00
Small	0.06	0.10	0.24	0.44	0.72	0.85	0.97	0.96	0.99	1.00
%	N/A	239%	118%	115%	68%	31%	−2%	−4%	2%	0%
SNR$_{mean}$										
Standard	N/A	5	16	56	42	63	104	112	118	124
Small	9	10	30	64	42	52	74	79	83	80
%	N/A	87%	85%	79%	0%	−18%	−28%	−29%	−30%	−35%
SNR$_{max}$										
Standard	N/A	8	28	52	71	108	165	167	161	166
Small	14	27	61	112	82	97	110	110	113	114
%	N/A	242%	119%	116%	15%	−10%	−33%	−35%	−30%	−31%

Standard = standard-voxel reconstruction (4×4×4 mm^3); N/A = not applicable; small = small-voxel reconstruction (2×2×2 mm^3).

Figure 2 presents the CRC$_{mean}$ and CRC$_{max}$ for the 10 spheres (the smallest 4 from the microphantom) for both reconstruction types. Furthermore, it includes the relative changes in CRC between the standard- and small-voxel reconstruction. As can be seen in this figure, for the spheres 13 mm or less, both the CRC$_{mean}$ and the CRC$_{max}$ were higher on the small-voxel reconstruction, inducing relative increases up to 80% for the CRC$_{mean}$ and 200% for the CRC$_{max}$.

Patient Study

Regarding quantitative analysis, the average lesion volume was 1.18 mL (diameter, ~18 mm), with 21 lesions smaller than 0.75 mL (diameter, ~11 mm). The average background noise was 19% higher on the small-voxel images (17% vs. 20% for standard- and small-voxel images, respectively).

The average changes in SUV$_{mean}$ and SUV$_{max}$ we found using the small-voxel images were 17% ($p<0.001$) and 32% ($p<0.001$), respectively. These values increased up to 21% and 44%, respectively, for lesions less than 0.75 mL. The increases in SNR$_{mean}$ and SNR$_{max}$ were 13% ($p=0.015$) and 27% ($p<0.001$), respectively. For lesions less than 0.75 mL, these values improved toward 23% and 46%. We found moderate

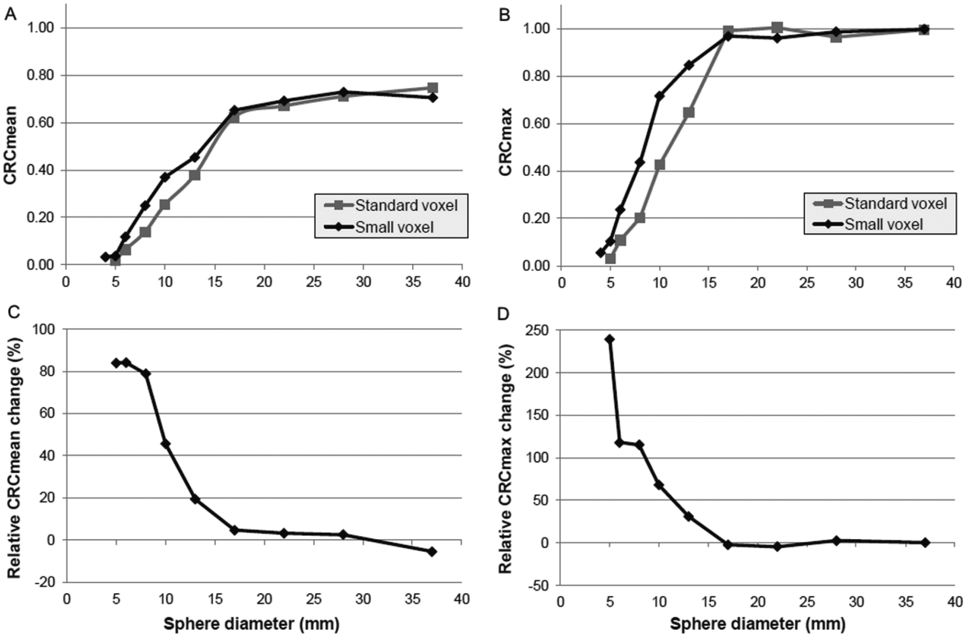

Figure 2 CRC_{mean} (A) and CRC_{max} (B) for phantom spheres using standard- and small-voxel reconstructions, with relative changes (%) for both parameters presented in plot C and D. For small spheres (≤13 mm), we found increases for CRC_{mean} and CRC_{max} using small-voxel reconstruction, with highest relative increases for 5- and 6-mm small spheres. As 4-mm small spheres could not be distinguished from background on standard-voxel reconstruction, no relative CRC changes were determined

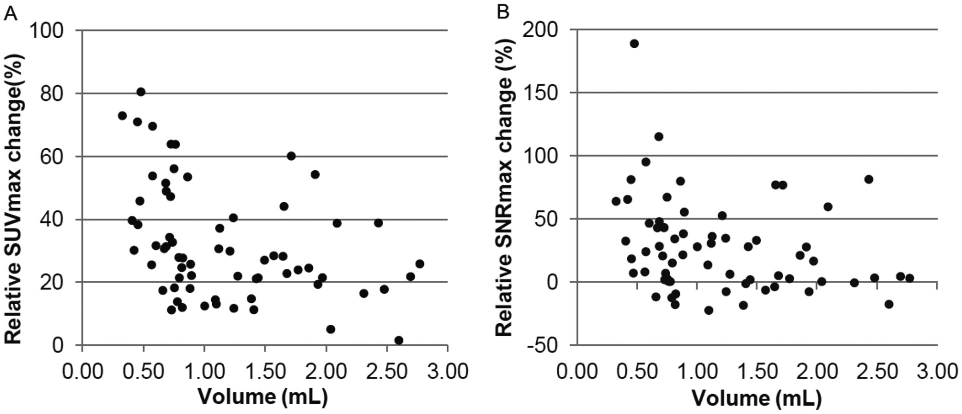

Figure 3 Relative changes in SUV_{max} (A) and SNR_{max} (B) for all 66 included lesions using small-voxel reconstruction instead of standard-voxel reconstruction. Average changes in SUV_{max} and SNR_{max} across all lesions were 32% and 27%, respectively. For lesions smaller than 0.75 mL, we found average SUV_{max} and SNR_{max} increases of 44% and 46%, respectively

correlations between lesion volume and relative changes in SUV_{mean}, SUV_{max}, SNR_{mean} and SNR_{max} with Pearson correlation coefficients of −0.34, −0.38, −0.23, and −0.27, respectively. Nevertheless, changes in SUV_{mean}, SUV_{max} and SNR_{max} correlated significantly with lesion volume ($p < 0.05$). The correlation between lesion volume and relative change in SNR_{mean} was nonsignificant ($p=0.07$). Relative changes in SUV_{max} and SNR_{max} for all lesions, using the small-voxel reconstruction instead of the standard-voxel reconstruction, are presented in **Figure 3**.

Regarding visual analysis, the 3 physicians preferred the small-voxel images in, respectively, 64%, 77%, and 88% of cases (average, 76%). Furthermore, in 88% of cases, at least 2 physicians preferred the small-voxel images.

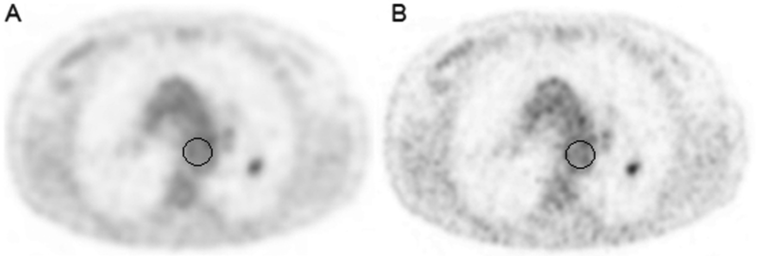

Figure 4 Transverse ^{18}F-FDG PET images using standard-voxel reconstruction (A) and small-voxel reconstruction (B). Lesion in left lung (volume, 0.68 mL) with SUV_{max} of 2.6 using standard-voxel reconstruction increased with 54% to 4.0 using small-voxel reconstruction. SNR_{max} increased with 115% (from 3.1 to 6.6). ROIs used for background measurements are illustrated by black circles

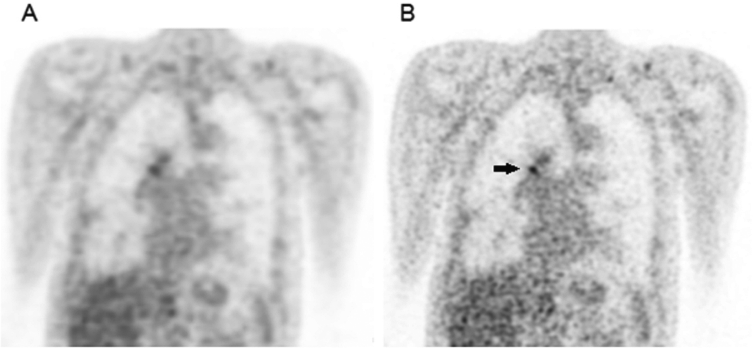

Figure 5 Coronal ^{18}F-FDG PET images with standard-voxel reconstruction (A) and small-voxel reconstruction (B). SUV_{max} of lesion in right hilar region (volume, 0.50 mL) with SUV_{max} of 3.0 using standard-voxel reconstruction increased with 46% to 4.4 on small-voxel reconstruction (black arrow). SNR_{max} increased with 77% (from 9.8 to 13.3)

In **Figure 4** and **Figure 5**, two clinical examples are presented comparing the standard- and small-voxel reconstructed PET images. The SUV_{max} and SNR_{max} of the lung lesion, visualized in **Figure 4**, increased with 54% and 115%, respectively. For the lesion in the right hilar region, as can be seen in **Figure 5**, we found SUV_{max} and SNR_{max} increases of 46% and 77%, respectively.

Discussion

In this investigation, we demonstrated that the detection of small lesions on a state-of-the-art TOF PET/CT device can be improved using reconstructions with smaller voxels. We found significant improvements in SUV and SNR, and moreover our physicians preferred the ^{18}F-FDG PET images reconstructed with 2×2×2 mm^3 voxels in most cases.

The CRC measurements in our phantom study for both standard- and small-voxel reconstructions are consistent with the results of Kolthammer et al.[16]. Furthermore, the improvement of CRCs for small-voxel reconstructions implies an improved image resolution, which has a direct impact on the interpretation of clinical SUV measurements of small lesions.

The use of a small-voxel reconstruction also influences image quality in terms of image noise. With equal administered ^{18}F-FDG dose and acquisition time, the small-voxel reconstruction implies less counts per voxel, and therefore the image noise intrinsically increases. Furthermore, image noise is influenced by the image reconstruction process and the use of different reconstruction settings such as relaxation and blob shape parameters [7, 24, 25]. The increase in noise on the small-voxel reconstruction explains the 30% decrease in SNR we found for the large spheres (≥17 mm) in our phantom study. However, we showed that despite the increase in noise, the SNR of small spheres and lesions significantly improved using the small-voxel reconstruction on a state-of-the-art TOF PET/CT device.

For this study, we used default settings provided by the manufacturer, for both the standard- and the small-voxel reconstructions. Although it is expected that these settings are suitable for clinical PET/CT studies, these may not be the most optimal settings. Hence, optimization of the reconstruction settings such as the number of iterations, subsets, and blob and relaxation parameters could possibly further improve the detection of small lesions [26-28]. Moreover, previous studies have shown the added value of modeling of the point-spread function for the detection of small lesions [13, 14].

In addition, in this study we evaluated the small-voxel reconstructions on the phantoms with a sphere-to-background ratio of 10, according to EANM procedure guidelines [17]. It would be valuable also to perform phantom studies with lower concentration ratios, for example, with a sphere-to-background ratio of 4, to study the impact of small-voxel reconstructions on the detectability of lesions with low contrast.

In this study, 3 nuclear medicine physicians were asked to compare the standard- and small-voxel reconstructed images and to give their preference. Before this study was executed, the physicians were not yet familiar with small-voxel reconstructed images. However, they all preferred the small-voxel reconstructed images in most of the cases, indicating that, in general, the higher image noise level on small-voxel images is accepted, with the advantage of improved small lesion detectability.

For the 3 physicians, the small-voxel image preference ranged between 64% and 88%. This disagreement can be explained by the subjective origin of the study, small differences in experience with small-voxel images, and the inclusion of some cases in which the difference in lesion detectability between standard- and small-voxel images was small, leading to some subjective random choices. However, the introduction of small-voxel images is subject to a learning effect and therefore we expect the preference to further increase after more experience with small-voxel reconstructions. An increase in physicians’ experience will probably also reduce interobserver disagreement.

A limitation of this study is that we did not assess the clinical impact of the small-voxel reconstruction in terms of sensitivity and specificity, which was outside the scope of this study. However, we found improved CRCs and SNRs in small (phantom) spheres and higher SUVs and SNRs for small lesions. Therefore, we expect that cutoff values for small-lesion detection, for example, as published by Tournoy et al.[5] and Li et al.[29], will further increase for ^{18}F-FDG PET studies acquired with state-of-the-art TOF PET/CT scanners, moreover for small-voxel reconstructions. Recently, this expectation was also discussed by Kolthammer et al.[16]. Validation studies are necessary to determine sensitivity and specificity and define new cutoff values to distinguish benign from malignant small lesions using state-of-the-art TOF PET/CT.

Conclusion

On the basis of our study, it is expected that detection of small lesions using ^{18}F-FDG PET improves using small-voxel reconstructions on a state-of-the-art TOF PET/CT system. Supported by a phantom study, there was a preference by the physicians toward ^{18}F-FDG PET images reconstructed with 2×2×2 mm^3 voxels and a profound increase in SUV and SNR for small lesions (<11 mm). Validation studies are necessary to determine the impact of small-voxel reconstructions in terms of sensitivity and specificity. Furthermore, new (probably higher) cutoffs and lesion-to-background values need to be defined, to distinguish benign from malignant small lesions using small-voxel reconstructions on a state-of-the-art TOF PET/CT device.

Declarations

Disclosure

This work was supported by a research agreement between the Department of Nuclear Medicine, Isala, and Philips Healthcare regarding new PET technologies. The content of the article was solely the responsibility of the authors. No other potential conflict of interest relevant to this article was reported.

References

1. Kanzaki R, Higashiyama M, Fujiwara A, Tokunaga T, Maeda J, Okami J, Kozuka T, Hosoki T, Hasegawa Y, Takami M. Occult mediastinal lymph node metastasis in NSCLC patients diagnosed as clinical N0-1 by preoperative integrated FDG-PET/CT and CT: Risk factors, pattern, and histopathological study. Lung Cancer 2011;71:333-7.
2. Cerfolio RJ, Ojha B, Bryant AS, Raghuveer V, Mountz JM, Bartolucci AA. The accuracy of integrated PET-CT compared with dedicated PET alone for the staging of patients with nonsmall cell lung cancer. Ann Thorac Surg 2004;78:1017-23.
3. Poeppel TD, Krause BJ, Heusner TA, Boy C, Bockisch A, Antoch G. PET/CT for the staging and follow-up of patients with malignancies. Eur J Radiol 2009;70:382-92.
4. Lv Y, Yuan D, Wang K, Miao X, Qian Q, Wei S, Zhu X, Song Y. Diagnostic performance of integrated positron emission tomography/computed tomography for mediastinal lymph node staging in non-small cell lung cancer: a bivariate systematic review and meta-analysis. J Thorac Oncol 2011;6:1350-8.
5. Tournoy KG, Maddens S, Gosselin R, Van Maele G, Van Meerbeeck JP, Kelles A. Integrated FDG-PET/CT does not make invasive staging of the intrathoracic lymph nodes in non-small cell lung cancer redundant: a prospective study. Thorax 2007;62:696-701.
6. Takamochi K, Yoshida J, Murakami K, Niho S, Ishii G, Nishimura M, Nishiwaki Y, Suzuki K, Nagai K. Pitfalls in lymph node staging with positron emission tomography in non-small cell lung cancer patients. Lung Cancer 2005;47:235-42.
7. Conti M. Focus on time-of-flight PET: the benefits of improved time resolution. Eur J Nucl Med Mol Imaging 2011;38:1147-57.
8. Soret M, Bacharach SL, Buvat I. Partial-volume effect in PET tumor imaging. J Nucl Med 2007;48:932-45.
9. Karp JS, Surti S, Daube-Witherspoon M, Muehllehner G. Benefit of time-of-flight in PET: experimental and clinical results. J Nucl Med 2008;49:462-70.
10. Lois C, Jakoby BW, Long MJ, Hubner KF, Barker DW, Casey ME, Conti M, Panin VY, Kadrmas DJ, Townsend DW. An assessment of the impact of incorporating time-of-flight information into clinical PET/CT imaging. J Nucl Med 2010;51:237-45.
11. Kadrmas DJ, Casey ME, Conti M, Jakoby BW, Lois C, Townsend DW. Impact of time-of-flight on PET tumor detection. J Nucl Med 2009;50:1315-23.
12. Daube-Witherspoon M, Surti S, Perkins AE, Karp JS. Determination of accuracy and precision of lesion uptake measurements in human subjects with time-of-flight PET. J Nucl Med 2014;55:602-7.
13. Schaefferkoetter J, Casey M, Townsend D, El Fakhri G. Clinical impact of time-of-flight and point response modeling in PET reconstructions: a lesion detection study. Phys Med Biol 2013;58:1465-78.

14. Lasnon C, Hicks RJ, Beauregard J, Milner A, Paciencia M, Guizard A, Bardet S, Gervais R, Lemoel G, Zalcman G. Impact of point spread function reconstruction on thoracic lymph node staging with 18F-FDG PET/CT in non–small cell lung cancer. Clin Nucl Med 2012;37:971-6.
15. Vogel WV, Wensing BM, van Dalen J,A., Krabbe PFM, van den Hoogen F,J.A., Oyen WJG. Optimised PET reconstruction of the head and neck area: improved diagnostic accuracy. Eur J Nucl Med Mol Imaging 2005;32:1276-82.
16. Kolthammer JA, Su K, Grover A, Narayanan M, Jordan DW, Muzic RF. Performance evaluation of the Ingenuity TF PET/CT scanner with a focus on high count-rate conditions. Phys Med Biol 2014;59:3843-59.
17. Boellaard R, O'Doherty M,J., Weber WA, Mottaghy FM, Lonsdale MN, Stroobants SG, Oyen WJG, Kotzerke J, Hoekstra OS, Pruim J. FDG PET and PET/CT: EANM procedure guidelines for tumour PET imaging: version 1.0. Eur J Nucl Med Mol Imaging 2010;37:181-200.
18. de Groot E,H., Post N, Boellaard R, Wagenaar NRL, Willemsen ATM, van Dalen J,A. Optimized dose regimen for whole-body FDG-PET imaging. EJNMMI Res 2013;3:63-72.
19. Lewitt RM. Multidimensional digital image representations using generalized Kaiser–Bessel window functions. J Opt Soc Am 1990;7:1834-46.
20. Matej S, Lewitt RM. Practical considerations for 3-D image reconstruction using spherically symmetric volume elements. IEEE Trans Med Imaging 1996;15:68-78.
21. Iagaru A, Mittra E, Mosci C, Dick DW, Sathekge M, Prakash V, Iyer V, Lapa P, Isidoro J, De Lima J,M. Combined 18F-fluoride and 18F-FDG PET/CT scanning for evaluation of malignancy: results of an international multicenter trial. J Nucl Med 2013;54:176-83.
22. Subedi N, Scarsbrook A, Darby M, Korde K, Mc Shane P, Muers MF. The clinical impact of integrated FDG PET–CT on management decisions in patients with lung cancer. Lung Cancer 2009;64:301-7.
23. Reed CE, Harpole DH, Posther KE, Woolson SL, Downey RJ, Meyers BF, Heelan RT, MacApinlac HA, Jung S, Silvestri GA. Results of the American College of Surgeons Oncology Group Z0050 trial: the utility of positron emission tomography in staging potentially operable non–small cell lung cancer. J Thorac Cardiovasc Surg 2003;126:1943-51.
24. Daube-Witherspoon M, Matej S, Karp JS. Assessment of image quality with a fast fully 3D reconstruction algorithm. IEEE Nucl Sci Symp Conf Rec 2001;4:2238-42.
25. Daube-Witherspoon ME, Matej S, Karp JS, Lewitt RM. Application of the row action maximum likelihood algorithm with spherical basis functions to clinical PET imaging. IEEE Transactions Nucl Sci 2001;48:24-30.
26. Makris NE, Huisman MC, Kinahan PE, Lammertsma AA, Boellaard R. Evaluation of strategies towards harmonization of FDG PET/CT studies in multicentre trials: comparison of scanner validation phantoms and data analysis procedures. Eur J Nucl Med Mol Imaging 2013;40:1507-15.

27. Groheux D, Martineau A, Vrigneaud J, Hindie E, Baillet G, Moretti J. Effect of variation in relaxation parameter value on LOR-RAMLA reconstruction of 18F-FDG PET studies. Nucl Med Commun 2009;30:926-33.
28. Yamashita S, Yokoyama K, Onoguchi M, Yamamoto H, Hiko S, Horita A, Nakajima K. Feasibility of deep-inspiration breath-hold PET/CT with short-time acquisition: detectability for pulmonary lesions compared with respiratory-gated PET/CT. Ann Nucl Med 2014;28:1-10.
29. Li S, Zheng Q, Ma Y, Wang Y, Feng Y, Zhao B, Yang Y. Implications of false negative and false positive diagnosis in lymph node staging of NSCLC by means of 18F-FDG PET/CT. PloS one 2013;8:e78552.

CHAPTER 9

9

Diagnostic implications of a small-voxel reconstruction for loco-regional lymph node characterization in breast cancer patients using FDG-PET/CT

Authors

Daniëlle Koopman[1,2] | Jorn A. van Dalen[3] | Hester Arkies[1]
Ad H. J. Oostdijk[1] | Anne Brecht Francken[4] | Jos Bart[5]
Cornelis H. Slump[2] | Siert Knollema[1] | Pieter L. Jager[1]

Author Affiliations

1: Department of Nuclear Medicine, Isala, Zwolle, the Netherlands
2. MIRA Institute for Biomedical Technology and Technical Medicine, University of Twente, Enschede, the Netherlands
3: Department of Medical Physics, Isala, Zwolle, the Netherlands
4: Department of Surgery, Isala, Zwolle, the Netherlands
5: Department of Pathology, Isala, Zwolle, the Netherlands

Published in
EJNMMI Research 2018;8:3-12

Abstract

Background

We evaluated the diagnostic implications of a small-voxel reconstruction for lymph node characterization in breast cancer patients, using state-of-the-art FDG-PET/CT. We included 69 FDG-PET/CT scans from breast cancer patients. PET data were reconstructed using standard 4×4×4 mm^3 and small 2×2×2 mm^3 voxels. Two hundred thirty loco-regional lymph nodes were included, of which 209 nodes were visualised on PET/CT. All nodes were visually scored as benign or malignant, and SUV_{max} and TB_{ratio} ($=SUV_{max}/SUV_{background}$) were measured. Final diagnosis was based on histological or imaging information. We determined the accuracy, sensitivity and specificity for both reconstruction methods and calculated optimal cut-off values to distinguish benign from malignant nodes.

Results

Sixty-one benign and 169 malignant lymph nodes were included. Visual evaluation accuracy was 73% (sensitivity 67%, specificity 89%) on standard-voxel images and 77% (sensitivity 78%, specificity 74%) on small-voxel images ($p=0.13$). Across malignant nodes visualised on PET/CT, the small-voxel score was more often correct compared with the standard-voxel score (89 vs. 76%, $p<0.001$). In benign nodes, the standard-voxel score was more often correct (89 vs. 74%, $p=0.04$).

Quantitative data were based on the 61 benign and 148 malignant lymph nodes visualised on PET/CT. SUVs and TB_{ratio} were on average 3.0 and 1.6 times higher in malignant nodes compared to those in benign nodes ($p<0.001$), on standard- and small-voxel PET images respectively. Small-voxel PET showed average increases in SUV_{max} and TB_{ratio} of typically 40% over standard-voxel PET. The optimal SUV_{max} cut-off using standard-voxels was 1.8 (sensitivity 81%, specificity 95%, accuracy 85%) while for small-voxels, the optimal SUV_{max} cut-off was 2.6 (sensitivity 78%, specificity 98%, accuracy 84%). Differences in accuracy were non-significant.

Conclusions

Small-voxel PET/CT improves the sensitivity of visual lymph node characterization and provides a higher detection rate of malignant lymph nodes. However, small-voxel PET/CT also introduced more false-positive results in benign nodes. Across all nodes, differences in accuracy were non-significant. Quantitatively, small-voxel images require higher cut-off values. Readers have to adapt their reference standards.

Keywords

State-of-the-art PET/CT; Small-voxel reconstruction; Breast cancer; Loco-regional lymph nodes

Background

In recent years, there has been an increasing role for fluorine-18 fluordeoxyglucose positron emission tomography (FDG-PET) combined with computed tomography (CT) in the diagnostic evaluation of patients with stage II–IV primary breast cancer [1, 2]. FDG-PET/CT has now largely replaced conventional staging that included a bone scan, abdominal echography and chest x-ray. This is due to PET/CT's higher accuracy and the ability to perform whole-body staging in a single session [1, 3, 4].

In patients with stage II–IV primary breast cancer, accurate detection of loco-regional lymph nodes and distant metastasis is crucial for treatment selection and prognosis prediction. However, the sensitivity and detection rate of small lesions and lesions with low metabolism using FDG-PET are restricted, due to the limited PET spatial resolution [5, 6]. For axillary lymph node staging using FDG-PET/CT, a systematic review based on seven studies found an average sensitivity of 56% with 93% specificity [7]. More specifically, for micro-metastatic lesions (diameter ≤ 2 mm), a sensitivity of 11% was reported, while for macro-metastatic lesions (diameter > 2 mm), the sensitivity was 57% [7].

A PET reconstruction setting that possibly improves small lesion detection and sensitivity is the voxel size. In current practice, the image voxel size for whole-body FDG-PET scans is typically around $4 \times 4 \times 4$ mm^3 [8]. However, it has been suggested that in combination with new highly sensitive time of flight (TOF) PET/CT cameras, the use of reconstructions with smaller voxels might further improve the detection of small lesions [8, 9]. In a previous study, we have assessed to what extent small lesion detectability is influenced by the voxel size [10]. With the use of small $2 \times 2 \times 2$ mm^3 voxels, we found a profound increase in the standardized uptake value (SUV) and an improvement in signal-to-noise ratio (SNR) for small lesions, as compared to the values on PET images reconstructed with default $4 \times 4 \times 4$ mm^3 voxels.

In clinical trials that assessed the value of FDG-PET/CT in primary breast cancer patients scheduled for neo-adjuvant chemotherapy, the use of small-voxels for loco-regional lymph node characterization has been reported already [11, 12]. However, those studies did not compare standard- and small-voxel reconstructions in a clinical setting. Therefore, the diagnostic implications and potential clinical benefit of small $2 \times 2 \times 2$ mm^3 voxels, in terms of small lesion detection and sensitivity, remain unknown. The purpose of this study is to evaluate the diagnostic implications of a small-voxel reconstruction for loco-regional lymph node characterization in breast cancer patients, using state-of-the-art FDG-PET/CT.

Methods

Inclusion

In this study, we have included 69 consecutive women with primary stage II–IV ductal primary breast cancer who had been referred for a pre-treatment whole-body FDG-PET/CT scan. We only included patients with at least one loco-regional lymph node which could be classified as benign or malignant based on histological or imaging information. We received a waiver from the Medical Ethical Committee of our institution (METC Isala, Zwolle) to perform this retrospective study, as it deals with an evaluation of clinically indicated scans. Informed consent was obtained from all individual participants included in the study.

PET/CT data acquisition

Patients fasted for at least 6 h prior to scanning. Before intravenous injection of FDG, blood glucose levels were measured to ensure a value below 10 mmol/L. The mean glucose level was 5.4 mmol/L (range 3.8–9.3 mmol/L). A dedicated dose protocol depending quadratically on patients' body weight was used. This protocol is described by the formula $A = 3.8 \times w^2/t$, where A is the FDG activity to administer (in megabecquerel), w is the patients' body weight (in kilogram), and t is the acquisition time per bed position (in seconds). This approach has been shown to result in an image quality that does not depend on patient's weight [13]. Acquisition times for the patient studies were 1 and 2 min per bed position for patients with body weight ≤ 80 and > 80 kg, respectively. The average administered FDG activity was 331 MBq (range 155–533 MBq).

All scans were acquired with patients in supine position, using a state-of-the-art PET/CT scanner (Ingenuity TF, Philips Healthcare, Cleveland, OH, USA). This fully three-dimensional TOF PET scanner is combined with a 128-slice CT scanner. The PET scan was acquired 60 min post-injection, using a whole-body protocol. Before PET imaging, a CT scan was acquired for attenuation correction. The CT scan parameters were tube voltage 120 kV, dose modulation with an average tube current of 53 mA (range 37–94 mA), slice collimation 64×0.625 mm, pitch 0.83 and rotation time 0.5 s.

PET/CT data reconstruction

PET data were reconstructed using a list-mode TOF algorithm and line-of-response row-action maximum-likelihood algorithm method [14, 15], called BLOB-OS-TF. Images were reconstructed in two types of matrices: 144×144 matrices with voxel size $4{\times}4{\times}4$ mm^3 (standard-voxels) and 288×288 matrices with voxel size $2{\times}2{\times}2$ mm^3 (small-voxels). For the standard-voxel reconstruction, the blob had a 2.5-mm radius with a blob shape parameter of 8.4 mm. The blob radius and shape parameter for the small-voxel reconstruction were 2.8 and 6.4 mm, respectively. Furthermore, the relaxation parameters for the standard- and small-voxel reconstructions were 1.0 and 0.5, respectively. For both types of voxel reconstructions, 3 iterations and 43 subsets were applied. All reconstruction parameters were default settings recommended by the vendor. Point-spread function modelling was not applied.

CT data were reconstructed using an iterative reconstruction algorithm (iDose, Philips Healthcare, Cleveland, OH, USA) with iDose level 4 and a slice thickness of 3 mm. The administered FDG activity and PET/CT acquisition protocols were consistent with European Association of Nuclear Medicine (EANM) guidelines for tumour PET imaging [16, 17]. Moreover, the reconstructed PET images with standard-voxels fulfilled the EANM research Ltd. (EARL) accreditation specifications [18]. The small-voxel reconstruction does not fulfil the EARL accreditation specifications, because the recovery curves for the small 10- to 13-mm spheres increase up to values above the maximum EARL specifications [10].

Visual evaluation

Integrated PET/CT data were reviewed on a dedicated workstation (IntelliSpace Portal 6, Philips Healthcare, Cleveland, OH, USA). First, each PET/CT scan was evaluated by two nuclear medicine (NM) physicians, with more than 5 years of experience in PET/CT viewing. They were blinded to the patient record and histological information and interpreted the PET/CT data by simultaneous viewing of PET, CT and fused PET/CT images. Both the standard- and small-voxel images were evaluated blindly, both separately and randomly. The NM physicians scored all loco-regional lymph nodes showing focal FDG-uptake on the standard- or small-voxel images. They integrated their PET reading with the presence, absence, shape and size of lymph nodes on the low-dose CT scan, in an identical fashion as used in clinical interpretation.

Initially, each lymph node was scored using a five-point ordinal scale with 1: certainly benign, 2: probably benign, 3: equivocal, 4: probably malignant and 5: certainly malignant. If this initial interpretation between both physicians differed, consensus was reached. This was needed for 39 lymph nodes (19%) on standard-voxel images and for 43 lymph nodes (21%) on small-voxels images. Next, to be able to evaluate the lymph node characterization performance, each lesion was assigned as benign or malignant using the following method. All lymph nodes with a score of 1 or 2 were allocated as benign. All lymph nodes with scores of 4 and 5 were allocated as malignant. Lymph nodes with a score of 3 were once again evaluated on the PET/CT images, and they received an ultimate score as benign or malignant.

Quantitative evaluation

All scored lymph nodes were evaluated semi-quantitatively by an experienced PET reader blinded to the patient record, histological information and visual PET/CT scores. The maximum standardized uptake value (SUV_{max}) was derived on the axial slice that contained the highest FDG-uptake of the lesion.

Next, we calculated the lymph node-to-background ratio (TB_{ratio}), defined as the ratio between the lymph node SUV_{max} and the average SUV in the background ($SUV_{background}$). To measure the $SUV_{background}$, we defined two regions of interest (ROI1 and ROI2) on the axial PET image. ROI1 enclosed both the lymph node under study and a surrounding background area of 800 mm^2, while ROI2 only enclosed the lymph node. For both ROIs, the area size and the average SUV (SUV_{mean}) were collected to calculate the $SUV_{background}$ in a donut-shaped ROI using **Formula 1**:

$$SUV_{background} = \frac{(\text{ROI1 } SUV_{mean} \times \text{ROI1area}) - (\text{ROI2 } SUV_{mean} \times \text{ROI2area})}{\text{ROI1area} - \text{ROI2area}} \tag{1}$$

Finally, for all the scored lymph nodes, we measured the short-axis diameter on the axial slice of the attenuation CT scan.

Final diagnosis

The final diagnosis for each lymph node was based on histological information, follow-up (FU) imaging (FDG-PET/CT, contrast-enhanced CT or magnetic resonance imaging (MRI)) or additional imaging (contrast-enhanced CT or MRI) in the following way (**Figure 1**). For patients who initially underwent a surgical resection that included sentinel lymph node biopsy or axillary lymph node dissection, the final diagnosis was based on the histological information obtained during surgery. Pathology examination was part of the clinical evaluation and was centralised at our institution. Lymph nodes were histologically processed by formalin fixation followed by paraffin embedding, according to standardized procedures.

The lymph nodes were serially sectioned at 250 µm at three levels and stained with both hematoxylin and eosin, with an immune-histochemical cytokeratin staining (panCK). The immune-histochemical procedure was performed by a fully automated procedure, using pre-diluted antibodies on the Ventana Benchmark system (Roche Ventana, Tucson AZ, USA). The sizes of the metastases were measured on a conventional bright-field microscope (Leica, DM4000, Leica microsystems Germany) using a micro-measuring scale on glass slide (definition = 0.1 mm). In all lymph nodes, the largest diameter of a metastasis was reported.

For patients who were treated with neo-adjuvant chemotherapy, the final diagnosis was based on the response to therapy as visualised on FU imaging combined with the histological information that was available from the subsequent surgical resection. For these patients, lesions were considered malignant when they showed a decrease in size or FDG-uptake induced by subsequent chemotherapy. Furthermore, lesions that were stable in size and FDG-uptake during neo-adjuvant therapy were considered to be benign unless there was proof of malignancy from histological information obtained during surgery. When histological information or FU imaging was not available, the final diagnosis was based on the results of additional contrast-enhanced CT or MRI.

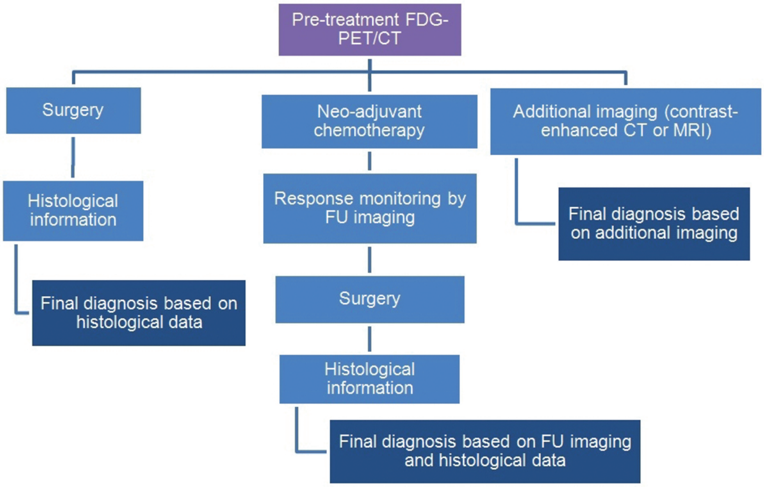

Figure 1 Flow chart showing the method to derive the final diagnosis per patient (*n*)

Additionally, we collected information on all malignant loco-regional lymph nodes that were found during surgical resection but which had not been visualised on FDG-PET or the attenuation CT. For those lesions, we recorded the metastatic deposit size that was measured during a separate pathology examination, performed by one pathologist (JB). For visual PET performance evaluation, these lymph nodes were regarded as benign nodes on PET. Furthermore, for quantitative PET evaluation, these lymph nodes were not taken into account because it was not possible to perform measurements on PET images.

Lymph node characterization

Visual evaluation scores were analysed on a lesion-per-lesion basis, by comparing the scores on standard- and small-voxel images for each lymph node. Quantitatively, we calculated average values for SUV_{max} and TB_{ratio} in both benign and malignant lymph nodes and for both voxel reconstructions. We created receiver operator curves (ROC) and calculated the area under the curve (AUC) with a 95% confidence interval (CI) for SUV_{max} and TB_{ratio}. For both reconstruction methods, we determined the sensitivity, specificity and accuracy for lymph node characterization from the visual and quantitative PET/CT evaluation, using the final diagnosis as a reference standard. We calculated optimal cut-off values for SUV_{max} and TB_{ratio} to distinguish benign from malignant lymph nodes on both voxel reconstructions. These cut-off values were based on the highest combined sensitivity and specificity (highest sum).

Statistical analysis

We used the McNemar test for paired samples to compare the visual scores for both reconstructions with the final diagnosis. Quantitative results were presented as mean ± standard deviation (SD). We included ranges in uptake values and lymph node size. Differences in SUV_{max} and TB_{ratio} between benign and malignant lymph nodes were evaluated using the Mann-Whitney *U* test. Furthermore, to evaluate differences in characterization performances between standard and small-voxels for SUV_{max} and TB_{ratio}, we compared the AUCs using a chi-square test. Additionally, the characterization performances for SUV_{max} and TB_{ratio} using optimal cut-off values were evaluated with the McNemar test for paired samples. A p value less than 0.05 was considered to indicate statistical significance.

Results

Patient characteristics

Clinical data from 69 patients are shown in **Table 1**. In total, 230 loco-regional lymph nodes were investigated (mean 3 ± 2 lymph nodes per patient). We have included 61 benign lymph nodes with an average size of 6 mm (range 3–12 mm), and 169 malignant lymph nodes with an average size of 8 mm (range 1–32 mm). During surgical resection in 11 patients, 21 malignant lymph nodes were found that were not visualised on PET/CT images. This group consisted of 6 micro-metastases (diameter ≤ 2 mm) and 15 macro-metastases with sizes varying between 2 and 7 mm diameter. The remaining 209 loco-regional lymph nodes, which were visualised on PET/CT, were visually and quantitatively evaluated in this study.

Table 1 General characteristics

Patient characteristics (*n* = 69)	Age (years)	53 ± 12 (mean ± SD)
	Body weight (kilogram)	76 ± 14
Hormonal receptor status	Oestrogen	51 pos., 16 neg., 2 unknown
	Progesterone	37 pos., 30 neg., 2 unknown
	Human epidermal growth factor receptor 2	19 pos., 48 neg., 2 unknown
Loco-regional lymph nodes (*n* = 230)	Location	
	Left region	108
	Right region	122
	Final diagnosis	
	Benign	61
	Malignant	169
	Final diagnosis based on the following:	
	Histological proof	128 (56%)
	FU imaging	99 (43%)
	Additional imaging	3 (1%)

pos. positive, neg. negative

Visual evaluation

For 173 out of 209 lymph nodes (83%), visual interpretation scores were exactly similar for both small and standard-voxels. Furthermore, 32 lymph nodes (15%) were scored malignant on the small-voxel images but benign on the standard-voxel images. Contrarily, four lymph nodes (2%) were scored benign on the small-voxel images but malignant on the standard-voxel images.

In **Table 2**, the final diagnosis of each lymph node is compared with the visual scores on both voxel reconstructions. Sensitivity, specificity and accuracy for standard-voxel PET/CT images in visual evaluation were 67%, 89% and 73%, respectively. For small-voxel PET/CT images, we found a sensitivity, specificity and accuracy of 78%, 74% and 77%, respectively. Across all lymph nodes, the differences in accuracy were not statistically significant (p=0.13).

Limiting this analysis to the 148 malignant lymph nodes that were visualised on PET/CT, the small-voxel score was correct in 132 cases (89%) while the standard-voxel score was correct in 113 cases (76%), p<0.001. In benign lymph nodes (*n* = 61) only, the small-voxel score was correct in 45 cases (74%) vs. 54 correct scores (89%) on standard-voxel images (p=0.04).

Table 2 Table comparing the final diagnosis with standard-voxel or small-voxel PET/CT visual scores for malignant lymph nodes, benign lymph nodes and all lymph nodes. For malignant lymph nodes, the small-voxel score was more often correct as compared to the standard-voxel score ($p<0.001$), while for benign lymph nodes, the standard-voxel score was more often correct ($p=0.04$). Across all lymph nodes visualised on PET/CT, accuracies of standard- and small-voxel scores were comparable ($p=0.13$)

	Small-voxel correct	Small-voxel not correct	p-value
Malignant lymph nodes (*n* = 148)			
Standard-voxel correct	112	1	< 0.001
Standard-voxel not correct	20	15	
Benign lymph nodes (*n* = 61)			
Standard-voxel correct	42	12	0.04
Standard-voxel not correct	3	4	
All lymph nodes (*n* = 209)			
Standard-voxel correct	154	13	0.13
Standard-voxel not correct	23	19	

Quantitative evaluation

SUV_{max} and TB_{ratio} across all lymph nodes are shown in **Table 3**. For both SUV_{max} and TB_{ratio}, and in both types of voxel reconstructions, uptake values for malignant lymph nodes were averagely a factor of 3.0 and 1.6 higher, respectively, as compared to those for benign nodes ($p<0.001$). Furthermore, the use of small-voxels resulted in SUV increases of typically 40% (**Table 3**).

Table 3 SUV_{max} and TB_{ratio} for benign and malignant lymph nodes as measured on standard- and small-voxel PET images. SUV_{max} and TB_{ratio} for malignant lymph nodes were averagely 3.0 and 1.6 times as high as compared to benign nodes for both types of voxel reconstructions ($p<0.001$). Mean SUV_{max} and TB_{ratio} typically increased with 40% when using small-voxels ($p<0.001$)

		Benign lymph nodes (n = 61)	Malignant lymph nodes (n = 148)
SUV_{max}	Standard-voxels	1.1 ± 0.4 (mean ± SD)	4.4 ± 3.3
	Small-voxels	1.5 ± 0.5	5.9 ± 4.1
	Percent change	37%	40%
TB_{ratio}	Standard-voxels	2.0 ± 0.7	5.3 ± 4.2
	Small-voxels	2.8 ± 1.4	7.3 ± 5.2
	Percent change	44%	43%

Lymph node characterization by quantitative evaluation

Table 4 shows the sensitivity, specificity and accuracy of lymph node characterization for standard- and small-voxel PET images, using optimal cut-off values for SUV_{max} and TB_{ratio}. Furthermore, receiver operator curves (ROC) for

SUV_{max} and TB_{ratio} are shown in **Figure 2**. TB_{ratio} had a significantly lower AUC as compared to the SUV_{max} parameter, for both standard and small-voxels ($p=0.003$ and $p=0.002$). AUC values for standard- and small-voxel images were comparable for both SUV parameters, with $p=0.71$ for SUV_{max} and $p=0.61$ for TB_{ratio}. Additionally, no significant differences were found in characterization performances based on the accuracy between standard- and small-voxel images, with $p=0.11$ for SUV_{max} and $p=0.29$ for TB_{ratio}. **Table 4** shows that the use of small-voxels required higher SUV cut-offs for accurate lymph node characterization.

Table 4 Sensitivity, specificity and accuracy for SUV_{max} and TB_{ratio} at optimal cut-offs, determined for standard- and small-voxel PET. The use of small-voxel images requires higher SUV cut-offs for accurate lymph node characterization. Furthermore, SUV_{max} showed a higher performance as compared to TB_{ratio}, with $p=0.04$ for standard-voxels and $p<0.001$ for small-voxels. However, the characterization performances were similar for standard- and small-voxel images, with $p=0.11$ for SUV_{max} and $p=0.29$ for TB_{ratio}

		Optimal cut-off	Sensitivity	Specificity	Accuracy
SUV_{max}	Standard-voxels	1.8	81%	95%	85%
	Small-voxels	2.6	78%	98%	84%
TB_{ratio}	Standard-voxels	2.4	80%	82%	80%
	Small-voxels	3.3	84%	77%	82%

Clinical examples

Figure 3 shows FDG-PET/CT images from a patient with breast cancer. The visual score of the axillary lymph node altered from benign on standard-voxel PET/CT to malignant on small-voxel PET/CT. Furthermore, SUV_{max} of this lymph node increased by 57% on small-voxel images. Follow-up imaging showed that this lymph node responded to chemotherapy, which indicated that this lesion was malignant. This confirmed the small-voxel score and the classification by the optimal SUV_{max} cut-off shown in **Table 4**.

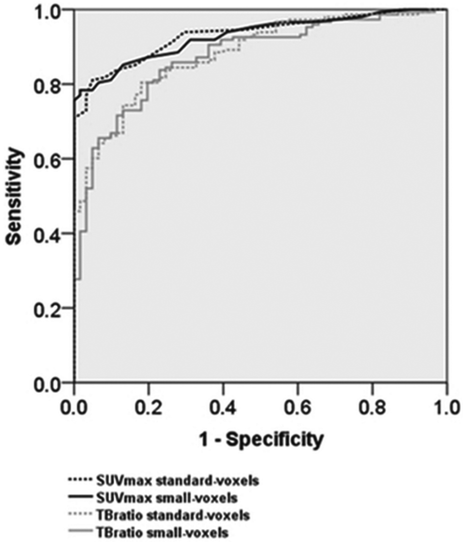

Figure 2 ROC curves for lymph node characterization using SUV_{max} and TB_{ratio}, measured on standard- and small-voxel PET images. AUCs for SUV_{max} were 0.93 (95% CI 0.90–0.97) and 0.93 (95% CI 0.90–0.96) for standard- and small-voxels, respectively (p=0.71). AUCs for TB_{ratio} were 0.88 (95% CI 0.84–0.93) and 0.87 (95% CI 0.82–0.92) for standard- and small-voxels respectively (p=0.61). AUCs for SUV_{max} were significantly higher as compared to AUCs for TB_{ratio}, for both standard- and small-voxels (p=0.003 and p=0.002)

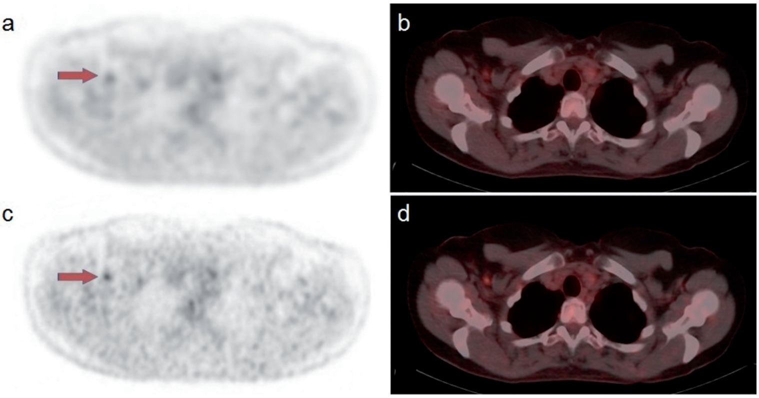

Figure 3 FDG-PET/CT images of a patient with proven breast cancer. a. Axial PET image, standard-voxels. **b.** Axial-fused PET/CT image, standard-voxels. **c.** Axial PET image, small-voxels. **d.** Axial-fused PET/CT image, small-voxels. SUV_{max} for this small lymph node (red arrows) increased from 2.1 on standard-voxel PET with visual score benign to SUV_{max} 3.3 on small-voxel PET and visual score malignant. On follow-up imaging after chemotherapy, this lymph node showed regression, which indicated that the lymph node was malignant. This confirmed the small-voxel score and the classification using the optimal SUV_{max} cut-off

Figure 4 shows FDG-PET/CT images from a breast cancer patient, with a small axillary lymph node. The visual score was benign on standard-voxel images while it was scored malignant on small-voxel images. In this case, SUV_{max} increased with 64% on small-voxel images. However, during sentinel node biopsy, no malignancy was found. This indicated that this lymph node was benign and the standard-voxel score was correct.

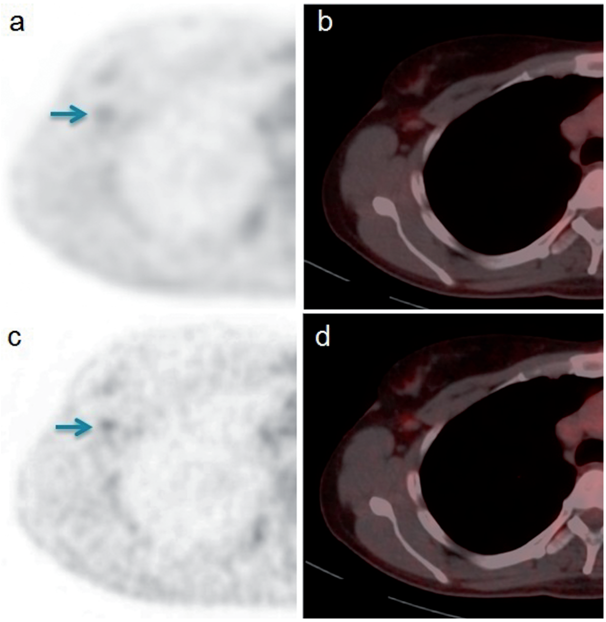

Figure 4 FDG-PET/CT images of a patient with proven breast cancer. a. Axial PET image, standard-voxels. **b.** Axial-fused PET/CT image, standard-voxels. **c.** Axial PET image, small-voxels. **d.** Axial-fused PET/CT image, small-voxels. For this lymph node, with short-axis diameter 5 mm in the right axillary region (blue arrows), SUV_{max} values were 1.4 and 2.3 (increase 64%) on standard- and small-voxel images, respectively. Furthermore, the visual scores were benign on standard-voxel PET and malignant on small-voxel PET. The sentinel node biopsy procedure did not reveal any malignancy. This indicates that this lymph node was benign, confirming the standard-voxel score and confirming the classification using the optimal SUV_{max} cut-off

Discussion

This study shows that small-voxel PET reconstructions improve the diagnostic sensitivity in the detection of lymph node metastases in breast cancer, at the expense of an impaired specificity. Based on visual evaluation of PET/CT images, the lymph node characterization accuracy did not change when using small-voxels instead of standard-voxels ($p=0.13$). Nevertheless, limiting the analysis to malignant lymph nodes only, the small-voxel images were correct in 89% while the standard-voxel images provided concordant scores in only 76% of the cases ($p<0.001$). This shows that the visual evaluation and detection of malignant axillary lymph nodes improves using small-voxel PET/CT. Contrarily, benign lymph nodes were more often correctly scored on standard-voxel images as compared to those on the small-voxel images (74 vs. 89%, $p=0.04$).

Quantitatively, we found significant differences between benign and malignant lymph nodes for both parameters SUV_{max} and TB_{ratio} and both PET voxel sizes ($2\times2\times2$ mm^3 and $4\times4\times4$ mm^3). Furthermore, the use of small-voxels resulted in higher FDG-uptake values of typically 40% for both benign and malignant lymph nodes. This increase is comparable with previously published values [10].

This study shows that the visual evaluation of malignant lymph nodes results in a higher accuracy and sensitivity when using small-voxel PET/CT. However, when looking quantitatively, both reconstruction voxel types can be used interchangeably for accurate loco-regional lymph node characterization. Furthermore, across all lymph nodes, both the quantitative and visual evaluation showed comparable performances in disease characterization. Moreover, when using small-voxel reconstructions, PET readers have to be aware of the risk of false-positives and the need of higher cut-off values to distinguish benign from malignant nodes. In the past, all visually FDG-positive axillary lymph nodes were considered as metastatic, because that approach resulted in high specificity [11, 12]. However, we demonstrated that on small-voxel PET images, benign loco-regional lymph nodes can also show some increased FDG-uptake. In the literature, this phenomenon has been described as well for the visualisation of benign nodes on PET images that incorporated point-spread function (PSF) modelling [19, 20]. Clinically, the main feature of small-voxel PET is the ability to detect more malignant axillary lymph nodes. This could lead to a higher disease stage and thereby potentially changes treatment. For example when the N-stage based on PET changes from N1 to N2, this could give rise to treat the patient with neo-adjuvant chemotherapy before surgery. Generally, with an improved detection of malignant axillary lymph nodes, the role of PET as an additional tool in the treatment decision plan can be further extended.

Between the two parameters, SUV_{max} and TB_{ratio}, which were evaluated in this study, we found a significant difference in clinical performance. For both voxel reconstruction types, the SUV_{max} parameter was significantly better in distinguishing benign from malignant lymph nodes. This indicates that during quantitative PET evaluation, it is not required to take the surrounding background uptake around the lymph node into account for accurate characterization of loco-regional lymph nodes.

Despite the use of a small-voxel PET reconstruction, the detection rate with FDG-PET/CT for small metastases remains restricted. In our study, 21 out of 230 lymph nodes were not visualised on PET/CT images but were only found during the histological procedures after surgery. It is very likely that the size and/or the metabolic volume of those undetected lymph node metastasis was not large enough to be visualised with PET [2]. Currently, several developments in PET technology are taking place to further improve the diagnostic performance of PET/CT systems [21]. Together with the development of more specific radionuclide tracers for breast cancer, this may further improve the detection rate of PET/CT [22].

A limitation of this study is that the analysis was based on PET images together with low-dose CT only. Possibly, we did not incorporate all additional findings in case a diagnostic contrast-enhanced CT was obtained. It is likely that adding more CT aspects of lymph nodes, such as spherical shape and the absence of intra-nodal fat, will further improve the sensitivity, specifically of small-voxel reconstructions, and further reduce the false-positive rate. Moreover, there were some differences in visual scores between the two observers as consensus scoring was needed in 20% of the cases. This can be partly explained by the use of a five-point scoring system, which easily introduces small differences in visual scores between observers. Furthermore, the lack of a gold standard for the relatively new small-voxel PET images may have led to differences between observers. There is a learning curve involved in this new detailed method of reading the axilla in breast cancer patients. Also, possibly, results will improve by rigorous comparison with non-involved small nodes in the contralateral axilla as a normal reference.

The present study has some other limitations. The retrospective study design may have led to some bias in our study population, since only patients with a known lymph node status were included in this study. Additionally, since not all patients had a lymph node dissection, some microscopic nodes may have been missed in some patients. Moreover, the final diagnosis per lymph node in this study was based on three different references: histological data, FU imaging and additional imaging. Although the value of additional imaging as a reference method can be difficult, the number of final diagnoses that was based on this method was very limited (1%). Moreover, FDG-PET may give a false-positive result, e.g. in case of an inflammation after biopsy which would also disappear after, but not due to, neo-adjuvant chemotherapy.

Some recommendations can be made for further research. The small-voxel reconstruction protocol could be further optimized to improve image quality and lesion detectability. Recently, Bellevre et al.[19] demonstrated that the use of PSF modelling improved the performance of axillary staging in breast cancer patients. A combination of small-voxels and PSF modelling could be explored. Furthermore, the number of iterations and subsets could be optimized [20, 23, 24]. Meanwhile, other evaluation methods could be considered. For example, the value of combined standard- and small-voxel PET in visual evaluation can be explored, to further improve the accuracy. Also, the use of SUV_{peak} could potentially decrease differences between both reconstructions as it is less influenced by image noise as compared to SUV_{max} [25]. Furthermore, the added value of the optimal SUV cut-offs as proposed in this study, onto the visual evaluation of small-voxel PET, can be studied. Also, optimal SUV cut-offs can be different in other types of breast cancers and may be influenced when incorporating data on the tumour proliferation index (ki67) or the hormone receptor status.

Apart from this, it can be interesting to study the clinical impact of small-voxel images in other body regions and for other diseases. For example, we previously evaluated the impact of a state-of-the-art PET/CT scanner on the visualisation and quantification of adrenal glands, using a standard-voxel reconstruction [26]. This could be extended towards an evaluation of the impact of a small-voxel reconstruction on adrenal gland quantification and classification with FDG-PET/CT.

Conclusions

We evaluated the diagnostic properties of a small-voxel reconstruction for loco-regional lymph node staging in 69 patients with breast cancer, using state-of-the-art TOF FDG-PET/CT. The use of small-voxels improves the sensitivity of visual PET/CT evaluation in malignant lymph nodes, as compared to standard-voxel analysis. However, it also introduced more false-positive results for benign nodes. Across all nodes, differences in accuracy were non-significant. Quantitatively, a small-voxel reconstruction implicates higher SUV cut-off values when differentiating benign from malignant axillary lymph nodes. In case small-voxel images are used, readers have to adapt their reference standards visually and quantitatively.

Competing interests

The Department of Nuclear Medicine, Isala, has established a research cooperation with Philips Healthcare regarding new PET technologies. The content of the article was solely the responsibility of the authors. No other potential conflicts of interest relevant to this article were reported.

References

1. Riegger C, Herrmann J, Nagarajah J, Hecktor J, Kuemmel S, Otterbach F, Hahn S, Bockisch A, Lauenstein T, Antoch G. Whole-body FDG PET/CT is more accurate than conventional imaging for staging primary breast cancer patients. Eur J Nucl Med Mol Imaging 2012;39:852-63.
2. Groheux D, Espié M, Giacchetti S, Hindié E. Performance of FDG PET/CT in the clinical management of breast cancer. Radiology 2013;266:388-405.
3. Groheux D, Giacchetti S, Delord M, Hindié E, Vercellino L, Cuvier C, Toubert M, Merlet P, Hennequin C, Espié M. 18F-FDG PET/CT in staging patients with locally advanced or inflammatory breast cancer: comparison to conventional staging. J Nucl Med 2013;54:5-11.
4. Koolen BB, Peeters, Marie-Jeanne T. F. D. Vrancken, Aukema TS, Vogel WV, Oldenburg HSA, van der Hage J,A., Hoefnagel CA, Stokkel MPM, Loo CE, Rodenhuis S. 18F-FDG PET/CT as a staging procedure in primary stage II and III breast cancer: comparison with conventional imaging techniques. Breast Cancer Res Treat 2012;131:117-26.
5. Soret M, Bacharach SL, Buvat I. Partial-volume effect in PET tumor imaging. J Nucl Med 2007;48:932-45.
6. Houshmand S, Salavati A, Hess S, Werner TJ, Alavi A, Zaidi H. An update on novel quantitative techniques in the context of evolving whole-body PET imaging. PET clin 2015;10:45-58.
7. Cooper KL, Harnan S, Meng Y, Ward SE, Fitzgerald P, Papaioannou D, Wyld L, Ingram C, Wilkinson ID, Lorenz E. Positron emission tomography (PET) for assessment of axillary lymph node status in early breast cancer: a systematic review and meta-analysis. Eur J Surg Oncol 2011;37:187-98.
8. Conti M. Focus on time-of-flight PET: the benefits of improved time resolution. Eur J Nucl Med Mol Imaging 2011;38:1147-57.
9. Morey AM, Noo F, Kadrmas DJ. Effect of using 2 mm voxels on observer performance for PET lesion detection. IEEE Trans Nucl Sci 2016;63:1359-66.
10. Koopman D, van Dalen J,A., Lagerweij MCM, Arkies H, de Boer J, Oostdijk AHJ, Slump CH, Jager PL. Improving the detection of small lesions using a state-of-the-art time-of-flight PET/CT system and small-voxel reconstructions. J Nucl Med Technol 2015;43:21-7.
11. Aukema TS, Straver ME, Peeters MTV, Russell NS, Gilhuijs KG, Vogel WV, Rutgers EJ, Olmos RAV. Detection of extra-axillary lymph node involvement with FDG PET/CT in patients with stage II–III breast cancer. Eur J Cancer 2010;46:3205-10.
12. Koolen BB, Olmos RAV, Elkhuizen PH, Vogel WV, Peeters MTV, Rodenhuis S, Emiel JT. Locoregional lymph node involvement on 18F-FDG PET/CT in breast cancer patients scheduled for neoadjuvant chemotherapy. Breast Cancer Res Treat 2012;135:231-40.
13. de Groot E,H., Post N, Boellaard R, Wagenaar NRL, Willemsen ATM, van Dalen J,A. Optimized dose regimen for whole-body FDG-PET imaging. EJNMMI Res 2013;3:63-72.

14. Lewitt RM. Multidimensional digital image representations using generalized Kaiser–Bessel window functions. J Opt Soc Am 1990;7:1834-46.
15. Matej S, Lewitt RM. Practical considerations for 3-D image reconstruction using spherically symmetric volume elements. IEEE Trans Med Imaging 1996;15:68-78.
16. Boellaard R, O'Doherty M,J., Weber WA, Mottaghy FM, Lonsdale MN, Stroobants SG, Oyen WJG, Kotzerke J, Hoekstra OS, Pruim J. FDG PET and PET/CT: EANM procedure guidelines for tumour PET imaging: version 1.0. Eur J Nucl Med Mol Imaging 2010;37:181-200.
17. Boellaard R, Delgado-Bolton R, Oyen WJG, Giammarile F, Tatsch K, Eschner W, Verzijlbergen FJ, Barrington SF, Pike LC, Weber WA. FDG PET/CT: EANM procedure guidelines for tumour imaging: version 2.0. Eur J Nucl Med Mol Imaging 2015;42:328-54.
18. EARL. FDG-PET/CT Accreditation. EARL. http://earl.eanm.org/cms/website.php?id=/en/projects/fdg_pet_ct_accreditation/accreditation_specifications.htm. 2016.
19. Bellevre D, Fournier C, Switsers O, Dugué AE, Levy C, Allouache D, Desmonts C, Crouet H, Guilloit J, Grellard J. Staging the axilla in breast cancer patients with 18F-FDG PET: how small are the metastases that we can detect with new generation clinical PET systems?. Eur J Nucl Med Mol Imaging 2014;41:1103-12.
20. Lasnon C, Hicks RJ, Beauregard J, Milner A, Paciencia M, Guizard A, Bardet S, Gervais R, Lemoel G, Zalcman G. Impact of point spread function reconstruction on thoracic lymph node staging with 18F-FDG PET/CT in non–small cell lung cancer. Clin Nucl Med 2012;37:971-6.
21. van der Vos, C S, Koopman D, Rijnsdorp S, Arends AJ, Boellaard R, van Dalen JA, Lubberink M, Willemsen ATM, Visser EP. Quantification, improvement, and harmonization of small lesion detection with state-of-the-art PET. Eur J Nucl Med Mol Imaging 2017;44:4-16.
22. Linden HM, Dehdashti F. Novel methods and tracers for breast cancer imaging. Semin Nucl Med 2013;43:324-9.
23. Schaefferkoetter J, Casey M, Townsend D, El Fakhri G. Clinical impact of time-of-flight and point response modeling in PET reconstructions: a lesion detection study. Phys Med Biol 2013;58:1465-78.
24. Vogel WV, Wensing BM, van Dalen J,A., Krabbe PFM, van den Hoogen F,J.A., Oyen WJG. Optimised PET reconstruction of the head and neck area: improved diagnostic accuracy. Eur J Nucl Med Mol Imaging 2005;32:1276-82.
25. Akamatsu G, Ikari Y, Nishida H, Nishio T, Ohnishi A, Maebatake A, Sasaki M, Senda M. Influence of statistical fluctuation on reproducibility and accuracy of SUVmax and SUVpeak: a phantom study. J Nucl Med Technol 2015;43:222-6.
26. Koopman D, van Dalen J,A., Stigt JA, Slump CH, Knollema S, Jager PL. Current generation time-of-flight 18F-FDG PET/CT provides higher SUVs for normal adrenal glands, while maintaining an accurate characterization of benign and malignant glands. Ann Nucl Med 2016;30:145-52.

CHAPTER 10

10

Letter to the Editor: Small-voxel reconstructions significantly influence SUVs in PET imaging

Authors

Daniëlle Koopman[1,2] | Pieter L. Jager[1] | Jorn A. van Dalen[3]

Author Affiliations

1: Department of Nuclear Medicine, Isala, Zwolle, the Netherlands
2: MIRA Institute for Biomedical Technology and Technical Medicine, University of Twente, Enschede, the Netherlands
3: Department of Medical Physics, Isala, Zwolle, the Netherlands

Published in

European Journal of Nuclear Medicine and Molecular Imaging 2019;46:1751-1752

Dear Sir,

We read with great interest the recent article by Fuentes-Ocampo et al. entitled “Digital vs. analog PET/CT: intra-subject comparison of the SUV_{max} in target lesions and reference regions” [1]. The authors aimed to assess whether digital photon counting technology in digital PET provides better quantification of SUV_{max} in lesions and reference regions than analogue PET. They conclude that both improved photon counting technology in digital PET and the effects of delayed increased uptake and retention significantly increase SUV_{max}, and that this has to be taken into account before the systems can be used interchangeably in follow-up studies.

In our opinion, there is an important limitation in their PET image reconstruction method that is not mentioned in their paper. Fuentes-Ocampo et al. compared digital PET using 2-mm voxel reconstructions with conventional PET using 4-mm voxel reconstructions. This difference in reconstruction approach invalidates their comparison, because the introduction of 2-mm voxel reconstructions on a conventional PET system already significantly increases SUVs [2, 3]. Fuentes-Ocampo et al. did not even cite these published studies. For example, in a conventional FDG PET study in 39 patients, we found an increase in SUV_{max} of 32% across 66 lesions when using small 2-mm voxels instead of 4-mm voxels, and the value increased to as high as 44% for lesions smaller than 11 mm diameter [2]. In comparison, Fuentes-Ocampo et al. reported a mean percentage difference of 35% across 87 lesions. This puts the conclusion of their paper on digital PET in a different light.

Perhaps it was not possible to perform 2-mm voxel reconstructions on the conventional PET system used by Fuentes-Ocampo et al. However, at least it should have been mentioned in the Discussion as a main study limitation, since it could have had a larger effect than the effects of two other limitations that were mentioned: the number of iterations and subsets, and the use of point-spread function modelling.

We emphasize that the image voxel size has a large effect on SUV_{max}, even on conventional non-digital scanners, and should therefore not be ignored in PET comparison studies. The use of both photon counting technology and different reconstruction settings, including voxel size, should be taken into account before different systems can be used interchangeably in follow-up studies.

References

1. Fuentes-Ocampo F, López-Mora DA, Flotats A, Paillahueque G, Camacho V, Duch J, Fernández A, Domènech A, Estorch M, Carrió I. Digital vs. analog PET/CT: intra-subject comparison of the SUVmax in target lesions and reference regions. Eur J Nucl Med Mol Imaging 2019;46:1745-50.
2. Koopman D, van Dalen J,A., Lagerweij MCM, Arkies H, de Boer J, Oostdijk AHJ, Slump CH, Jager PL. Improving the detection of small lesions using a state-of-the-art time-of-flight PET/CT system and small-voxel reconstructions. J Nucl Med Technol 2015;43:21-7.
3. Koopman D, van Dalen JA, Arkies H, Oostdijk AHJ, Francken AB, Bart J, Slump CH, Knollema S, Jager PL. Diagnostic implications of a small-voxel reconstruction for loco-regional lymph node characterization in breast cancer patients using FDG-PET/CT. EJNMMI Res 2018;8:3-12.

CHAPTER 11

11

Performance of digital PET compared to high-resolution conventional PET in patients with cancer

Authors

Daniëlle Koopman[1,2] | Pieter L. Jager[1] | Henk Stevens[1]
Cornelis H. Slump[2] | Siert Knollema[1] | Jorn A. van Dalen[3]

Author Affiliations
1: Department of Nuclear Medicine, Isala, Zwolle, the Netherlands
2: Technical Medicine Center, University of Twente, Enschede, the Netherlands
3: Department of Medical Physics, Isala, Zwolle, the Netherlands

Submitted to
Journal of Nuclear Medicine

Abstract

Purpose

Recently introduced PET systems using silicon photomultipliers (SiPM) with digital readout (dPET) have an improved timing and spatial resolution, aiming at a better image quality, over conventional PET (cPET) systems. We prospectively evaluated the performance of a dPET system in patients with cancer, as compared to high-resolution (HR) cPET imaging.

Methods

After a single FDG-injection, 66 patients underwent dPET (Vereos, Philips Healthcare) and cPET (Ingenuity TF, Philips Healthcare) imaging in a randomised order. We used HR-reconstructions (2x2x2 mm^3 voxels) for both scanners and determined SUV_{max}, SUV_{mean}, lesion-to-background ratio (LBR), metabolic tumour volume (MTV) and lesion diameter in up to 5 FDG-positive lesions per patient. Furthermore, we counted the number of visible and measurable lesions on each PET scan. Two experienced nuclear medicine (NM) specialists, who were blinded to the scanner type, determined the TNM score from both image sets in 30 patients who were referred for initial staging. For all 66 patients and for both scans, these NM specialists separately and blindly evaluated the image quality (4-point scale) and determined the scan preference.

Results

We included 238 lesions (median size 9 mm) that were visible and measurable on both PET scans. We found 37 additional lesions on dPET in 27 patients (41%), which were unmeasurable (n=14) or invisible (n=23) on cPET. SUV_{mean}, $SUV_{max,}$ LBR and MTV on cPET were 5.2±3.9 (mean±SD), 6.9±5.6, 5.0±3.6 and 2991±13251 mm^3, respectively. On dPET SUV_{mean}, SUV_{max} and LBR increased 24%, 23% and 27%, respectively ($p<0.001$) while MTV decreased 13% ($p<0.001$) compared to cPET. Visual analysis showed TNM upstaging with dPET in 4/30 patients (13%). dPET images also scored higher in image quality ($p=0.003$) and were visually preferred in the majority of cases (65%).

Conclusion

Digital PET improved the detection of small lesions, upstaged the disease and images were visually preferred as compared to high-resolution conventional PET. More studies are necessary to confirm the superior diagnostic performance of digital PET.

Keywords

Digital PET; Conventional PET; FDG-PET; lesion detection; cancer imaging

Introduction

Positron Emission Tomography (PET) combined with Computed Tomography (CT), using fluor-18 fluordeoxyglucose (FDG), is increasingly important for cancer detection, disease staging and restaging, patient management and follow-up imaging in patients with cancer [1-4]. However, two major limitations of PET scanners are the limited system sensitivity, resulting in a low signal-to-noise ratio (SNR) and the low spatial resolution [5, 6] which introduces the partial volume effect (PVE) [7]. This PVE hampers the detection of small lesions (<20 mm), especially in case of low metabolic activity, because they appear blurred in the PET image, resulting in an underestimation of lesion FDG-uptake combined with an overestimation of lesion size [8].

A recent development in PET technology is the introduction of silicon photomultipliers (SiPM) with digital readout [9], replacing the conventional photomultipliers. It has been shown that PET systems with digital SiPMs have an improved spatial and timing resolution, potentially resulting in a better image quality with higher standardized uptake values (SUVs) compared to conventional PET (cPET) systems [10-12].

Previous studies compared cPET and dPET scans in patients with cancer using a prototype dPET [13] and clinically available dPET systems [14-16]. In general, these studies compared dPET using high-resolution (HR) reconstructions with cPET using standard-resolution (SR) reconstructions. It has been shown that moving from SR to HR reconstructions in cPET scans, e.g. by using smaller voxels, significantly improves image quality and already results in typically 25% higher SUVs and SNRs [17, 18]. It is unclear which part of the previously reported improvements in image quality and higher SUVs for dPET was the result of the dPET system and which part was due to the difference in image reconstruction between both PET systems [19]. Therefore, we prospectively evaluated the performance of a dPET scanner as compared to a cPET scanner in patients with various types of cancer, using HR reconstructions for both systems. We performed semi-quantitative and visual assessments and also investigated the effect of dPET on lesion detection capabilities as well as the impact on the TNM disease stage.

Materials and methods

Inclusion

In this initial evaluation we prospectively included 66 patients with proven cancer who were referred for whole-body FDG-PET/CT for disease staging or restaging purposes, as part of an ongoing prospective single-centre side-by-side PET comparison study. Written informed consent was obtained from all participants included in this study. The Medical Ethical Committee of our institute (METC Isala, Zwolle, Netherlands) approved the study protocol (NL52329.075.15) and the study was registered at clinicaltrials.gov with identifier #NCT03457506.

PET/CT acquisition

Patients fasted for at least 6h prior to the start of the first PET scan. Patients were administered an FDG-activity based on $A = 6.2\, w^2/t$, where A is the administered activity (in MBq), w the patient's body weight (in kg) and t the acquisition time per bed position (in s) [20].

For each patient whole-body PET/CT scans from head to groin were acquired in supine position using a state-of-the-art time-of-flight (TOF) PET/CT scanner with conventional photomultiplier technology (cPET, Ingenuity TF, Philips Healthcare) and a TOF-PET/CT scanner with digital SiPMs (dPET, Vereos, Philips Healthcare). The PET scanning order was randomized per patient. 27 patients were first scanned on dPET followed by cPET (*dPET-first*) and 39 patients were first scanned on cPET and then on dPET (*dPET-second*). Per patient we collected ΔT_{cPET} and ΔT_{dPET}, defined as the time between FDG-administration and start of the cPET scan and dPET scan, respectively.

PET acquisition times of the first scan were 72 s and 144 s per bed position for patients with body weight ≤80 kg and >80 kg, respectively. For the second scan we used the acquisition time of the first scan, corrected for fluor-18 decay between the two scans. The average administered FDG-activity was 397 MBq (range 212-660 MBq). Prior to each PET scan a CT scan was acquired for attenuation correction. The CT scan parameters were 120 kV, 64 mAs (range 35-136 mAs), 64×0.625 mm slice collimation, a pitch of 0.83 and a rotation time of 0.5 s.

PET/CT reconstruction

We used PET reconstructions resulting in HR images, better suited for small lesion detection. For cPET, we applied an ordered subset expectation maximization (OSEM) TOF-PET HR reconstruction with 2x2x2 mm^3 voxels, a relaxation parameter of 0.6, 3 iterations and 43 subsets, without point spread function (PSF) modelling.

For dPET we performed an OSEM TOF-PET HR reconstruction with 2x2x2 mm^3 voxels, 3 iterations and 17 subsets, without post-smoothing or PSF modelling, as previously described [21]. Attenuation correction was applied using iteratively reconstructed CT data with iDose level 4 and a slice thickness of 3 mm.

Semi-quantitative evaluation

We performed background measurements in the reconstructed PET images by drawing two regions-of-interest (ROIs) of 1000 mm^2 in three axial slices containing healthy liver tissue. The average noise level in the liver was determined as the ratio between the standard deviation (SD) and the average SUV (SUV_{liver}).

We also evaluated the lesion detection capabilities for both PET scanners. An experienced PET reader counted the number of lesions with increased FDG-uptake on both PET scans in a blinded-fashion. Thereby, we gathered all lesions that were unmeasurable or invisible on one of both PET scans as follows:

- *unmeasurable lesion:* it was not possible to define a 70% isocontour volume-of-interest (VOI) based on the maximum pixel value without contaminating the lesion VOI with background tissue. This can occur when there is a relatively low lesion-to-background contrast and/or heterogeneous uptake of FDG [22].
- *invisible lesion:* it was visible on only one of the PET scans

For each patient a maximum of 5 FDG-positive lesions were included in the semi-quantitative evaluation to prevent bias from patients with many lesions. In case a patient had more than 5 eligible lesions, we selected the 5 lesions with the smallest diameter on the CT scan that were measurable on both PET scans. For all measurable lesions on both scans, we derived the mean and maximum standardized uptake value (SUV_{mean} and SUV_{max}) and the metabolic tumour volume (MTV) in mm^3 on cPET and dPET images, using IntelliSpace Portal (Version 9, Philips Healthcare). The MTV was defined as the volume of tumour tissue with increased FDG-uptake. SUV_{mean} and MTV were based on the lesion-VOI that was set at 70% of the maximum pixel value [23]. Moreover, we calculated the lesion-to-background ratio (LBR) by dividing lesion's SUV_{max} to the SUV_{mean} in the background (SUV_{bkg}) directly surrounding the lesion, using the method that we described previously [18]. Finally, we collected the size of each lesion by measuring the short-axis diameter on the axial CT slice.

TNM scoring

Two experienced nuclear medicine (NM) specialists who were blinded to scanner type, together determined the TNM score on both image sets of 30 patients who were referred for initial disease staging, excluding the 5 patients with initial staging for lymphoma. Next, TNM score differences between both scans were collected per patient. We used the latest published version of the TNM system for each type of cancer, as available in August 2019.

Visual analysis and preferences

Both NM specialists separately compared both PET scans side-by-side, blinded to scanner type. With a 4-point score, they rated the image quality of each PET scan as *1: poor, 2: moderate, 3: good* or *4: excellent* and the diagnostic confidence per scan as *1: uncertain, 2: moderate certainty, 3: good certainty* or *4: high certainty.* Furthermore, they determined their preference (*scan 1, scan 2* or *no preference*) for all 66 patients, again blinded to scanner type. In discrepant cases between both NM specialists, a third expert reader performed an additional read.

Statistical analysis

Semi-quantitative data are presented as mean ± standard deviation (SD). Data distribution normality was evaluated using the Shapiro-Wilk test. For data that were not normally distributed, the median is included as well. We performed an independent-samples t-test to compare patient and scan characteristics (age, body weight, administered FDG-activity, ΔT and lesion size) between patients in both scanning groups. The average SUV_{mean}, SUV_{max}, LBR and MTV as measured on cPET and dPET were compared using the Wilcoxon signed-rank test. The noise in the liver as measured with both scanners was compared using a paired-samples t-test. Furthermore, for all semi-quantitative lesion-parameters (SUV_{mean}, SUV_{max}, LBR and MTV) we calculated the relative difference Δx between cPET and dPET using **Formula 1**:

$$\Delta x = (value\ dPET - value\ cPET)/value\ cPET \qquad (1)$$

We used the independent-samples Mann-Whitney U test to compare Δx between lesions in the dPET-first group and the dPET-second group. Furthermore, we performed the F-test and calculated Pearson correlation coefficients between ΔT_{dPET} and Δx, respectively. Finally, a chi-square test was performed to compare image quality and diagnostic confidence scores between cPET and dPET. A p-value less than 0.05 was considered to indicate statistical significance.

Results

Patient and scan characteristics from all patients are shown in **Table 1**. We included 238 FDG-positive lesions with an average size of 12±12 mm (median 9 mm, range 4-90 mm) in 66 patients. The average lesion size was similar in both scanning groups with 12±9 mm in the dPET-first group and 13±13 mm in the dPET-second group (p=0.80).

Table 1 Patient and scan characteristics

	dPET-first group (n=27)	dPET-second group (n=39)	p-value
Gender (n)			
Male	15	23	
Female	12	16	
Age (in years)[a]	65 ± 11	70 ± 17	0.19
Cancer type			
Lung cancer	17	22	
Breast cancer	7	3	
Oesophageal cancer	0	8	
Other	3	6	
PET scan indication			
Initial disease staging	14	21	
Restaging or follow up	13	18	
Body weight (in kg)[a]	84 ± 19	78 ± 15	0.14
Administered FDG-activity (in MBq)[a]	393 ± 111	400 ± 93	0.77
ΔT			
until first PET scan (in min)[a]	62 ± 9	65 ± 10	0.18
until second PET scan (in min)[a]	95 ± 12	97 ± 12	0.48

[a] Continuous variables are described as mean ± SD

Lesion detection capabilities

In 27 out of 66 patients (41%) we found a total of 37 additional FDG-positive lesions on the dPET images, that were unmeasurable (n=14) or invisible (n=23) on the cPET images. Eight of these lesions were detected when dPET was performed first (4 unmeasurable, 4 invisible). The remaining 28 lesions (10 unmeasurable, 19 invisible) appeared on the dPET-second scan, i.e. after prolonged FDG-uptake time. No additional lesions were found on cPET images.

Semi-quantitative results

The average SUV_{mean}, SUV_{max}, LBR and MTV across 238 lesions as measured on cPET and dPET images are shown in **Table 2**. With dPET we found average increases of 24%, 23% and 27% in SUV_{mean}, SUV_{max} and LBR compared to cPET, respectively (p<0.001), while the average MTV decreased with 13% on dPET. This decrease in MTV is also visible in **Figure 1,** showing a histogram with the number of lesions in MTV-subgroups as measured on cPET and dPET. With MTV measurements performed on dPET, there were more lesions with a volume smaller than 200 mm^3. Furthermore, the image noise in the liver was slightly higher on dPET (14.7%±1.9%) compared to cPET (13.3%±1.8%) ($p<0.001$).

Table 2 Semi-quantitative values as measured on both scanners across all lesions (n=238) and relative differences between cPET and dPET. SUV_{mean}, SUV_{max} and LBR were typically 25% higher on dPET ($p<0.001$), while the MTV (in mm^3) was on average 13% lower on dPET ($p<0.001$)

		SUV_{mean}	SUV_{max}	LBR	MTV (in mm^3)
cPET	Mean ± SD	5.2 ± 3.9	6.9 ± 5.6	5.0 ± 3.6	2991 ± 13251
	Median	3.8	4.9	3.8	492
dPET	Mean ± SD	6.2 ± 4.4	8.3 ± 6.7	6.1 ± 4.1	2692 ± 10219
	Median	4.7	6.0	4.9	360
Relative difference Δx (%)		24% ± 23%	23% ± 24%	27% ± 33%	-13% ± 35%

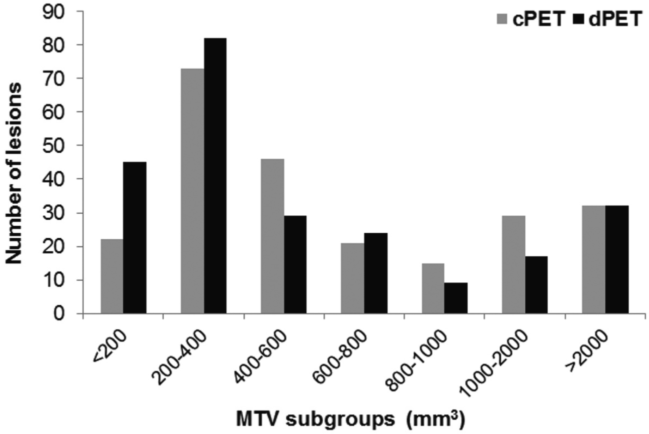

Figure 1 Histogram showing the decrease in MTV on dPET images as compared to cPET, especially for lesions <200 mm^3

The relative difference per lesion-parameter between cPET and dPET is presented in **Table 3** for both scanning groups. ΔSUV_{mean}, ΔSUV_{max} and ΔLBR were significantly higher for lesions in the dPET-second group as compared to lesions in the dPET-first group ($p<0.001$) while ΔMTV was similar in both scanning groups ($p=0.18$). In particular, in the dPET-first group we found an average increase of 9% for both ΔSUV_{mean} and ΔSUV_{max} on dPET while for lesions in the dPET-second group we found average increases of 35% and 34% on dPET, respectively.

Table 3 Relative differences in semi-quantitative parameters between cPET and dPET per scanning group. ΔSUV_{mean}, ΔSUV_{max} and ΔLBR were significantly higher for lesions included in the dPET-second group compared to the dPET-first group, indicating that the scanning order and FDG-uptake time have significant impact on relative differences between cPET and dPET for these parameters. ΔMTV was similar across both groups

	dPET-first (n=101)	dPET-second (n=137)	p-value
ΔSUV_{mean} [a]	9% ± 17%	35% ± 21%	<0.001
ΔSUV_{max} [a]	9% ± 17%	34% ± 22%	<0.001
ΔLBR [a]	7% ± 27%	42% ± 28%	<0.001
ΔMTV [a]	-10% ± 33%	-15% ± 37%	0.18

[a] Continuous variables are described as mean ± SD

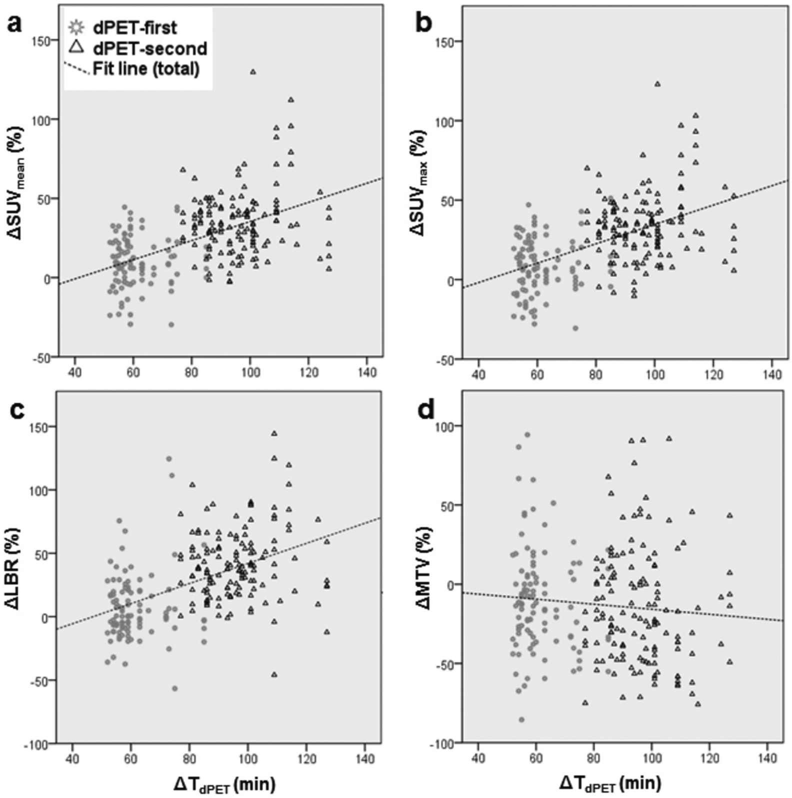

Figure 2 Scatter plots comparing ΔSUV_{mean} (a), ΔSUV_{max} (b), ΔLBR (c) and ΔMTV (d) with ΔT_{dPET} for lesions in the dPET-first and dPET-second group. The relative change in SUV_{mean}, SUV_{max} and LBR increased with prolonged ΔT_{dPET} ($p<0.001$) while we found no correlation between ΔMTV and ΔT_{dPET} ($p=0.14$)

In **Figure 2**, the relative change from cPET to dPET for all lesion-parameters is compared with ΔT_{dPET} across all lesions. It shows that ΔSUV_{mean}, ΔSUV_{max} and ΔLBR further increased at prolonged ΔT_{dPET} ($p<0.001$) with correlation coefficients of 0.53, 0.52 and 0.50, respectively. ΔMTV was not correlated with ΔT_{dPET} ($p=0.14$, correlation coefficient -0.09).

TNM staging

We found TNM upstaging with dPET in 4/30 patients (13%). Clinical information about these four cases is presented in **Table 4**. In three of these cases this dPET scan was acquired after the cPET scan (*dPET-second group*). No TNM upstaging was found with cPET.

Table 4 Description of four patients with TNM upstaging on dPET

Pt	Diagnosis	Scanning group	TNM stage on cPET	TNM stage on dPET	Additional information
1	Breast cancer	dPET-second	T4N0M0	T4N3M0	Suspected internal mammary lymph node metastasis. Confirmed by pathology results.
2	Lung cancer	dPET-first	T4N3M1a	T4N3M1b	Suspected right adrenal gland metastasis on dPET. No validation information available.
3	Lung cancer	dPET-second	T1aN2M0	T1aN3M0	Suspected lymph node metastasis near the thyroid gland. Further SUV rise on follow-up FDG-PET scans after 6 and 12 months.
4	Oesophageal cancer	dPET-second	T1N0M0	T1N0M1	Suspected FDG-positive lesion in the right pelvis region. No validation information available.

FDG-PET images from a patient with breast cancer with TNM upstaging on dPET are shown in **Figure 3**. The TNM score on the cPET scan was T4N0M0 but the dPET scan showed a FDG-positive internal mammary lymph node (SUV_{mean} 3.2, SUV_{max} 4.0, MTV 264 mm^3) that was not visible on cPET, revealing N3 disease. After surgery, pathology findings confirmed that this lymph node was malignant.

Another example with FDG-PET images from a patient with lung cancer in the *dPET-second* group is presented in **Figure 4**. In this case, the dPET scan showed three additional FDG-positive lesions with anatomical substrate on the CT scan which were not visible on cPET images.

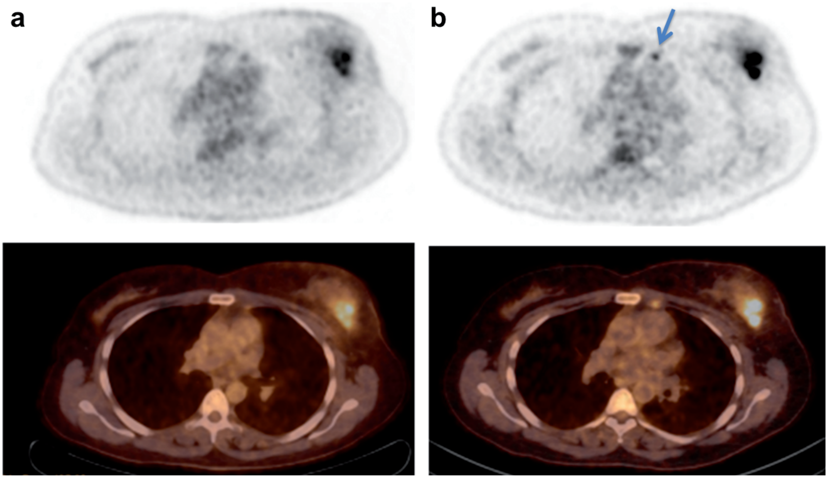

Figure 3 FDG-PET/CT images from a patient with breast cancer with upstaging from T4N0M0 on cPET (ΔT=54 min) (a) to T4N3M0 on dPET (ΔT=106 min) (b). dPET images revealed a FDG-positive internal mammary lymph node (blue arrow) with a diameter of 7 mm. During surgery, a sentinel node procedure was performed and it was confirmed by pathology that this lymph node was malignant

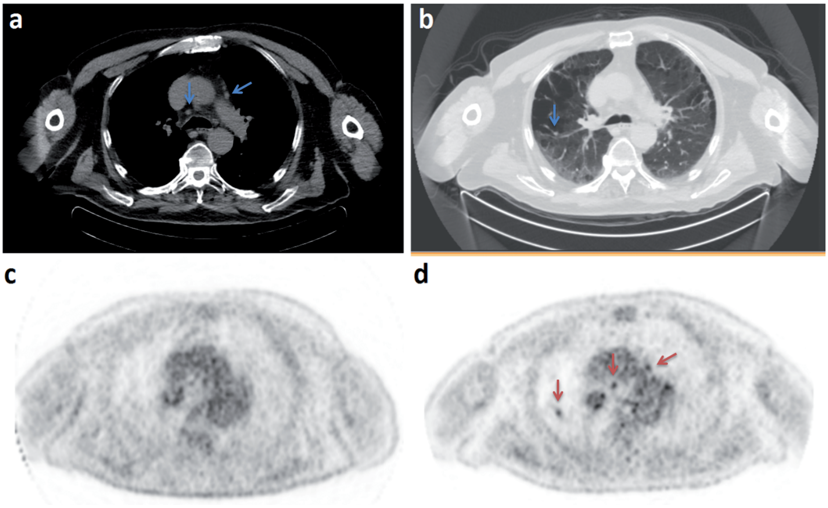

Figure 4 FDG-PET/CT images from a patient with lung cancer with three additional lesions on the dPET scan (d). a: CT scan showing two small lymph nodes in the mediastinum (blue arrows). **b:** CT scan (lung window) showing a small lung lesion (4 mm diameter) in the right lung (blue arrow). **c**: FDG-PET image acquired on cPET (ΔT=73 min) without FDG-positive lesions. **d**: FDG-PET image acquired on dPET (ΔT=114 min) showing three FDG-positive lesions (red arrows) corresponding to three lesions that are also visible on the CT scan (**a, b**)

Visual analysis and preferences

The results of image quality and diagnostic confidence scores are presented in **Figure 5.** dPET resulted in better image quality scores compared to cPET (p=0.003) while the diagnostic certainty of both scans was comparable (p=0.69). The majority of all PET scans resulted in a 'good' image quality (94% for cPET, 83% for dPET) while 15% of the dPET scans were regarded to have an 'excellent' image quality. The remaining 6% (cPET) and 2% (dPET) of the scans were scored as 'moderate' image quality.

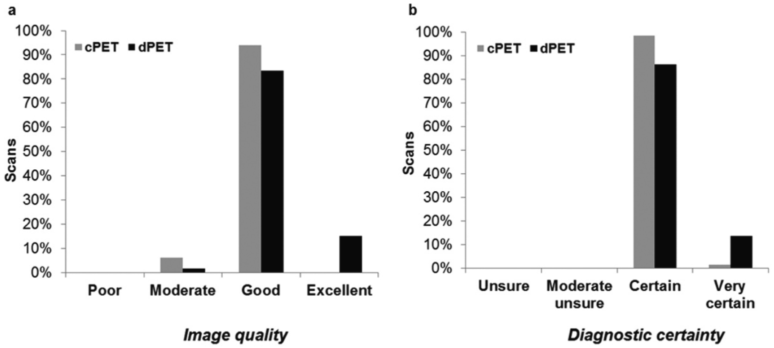

Figure 5 Bar plots showing image quality (a) and diagnostic certainty scores (b) of cPET and dPET scans. Higher image quality scores were found for dPET scans (p=0.003) while the diagnostic certainty was comparable between cPET en dPET scans (p=0.68)

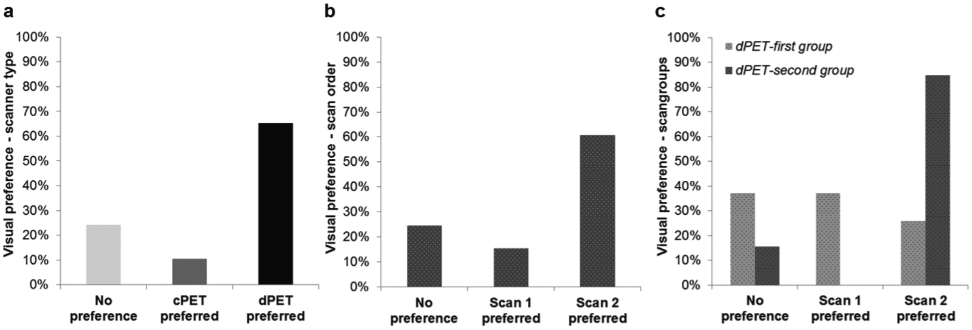

Figure 6 Bar plots showing scanner type preferences (a), scan order preferences (b) and scan order preferences per scanning group (c). Overall, the dPET scan as well as the second scan were preferred in the majority of the cases (65% and 61%, respectively). Moreover, the dPET scan was preferred in 85% of the cases when it was acquired after the cPET scan

The visual scan preference per patient is shown in **Figure 6.** The dPET scan was preferred in 65% of the cases, while the remaining 35% included both cPET scan preferences (11%) and no preferences (24%). Furthermore, the scan acquired after prolonged FDG-uptake (scan 2) was preferred in 61% of the cases while the first scan was preferred in only 15% of the cases. In the dPET-second group, the dPET scan was preferred in 85% of the cases while in the dPET-first subgroup the preferences scores were more widely distributed with 37% preference for scan 1 (being dPET), 26% preference for scan 2 (being cPET) and 37% of the scans with no preference.

Discussion

We performed the first prospective study that compared HR cPET with HR dPET in a relatively large cohort of 66 patients. With dPET we observed significantly higher semi-quantitative values as compared to cPET. Furthermore, in 27 out of 66 patients (41%) we found additional lesions on dPET and in 4 patients (13%) we observed TNM upstaging on dPET as compared to cPET. Moreover, dPET images provided a better image quality and were visually preferred by the NM specialists.

This study shows that dPET provides an improved lesion detection capability. We detected 37 additional lesions with dPET that were unmeasurable or invisible on cPET images. Most of these lesions (78%) were found on the dPET scan that was acquired *after* the cPET scan, thus with prolonged FDG-uptake time, albeit we also detected 8 additional lesions (22%) on the dPET scan that was acquired *prior to* the cPET scan. We have not found additional lesions on cPET, neither in the dPET-first nor in the dPET-second group. At least three other studies previously observed additional lesions on dPET as compared to cPET. Nguyen et al.[13] reported 8 additional lesions in 21 patients while Barrato et al.[14] found 37 additional lesions with focal FDG uptake in 50 patients. However, in these studies all dPET scans were acquired *after* the cPET acquisition which may introduce a bias due to prolonged FDG-uptake [24]. Another study by López-Mora et al.[16] reported 22 additional small (<10 mm) lesions on dPET images in 100 patients. However, they compared SR cPET with HR dPET and this difference in voxel sizes may influence the lesion detection capabilities as well. Furthermore, although they randomised the PET scanning order, it was not described whether the additional lesions were detected on the dPET-first or dPET-second scan.

Our semi-quantitative analysis showed average increases of 24% (SUV_{mean}), 23% (SUV_{max}) and 27% (LBR) across 238 FDG-positive lesions when using HR dPET instead of HR cPET. The corresponding standard deviations of 23%, 24% and 33% demonstrate that there was a wide distribution in relative changes between lesions (**Figure 2)**. This variation is partly caused by methodological aspects such as the impact of prolonged FDG-uptake time [24] and test-retest variations [22, 25] between two PET scans.

Nevertheless, the average semi-quantitative increases with dPET in our study were lower than findings from earlier cPET-dPET comparisons. For example, Barrato et al.[14] reported an average SUV increase of 53% with dPET across 107 lesions. This increase is more than twice as high as the ΔSUV in our study. This can partly be explained by the difference in scanning order because in their study all dPET scans were acquired *after* the cPET scans and this could result in ΔSUV overestimations assigned to the dPET system [24]. Moreover, there were also some differences between their cPET and dPET reconstruction protocol which may further cause their larger SUV difference between both PET systems. Another study by Fuentes-Ocampo et al.[15] recently reported an average SUV increase of 35% across 87 lesions in 87 oncological patients but they compared SR cPET with HR dPET. This difference in reconstruction approach makes their comparison unvalid [19]. As we previously demonstrated, the use of a HR cPET reconstruction already results in SUV increases of typically 25% as compared to SR cPET [17, 18].

Furthermore, we observed a 13% decrease in lesion-MTV with dPET as compared to cPET, using 70% SUV_{max} thresholds. This decrease is likely caused by the higher resolution of the dPET system that decreases the PVE. Nguyen et al.[13] also compared tumour volume as measured on cPET and dPET in a study on 11 patients with 24 lesions. Using 35% and 50% SUV_{max} thresholds for delineation, they reported tumour volume decreases of 31% and 19%, respectively. They stated that dPET has the potential to provide more robust and accurate tumour delineation and this can be beneficial for radiotherapy planning and systematic treatment monitoring [13].

The impact of prolonged FDG-uptake time is significant, which makes PET system comparisons after a single FDG injection difficult. Between the two scanning groups in our study, dPET-first and dPET-second, we observed significant differences in ΔSUV_{mean}, ΔSUV_{max} and ΔLBR. For example, the average ΔSUV_{mean} in the dPET-first group was only 9% whereas the average ΔSUV_{mean} in dPET-second group was 35%. Based on these averages, we expect that about (35%-9%)/2=12% of the higher SUVs on the second scan can be attributed to the prolonged scan time, which was on average 32 minutes in our study. For certain tumour types, it has been reported that these time-dependent SUV increases can be even higher [24, 26]. Fuentes-Ocampo et al.[15] also reported significant differences between both scanning groups with higher dPET SUVs in the dPET-second group. Overall, this demonstrates that in FDG-PET comparison studies where the scan on the newer system is always acquired *after* the scan on the older system [13, 14, 27], an overestimation of the added value of the newer PET system is likely.

The ultimate outcome of better PET detection is a better staging performance. In our study, visual analysis by two NM specialists revealed TNM upstaging with dPET in 4 out of 66 patients. In one case the additional finding on dPET that resulted in upstaging was confirmed by pathology while in another case the extra finding was confirmed on follow-up FDG-PET imaging showing a SUV rise for the suspected lesion. Moreover, the results of our visual analysis comparing cPET with dPET are in line with our semi-quantitative findings. Overall, dPET scans resulted in a better image quality and were visually preferred, especially when the dPET scan was acquired *after* the cPET scan (85% preference score).

The present study also has some limitations. We randomised the scanning order per patient in order to reduce the impact of prolonged FDG-uptake. However, the number of patients per scanning group was not identical as we included 27 patients in the dPET-first group and 39 patients in the dPET-second group. This may cause some overestimation of the SUV increase that is assigned to dPET, although we demonstrated that general patient characteristics and lesion sizes between both groups were similar. Moreover, we aimed to perform a comparison of cPET and dPET using HR reconstructions for small lesion detection in order to solely determine the impact of new dPET technology. However, the image reconstructions were not similar as we did not have the same software possibilities available. Yet, we performed an extensive comparison between both PET systems in a substantial group of 66 patients with 238 FDG-positive lesions. Another limitation of our study is that we did not evaluate the diagnostic performance of dPET in terms of sensitivity, specificity and accuracy due to limited verification data. Further studies are required for this purpose.

Conclusion

In this prospective head-to-head evaluation, digital PET improved the detection of small lesions over high-resolution conventional PET. Digital PET scans were visually preferred by experienced readers, additional lesions were detected in 41% of the patients and the disease was upstaged in 13%. More studies are necessary to confirm the superior diagnostic performance of digital PET.

Competing interests

The Department of Nuclear Medicine, Isala, has established a research cooperation with Philips Healthcare regarding new PET technologies. The content of the article was solely the responsibility of the authors. No other potential conflicts of interest relevant to this article were reported.

Funding

This work was supported by a research agreement between the Department of Nuclear Medicine, Isala, and Philips Healthcare regarding new PET technologies.

References

1. Bar-Shalom R, Yefremov N, Guralnik L, Gaitini D, Frenkel A, Kuten A, Altman H, Keidar Z, Israel O. Clinical performance of PET/CT in evaluation of cancer: additional value for diagnostic imaging and patient management. J Nucl Med 2003;44:1200-9.
2. Branstetter IV BF, Blodgett TM, Zimmer LA, Snyderman CH, Johnson JT, Raman S, Meltzer CC. Head and neck malignancy: is PET/CT more accurate than PET or CT alone?. Radiology 2005;235:580-6.
3. Rosen EL, Eubank WB, Mankoff DA. FDG PET, PET/CT, and breast cancer imaging. Radiographics 2007;27:S229.
4. Fischer B, Lassen U, Mortensen J, Larsen S, Loft A, Bertelsen A, Ravn J, Clementsen P, Høgholm A, Larsen K. Preoperative staging of lung cancer with combined PET–CT. N Engl J Med 2009;361:32-9.
5. Takamochi K, Yoshida J, Murakami K, Niho S, Ishii G, Nishimura M, Nishiwaki Y, Suzuki K, Nagai K. Pitfalls in lymph node staging with positron emission tomography in non-small cell lung cancer patients. Lung Cancer 2005;47:235-42.
6. Poeppel TD, Krause BJ, Heusner TA, Boy C, Bockisch A, Antoch G. PET/CT for the staging and follow-up of patients with malignancies. Eur J Radiol 2009;70:382-92.
7. van der Vos, C S, Koopman D, Rijnsdorp S, Arends AJ, Boellaard R, van Dalen JA, Lubberink M, Willemsen ATM, Visser EP. Quantification, improvement, and harmonization of small lesion detection with state-of-the-art PET. Eur J Nucl Med Mol Imaging 2017;44:4-16.
8. Soret M, Bacharach SL, Buvat I. Partial-volume effect in PET tumor imaging. J Nucl Med 2007;48:932-45.
9. Frach T, Prescher G, Degenhardt C, de Gruyter R, Schmitz A, Ballizany R. The digital silicon photomultiplier—Principle of operation and intrinsic detector performance. IEEE Nucl Sci Symp Conf Rec 2009:1959-65.
10. Hsu DF, Ilan E, Peterson WT, Uribe J, Lubberink M, Levin CS. Studies of a next-generation silicon-photomultiplier–based time-of-flight PET/CT system. J Nucl Med 2017;58:1511-8.
11. Rausch I, Ruiz A, Valverde-Pascual I, Cal-González J, Beyer T, Carrio I. Performance evaluation of the Vereos PET/CT system according to the NEMA NU2-2012 standard. J Nucl Med 2019;60:561-7.
12. van Sluis JJ, de Jong J, Schaar J, Noordzij W, van Snick P, Dierckx R, Borra R, Willemsen A, Boellaard R. Performance characteristics of the digital Biograph Vision PET/CT system. J Nucl Med 2019;60:1031-6.
13. Nguyen NC, Vercher-Conejero J, Sattar A, Miller MA, Maniawski PJ, Jordan DW, Muzic RF, Su K, O’Donnell J,K., Faulhaber PF. Image quality and diagnostic performance of a digital PET prototype in patients with oncologic diseases: Initial experience and comparison with analog PET. J Nucl Med 2015;56:1378-85.

14. Baratto L, Park SY, Hatami N, Davidzon G, Srinivas S, Gambhir SS, Iagaru A. 18F-FDG silicon photomultiplier PET/CT: A pilot study comparing semi-quantitative measurements with standard PET/CT. PloS one 2017;12:e0178936.
15. Fuentes-Ocampo F, López-Mora DA, Flotats A, Paillahueque G, Camacho V, Duch J, Fernández A, Domènech A, Estorch M, Carrió I. Digital vs. analog PET/CT: intra-subject comparison of the SUVmax in target lesions and reference regions. Eur J Nucl Med Mol Imaging 2019;46:1745-50.
16. López-Mora DA, Flotats A, Fuentes-Ocampo F, Camacho V, Fernández A, Ruiz A, Duch J, Sizova M, Domènech A, Estorch M. Comparison of image quality and lesion detection between digital and analog PET/CT. Eur J Nucl Med Mol Imaging 2019;46:1383-90.
17. Koopman D, van Dalen J,A., Lagerweij MCM, Arkies H, de Boer J, Oostdijk AHJ, Slump CH, Jager PL. Improving the detection of small lesions using a state-of-the-art time-of-flight PET/CT system and small-voxel reconstructions. J Nucl Med Technol 2015;43:21-7.
18. Koopman D, van Dalen JA, Arkies H, Oostdijk AHJ, Francken AB, Bart J, Slump CH, Knollema S, Jager PL. Diagnostic implications of a small-voxel reconstruction for loco-regional lymph node characterization in breast cancer patients using FDG-PET/CT. EJNMMI Res 2018;8:3-12.
19. Koopman D, Jager PL, van Dalen JA. Small-voxel reconstructions significantly influence SUVs in PET imaging. Eur J Nucl Med Mol Imaging 2019;46:1751-2.
20. de Groot E,H., Post N, Boellaard R, Wagenaar NRL, Willemsen ATM, van Dalen J,A. Optimized dose regimen for whole-body FDG-PET imaging. EJNMMI Res 2013;3:63-72.
21. Koopman D, Koerkamp MG, Jager PL, Arkies H, Knollema S, Slump CH, Sanches PG, van Dalen JA. Digital PET compliance to EARL accreditation specifications. EJNMMI Phys 2017;4:9-14.
22. de Langen AJ, Vincent A, Velasquez LM, van Tinteren H, Boellaard R, Shankar LK, Boers M, Smit EF, Stroobants S, Weber WA. Repeatability of 18F-FDG uptake measurements in tumors: a metaanalysis. J Nucl Med 2012;53:701.
23. Velasquez LM, Boellaard R, Kollia G, Hayes W, Hoekstra OS, Lammertsma AA, Galbraith SM. Repeatability of 18F-FDG PET in a multicenter phase I study of patients with advanced gastrointestinal malignancies. J Nucl Med 2009;50:1646-54.
24. Lowe VJ, DeLong DM, Hoffman JM, Coleman RE. Optimum scanning protocol for FDG-PET evaluation of pulmonary malignancy. J Nucl Med 1995;36:883-7.
25. Kramer GM, Frings V, Hoetjes N, Hoekstra OS, Smit EF, de Langen AJ, Boellaard R. Repeatability of quantitative whole-body 18F-FDG PET/CT uptake measures as function of uptake interval and lesion selection in non–small cell lung cancer patients. J Nucl Med 2016;57:1343-9.
26. Shankar LK, Hoffman JM, Bacharach S, Graham MM, Karp J, Lammertsma AA, Larson S, Mankoff DA, Siegel BA, Van den Abbeele A. Consensus recommendations for the use of 18F-FDG PET as an indicator of therapeutic response in patients in National Cancer Institute Trials. J Nucl Med 2006;47:1059-66.

27. Sonni I, Park S, Baratto L, Hatami N, Davidzon G, Srinivas S, Gambhir S, Iagaru A. Initial experience with a SiPM-based PET/CT scanner: Influence of acquisition time on image quality. J Nucl Med 2017;58:1369.

PART III

CHAPTER 12

12

Summary and future perspectives

Author

Daniëlle Koopman[1,2]

Author Affiliations
1: Department of Nuclear Medicine, Isala, Zwolle, the Netherlands
2: Technical Medicine Center, University of Twente, Enschede, the Netherlands

Unpublished

Introduction and aim

Positron emission tomography/computed tomography (PET/CT) imaging, using fluor-18 (^{18}F) fluordeoxyglucose (FDG) plays an important role in the diagnostic evaluation of cancer [1-4]. In daily practice FDG-PET/CT images are visually assessed together with semi-quantitative parameters such as the standardised uptake value (SUV). SUV measurements complement the visual interpretation and allow prediction of treatment response and prognosis [5-7] but are influenced by many biological and technical factors, including patient preparation, data acquisition, image reconstruction and processing [8, 9]. There are ongoing efforts towards standardisation of PET imaging to improve semi-quantitative comparisons of PET scans between patients, scanners and medical centres. Thanks to the development of European guidelines by the European Association of Nuclear Medicine (EANM) and the start of the EARL accreditation program for FDG-PET/CT tumour imaging, the variability in semi-quantitative FDG-PET scans has been reduced in recent years [10-12].

PET imaging has two major limitations. The first limitation is its low spatial resolution, causing a limited detectability of small lesions (<20 mm), especially with low metabolism [13, 14]. The second limitation is the limited system sensitivity, resulting in a relatively low signal-to-noise ratio (SNR) [15]. Since the clinical introduction of whole-body PET 20 years ago, several techniques such as the use of time-of-flight (TOF) information in the image reconstruction, digital PET (dPET) detectors and new image reconstructions were developed to improve the image quality and diagnostic performance of PET.

The incorporation of TOF information in the reconstruction algorithm improves PET image quality because TOF enhances the SNR while the same number of photon coincidences is obtained [16]. Many studies demonstrated that TOF-PET resulted in a better image quality with improved small lesion detection, in particular in obese patients [17-19].

Another more recent development was the introduction of dPET technology. Since 2017 three vendors (GE Healthcare, Philips Healthcare and Siemens Healthineers) replaced the conventional photomultiplier tubes (PMTs) in PET detectors by silicon photomultipliers (SiPM) with digital readout [20-23]. dPET systems have a better coincidence timing resolution, higher photon detection efficiency, better spatial resolution and higher system sensitivity as compared conventional PET (cPET) systems [21-24]. Consequently, PET systems with digital detectors potentially provide an improved image quality with higher SNRs and better small lesion detection.

Further, in current practice the image voxel size for whole-body FDG-PET scans is relatively large (typically 4x4x4 mm^3) [18, 25]. This provides PET images with acceptable noise levels but it amplifies the partial volume effect (PVE), thereby limiting small lesion detection. New TOF-PET cameras have the possibility to perform reconstructions with smaller voxels and this may improve small lesion detection as well.

The **aim** of this thesis is to evaluate the impact of these recent improvements in PET technology on the detection of small lesions in cancer imaging. We studied the influence of *conventional TOF-PET* scanners and *small-voxel reconstructions* on small lesion detectability in lung and breast cancer. Furthermore, we studied *digital TOF-PET scanners* and determined their impact on semi-quantitative uptake measurements, image quality and lesion detectability in patients with cancer. Moreover, we evaluated the impact of conventional and digital PET scanners on European guidelines and especially on *EARL demands* for two different radionuclides.

Thesis overview

Part I – PET standardisation

In **Part I** of this thesis we investigated how recent developments in PET technology and scan protocols can be incorporated to further standardise PET imaging.

Chapter 2 contains an overview of many technical developments that improved cancer imaging with PET/CT in recent years. It describes that the introduction of TOF, point spread function (PSF) modelling and new image reconstructions with smaller voxels have improved small lesion detection with PET. Further clinical benefit is expected from dPET and regularised reconstruction methods. Other techniques were developed for specific problems such as metal artefact reduction and respiratory gating. Together, all these developments provide the opportunity to improve quality and quantification of PET/CT cancer imaging. Three topics described in this review are addressed in more detail in following chapters of this thesis: the administration of a bodyweight-dependent FDG-activity (Chapter 3), the use of small-voxel reconstructions (Chapter 8 and 9) and the impact of digital SiPMs on PET image quality (Chapter 11).

Recently, it has been demonstrated that administrating an FDG-activity that depends quadratically on a patients' body weight can provide a constant image quality across patients [26]. In **Chapter 3** we provide a practical method on how to implement this into clinical practice using the NEMA image quality (IQ) phantom, following European guidelines. This methodology was applied using a state-of-the-art PET/CT scanner. The formula that we derived prescribes the FDG-activity to administer to individual patients for whole-body PET examinations and fulfils recent insights on patient-specific FDG-activity administrations. The method described in Chapter 3 is generally applicable to any PET system, using a specified image reconstruction and scan time per bed position.

Current EANM guidelines on FDG-PET tumour imaging are based on cPET systems and therefore it was unknown if dPET systems with digital SiPMs, that potentially provide an improved image quality over conventional systems, are able to fulfil EARL accreditation standards as well. This was evaluated in **Chapter 4** for a recently introduced TOF-dPET system. We performed a phantom study following EANM guidelines using a NEMA IQ phantom with six spheres filled with ^{18}F. For each sphere we calculated the contrast recovery coefficient (CRC), which is defined as the ratio between the measured (maximum or mean) ^{18}F concentration in the image and the true ^{18}F concentration in the sphere. We demonstrated that this dPET system typically showed CRCs above the upper limits of EARL specifications, especially for small objects. To meet EARL standards for dPET, the use of relatively large 4x4x4 mm^3 voxels and a Gaussian post-smoothing filter of 2 to 4 mm are therefore recommended.

Once different PET systems fulfil EARL specifications, it is expected that they provide PET scans with comparable semi-quantitative results. This was investigated in **Chapter 5** on whole-body FDG-PET scans from 50 patients with cancer using an EARL-accredited cPET and dPET scanner. Across 128 FDG-positive lesions with an average size of 19±14 mm, the average difference in SUV (ΔSUV) was 6-8% with dPET values being higher in most cases. Furthermore, we found repeatability coefficients of 27% (ΔSUV_{mean} en ΔSUV_{peak}) and 33% (ΔSUV_{max}) ($p<0.001$), indicating that only a limited number of lesions showed a SUV difference of more than 30%. These findings indicate that EARL standardisation works.

In addition to the widely used ^{18}F radionuclides, gallium-68 (^{68}Ga) labelled peptides are increasingly used for PET imaging including in multi-centre trials [27]. However, EARL specifications have not been determined yet for ^{68}Ga. In **Chapter 6** we evaluated the variation in semi-quantification with ^{68}Ga-PET in a multi-centre setting. Eight centres in Europe with thirteen different PET/CT systems performed ^{18}F and ^{68}Ga acquisitions using a cylindrical phantom and a NEMA IQ phantom. This study showed that ^{68}Ga CRCs perform at the lower limits of current EARL CRC standards for ^{18}F. For practical reasons we recommend to use the ^{18}F EARL-approved reconstruction settings for ^{68}Ga-PET quantification in multi-centre trials. This should be extended by a cross-calibration verification between ^{68}Ga measured by the dose calibrator and by the PET system.

Part II - PET optimisation

In **Part II** of this thesis we investigated the value of three recent developments in PET technology: TOF (Chapter 7), small-voxel reconstructions (Chapter 8, 9 and 10) and dPET (Chapter 10 and 11). We evaluated the impact of these technologies on PET image quality and small lesion detectability in patients with cancer, focussed on lung cancer and breast cancer.

For example, the latest generation of cPET scanners, incorporating the TOF technique, may lead to a better detection of adrenal metastases. Moreover it could change how nuclear medicine (NM) specialists should evaluate these glands on FDG-PET images to distinguish benign from malignant ones. In **Chapter 7** we analysed the impact of a conventional TOF-PET/CT scanner, using EARL-compatible reconstructions, on adrenal gland SUV and the adrenal-to-liver (AL) ratio in 88 patients with suspected lung cancer. With a SUV_{max} cut-off value of 3.7, 96% sensitivity and 96% specificity was obtained. A cut-off value of 1.8 for the AL ratio resulted in 91% sensitivity and 97% specificity. Compared with literature based on a previous generation of non-TOF PET scanners, TOF-PET imaging provided higher SUVs for benign adrenal glands while a highly accurate distinction between benign and malignant glands remained. Clinical implementation of TOF-PET requires the use of higher cut-off levels to distinguish between benign and malignant glands, as well as visual adaptation by PET readers.

In Chapter 7 we still applied an EARL-compatible PET reconstruction with relatively large voxels (4x4x4 mm^3). In combination with TOF-PET cameras, the use of reconstructions with smaller 2x2x2 mm^3 voxels might further improve the detection of small lesions [18]. In **Chapter 8** this was investigated on the NEMA IQ phantom (sphere sizes 10-37 mm), a micro hollow sphere phantom (sphere sizes 4-8 mm) and 39 patients with lung cancer, using the same TOF-PET/CT scanner as in Chapter 7. This study showed that the use of a small-voxel reconstruction led to higher CRCs and SNRs for small spheres ($\leq$13 mm) with relative increases up to 80% (CRC_{mean}) and 200% (CRC_{max}) for the smallest spheres. The average increase of SNR_{mean} and SNR_{max} across all phantom spheres was 12% and 39%, respectively. Moreover, the evaluation of 66 FDG-positive lesions in the patient study showed that when using small voxels, SUV_{mean} and SUV_{max} increased with 17% and 32%, respectively ($p<0.01$). Additionally, the mean and maximum SNR increased by 20% and 27%, respectively ($p<0.01$). Finally, three NM specialists preferred the small-voxel images in 76% of the cases. In conclusion, we can improve small lesion detection with FDG-PET when using small-voxel reconstructions.

In Chapter 8 we did not yet assess the diagnostic implications and potential clinical benefit of these small-voxel reconstructions. This was evaluated in **Chapter 9** by loco-regional axillary lymph node characterisation in 69 patients with breast cancer, using the same state-of-the-art TOF-PET/CT system. Two NM specialists visually evaluated all scans and semi-quantitative parameters were collected by measuring the SUV_{max} and tumour-to-background ratio (TB_{ratio}). Based on the evaluation of 61 benign and 169 malignant axillary lymph nodes, we found that small-voxel PET/CT improved the sensitivity of visual lymph node characterization from 76% to 89% ($p<0.001$). This provides a higher detection rate of malignant lymph nodes. However, small-voxel PET/CT also introduced more false-positive results in benign nodes during visual evaluation. Across all nodes, there was no difference in accuracy between standard and small-voxel PET ($p=0.13$). Quantitatively, a small-voxel reconstruction showed average increases in SUV_{max} and TB_{ratio} of typically 40% over standard-voxel PET. This resulted in higher SUV cut-off values, moving from 1.8 to 2.6, when differentiating benign from malignant axillary lymph nodes. This implicates that PET readers have to adapt their reference standards visually and quantitatively when using small-voxel PET images.

In the preceding chapters we have determined the value of small-voxel reconstructions on cPET. A similar impact of small-voxel reconstructions using dPET can be expected as well and this should be kept in mind for fair comparisons between PET scanners. **Chapter 10** contains a Letter to the Editor with our reply to a recent paper of Fuentes-Ocampo et al.[28]. They compared cPET and dPET in 100 oncological patients and found a mean SUV percentage difference of 35% across 87 lesions, which they attributed to the dPET technology. However in their study they applied a standard-voxel reconstruction (4x4x4 mm^3) on their cPET scanner, while they used smaller (2x2x2 mm^3) voxels with their dPET scanner. This difference in voxel size between the two PET scanners was not taken into account when they evaluated their results. This invalidates their comparison as the use of small-voxel reconstructions on cPET already results in increased SUVs, as demonstrated in Chapter 8 and Chapter 9. In our Letter we emphasized that the image voxel size has a large effect on SUV and should therefore not be ignored in PET comparison studies.

Finally in **Chapter 11**, we prospectively evaluated the visual and semi-quantitative performance of dPET compared to high-resolution cPET in 66 patients with various types of cancer. When using 2x2x2 mm^3 high-resolution (HR) reconstructions for both systems, we found approximately 25% higher SUVs with dPET as compared to cPET ($p<0.001$). dPET images were also visually preferred in the majority of cases (65%). Furthermore with dPET, we found 37 additional lesions in 27 patients (41%) and TNM upstaging in 13% of the patients. More studies are necessary to confirm the superior diagnostic performance of digital PET.

Future perspectives

Since the clinical introduction of whole-body PET for oncology imaging 20 years ago, multiple advances have taken place that improved small lesion detectability. In Chapter 2 we described which new hardware, software, acquisition and reconstruction methods were introduced by the current generation of PET/CT scanners. In the following paragraphs, further developments are described that can influence PET standardisation and further improve PET image quality and small lesion detection in the future.

Impact of new PET technology on standardisation

EARL update

A challenge in standardising PET/CT performance is the development of new techniques that improve PET image quality. In Chapter 4 we showed that an image reconstruction with relatively large voxels and a Gaussian post-smoothing filter is needed to fulfil EARL specifications with a dPET system. As PET technology continuously evolves, updated EARL specifications are needed in the future. This was investigated in 2018 by Kaalep et al.[29] by using four cPET systems from three major vendors equipped with TOF and PSF modelling techniques. They proposed an update of the EARL accreditation specifications to support higher CRCs. The EARL organisation has adapted this proposal into their accreditation program and for full implementation a transition phase of two years is expected. Moreover in the future, the use of smaller phantom spheres, for example as available in a micro phantom that we used in Chapter 8, is warranted to be able to compare reconstruction algorithms for smaller sphere sizes and to standardise the quantification of small lesions across scanners.

New semi-quantitative methods

Another approach that may further improve PET standardization is the use of semi-quantitative measures that are more reproducible and robust than SUV_{mean} and SUV_{max} [29]. An example is the SUV_{peak} parameter, defined as the average SUV within a fixed-size region of interest (ROI), typically 1 cm^3, centred on a part of the tumour with high uptake of the radiopharmaceutical [30]. Thanks to its larger ROI volume, SUV_{peak} is less influenced by image noise than SUV_{max}. Unfortunately, there are various definitions of SUV_{peak} with differences in ROI shapes (cubic, circular, spherical), locations and sizes (7-17 mm) and these can significantly affect the results [31]. Furthermore with the majority of current SUV_{peak} definitions, the SUV_{peak} of sub-centimetre lesions is underestimated because the peak VOI size is exceeding the size of the lesion [29].

Standardised and optimised reconstructions

For PET systems that incorporate new technology, EARL-compatible reconstructions can be used for standardised quantification. However for optimal visual assessment, a different HR image reconstruction providing higher SNRs and better lesion detectability is frequently preferred [11, 32]. To fulfil both demands, often two sets of PET reconstructions are generated. Recently, a software tool (EQ.PET, Siemens Healthineers) has been developed that provides a single set of PET images that combines standardised SUVs with optimal HR images for visual assessment [33, 34]. The use of such an approach can save reconstruction and image interpretation time [34]. However, the current tool is only applicable to scanners and reconstruction algorithms of the vendor that developed it [33]. For the future, a vendor-neutral solution is desirable.

Further development of TOF-PET

The TOF performance of a PET system has been improved considerably since its introduction, thanks to technical developments as the digital SiPMs [35]. The first TOF-PET/CT scanner (Gemini TF, Philips Healthcare) was introduced in 2006 with a coincidence timing resolution of 600 ps [16] whereas the newest digital TOF-PET/CT system (Biograph Vision, Siemens Healthineers), introduced in 2018, has a timing resolution of 210 ps [22]. This further facilitates the use of larger matrix sizes and consequently smaller voxels [36], which in turn potentially improves small lesion detection, as demonstrated in Chapter 8 and Chapter 9. Besides, TOF gain can also be used to reduce the amount of radioactivity that is administered to patients and/or it can be used to reduce the scan time, while maintaining image quality. In the future, an even higher TOF performance can be expected. Lecoq [37] recently described a systematic approach by different research groups worldwide aiming to achieve a timing resolution below 100 ps. Even a TOF performance of 10 ps was regarded possible by Lecoq [37], although it will be extremely challenging. If such technology becomes available in future clinical practice, it is expected to introduce a paradigm shift in PET imaging because it allows major improvements in system sensitivity. This would allow substantial dose reductions, shorter scan times and/or further improvement of PET image quality [37]. This may also allow PET-guided biopsies and PET imaging during interventional procedures.

New reconstruction methods

In the near future it is expected that new image reconstruction methods can further improve PET image quality and small lesion detection. GE Healthcare has recently introduced a Bayesian penalized likelihood reconstruction algorithm (BSREM) which provides a better image resolution and reduced image noise as compared to the widely used Ordered Subset Expectation Maximization (OSEM) algorithm [38]. Last year it has been shown that on FDG-PET/CT scans from patients with various types of cancer, BSREM provides an improved image quality, tumour conspicuity and image sharpness over OSEM [39, 40]. Moreover, Chilcott et al.[41] recently demonstrated that the use of BSREM results in a more consistent image quality and SNR in the liver than OSEM does, with the greatest benefit for the heaviest patients. It is expected that other vendors will incorporate Bayesian reconstruction methods as well.

Another technology that may improve PET image quality is data-driven motion correction [42, 43]. This method extracts motion information from the PET acquisition signal itself. Compared to physical motion-measurements that we described in Chapter 2, data-driven motion correction has multiple advantages: it is operator-independent and can be implemented fully automated as a software solution while changes in the acquisition protocol are not required [44].

Artificial intelligence

An emerging field in medical imaging is the application of artificial intelligence (AI) methodologies, in particular machine learning and deep learning, by automatically quantifying radiographic patterns. AI is expected to have great utility in the detection, characterization and monitoring of tumours [45]. An example is the computer-aided detection of pulmonary nodules using PET/CT. In 2018, Schwyzer et al.[46] demonstrated that machine- and deep learning algorithms could aid almost fully automated lung cancer detection, even at ten- and thirty-fold reduced radiation doses. This may lead to new applications for FDG-PET. AI programs are also used to obtain information, which means that large amounts of quantitative features are extracted from medical images using data-characterisation algorithms [47]. This is known as radiomics. In recent years it has been shown that several features from PET images reflect intratumoral heterogeneity and this is related to tumour features [48]. Thereby, radiomics potentially reveal unique disease characteristics and could provide additional diagnostic and prognostic value.

Both optimisation and standardisation of PET images are required for the implementation of radiomic features. Aide et al.[49] recently showed that the characterization of breast cancer requires HR PET images, especially when looking for relations between tumour heterogeneity on FDG-PET, using radiomic features and histological characteristics of the tumour. Meanwhile, PET standardisation remains essential as well, since differences in scanner models, acquisition and reconstruction protocols influence radiomic features and their outcomes [50].

Total-body PET

Recently, the construction of the world's first human total-body (TB) PET/CT scanner has been completed [51]. While clinically available PET systems have an axial field-of-view of typically 15 to 25 cm, this TB PET system has a 194 cm field-of-view. This enables visualisation of the entire human body with simultaneous coverage of all tissues and organs within one acquisition. Moreover with TB PET, detectors capture the majority of emitted photons, enabling a 40-fold gain in effective system sensitivity and a 6-fold increase in SNR compared to current clinical PET scanners [52]. This can enhance image quality (**Figure 1**) and can reduce scan times and/or the required amount of radioactivity. Furthermore, the system provides the possibility of TB dynamic acquisitions with high temporal resolution. Meanwhile, TB PET also brings many challenges, predominantly concerning system engineering and device expenses [52]. Future studies will have to demonstrate the value of TB PET imaging [51].

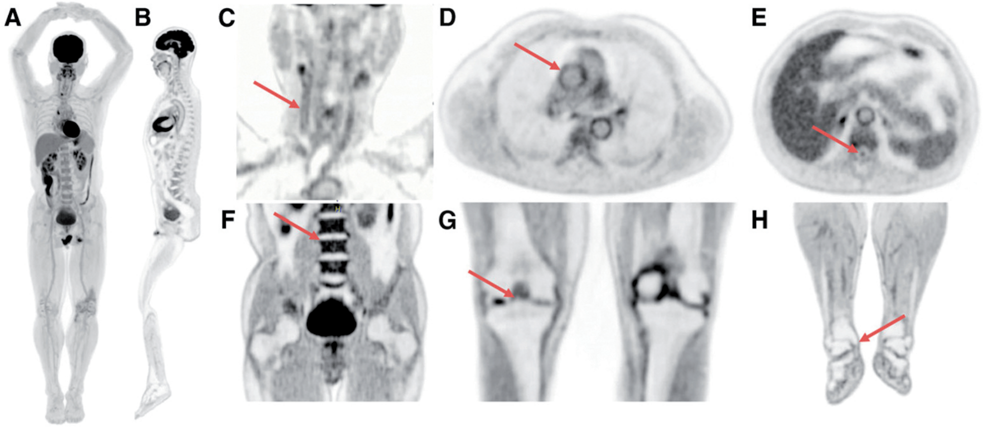

Figure 1 Total-body PET scan from a healthy volunteer, showing a total-body image in coronal (A) and sagittal view (B), head/neck view with carotid artery walls (C), chest view showing the walls of major blood vessels (D), abdominal view with spinal canal (E), abdominal-pelvis view including vertebra's (F), knees with osteophytes (G) and lower extremities with detailed view of the medial tibial malleolus (H). Images obtained from [51]

Clinical implementation and validation of new PET technology

In this thesis we demonstrated that new technologies have improved PET image quality and thereby small lesion detection. However for NM specialists, these developments could also make the evaluation of PET images more complicated. With an improved image quality, images contain more details that have to be interpreted, while there is a risk of false-positive findings as well (Chapter 7 and Chapter 9). NM specialists have to adapt their reference standards and common SUV cut-off values to distinguish between benign and malignant lesions. Ultimately, the question is which image quality is most suitable to support the clinical demand. This may depend on the imaging purpose as well, whether the PET scan is performed for tumour detection, TNM staging, treatment response evaluation or follow-up.

New PET technology may lead to a paradigm shift in oncology imaging. First of all, it is likely that PET imaging becomes more accessible and cost-effective because a FDG-PET scan with an image quality that fulfils EANM guidelines can yet be acquired using a limited amount of radioactivity and a total scan duration of only 5 to 10 minutes [22]. With future technical developments as described in this chapter, it is likely that these scan durations can be reduced even further. On the other hand, HR PET imaging may provide new added value in disease characterisation and staging in certain types of cancer where with previous generations of PET scanners the diagnostic value of PET appeared to be limited, for example in pancreatic and colorectal cancer [53, 54]. An illustration of the potential of ultra-HR dPET is shown in **Figure 2** with a FDG-PET scan from a patient with liver-metastasized pancreatic cancer. With an ultra-HR 1x1x1 mm^3 voxel reconstruction of the digital PET scan with a three-times longer scan duration (**Figure 2C**), multiple small liver metastases were detected that were not visualised on **Figure 2A** (standard EARL scan) and only poorly visualised on **Figure 2B** (HR reconstruction with standard scan duration).

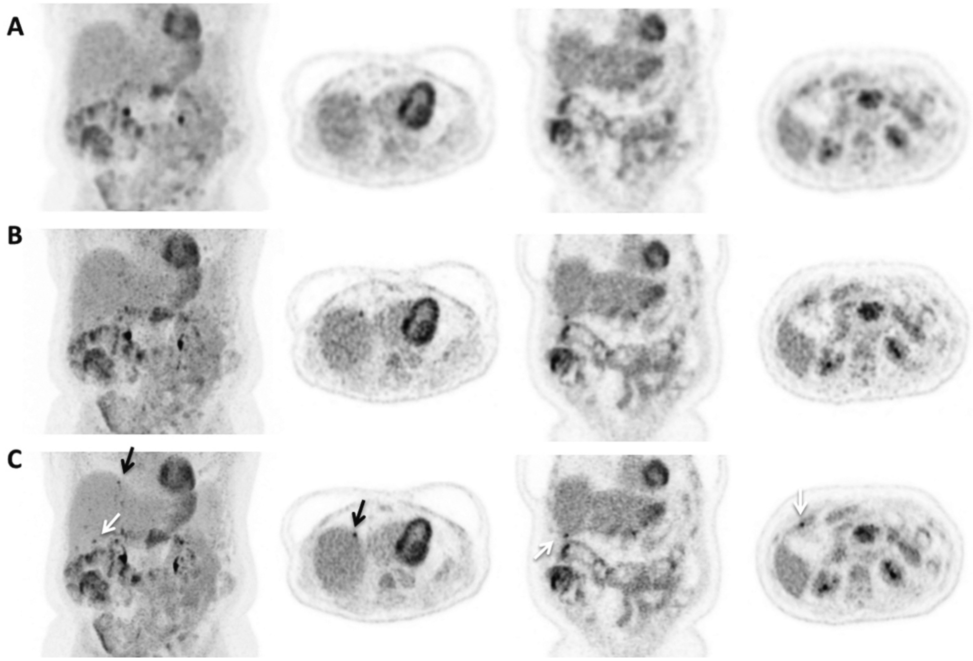

Figure 2 FDG-PET images from a patient with liver-metastasized pancreatic cancer. **A:** dPET scan fulfilling EARL-standards, without any visible lesions in the liver. **B:** HR dPET scan using optimised reconstruction settings (as described in Chapter 11), only poorly visualising the lesions in the liver. **C:** dPET scan acquired with a three-times longer scan duration and reconstructed with ultra-HR settings, showing a clear lesion detectability of multiple liver metastasis (arrows)

References

1. Bar-Shalom R, Yefremov N, Guralnik L, Gaitini D, Frenkel A, Kuten A, Altman H, Keidar Z, Israel O. Clinical performance of PET/CT in evaluation of cancer: additional value for diagnostic imaging and patient management. J Nucl Med 2003;44:1200-9.
2. Branstetter IV BF, Blodgett TM, Zimmer LA, Snyderman CH, Johnson JT, Raman S, Meltzer CC. Head and neck malignancy: is PET/CT more accurate than PET or CT alone?. Radiology 2005;235:580-6.
3. Rosen EL, Eubank WB, Mankoff DA. FDG PET, PET/CT, and breast cancer imaging. Radiographics 2007;27:S229.
4. Fischer B, Lassen U, Mortensen J, Larsen S, Loft A, Bertelsen A, Ravn J, Clementsen P, Høgholm A, Larsen K. Preoperative staging of lung cancer with combined PET–CT. N Engl J Med 2009;361:32-9.
5. Lin C, Itti E, Haioun C, Petegnief Y, Luciani A, Dupuis J, Paone G, Talbot J, Rahmouni A, Meignan M. Early 18F-FDG PET for prediction of prognosis in patients with diffuse large B-cell lymphoma: SUV-based assessment versus visual analysis. J Nucl Med 2007;48:1626-32.
6. de Geus-Oei L, van der Heijden, Henricus FM, Corstens FH, Oyen WJG. Predictive and prognostic value of FDG-PET in nonsmall-cell lung cancer: a systematic review. Cancer 2007;110:1654-64.
7. Huang W, Zhou T, Ma L, Sun H, Gong H, Wang J, Yu J, Li B. Standard uptake value and metabolic tumor volume of 18 F-FDG PET/CT predict short-term outcome early in the course of chemoradiotherapy in advanced non-small cell lung cancer. Eur J Nucl Med Mol Imaging 2011;38:1628.
8. Vriens D, Visser EP, de Geus-Oei L, Oyen WJG. Methodological considerations in quantification of oncological FDG PET studies. Eur J Nucl Med Mol Imaging 2010;37:1408-25.
9. Adams MC, Turkington TG, Wilson JM, Wong TZ. A systematic review of the factors affecting accuracy of SUV measurements. Am J Roentgenol 2010;195:310-20.
10. Boellaard R, O'Doherty M,J., Weber WA, Mottaghy FM, Lonsdale MN, Stroobants SG, Oyen WJG, Kotzerke J, Hoekstra OS, Pruim J. FDG PET and PET/CT: EANM procedure guidelines for tumour PET imaging: version 1.0. Eur J Nucl Med Mol Imaging 2010;37:181-200.
11. Boellaard R, Delgado-Bolton R, Oyen WJG, Giammarile F, Tatsch K, Eschner W, Verzijlbergen FJ, Barrington SF, Pike LC, Weber WA. FDG PET/CT: EANM procedure guidelines for tumour imaging: version 2.0. Eur J Nucl Med Mol Imaging 2015;42:328-54.
12. Kaalep A, Sera T, Oyen WJG, Krause BJ, Chiti A, Liu Y, Boellaard R. EANM/EARL FDG-PET/CT accreditation - summary results from the first 200 accredited imaging systems. Eur J Nucl Med Mol Imaging 2018;45:412-22.

13. Takamochi K, Yoshida J, Murakami K, Niho S, Ishii G, Nishimura M, Nishiwaki Y, Suzuki K, Nagai K. Pitfalls in lymph node staging with positron emission tomography in non-small cell lung cancer patients. Lung Cancer 2005;47:235-42.
14. Berg E, Cherry SR. Innovations in instrumentation for positron emission tomography. Semin Nucl Med 2018;48:311-31.
15. Budinger TF. PET instrumentation: what are the limits?. Semin Nucl Med 1998;28:247-67.
16. Surti S, Kuhn A, Werner ME, Perkins AE, Kolthammer J, Karp JS. Performance of Philips Gemini TF PET/CT scanner with special consideration for its time-of-flight imaging capabilities. J Nucl Med 2007;48:471-80.
17. Kadrmas DJ, Casey ME, Conti M, Jakoby BW, Lois C, Townsend DW. Impact of time-of-flight on PET tumor detection. J Nucl Med 2009;50:1315-23.
18. Conti M. Focus on time-of-flight PET: the benefits of improved time resolution. Eur J Nucl Med Mol Imaging 2011;38:1147-57.
19. Akamatsu G, Ishikawa K, Mitsumoto K, Taniguchi T, Ohya N, Baba S, Abe K, Sasaki M. Improvement in PET/CT image quality with a combination of point-spread function and time-of-flight in relation to reconstruction parameters. J Nucl Med 2012;53:1716-22.
20. Frach T, Prescher G, Degenhardt C, de Gruyter R, Schmitz A, Ballizany R. The digital silicon photomultiplier—Principle of operation and intrinsic detector performance. IEEE Nucl Sci Symp Conf Rec 2009:1959-65.
21. Hsu DF, Ilan E, Peterson WT, Uribe J, Lubberink M, Levin CS. Studies of a next-generation silicon-photomultiplier–based time-of-flight PET/CT system. J Nucl Med 2017;58:1511-8.
22. van Sluis JJ, de Jong J, Schaar J, Noordzij W, van Snick P, Dierckx R, Borra R, Willemsen A, Boellaard R. Performance characteristics of the digital Biograph Vision PET/CT system. J Nucl Med 2019;60:1031-6.
23. Rausch I, Ruiz A, Valverde-Pascual I, Cal-González J, Beyer T, Carrio I. Performance evaluation of the Vereos PET/CT system according to the NEMA NU2-2012 standard. J Nucl Med 2019;60:561-7.
24. Slomka PJ, Pan T, Germano G. Recent advances and future progress in PET instrumentation. Semin Nucl Med 2016;46:5-19.
25. Kolthammer JA, Su K, Grover A, Narayanan M, Jordan DW, Muzic RF. Performance evaluation of the Ingenuity TF PET/CT scanner with a focus on high count-rate conditions. Phys Med Biol 2014;59:3843-59.
26. de Groot E,H., Post N, Boellaard R, Wagenaar NRL, Willemsen ATM, van Dalen J,A. Optimized dose regimen for whole-body FDG-PET imaging. EJNMMI Res 2013;3:63-72.
27. Perera M, Papa N, Christidis D, Wetherell D, Hofman MS, Murphy DG, Bolton D, Lawrentschuk N. Sensitivity, specificity, and predictors of positive 68Ga–prostate-specific membrane antigen positron emission tomography in advanced prostate cancer: a systematic review and meta-analysis. Eur Urol 2016;70:926-37.

28. Fuentes-Ocampo F, López-Mora DA, Flotats A, Paillahueque G, Camacho V, Duch J, Fernández A, Domènech A, Estorch M, Carrió I. Digital vs. analog PET/CT: intra-subject comparison of the SUVmax in target lesions and reference regions. Eur J Nucl Med Mol Imaging 2019;46:1745-50.
29. Kaalep A, Sera T, Rijnsdorp S, Yaqub M, Talsma A, Lodge MA, Boellaard R. Feasibility of state of the art PET/CT systems performance harmonisation. Eur J Nucl Med Mol Imaging 2018;45:1344-61.
30. Wahl RL, Jacene H, Kasamon Y, Lodge MA. From RECIST to PERCIST: evolving considerations for PET response criteria in solid tumors. J Nucl Med 2009;50:122S.
31. Vanderhoek M, Perlman SB, Jeraj R. Impact of the definition of peak standardized uptake value on quantification of treatment response. J Nucl Med 2012;53:4-11.
32. Lasnon C, Desmonts C, Quak E, Gervais R, Do P, Dubos-Arvis C, Aide N. Harmonizing SUVs in multicentre trials when using different generation PET systems: prospective validation in non-small cell lung cancer patients. Eur J Nucl Med Mol Imaging 2013;40:985-96.
33. Quak E, Le Roux P, Hofman MS, Robin P, Bourhis D, Callahan J, Binns D, Desmonts C, Salaun P, Hicks RJ. Harmonizing FDG PET quantification while maintaining optimal lesion detection: prospective multicentre validation in 517 oncology patients. Eur J Nucl Med Mol Imaging 2015;42:2072-82.
34. Lasnon C, Salomon T, Desmonts C, Dô P, Oulkhouir Y, Madelaine J, Aide N. Generating harmonized SUV within the EANM EARL accreditation program: software approach versus EARL-compliant reconstruction. Ann Nucl Med 2017;31:125-34.
35. Degenhardt C, Rodrigues P, Trindade A, Zwaans B, Mülhens O, Dorscheid R, Thon A, Salomon A, Frach T. Performance evaluation of a prototype positron emission tomography scanner using digital photon counters (DPC). IEEE Nucl Sci Symp Conf Rec 2012.
36. Conti M, Bendriem B. The new opportunities for high time resolution clinical TOF PET. Clin Transl Imaging 2019;7:139-47.
37. Lecoq P. Pushing the limits in time-of-flight PET imaging. IEEE Transactions on Radiation and Plasma Medical Sciences 2017;1:473-85.
38. Teoh EJ, McGowan DR, Macpherson RE, Bradley KM, Gleeson FV. Phantom and clinical evaluation of the Bayesian penalized likelihood reconstruction algorithm Q. Clear on an LYSO PET/CT system. J Nucl Med 2015;56:1447-52.
39. Messerli M, Stolzmann P, Egger-Sigg M, Trinckauf J, D'Aguanno S, Burger IA, von Schulthess GK, Kaufmann PA, Huellner MW. Impact of a Bayesian penalized likelihood reconstruction algorithm on image quality in novel digital PET/CT: clinical implications for the assessment of lung tumors. EJNMMI Phys 2018;5:27-39.
40. Matti A, Lima GM, Pettinato C, Pietrobon F, Martinelli F, Fanti S. How do the more recent reconstruction algorithms affect the interpretation criteria of PET/CT Images?. Nucl Med Mol Imaging 2019;53:216-22.

41. Chilcott AK, Bradley KM, McGowan DR. Effect of a Bayesian penalized likelihood pet reconstruction compared with ordered subset expectation maximization on clinical image quality over a wide range of patient weights. Am J Roentgenol 2018;210:153-7.
42. Büther F, Vehren T, Schäfers KP, Schäfers M. Impact of data-driven respiratory gating in clinical PET. Radiology 2016;281:229-38.
43. Kesner AL. The relevance of data driven motion correction in diagnostic PET. Eur J Nucl Med Mol Imaging 2017;44:2326-7.
44. Kesner AL, Kuntner C. A new fast and fully automated software based algorithm for extracting respiratory signal from raw PET data and its comparison to other methods. Med Phys 2010;37:5550-9.
45. Bi WL, Hosny A, Schabath MB, Giger ML, Birkbak NJ, Mehrtash A, Allison T, Arnaout O, Abbosh C, Dunn IF. Artificial intelligence in cancer imaging: Clinical challenges and applications. CA Cancer J Clin 2019;69:127-57.
46. Schwyzer M, Ferraro DA, Muehlematter UJ, Curioni-Fontecedro A, Huellner MW, von Schulthess GK, Kaufmann PA, Burger IA, Messerli M. Automated detection of lung cancer at ultralow dose PET/CT by deep neural networks–Initial results. Lung Cancer 2018;126:170-3.
47. Lee JW, Lee SM. Radiomics in oncological PET/CT: clinical applications. Nucl Med Mol Imaging 2018;52:170-89.
48. Yip SS, Aerts HJ. Applications and limitations of radiomics. Phys Med Biol 2016;61:R150.
49. Aide N, Salomon T, Blanc-Fournier C, Grellard J, Levy C, Lasnon C. Implications of reconstruction protocol for histo-biological characterisation of breast cancers using FDG-PET radiomics. EJNMMI Res 2018;8:114-24.
50. Uribe CF, Mathotaarachchi S, Gaudet VC, Smith KC, Rosa-Neto P, Benard F, Black SE, Zukotynski K. Part 1: Introduction to machine learning in the nuclear medicine context. J Nucl Med 2019;60:451-8.
51. Badawi RD, Shi H, Hu P, Chen S, Xu T, Price PM, Ding Y, Spencer BA, Nardo L, Liu W. First human imaging studies with the EXPLORER total-body PET Scanner. J Nucl Med 2019;60:299-303.
52. Cherry SR, Badawi RD, Karp JS, Moses WW, Price P, Jones T. Total-body imaging: transforming the role of positron emission tomography. Sci Transl Med 2017;9:1-7.
53. Landelijke werkgroep Gastro-intestinale tumoren. Pancreascarcinoom, Landelijke richtlijn, Versie 2.0 2011.
54. Landelijke werkgroep Gastro Intestinale Tumoren. Colorectaal carcinoom, Landelijke richtlijn, Versie: 3.0 2014.

CHAPTER 13

13

Nederlandse samenvatting en toekomstperspectief

Auteur

Daniëlle Koopman[1,2]

Auteur Affiliaties
1: Afdeling Nucleaire geneeskunde, Isala, Zwolle, Nederland
2: Technisch Medisch Centrum, Universiteit Twente, Enschede, Nederland

Niet gepubliceerd

Introductie en doel

Positron emissie tomografie/computer tomografie (PET/CT) beeldvorming met fluor-18 (^{18}F) fluordeoxyglucose (FDG) speelt een belangrijke rol in het diagnostisch traject van patiënten met kanker [1-4]. In de dagelijkse praktijk worden FDG-PET/CT beelden visueel beoordeeld in combinatie met semi-kwantitatieve parameters zoals de 'standardised uptake value' (SUV). SUV metingen bieden een aanvulling op de visuele beoordeling en geven de mogelijkheid om een voorspelling te doen over de te verwachten respons op de behandeling en de prognose [5-7]. SUV metingen worden echter beïnvloed door allerlei biologische en technische factoren zoals de voorbereiding van de patiënt op het onderzoek, de data-acquisitie, de beeldreconstructie en beeldverwerking [8, 9]. Er wordt voortdurend gewerkt aan standaardisatie van de beeldvorming met PET om de semi-kwantitatieve vergelijking van PET scans tussen patiënten, scanners en ziekenhuizen te verbeteren. Dankzij de ontwikkeling van Europese richtlijnen door de European Association of Nuclear Medicine (EANM) en de start van het EARL accreditatieprogramma voor beeldvorming van tumoren met FDG-PET/CT is de variatie in semi-kwantificatie tussen FDG-PET scans de afgelopen jaren sterk gereduceerd [10-12].

PET beeldvorming heeft twee belangrijke beperkingen. De eerste is de lage spatiële resolutie, resulterend in een minder goede detectie van kleine laesies (<20 mm), met name die met een laag metabolisme [13, 14]. De tweede beperking is de systeem-sensitiviteit die leidt tot een relatief lage signaal-ruis verhouding (SNR) [15]. Sinds de klinische introductie van de PET scan voor het gehele lichaam 20 jaar geleden zijn er diverse technieken ontwikkeld, zoals het gebruik van time-of-flight (TOF) informatie in de beeldreconstructie, digitale PET (dPET) detectoren en nieuwe beeldreconstructietechnieken. Deze technieken zijn allen gericht op het verbeteren van de beeldkwaliteit en het verhogen van de diagnostische waarde van PET.

Het toevoegen van TOF informatie in het reconstructie-algoritme verbetert de PET beeldkwaliteit omdat TOF de SNR verhoogt bij eenzelfde hoeveelheid verzamelde foton-coïncidenties [16]. Diverse studies hebben aangetoond dat TOF-PET leidt tot een betere beeldkwaliteit met verbeterde detectie van kleine laesies, vooral bij patiënten met obesitas [17-19].

Een andere, recentere ontwikkeling is de introductie van dPET technologie. Sinds 2017 hebben drie fabrikanten (GE Healthcare, Philips Healthcare en Siemens Healthineers) de conventionele fotomultiplier buizen (PMTs) vervangen door silicium fotomultipliers (SiPMs) met digitale uitlezing [20-23]. dPET systemen hebben een betere tijdresolutie, hogere fotondetectie-efficiëntie, betere spatiële resolutie en een hogere systeem-sensitiviteit in vergelijking met conventionele PET (cPET) systemen [21-24]. Hierdoor bieden PET systemen met digitale detectoren in potentie een betere beeldkwaliteit met hogere SNRs en verbeterde detectie van kleine laesies.

Verder wordt bij FDG-PET tegenwoordig gebruik gemaakt van relatief grote voxels in de beeldreconstructie (typisch 4x4x4 mm^3) [18, 25]. Dit levert PET beelden met een acceptabel ruisniveau maar het versterkt ook het ‘partial volume effect’ (PVE) wat de detectie van kleine laesies beperkt. Nieuwe TOF-PET scanners hebben de mogelijkheid om beeldreconstructies met kleinere voxels te maken en dit zou de detectie van kleine laesies ook kunnen verbeteren.

Het **doel** van dit proefschrift is het evalueren van de impact van deze recente ontwikkelingen in PET technologie op de detectie van kleine laesies bij de beeldvorming van kanker. We onderzochten de invloed van *conventionele TOF-PET scanners* en *reconstructies met kleine voxels* op de detectie van kleine laesies in patiënten met longkanker en borstkanker. Verder bestudeerden we *digitale TOF-PET scanners* en bepaalden de invloed hiervan op SUV metingen, beeldkwaliteit en de detectie van kleine laesies bij patiënten met kanker. Ook onderzochten we de invloed van conventionele en digitale PET scanners op *Europese richtlijnen* en in het bijzonder op EARL accreditatie-eisen voor twee verschillende radionucliden.

Proefschrift overzicht

Deel I – PET standaardisatie

In **deel I** van dit proefschrift onderzochten we hoe recente ontwikkelingen in PET technologie en scanprotocollen ingezet kunnen worden om de PET beeldvorming verder te standaardiseren.

Hoofdstuk 2 geeft een overzicht van diverse technische ontwikkelingen waardoor de beeldvorming van kanker met PET/CT de afgelopen jaren is verbeterd. We hebben beschreven hoe de ontwikkeling van TOF, point spread functie (PSF) modellering en nieuwe beeldreconstructietechnieken met kleine voxels de detectie van kleine laesies met PET heeft verbeterd. Verder is beschreven dat klinisch voordeel wordt verwacht van dPET en geregulariseerde reconstructiemethoden. Ook zijn er andere technieken ontwikkeld voor specifieke problemen, zoals metaal-artefactreducties en correcties van ademhalingsbewegingen. Samen bieden al deze ontwikkelingen de mogelijkheid om de kwaliteit en kwantificatie van PET/CT beeldvorming bij patiënten met kanker te verbeteren. Drie onderwerpen die beschreven zijn in dit overzichtsartikel worden in meer detail uitgewerkt in de volgende hoofdstukken van dit proefschrift: de toediening van een gewichtsafhankelijke FDG-activiteit (Hoofdstuk 3), het gebruik van kleine voxel reconstructies (Hoofdstuk 8 en 9) en de invloed van digitale SiPMs op de PET beeldkwaliteit (Hoofdstuk 11).

Recent is aangetoond dat het gebruik van een FDG-activiteit die kwadratisch afhankelijk is van het gewicht van de patiënt, leidt tot een constante beeldkwaliteit bij patiënten [26]. **Hoofdstuk 3** bevat een praktische methode waarin beschreven wordt hoe deze kwadratische dosering met behulp van het NEMA beeldkwaliteit (IQ) fantoom in de klinische praktijk kan worden toegepast met inachtneming van Europese richtlijnen. Wij hebben deze methode toegepast op een moderne PET/CT scanner. De formule die we hebben afgeleid beschrijft de FDG-activiteit die toegediend moet worden aan individuele patiënten en voldoet aan recente inzichten omtrent patiënt-specifieke FDG doseringen. De methode beschreven in Hoofdstuk 3 is generiek toepasbaar op elk PET systeem bij gebruik van een specifieke beeldreconstructie en een vaste scantijd per bedpositie.

De huidige EANM richtlijnen voor beeldvorming van tumoren met FDG-PET zijn gebaseerd op cPET systemen en daarom was het onbekend of dPET systemen met digitale SiPMs, die potentieel een betere beeldkwaliteit bieden dan conventionele systemen, ook in staat zijn om te voldoen aan de EARL accreditatiestandaarden. In **Hoofdstuk 4** is dit onderzocht voor een recent geïntroduceerd TOF-dPET systeem. We hebben een fantoomstudie uitgevoerd op basis van de EANM richtlijnen. Met behulp van een NEMA IQ fantoom met zes bollen van verschillende grootte en gevuld met ^{18}F, hebben we voor elke bol de contrast recovery coëfficiënt (CRC) berekend. De CRC is gedefinieerd als de ratio tussen de gemeten (maximale of gemiddelde) ^{18}F concentratie in het PET beeld en de daadwerkelijke ^{18}F concentratie in de bol. We hebben aangetoond dat dit dPET systeem CRC waarden gaf die hoger dan de bovengrens van de EARL voorschriften lagen, met name voor de kleinste bollen. Om met dPET te voldoen aan de EARL standaard wordt daarom aangeraden om gebruik te maken van relatief grote 4x4x4 mm^3 voxels en een Gaussisch post-smoothing filter van 2 tot 4 mm.

Voor PET systemen die voldoen aan de EARL specificaties is de verwachting dat ze ook vergelijkbare semi-kwantitatieve resultaten opleveren. Dit hebben we onderzocht in **Hoofdstuk 5** door middel van FDG-PET scans van 50 patiënten met kanker waarbij gebruik werd gemaakt van een EARL-geaccrediteerde cPET en dPET scanner. Op basis van 128 FDG-positieve laesies met een gemiddelde grootte van 19±14 mm vonden we een gemiddeld SUV verschil (ΔSUV) van 6-8%, met in de meeste gevallen hogere SUV-waarden voor de dPET scanner. Verder vonden we reproduceerbaarheidscoëfficiënten van 27% (ΔSUV_{mean} en ΔSUV_{peak}) en 33% (ΔSUV_{max}) ($p<0{,}001$). De SUV variatie in deze studie werd voornamelijk veroorzaakt door een combinatie van drie factoren: een verschil in CRCs tussen het cPET en dPET systeem, de invloed van een langere FDG-opname in de patiënt en de test-hertest variatie. Deze studie laat zien dat EARL standaardisatie werkt.

In aanvulling op de veelgebruikte ^{18}F radionucliden, worden gallium-68 (^{68}Ga) gelabelde peptiden steeds vaker gebruikt voor PET beeldvorming, ook bij multicenter studies [27]. Er zijn echter nog geen EARL specificaties vastgesteld voor ^{68}Ga. In **Hoofdstuk 6** hebben we daarom de semi-kwantitatieve variatie van ^{68}Ga-PET geëvalueerd in een multicenter onderzoek. Acht centra in Europa met dertien verschillende PET/CT systemen hebben ^{18}F en ^{68}Ga acquisities uitgevoerd van zowel een cilindrisch fantoom als een NEMA IQ fantoom. Uit dit onderzoek bleek dat ^{68}Ga CRCs opleverde die onder de ondergrens van de huidige CRC standaarden voor ^{18}F liggen. Om praktische redenen wordt echter aanbevolen om toch de ^{18}F EARL-compatibele reconstructie-instellingen te gebruiken voor ^{68}Ga-PET kwantificatie in multicenter studies. Hierbij dient wel een cross-kalibratie uitgevoerd te worden tussen ^{68}Ga gemeten met de dosiskalibrator en met het PET systeem.

Deel II – PET optimalisatie

In **deel II** van dit proefschrift hebben we de waarde van drie recente ontwikkelingen in PET technologie onderzocht: TOF (Hoofdstuk 7), reconstructies met kleine voxels (Hoofdstuk 8, 9 en 10) en dPET (Hoofdstuk 10 en 11). We hebben de impact van deze technologieën op de PET beeldkwaliteit en detecteerbaarheid van kleine laesies onderzocht bij patiënten met kanker, in het bijzonder bij longkanker en borstkanker.

Als voorbeeld van het opsporen van kleine laesies zouden de nieuwste generatie TOF-cPET scanners mogelijk kunnen leiden tot een betere detectie van bijniermetastasen. Bovendien kan dit invloed hebben op de wijze waarop nucleair geneeskundigen de bijnieren beoordelen op FDG-PET scans, specifiek bij het onderscheiden van benigne en maligne bijnieren. In **Hoofdstuk 7** hebben we geanalyseerd wat de impact is van een conventionele TOF-PET/CT scanner bij gebruik van een EARL-compatibele reconstructie op de SUV van de bijnieren en op de bijnier-lever ratio bij 88 patiënten met longkanker. Met een SUV_{max} drempelwaarde van 3,7 werd een sensitiviteit van 96% en een specificiteit van eveneens 96% gevonden. Een drempelwaarde van 1,8 voor de bijnier-lever ratio leidde tot 91%

sensitiviteit en 97% specificiteit. In vergelijking met literatuur gebaseerd op een eerdere generatie niet-TOF PET scanners, leidt TOF-PET beeldvorming derhalve tot hogere SUVs voor benigne bijnieren terwijl het onderscheid tussen benigne en maligne bijnieren zeer nauwkeurig blijft. Klinische implementatie van TOF-PET vereist dus het gebruik van hogere SUV drempelwaarden om onderscheid te maken tussen benigne en maligne bijnieren, evenals aanpassingen in de visuele evaluatie door PET beoordelaars.

In Hoofdstuk 7 werd nog gebruik gemaakt van een EARL-compatibele PET reconstructie met relatief grote 4x4x4 mm^3 voxels. Met TOF-PET scanners kan het gebruik van reconstructies met kleine voxels (2x2x2 mm^3) de detectie van kleine laesies mogelijk verder verbeteren [18]. Dit is onderzocht in **Hoofdstuk 8** met een NEMA IQ fantoom (bol diameters 10-37 mm), een micro fantoom (bol diameters 4-8 mm) en bij 39 patiënten met longkanker, waarbij gebruik is gemaakt van dezelfde TOF-PET/CT scanner als in Hoofdstuk 7. Dit onderzoek toonde aan dat het gebruik van een reconstructie met kleine voxels leidde tot hogere CRCs en SNRs voor kleine fantoombollen (≤13 mm) met relatieve toenames tot 80% (CRC_{mean}) en 200% (CRC_{max}) voor de allerkleinste bollen. De gemiddelde toename in SNR_{mean} and SNR_{max} over alle fantoombollen was respectievelijk 12% en 39%. Verder bleek uit de evaluatie van 66 FDG-positieve laesies in de patiëntenstudie dat bij gebruik van kleine voxels de SUV_{mean} and SUV_{max} toenamen met respectievelijk 17% en 32% ($p<0,01$). Ook namen de gemiddelde en maximale SNR toe met respectievelijk 20% en 27% ($p<0,01$). Tot slot verkozen drie nucleair geneeskundigen de beelden met kleine voxels in 76% van de gevallen boven de beelden met de standaard voxels. Op basis van dit onderzoek kan geconcludeerd worden dat de detectie van kleine laesies met FDG-PET verbeterd kan worden door gebruik te maken van een PET reconstructie met kleine voxels.

In Hoofdstuk 8 werd echter nog niet gekeken naar de diagnostische consequenties en de potentiële klinische meerwaarde van deze kleine voxels reconstructies. Dit hebben we geëvalueerd in **Hoofdstuk 9** door middel van locoregionale lymfeklier-karakterisatie bij 69 patiënten met borstkanker waarbij gebruik is gemaakt van hetzelfde moderne TOF-PET/CT systeem als in Hoofdstuk 8. Twee nucleair geneeskundigen hebben alle scans visueel beoordeeld en semi-kwantitatieve parameters werden verzameld door het meten van de SUV_{max} en tumor-achtergrond ratio (TB_{ratio}). Op basis van de evaluatie van 61 benigne en 169 maligne okselklieren bleek dat bij gebruik van PET/CT beelden met kleine voxels de sensitiviteit van de visuele lymfeklier-karakterisatie verbeterde van 76% naar 89% ($p<0,001$). Dit biedt een hogere detectiegraad van maligne lymfeklieren. De PET reconstructie met kleine voxels leidde echter ook tot meer fout-positieve resultaten bij benigne lymfeklieren tijdens de visuele beoordeling. De diagnostische accuratesse bleek gelijk tussen standaard en kleine voxel PET (p=0,13). Kwantitatief gezien leidde de kleine voxel reconstructie wel tot toenames in SUV_{max} en TB_{ratio} van gemiddeld 40% ten opzichte van standaard voxel PET. Dit resulteerde in hogere SUV drempelwaarden van 1,8 naar 2,6 om onderscheid te kunnen maken tussen benigne en maligne locoregionale lymfeklieren. Dit impliceert dat PET beoordelaars hun referentiestandaarden visueel en kwantitatief moeten aanpassen wanneer ze PET beelden met kleine voxels beoordelen.

In de voorgaande hoofdstukken hebben we de waarde van kleine voxel reconstructies bepaald voor de cPET scanner. Een vergelijkbare impact van kleine voxel reconstructies kan worden verwacht bij gebruik van de dPET scanner en hier moet rekening mee gehouden worden bij het maken van eerlijke vergelijkingen tussen PET scanners. **Hoofdstuk 10** bevat een brief naar de editor van het tijdschrift EJNMMI met onze reactie op een recente publicatie van Fuentes-Ocampo et al.[28]. Zij vergeleken cPET en dPET bij 100 patiënten met kanker en ze rapporteerden een gemiddeld relatief SUV verschil van 35% bij 87 laesies, wat ze toewezen aan de dPET technologie. In deze studie werd echter een standaard voxel reconstructie (4x4x4 mm^3) gebruikt bij de cPET scanner terwijl ze kleinere (2x2x2 mm^3) voxels toepasten bij de dPET scanner. Dit verschil in voxelgrootte tussen de twee PET scanners werd niet meegenomen in de evaluatie van de resultaten. Dit maakt de vergelijking van de twee systemen oneerlijk aangezien het gebruik van een reconstructie met kleine voxels op een cPET systeem al leidt tot hogere SUVs, zoals aangetoond in Hoofdstuk 8 en Hoofdstuk 9. In onze brief aan de editor hebben we benadrukt dat de voxelgrootte van de PET beeldreconstructie een grote invloed heeft op SUV metingen, en dat hier rekening mee gehouden dient te worden in PET vergelijkingsstudies.

Tot slot hebben we in **Hoofdstuk 11** een prospectieve evaluatie uitgevoerd van de visuele en semi-kwantitatieve waarde van dPET scans ten opzichte van hoge-resolutie (HR) cPET scans bij 66 patiënten met verschillende soorten kanker. Bij gebruik van 2x2x2 mm^3 HR voxel reconstructies voor beide systemen leidden de dPET scans tot gemiddeld 25% hogere SUVs in vergelijking met cPET scans ($p<0.001$). Ook kregen de dPET beelden op basis van visuele beoordeling de voorkeur in de meerderheid van de scans (65%). Verder vonden we op de dPET scans 37 extra laesies in 27 patiënten (41%) en een hogere TNM stadiëring bij 13% van de patiënten. Vervolgonderzoek is nodig om de betere diagnostische performance van digitale PET te bevestigen.

Toekomstperspectief

Sinds de klinische introductie van PET scans voor oncologie beeldvorming 20 jaar geleden, zijn er diverse ontwikkelingen geïntroduceerd die de detectie van kleine laesies hebben verbeterd. In Hoofdstuk 2 hebben we reeds beschreven welke nieuwe hardware, software, acquisitie- en reconstructiemethoden geïntroduceerd zijn door de huidige generatie PET/CT scanners. In de volgende paragrafen worden nieuwe ontwikkelingen beschreven die in de toekomst PET standaardisatie kunnen beïnvloeden en de PET beeldkwaliteit en detectie van kleine laesies verder kunnen gaan verbeteren.

Invloed van nieuwe PET technologie op standaardisatie

EARL update

Een uitdaging in de standaardisatie van PET/CT is de ontwikkeling van nieuwe technieken die de beeldkwaliteit van PET verbeteren. In Hoofdstuk 4 hebben we aangetoond dat een beeldreconstructie met relatief grote voxels en een Gaussisch post-smoothing filter gebruikt moet worden om met een dPET scanner te kunnen voldoen aan EARL specificaties. Aangezien PET technologie zich voortdurend ontwikkelt, zijn in de toekomst nieuwe EARL specificaties nodig. Kaalep et al.[29] hebben in 2018 gekeken naar de prestaties van vier cPET systemen van drie grote leveranciers, voorzien van TOF en PSF modellering technologie en een voorstel gedaan voor een update van de EARL accreditatiespecificaties om hogere CRCs te kunnen behalen. De EARL organisatie heeft dit voorstel overgenomen in het accreditatieprogramma en voor volledige implementatie hiervan wordt een transitiefase van twee jaar verwacht. Verder is in de toekomst het gebruik van kleinere fantoombollen, bijvoorbeeld zoals beschikbaar in het microfantoom (Hoofdstuk 8), gewenst om nieuwe reconstructie-algoritmen ook bij kleinere bollen te kunnen vergelijken om zo de kwantificatie van laesies kleiner dan 10 mm tussen scanners te standaardiseren.

Nieuwe semi-kwantitatieve methoden

Een andere benadering waarmee de PET standaardisatie verder zou kunnen verbeteren is het gebruik van semi-kwantitatieve meetmethoden die beter reproduceerbaar en robuuster zijn dan SUV_{mean} and SUV_{max} [29]. Een voorbeeld hiervan is de SUV_{peak} parameter, gedefinieerd als de gemiddelde SUV in een vooraf bepaalde region-of-interest (ROI) van typisch 1 cm^3, gecentreerd in een tumorgedeelte met hoge opname van de radioactieve stof [30]. Dankzij de relatief grote ROI wordt de SUV_{peak} minder beïnvloed door ruis dan de SUV_{max}. Er zijn echter diverse definities voor de SUV_{peak} met verschillen in ROI vormen (kubus, circulair, bolvorming), locaties en groottes (7-17 mm) en gebruik hiervan geeft verschillende resultaten [31]. Ook is er met de meeste definities van SUV_{peak} momenteel sprake van een onderschatting van de SUV_{peak} bij laesies die kleiner zijn dan 1 cm, omdat de peak VOI groter is dan de laesie zelf [29].

Gestandaardiseerde en geoptimaliseerde reconstructies

Voor PET systemen met nieuwe technologie kunnen EARL-compatibele reconstructies gebruikt worden ten behoeve van gestandaardiseerde kwantificatie. Voor optimale visuele beoordeling wordt echter regelmatig de voorkeur gegeven aan een andere HR beeldreconstructie met hogere SNRs en betere laesiedetectie [11, 32]. Om aan wensen vragen te voldoen worden daarom regelmatig twee sets PET reconstructies gemaakt. Recent is een software pakket (EQ.PET, Siemens Healthineers) ontwikkeld dat één set PET beelden aanbiedt waarbij gestandaardiseerde SUVs gecombineerd worden met optimale HR beelden voor de visuele beoordeling [33, 34]. Het gebruik van deze aanpak kan zowel de reconstructietijd als de beeldinterpretatietijd reduceren [34]. De ontwikkelde methodiek is echter alleen beschikbaar voor scanners en reconstructiealgoritmen van de betreffende firma [33]. Voor de toekomst is een fabrikant-onafhankelijke oplossing wenselijk.

Verdere ontwikkeling van TOF-PET

Dankzij technische ontwikkelingen zoals de digitale SiPMs zijn de TOF prestaties van PET de afgelopen jaren aanzienlijk verbeterd [35]. De eerste TOF-PET/CT scanner (Gemini TF, Philips Healthcare) werd geïntroduceerd in 2006 met een coïncidentie tijdresolutie van 600 ps [16] terwijl het nieuwste digitale TOF-PET/CT systeem (Biograph Vision, Siemens Healthineers), geïntroduceerd in 2018, een tijdresolutie van 210 ps heeft [22]. Dit faciliteert het gebruik van een grotere matrix oftewel kleinere voxels [36], wat daardoor de detectie van kleine laesies in potentie verbetert, zoals aangetoond in Hoofdstukken 8 en 9. De winst in tijdresolutie kan ook gebruikt worden om de hoeveelheid radioactiviteit die wordt toegediend te verminderen en/of de scantijd te verkorten, terwijl de beeldkwaliteit behouden blijft. In de toekomst wordt een verdere verbetering van de tijdresolutie verwacht. Lecoq [37] beschreef recent een systematische aanpak door verschillende onderzoeksgroepen over de hele wereld met het doel een tijdresolutie van minder dan 100 ps te realiseren. Zelfs een TOF resolutie van 10 ps wordt mogelijk geacht door Lecoq [37], hoewel dit een extreme uitdaging zal zijn. Als dergelijke technologie in de toekomst beschikbaar komt in de klinische praktijk, zou dit een paradigmaverschuiving in PET beeldvorming kunnen veroorzaken omdat dit tot grote verbeteringen in systeemsensitiviteit zou leiden. Dit zou vervolgens gebruikt kunnen worden voor bijvoorbeeld forse reducties in de stralingsdosis, verkorting van de scantijd en/of het verder verhogen van de PET beeldkwaliteit [37]. Ook zou dit mogelijkheden kunnen bieden voor PET-gestuurde biopsieën en PET-doorlichting tijdens interventieprocedures.

Nieuwe reconstructiemethoden

De verwachting is dat in de nabije toekomst nieuwe beeldreconstructiemethoden de PET beeldkwaliteit en detectie van kleine laesies verder gaan verbeteren. GE Healthcare heeft recent een Bayesiaanse penalized likelihood reconstructie algoritme (BSREM) geïntroduceerd die leidt tot een betere beeldresolutie en vermindering van de ruis in het PET beeld ten opzichte van het veelgebruikte Ordered Subset Expectation Maximization (OSEM) algoritme [38]. Het afgelopen jaar is met FDG-PET/CT scans van patiënten met verschillende soorten kanker aangetoond dat BSREM een verbeterde beeldkwaliteit met meer detail en een betere zichtbaarheid van tumoren oplevert ten opzichte van OSEM [39, 40]. Verder hebben Chilcott et al.[41] onlangs beschreven dat het gebruik van BSREM resulteert in een meer consistente beeldkwaliteit en SNR in de lever in vergelijking met OSEM, wat vooral ten goede komt aan de beeldvorming van obese patiënten. De verwachting is dat andere fabrikanten ook Bayesiaanse reconstructiemethoden zullen introduceren.

Een andere technologie die de PET beeldkwaliteit verder zou kunnen verbeteren is de datagedreven bewegingscorrectie [42, 43]. Deze methode extraheert bewegingsinformatie direct vanuit het PET acquisitiesignaal. In vergelijking met fysieke bewegingsmetingen zoals beschreven in Hoofdstuk 2 heeft datagedreven bewegingscorrectie een aantal voordelen: het is gebruikersonafhankelijk en kan volledig automatisch geïmplementeerd worden als softwareoplossing waarbij er geen aanpassingen in het acquisitieprotocol noodzakelijk zijn [44].

Kunstmatige intelligentie

Een opkomend vakgebied in de medische beeldvorming is de toepassing van kunstmatige intelligentie (AI), in het bijzonder machine learning en deep learning, door het automatisch kwantificeren van patronen. AI kan van waarde zijn in de detectie, karakterisatie en monitoring van tumoren [45]. Een voorbeeld hiervan is de computergestuurde detectie van longnoduli met PET/CT. In 2018 lieten Schwyzer et al.[46] zien dat machine- en deep learning algoritmes vrijwel volledig geautomatiseerde detectie van longkanker mogelijk maken, zelfs bij een tien- tot dertigvoudige dosisreductie. Dit zou kunnen leiden tot nieuwe toepassingen voor FDG-PET. AI programma´s worden ook gebruikt om kwantitatieve kenmerken uit medische beelden te extraheren door middel van data-karakterisatie algoritmes

[47]. Dit staat bekend onder de term radiomics. In de afgelopen jaren is aangetoond dat dergelijke kenmerken een goede weergave vormen van de intra-tumorale heterogeniteit wat gerelateerd blijkt te zijn aan tumorkenmerken [48]. Zodoende zouden met radiomics in potentie unieke ziektekarakteristieken ontdekt kunnen worden met toegevoegde diagnostische en prognostische waarde.

Voor de implementatie van radiomics is zowel standaardisatie als optimalisatie van PET beelden vereist. Aide et al.[49] toonden recentelijk aan dat de karakterisatie van borstkanker HR PET beelden vereist, met name wanneer er gezocht wordt naar relaties tussen tumorheterogeniteit op FDG-PET door middel van radiomics en histologische karakteristieken van de tumor. Tegelijkertijd blijft ook PET standaardisatie essentieel aangezien verschillen tussen scanners, evenals verschillen in acquisitie- en reconstructieprotocollen, de kwantitatieve kenmerken van tumoren en dus uitkomsten kunnen beïnvloeden [50].

Total-body PET

Het afgelopen jaar werd de bouw van ’s werelds eerste total-body (TB) PET/CT scanner afgerond [51]. Terwijl klinisch beschikbare PET scanners een axiaal scanveld hebben van typisch 15 tot 25 cm, heeft dit TB PET systeem een axiaal scanveld van 194 cm. Dit maakt visualisatie van het gehele menselijk lichaam mogelijk met een enkele acquisitie. Verder wordt door het geometrisch rendement van deze TB PET scanner het merendeel van de uitgezonden fotonen gedetecteerd, wat een factor 40 aan winst oplevert in effectieve systeemsensitiviteit en een toename van een factor 6 in SNR in vergelijking met de huidige klinische PET scanners [52]. Dit kan de beeldkwaliteit verbeteren (**Figuur 1**) of gebruikt worden om de scantijd en/of benodigde hoeveelheid radioactiviteit te reduceren. Verder biedt het systeem de mogelijkheid om dynamische opnames van het gehele lichaam te maken met een hoge temporele resolutie. Ondertussen genereert TB PET ook de nodige uitdagingen, voornamelijk gericht op de bouw van de scanner en de kosten die hiermee gepaard gaan [52]. Toekomstige studies zullen moeten aantonen wat de waarde van het TB systeem zal zijn [51].

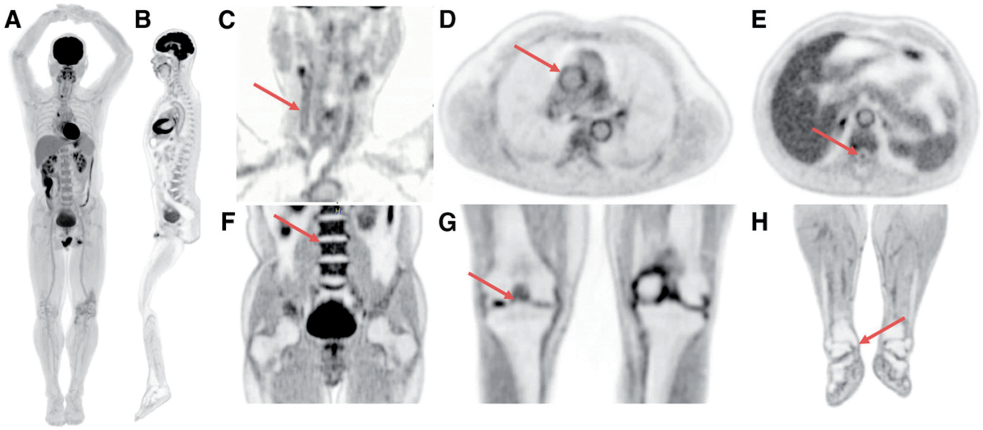

Figuur 1 Total-body PET scan van een gezonde vrijwilliger, met een scan van het gehele lichaam in coronaal (A) and sagittale oriëntatie (B), een beeld van het hoofd/hals gebied met de wanden van de halsslagaders (C), een beeld van de thorax inclusief de wanden van de grote vaten (D), een beeld van het abdomen en het wervelkanaal (E), een beeld van het abdomen/bekken gebied inclusief wervels (F), een beeld van de knieën met osteofyten (G) en een beeld van de onderste extremiteiten met een gedetailleerd beeld van de mediale tibiale malleolus (H). Beelden overgenomen uit [51]

Klinische implementatie en validatie van nieuwe PET technologie

In dit proefschrift hebben we aangetoond dat nieuwe PET technologie heeft geleid tot een betere beeldkwaliteit en verbeterde detectie van kleine laesies. Voor nucleair geneeskundigen kunnen deze ontwikkelingen het beoordelen van PET beelden echter ook gecompliceerder maken. Met een verbeterde beeldkwaliteit bevatten beelden ook meer details die geïnterpreteerd moeten worden en daarbij ontstaat een risico op fout-positieve bevindingen (Hoofdstuk 7 en Hoofdstuk 9). Nucleair geneeskundigen moeten hun referentiestandaarden aanpassen en ook hogere SUV drempelwaarden gebruiken om onderscheid te kunnen maken tussen benigne en maligne laesies. Uiteindelijk is de vraag welke beeldkwaliteit noodzakelijk is voor de klinische vraag. Dit kan afhangen van het doel van de beeldvorming, bijvoorbeeld of de PET scan wordt gemaakt voor tumordetectie, TNM stadiëring, beoordeling van de respons op een behandeling of follow-up onderzoek.

Nieuwe PET technologie kan leiden tot een paradigmaverschuiving in de beeldvorming van patiënten met kanker. Allereerst is het aannemelijk dat beeldvorming met PET gemakkelijker inzetbaar en kosten-effectiever wordt aangezien FDG-PET scans met een beeldkwaliteit die voldoet aan de EANM richtlijnen momenteel al gemaakt kunnen worden met een beperkte hoeveelheid radioactiviteit en een totale scantijd van 5 tot 10 minuten [22]. Met verdere technologische ontwikkelingen zoals beschreven in dit hoofdstuk is het waarschijnlijk dat deze scantijden in de toekomst nog verder gereduceerd kunnen worden. Aan de andere kant kan hoge-resolutie PET nieuwe toegevoegde waarde bieden in de karakterisatie en stadiëring van een aantal typen tumoren, zoals het pancreascarcinoom en colorectale tumoren, waar bij oudere generaties PET scanners de diagnostische waarde van PET beperkt was [53, 54]. Een illustratie van de potentie van ultra-HR dPET is te zien in **Figuur 2** waar een FDG-PET scan wordt getoond van een patiënt met een pancreascarcinoom met uitzaaiingen in de lever. Met een ultra-HR reconstructie van de digitale PET scan en extra lange scantijd (**Figuur 2C)** zijn meerdere kleine levermetastasen zichtbaar die niet zichtbaar zijn in **Figuur 2A** (standaard EARL scan) en slechts matig zichtbaar in **Figuur 2B** (HR reconstructie met een standaard scantijd).

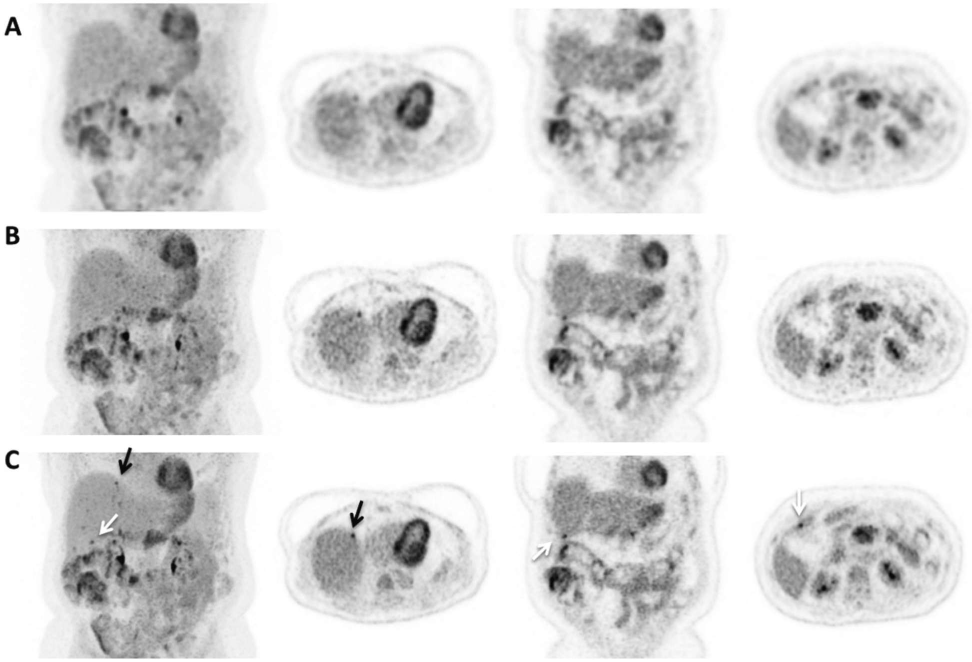

Figuur 2 FDG-PET beelden van een patiënt met pancreascarcinoom en meerdere bewezen levermetastasen. **A:** dPET scan die voldoet aan de EARL standaard, zonder zichtbare afwijkingen in de lever. **B:** HR dPET scan met optimale reconstructie-instellingen (zoals beschreven in Hoofdstuk 11), waarbij de afwijkingen in de lever matig zichtbaar zijn. **C:** dPET scan gemaakt met een drie keer zo lange scantijd en gereconstrueerd met ultra-HR instellingen waarbij meerdere levermetastasen duidelijk zichtbaar zijn (pijlen)

Referenties

1. Bar-Shalom R, Yefremov N, Guralnik L, Gaitini D, Frenkel A, Kuten A, Altman H, Keidar Z, Israel O. Clinical performance of PET/CT in evaluation of cancer: additional value for diagnostic imaging and patient management. J Nucl Med 2003;44:1200-9.
2. Branstetter IV BF, Blodgett TM, Zimmer LA, Snyderman CH, Johnson JT, Raman S, Meltzer CC. Head and neck malignancy: is PET/CT more accurate than PET or CT alone?. Radiology 2005;235:580-6.
3. Rosen EL, Eubank WB, Mankoff DA. FDG PET, PET/CT, and breast cancer imaging. Radiographics 2007;27:S229.
4. Fischer B, Lassen U, Mortensen J, Larsen S, Loft A, Bertelsen A, Ravn J, Clementsen P, Høgholm A, Larsen K. Preoperative staging of lung cancer with combined PET–CT. N Engl J Med 2009;361:32-9.
5. Lin C, Itti E, Haioun C, Petegnief Y, Luciani A, Dupuis J, Paone G, Talbot J, Rahmouni A, Meignan M. Early 18F-FDG PET for prediction of prognosis in patients with diffuse large B-cell lymphoma: SUV-based assessment versus visual analysis. J Nucl Med 2007;48:1626-32.
6. de Geus-Oei L, van der Heijden, Henricus FM, Corstens FH, Oyen WJG. Predictive and prognostic value of FDG-PET in nonsmall-cell lung cancer: a systematic review. Cancer 2007;110:1654-64.
7. Huang W, Zhou T, Ma L, Sun H, Gong H, Wang J, Yu J, Li B. Standard uptake value and metabolic tumor volume of 18 F-FDG PET/CT predict short-term outcome early in the course of chemoradiotherapy in advanced non-small cell lung cancer. Eur J Nucl Med Mol Imaging 2011;38:1628.
8. Vriens D, Visser EP, de Geus-Oei L, Oyen WJG. Methodological considerations in quantification of oncological FDG PET studies. Eur J Nucl Med Mol Imaging 2010;37:1408-25.
9. Adams MC, Turkington TG, Wilson JM, Wong TZ. A systematic review of the factors affecting accuracy of SUV measurements. Am J Roentgenol 2010;195:310-20.
10. Boellaard R, O'Doherty M,J., Weber WA, Mottaghy FM, Lonsdale MN, Stroobants SG, Oyen WJG, Kotzerke J, Hoekstra OS, Pruim J. FDG PET and PET/CT: EANM procedure guidelines for tumour PET imaging: version 1.0. Eur J Nucl Med Mol Imaging 2010;37:181-200.
11. Boellaard R, Delgado-Bolton R, Oyen WJG, Giammarile F, Tatsch K, Eschner W, Verzijlbergen FJ, Barrington SF, Pike LC, Weber WA. FDG PET/CT: EANM procedure guidelines for tumour imaging: version 2.0. Eur J Nucl Med Mol Imaging 2015;42:328-54.
12. Kaalep A, Sera T, Oyen WJG, Krause BJ, Chiti A, Liu Y, Boellaard R. EANM/EARL FDG-PET/CT accreditation - summary results from the first 200 accredited imaging systems. Eur J Nucl Med Mol Imaging 2018;45:412-22.

13. Takamochi K, Yoshida J, Murakami K, Niho S, Ishii G, Nishimura M, Nishiwaki Y, Suzuki K, Nagai K. Pitfalls in lymph node staging with positron emission tomography in non-small cell lung cancer patients. Lung Cancer 2005;47:235-42.
14. Berg E, Cherry SR. Innovations in instrumentation for positron emission tomography. Semin Nucl Med 2018;48:311-31.
15. Budinger TF. PET instrumentation: what are the limits?. Semin Nucl Med 1998;28:247-67.
16. Surti S, Kuhn A, Werner ME, Perkins AE, Kolthammer J, Karp JS. Performance of Philips Gemini TF PET/CT scanner with special consideration for its time-of-flight imaging capabilities. J Nucl Med 2007;48:471-80.
17. Kadrmas DJ, Casey ME, Conti M, Jakoby BW, Lois C, Townsend DW. Impact of time-of-flight on PET tumor detection. J Nucl Med 2009;50:1315-23.
18. Conti M. Focus on time-of-flight PET: the benefits of improved time resolution. Eur J Nucl Med Mol Imaging 2011;38:1147-57.
19. Akamatsu G, Ishikawa K, Mitsumoto K, Taniguchi T, Ohya N, Baba S, Abe K, Sasaki M. Improvement in PET/CT image quality with a combination of point-spread function and time-of-flight in relation to reconstruction parameters. J Nucl Med 2012;53:1716-22.
20. Frach T, Prescher G, Degenhardt C, de Gruyter R, Schmitz A, Ballizany R. The digital silicon photomultiplier—Principle of operation and intrinsic detector performance. IEEE Nucl Sci Symp Conf Rec 2009:1959-65.
21. Hsu DF, Ilan E, Peterson WT, Uribe J, Lubberink M, Levin CS. Studies of a next-generation silicon-photomultiplier–based time-of-flight PET/CT system. J Nucl Med 2017;58:1511-8.
22. van Sluis JJ, de Jong J, Schaar J, Noordzij W, van Snick P, Dierckx R, Borra R, Willemsen A, Boellaard R. Performance characteristics of the digital Biograph Vision PET/CT system. J Nucl Med 2019;60:1031-6.
23. Rausch I, Ruiz A, Valverde-Pascual I, Cal-González J, Beyer T, Carrio I. Performance evaluation of the Vereos PET/CT system according to the NEMA NU2-2012 standard. J Nucl Med 2019;60:561-7.
24. Slomka PJ, Pan T, Germano G. Recent advances and future progress in PET instrumentation. Semin Nucl Med 2016;46:5-19.
25. Kolthammer JA, Su K, Grover A, Narayanan M, Jordan DW, Muzic RF. Performance evaluation of the Ingenuity TF PET/CT scanner with a focus on high count-rate conditions. Phys Med Biol 2014;59:3843-59.
26. de Groot E,H., Post N, Boellaard R, Wagenaar NRL, Willemsen ATM, van Dalen J,A. Optimized dose regimen for whole-body FDG-PET imaging. EJNMMI Res 2013;3:63-72.
27. Perera M, Papa N, Christidis D, Wetherell D, Hofman MS, Murphy DG, Bolton D, Lawrentschuk N. Sensitivity, specificity, and predictors of positive 68Ga–prostate-specific membrane antigen positron emission tomography in advanced prostate cancer: a systematic review and meta-analysis. Eur Urol 2016;70:926-37.

28. Fuentes-Ocampo F, López-Mora DA, Flotats A, Paillahueque G, Camacho V, Duch J, Fernández A, Domènech A, Estorch M, Carrió I. Digital vs. analog PET/CT: intra-subject comparison of the SUVmax in target lesions and reference regions. Eur J Nucl Med Mol Imaging 2019;46:1745-50.
29. Kaalep A, Sera T, Rijnsdorp S, Yaqub M, Talsma A, Lodge MA, Boellaard R. Feasibility of state of the art PET/CT systems performance harmonisation. Eur J Nucl Med Mol Imaging 2018;45:1344-61.
30. Wahl RL, Jacene H, Kasamon Y, Lodge MA. From RECIST to PERCIST: evolving considerations for PET response criteria in solid tumors. J Nucl Med 2009;50:122S.
31. Vanderhoek M, Perlman SB, Jeraj R. Impact of the definition of peak standardized uptake value on quantification of treatment response. J Nucl Med 2012;53:4-11.
32. Lasnon C, Desmonts C, Quak E, Gervais R, Do P, Dubos-Arvis C, Aide N. Harmonizing SUVs in multicentre trials when using different generation PET systems: prospective validation in non-small cell lung cancer patients. Eur J Nucl Med Mol Imaging 2013;40:985-96.
33. Quak E, Le Roux P, Hofman MS, Robin P, Bourhis D, Callahan J, Binns D, Desmonts C, Salaun P, Hicks RJ. Harmonizing FDG PET quantification while maintaining optimal lesion detection: prospective multicentre validation in 517 oncology patients. Eur J Nucl Med Mol Imaging 2015;42:2072-82.
34. Lasnon C, Salomon T, Desmonts C, Dô P, Oulkhouir Y, Madelaine J, Aide N. Generating harmonized SUV within the EANM EARL accreditation program: software approach versus EARL-compliant reconstruction. Ann Nucl Med 2017;31:125-34.
35. Degenhardt C, Rodrigues P, Trindade A, Zwaans B, Mülhens O, Dorscheid R, Thon A, Salomon A, Frach T. Performance evaluation of a prototype positron emission tomography scanner using digital photon counters (DPC). IEEE Nucl Sci Symp Conf Rec 2012.
36. Conti M, Bendriem B. The new opportunities for high time resolution clinical TOF PET. Clin Transl Imaging 2019;7:139-47.
37. Lecoq P. Pushing the limits in time-of-flight PET imaging. IEEE Transactions on Radiation and Plasma Medical Sciences 2017;1:473-85.
38. Teoh EJ, McGowan DR, Macpherson RE, Bradley KM, Gleeson FV. Phantom and clinical evaluation of the Bayesian penalized likelihood reconstruction algorithm Q. Clear on an LYSO PET/CT system. J Nucl Med 2015;56:1447-52.
39. Messerli M, Stolzmann P, Egger-Sigg M, Trinckauf J, D'Aguanno S, Burger IA, von Schulthess GK, Kaufmann PA, Huellner MW. Impact of a Bayesian penalized likelihood reconstruction algorithm on image quality in novel digital PET/CT: clinical implications for the assessment of lung tumors. EJNMMI Phys 2018;5:27-39.
40. Matti A, Lima GM, Pettinato C, Pietrobon F, Martinelli F, Fanti S. How do the more recent reconstruction algorithms affect the interpretation criteria of PET/CT Images?. Nucl Med Mol Imaging 2019;53:216-22.

41. Chilcott AK, Bradley KM, McGowan DR. Effect of a Bayesian penalized likelihood pet reconstruction compared with ordered subset expectation maximization on clinical image quality over a wide range of patient weights. Am J Roentgenol 2018;210:153-7.
42. Büther F, Vehren T, Schäfers KP, Schäfers M. Impact of data-driven respiratory gating in clinical PET. Radiology 2016;281:229-38.
43. Kesner AL. The relevance of data driven motion correction in diagnostic PET. Eur J Nucl Med Mol Imaging 2017;44:2326-7.
44. Kesner AL, Kuntner C. A new fast and fully automated software based algorithm for extracting respiratory signal from raw PET data and its comparison to other methods. Med Phys 2010;37:5550-9.
45. Bi WL, Hosny A, Schabath MB, Giger ML, Birkbak NJ, Mehrtash A, Allison T, Arnaout O, Abbosh C, Dunn IF. Artificial intelligence in cancer imaging: Clinical challenges and applications. CA Cancer J Clin 2019;69:127-57.
46. Schwyzer M, Ferraro DA, Muehlematter UJ, Curioni-Fontecedro A, Huellner MW, von Schulthess GK, Kaufmann PA, Burger IA, Messerli M. Automated detection of lung cancer at ultralow dose PET/CT by deep neural networks–Initial results. Lung Cancer 2018;126:170-3.
47. Lee JW, Lee SM. Radiomics in oncological PET/CT: clinical applications. Nucl Med Mol Imaging 2018;52:170-89.
48. Yip SS, Aerts HJ. Applications and limitations of radiomics. Phys Med Biol 2016;61:R150.
49. Aide N, Salomon T, Blanc-Fournier C, Grellard J, Levy C, Lasnon C. Implications of reconstruction protocol for histo-biological characterisation of breast cancers using FDG-PET radiomics. EJNMMI Res 2018;8:114-24.
50. Uribe CF, Mathotaarachchi S, Gaudet VC, Smith KC, Rosa-Neto P, Benard F, Black SE, Zukotynski K. Part 1: Introduction to machine learning in the nuclear medicine context. J Nucl Med 2019;60:451-8.
51. Badawi RD, Shi H, Hu P, Chen S, Xu T, Price PM, Ding Y, Spencer BA, Nardo L, Liu W. First human imaging studies with the EXPLORER total-body PET Scanner. J Nucl Med 2019;60:299-303.
52. Cherry SR, Badawi RD, Karp JS, Moses WW, Price P, Jones T. Total-body imaging: transforming the role of positron emission tomography. Sci Transl Med 2017;9:1-7.
53. Landelijke werkgroep Gastro-intestinale tumoren. Pancreascarcinoom, Landelijke richtlijn, Versie 2.0 2011.
54. Landelijke werkgroep Gastro Intestinale Tumoren. Colorectaal carcinoom, Landelijke richtlijn, Versie: 3.0 2014.

APPENDICES

List of abbreviations

^{18}F	Fluor-18
3D	3-dimensional
^{68}Ga	Gallium-68
^{89}Zr	^{89}Zirconium
AI	Artificial intelligence
AL ratio	Adrenal-to-liver ratio
APD	Avalanche photodiodes
A_{ref}	Reference FDG activity
AUC	Area under the curve
BGO	Bismuth-germinate
BPL	Bayesian penalized likelihood
BSO	Bismuth-silicate
BSREM	Bayesian penalized likelihood reconstruction algorithm
B_{true}	True FDG activity concentration in the phantom background
C_{bg}	Mean FDG concentration measured in the phantom background
CBM	Continuous bed motion
CI	Confidence interval
$C_{measured}$	Measured FDG concentration in the sphere
COV	Coefficient of variation
COV_{max}	Maximal COV
cPET	Conventional PET
CRC	Contrast recovery coefficient
CRC_{max}	Maximum CRC
CRC_{mean}	Average CRC
CT	Computed tomography
C_{true}	True FDG concentration in the sphere
dPET	Digital PET
EANM	European Association of Nuclear Medicine
EARL	EANM research ltd
EUS-FNA	Endoscopic ultrasound-guided fine-needle aspiration
FDG	Fluor-18 fluordeoxyglucose
FOV	Field-of-view
FU	Follow up
FWHM	Full width half maximum
HR	High-resolution
IEC	International electrotechnical commission
IQ phantom	NEMA NU2-2001 image quality phantom

LBR	Lesion-to-background ratio
LOR	Line-of-response
LSO	Lutetium-oxyorthosilicate
LYSO	Lutetium-yttrium oxyorthosilicate
MAP	Maximum-a-posteriori
METC	Medical ethical committee
MIP	Maximum intensity projection
MLAA	Maximum likelihood of activity and attenuation
MLEM	Maximum likelihood estimation maximization
MRI	Magnetic resonance imaging
MTV	Metabolic tumour volume
NaI	Sodium-iodine
NECR	Noise equivalent count rate
NEMA	National Electrical Manufacturers Association
NM	Nuclear medicine
NSCLC	Non-small cell lung cancer
OSEM	Ordered subset expectation maximization
PET	Positron emission tomography
PMT	Photomultiplier tube
PSF	Point spread function
PSMA	Prostate-specific membrane antigen
PVE	Partial volume effect
RC	Recovery coefficient (Chapter 4 and 6)
RC	Repeatability coefficient (Chapter 5)
RC_{max}	Maximum activity concentration RC
RC_{mean}	Mean activity concentration RC
RC_{peak}	Peak activity concentration RC
ROC	Receiver operator curve
ROI	Region of interest
SD	Standard deviation
SD_{bg}	SD in the background of reconstructed images
SiPM	Silicon photomultiplier
SIRT	Selective internal radiation therapy
Small voxels	2x2x2 mm^3 voxels
SNR	Signal-to-noise ratio
SNR_{max}	Maximum SNR
SNR_{mean}	Average SNR
SPECT	Single-photon emission computed tomography
SR	Standard resolution
Standard voxels	4x4x4 mm^3 voxels

S_{true}	True FDG activity concentration in the phantom spheres
SUV	Standardised uptake value
$SUV_{background}$	Background SUV
SUV_{bkg}	Background SUV
SUV_{liver}	Average SUV in the liver
SUV_{max}	Maximum SUV
SUV_{mean}	Average SUV
SUV_{peak}	Peak SUV
T_a	Time of acquisition
TB	Total-body
TB_{ratio}	Ratio between SUV_{max} and $SUV_{background}$
T_m	Time of measurement
T_{min}	Minimal scan duration per bed position
TOF	Time-of-flight
UTE	Ultra-short echo time
VOI	Volume of interest
wCV	Within-subject coefficient of variation
w_{ref}	Reference body weight
ZTE	Zero echo time
ΔT	Time between FDG administration and start PET acquisition
ΔT_{cPET}	Time between FDG administration and start cPET acquisition
ΔT_{dPET}	Time between FDG administration and start dPET acquisition

List of publications

Peer-reviewed publications

In this thesis

1. **Koopman D**, van Dalen JA, Lagerweij MCM, Arkies H, de Boer J, Oostdijk AHJ, Slump CH, Jager PL. Improving the detection of small lesions using a state-of-the-art time-of-flight PET/CT system and small-voxel reconstructions. J Nucl Med Technol 2015;43:21-7. *18 citations*

2. **Koopman D**, van Dalen JA, Stigt JA, Slump CH, Knollema S, Jager PL. Current generation time-of-flight 18F-FDG PET/CT provides higher SUVs for normal adrenal glands, while maintaining an accurate characterization of benign and malignant glands. Ann Nucl Med 2016;30:145-52. *7 citations*

3. **Koopman D**, van Osch JAC, Jager PL, Tenbergen CJA, Knollema S, Slump CH, van Dalen JA. Technical note: how to determine the FDG activity for tumour PET imaging that satisfies European guidelines. EJNMMI Phys 2016;3:22-31. *4 citations*

4. van der Vos CS, **Koopman D**, Rijnsdorp S, Arends AJ, Boellaard R, van Dalen JA, Lubberink M, Willemsen ATM, Visser EP. Quantification, improvement, and harmonization of small lesion detection with state-of-the-art PET. Eur J Nucl Med Mol Imaging 2017;44;4-16. *50 citations*

5. **Koopman D**, Koerkamp MG, Jager PL, Arkies H, Knollema S, Slump CH, Sanches PG, van Dalen JA. Digital PET compliance to EARL accreditation specifications. EJNMMI Phys 2017;4:9-14. *3 citations*

6. **Koopman D**, van Dalen JA, Arkies H, Oostdijk AH, Francken AB, Bart J, Slump CH, Knollema S, Jager PL. Diagnostic implications of a small-voxel reconstruction for loco-regional lymph node characterization in breast cancer patients using FDG-PET/CT. EJNMMI Res 2018;8:3-12. *5 citations*

7. **Koopman D**, Jager PL, van Dalen JA. Small-voxel reconstructions significantly influence SUVs in PET imaging. Eur J Nucl Med Mol Imaging 2019;46:1751-1752. *1 citation*

8. Huizing DMV, **Koopman D**, van Dalen JA, Gotthardt M, Boellaard R, Sinaasappel M, Stokkel MPM, de Wit-van der Veen BJ. Multicentre Quantitative ^{68}Ga PET/CT Performance Harmonisation. *Paper accepted for publication in EJNMMI Physics*

Not in this thesis

1. **Koopman D**, van Dalen JA, Slump CH, Lots D, Timmer JR, Jager PL. Impact of image processing in the detection of ischaemia using CZT-SPECT/CT. Nucl Med Commun 2015;36:60-8. *4 citations*

2. Schreuder N, **Koopman D**, Jager PL, Kosterink JGW, van Puijenbroek E. Adverse events of diagnostic radiopharmaceuticals: a systematic review. Semin Nucl Med 2019;49:382-410.

Non-peer reviewed articles

1. **Koopman D**, van Dalen JA, Jager PL. Improved detection of a metastatic adrenal gland using FDG PET with small voxels. Bijzondere casus, Tijdschrift voor Nucleaire Geneeskunde, 2014;36.

2. **Koopman D,** PL Jager, van Dalen JA. Digitale PET: het recept voor lage dosering en snel scannen? Opinieartikel, MT Integraal, 2018.

Conference proceedings

1. **Koopman D**, van Dalen JA, Slump CH, Lots D, Vink D, Timmer JR, Jager PL. Impact of image processing in the detection of ischaemia using CZT-SPECT/CT. Poster presentation at the International Conference on Nuclear Cardiology and Cardiac CT, 2013, Berlin

2. **Koopman D**, van Dalen JA, Arkies H, de Boer J, Oostdijk AHJ, Slump CH, Jager PL. Improving the detection of small lesions with FDG-PET using a small voxel reconstruction. Poster presentation at the annual meeting of the European Association of Nuclear Medicine 2014, Gotheburg

3. **Koopman D,** van Dalen JA, van Osch JAC, Slump CH, Jager PL. Optimizing FDG-PET tumour imaging on a state-of-the-art PET/CT system using both EANM/EARL guidelines and a quadratic body-weight dependent dose regimen. Oral presentation at the annual meeting of the European Association of Nuclear Medicine 2014, Gotheburg

4. **Koopman D**, van Dalen JA, Slump CH, Jager PL. Clinical impact of a state-of-the-art time-of-flight PET/CT scanner for the detection and staging of adrenal glands. Oral presentation at the scientific meeting of the Dutch society of Nuclear Medicine 2014, Nijmegen

5. **Koopman D,** van Dalen JA, van Osch JAC, Slump CH, Jager PL. Verbeterde detectie van intra-thoracale lymfekliermetastasen met nieuwe PET/CT scanner in Isala. Poster presentation at the annual scientific research evening (Wetenschapsavond) of Isala, 2014, Zwolle

6. **Koopman D,** van Dalen JA, Knollema S, Slump CH, Jager PL. High detection performance and accurate staging of adrenal glands using state-of-the-art PET/CT. Poster presentation at the annual meeting of the Society of Nuclear Medicine and Molecular Imaging 2015, Baltimore

7. **Koopman D,** van Dalen JA, Knollema S, Slump CH, Jager PL. Impact of a high-resolution reconstruction using state-of-the-art PET/CT for intra-thoracic lymph node staging. Poster presentation at the annual meeting of the Society of Nuclear Medicine and Molecular Imaging 2015, Baltimore

8. **Koopman D**, Lots D, Francken AB, Arkies H, Jager PL, Slump CH, van Dalen JA. Reliable I-125 seed localization after neo-adjuvant chemotherapy to identify breast lesions in combination with sentinel node biopsy. Poster presentation at the annual meeting of the European Association of Nuclear Medicine 2015, Hamburg

9. van Dalen JA, **Koopman D**, van Osch JAC, Groot Koerkamp ML, Sanches PG, Jager PL. Imaging performance of a digital PET scanner: a comparison to analog systems. Poster presentation at the annual meeting of the Dutch medical physicist society 2016, Woudschoten

10. **Koopman D,** van Dalen JA, Arkies H, Francken AB, Bart J, Knollema S, Slump CH, Jager PL. A small voxel FDG-PET/CT reconstruction improves the visual evaluation of axillary lymph nodes in patients with breast cancer. Poster presentation at the annual meeting of the Society of Nuclear Medicine and Molecular Imaging 2016, San Diego

11. **Koopman D**, Groot Koerkamp ML, Arkies H, Jager PL, Knollema S, CH Slump, Sanches PG, van Dalen JA. Detectability of small objects using digital PET. ePoster presentation at the annual meeting of the European Association of Nuclear Medicine 2016, Barcelona

12. **Koopman D**, Groot Koerkamp ML, Arkies H, Jager PL, Knollema S, CH Slump, Sanches PG, van Dalen JA. Does digital PET fit EARL accreditation specifications for tumour imaging? Oral presentation at the annual meeting of the European Association of Nuclear Medicine 2016, Barcelona

13. **Koopman D,** van Dalen JA, Francken AB, Jager PL. Nieuwe PET/CT-scanner in Isala verbetert borstkanker diagnostiek. Oral presentation at the annual scientific research evening (Wetenschapsavond) of Isala, 2016, Zwolle

14. **Koopman D**, Noortman WA, Jager PL, Schreuder N, Slump CH, van Dalen JA. Optimizing administered Ga-68-DOTATOC activity for PET imaging. ePoster presentation at the annual meeting of the European Association of Nuclear Medicine 2017, Vienna

15. **Koopman D**, Noortman WA, Jager PL, Slump CH, van Dalen JA. Implications of a FDG-PET EARL protocol for Ga-68 PET imaging. Oral presentation at the annual meeting of the European Association of Nuclear Medicine 2017, Vienna

16. Assink N, van Dalen JA, **Koopman D**, Stevens H, Slump CH, Jager PL Impact of point-spread function modelling as a post-reconstruction deconvolution on FDG-PET image quality. ePoster presentation at the annual meeting of the European Association of Nuclear Medicine 2017, Vienna

17. **Koopman D**, Jager PL, Slump CH, van Dalen JA. Validation of an EARL protocol using digital PET. Oral presentation at the annual meeting of the European Association of Nuclear Medicine 2018, Düsseldorf. *Included in the Highlight Lecture of this meeting.*

18. Huizing DMV, **Koopman D**, van Dalen JA, Gotthardt M, Boellaard R, Sinaasappel M, Stokkel MPM, de Wit-van der Veen BJ. Multicentre ^{68}Gallium PET/CT performance harmonisation based on the EARL standards. Oral presentation at the annual meeting of the European Association of Nuclear Medicine 2018, Düsseldorf. *Included in the Highlight Lecture of this meeting.*

19. **Koopman D**, Jager PL, Slump CH, van Dalen JA. Justification for a quadratic FDG-dose regimen with digital PET imaging. ePoster presentation at the annual meeting of the European Association of Nuclear Medicine 2018, Düsseldorf

20. Zwart LGM, **Koopman D**, van Dalen JA, Francken AB, Slump CH, Jager PL. Improved lesion visibility in breast cancer patients using prone FDG-PET. ePoster presentation at the annual meeting of the European Association of Nuclear Medicine 2018, Düsseldorf

21. Tegelaar A, **Koopman D**, Jager PL, Slump CH, Rombouts EC, Winkels M, van Dalen JA. Need for randomization in side-by-side FDG-PET comparison studies. Oral presentation at the annual meeting of the European Association of Nuclear Medicine 2018, Düsseldorf

22. **Koopman D**, van Dalen JA, Stigt J, Slump CH, Winkels M, Rombouts EC, van Dalen JA. Improved small lesion detection in lung cancer patients with digital PET. ePoster presentation at the annual meeting of the European Association of Nuclear Medicine 2018, Düsseldorf

23. **Koopman D**, Jager PL, Slump CH, Knollema S, van Dalen JA. Variability of tumor-SUV using EARL-accredited PET scanners. Poster presentation at the annual meeting of the Society of Nuclear Medicine and Molecular Imaging 2019, Anaheim

24. **Koopman D**, Stevens H, van Dalen JA, Slump CH, Knollema S, Jager PL. Prospective comparison of digital PET with optimized conventional PET in cancer patients. Poster presentation at the annual meeting of the Society of Nuclear Medicine and Molecular Imaging 2019, Anaheim

25. Gerritse TJ, **Koopman D**, Oostdijk AHJ, Arkies H, Jager PL, Slump CH, van Dalen JA. Value of ultra-high resolution reconstructions in small lesion detection with FDG-PET. ePoster presentation at the annual meeting of the European Association of Nuclear Medicine 2019, Barcelona

26. Simons-Winters EG, **Koopman D**, Jager PL, Slump CH, van Dalen JA. Optimizing image reconstruction on digital PET. ePoster presentation at the annual meeting of the European Association of Nuclear Medicine 2019, Barcelona

27. **Koopman D**, Spenkelink IM, Jager PL, Arkies H, Slump CH, van Dalen JA. Optimizing image reconstruction for lesion assessment with I-124 PET. ePoster presentation at the annual meeting of the European Association of Nuclear Medicine 2019, Barcelona

Dankwoord

Dit proefschrift was uiteraard nooit tot stand gekomen zonder de bijdragen van vele mensen die ik via deze weg graag wil bedanken.

Allereerst wil ik alle patiënten bedanken die de afgelopen jaren toestemming hebben gegeven voor het gebruik van hun gegevens voor wetenschappelijk onderzoek op de afdeling. In het bijzonder bedank ik de 225 patiënten die in 2018 en 2019 deelnamen aan de vergelijkingsstudie van twee PET scanners. Dit heeft ons veel nieuwe inzichten opgeleverd over de optimale inzet van nieuwe PET technologie.

Beste copromotoren dr. P.L. Jager en dr. J.A. van Dalen, beste Jorn en Piet, ik weet nog goed dat ik kwam kennismaken voor mijn eerste TG-stage in de kelder van de Weezenlanden in augustus 2012. Wie had gedacht dat deze ontmoeting zeven jaar later tot dit mooie proefschrift zou leiden… ik in ieder geval niet! Hoewel de geplande studies naar de digitale PET scanner lang op zich lieten wachten heb ik nooit spijt gehad van onze ambitieuze plannen en zie hier het resultaat!

Beste Jorn, ik heb onze samenwerking altijd als bijzonder prettig ervaren. Je bent laagdrempelig bereikbaar en kijkt op eerlijke en pragmatische wijze naar nieuwe ideeën en dat maakt je een bijzonder effectieve klinisch fysicus en onderzoeker. Ook ben je een groot voorbeeld voor me in de manier waarop je studenten begeleidt. Ik ben dankbaar dat we dat ook veel samen konden doen!

Beste Piet, bedankt voor al jouw klinische en wetenschappelijke input de afgelopen jaren. Dit was essentieel om de patiënt niet uit het oog te verliezen op allerlei technische details. Je bent kritisch als het moet maar vooral ook complimenteus als het kan. Je directe doch motiverende manier van begeleiden heb ik altijd zeer gewaardeerd, dankjewel voor alles!

Beste promotor, prof.dr. ir. C.H. Slump, beste Kees, bedankt voor uw supervisie tijdens mijn stages, afstudeerproject èn promotieonderzoek. U gaf me veel vrijheid om mijn eigen plan te maken en uit te voeren, maar uw adviezen en tips waren toch ook regelmatig reden om het plan bij te stellen. Ook heb ik dankbaar gebruik gemaakt van de uitstekende cursussen op de UT, bedankt voor alle kansen!

Beste Siert, jij hebt met name op tactisch, strategisch en financieel vlak een belangrijke bijdrage geleverd aan het opstarten en uitvoeren van dit promotieonderzoek. Ook heb ik veel van je geleerd over het creëren van draagvlak en het vormen van een (toekomst)visie, dankjewel!

Geachte leden van de promotiecommissie, hartelijk dank voor het lezen en beoordelen van mijn proefschrift en het voeren van de verdediging.

Verder wil ik graag alle co-auteurs, binnen en buiten Isala, bedanken voor hun bijdrage aan de diverse studies. In het bijzonder wil ik mijn collega-promovendi Charlotte, Daphne en Nanno bedanken voor de leuke en leerzame samenwerkingen waarbij ik als co-auteur mocht fungeren!

Ook wil ik de gehele afdeling nucleaire geneeskunde van Isala bedanken voor het faciliteren en ondersteunen van mijn onderzoek de afgelopen jaren. Bedankt voor de gezelligheid in de koffiekamer en bij de afdelingsuitjes, en natuurlijk ook bedankt voor jullie steun bij de presentaties op de EANM!

Uiteraard wil ik ook de vakgroep nucleaire geneeskunde bedanken. Beste Ad, Hester, Piet, Henk, Jaep en Siert, jullie waren allemaal bereid om een bijdrage te leveren in de visuele beoordeling van de vele PET beelden en het meedenken over nieuwe onderzoeksmogelijkheden en het inbrengen van klinische vragen. Het draagvlak dat ik daarbij heb ervaren voor het uitvoeren van alle studies was geweldig! Ook Elise, Rowena, Beti, Brian, Eef en Sharon, bedankt voor jullie bijdrage en betrokkenheid als nucleair geneeskundigen in Isala.

Beste physician assistants, Janneke, Magdalena en Martijn, bedankt voor jullie hulp bij het opstarten en includeren van patiënten in de PETPET-studie, jullie betrokkenheid en bereidheid om mee te denken bij alle nieuwe onderzoeksplannen de afgelopen jaren.

Beste Joris, na meerdere verhuizingen binnen de afdeling kwamen we een paar jaar geleden in onze kleine maar fijne TG-kamer terecht. Die eigen plek met jou als kamergenoot is me altijd prima bevallen. Hoewel onze onderzoekslijnen gescheiden waren was je altijd beschikbaar om mee te denken, extra statistische tests te runnen en te brainstormen over allerlei innovaties, bedankt! Je bent een inspirerende collega en ik ben heel benieuwd waar de toekomst jou brengen gaat, succes!

Beste Amarins, als research coördinator was je van het begin (in Salzburg!) tot het eind (als paranimf) betrokken bij mijn promotieonderzoek. Jouw ervaring met wetenschappelijke studies heeft me regelmatig uit de brand geholpen en je was altijd bereid om te helpen en mee te denken. En natuurlijk ook bedankt dat je mijn paranimf wil zijn! Ik vind het tevens bewonderingswaardig dat je op zoek bent gegaan naar jouw ideale baan en ik wens je heel veel succes met de afronding van je opleiding!

Ook wil ik alle klinisch fysici bedanken voor het ondersteunen van het wetenschappelijk onderzoek, in het bijzonder Jorn, Jochen en Martine, bedankt! Ook Stoffer Reiffers, grondlegger van de nucleaire geneeskunde in Zwolle, bedankt voor de leerzame gesprekken in de eerste periode van mijn onderzoek.

Ik wil tevens alle TG en MBRT studenten bedanken die de afgelopen jaren betrokken waren bij onze PET oncologie-onderzoeken. Ellis, Tessa, Ilse, Ellen, Michelle, Lisanne, Nick, Wyanne, Maureen en Carlijn, bedankt! Ook de Isala-promovendi die mij de afgelopen jaren voorgingen, Ruud, Martijn, Mohamed en Elsemiek bedankt voor de leerzame periode en nodige gezelligheid. Sabine, bedankt voor jouw gezelligheid en veel succes met het voortzetten van jouw promotieonderzoek de komende jaren, je kunt het! Ook Nanno, Nannet, Daphne, Maaike en Denise, veel succes gewenst met jullie verdere promotietraject!

Ook de steun en het draagvlak van operationeel leidinggevenden is essentieel voor het uitvoeren van wetenschappelijk onderzoek. Bianca, Lenie en Jan Willem, bedankt voor jullie bijdrage en steun in het faciliteren van alle onderzoeken op de werkvloer!

Alle medisch nucleair werkers op de nucleaire geneeskunde, veel dank voor al jullie hulp bij het uitvoeren van de extra onderzoeken en het begeleiden van onze TG-studenten op de werkvloer. In het bijzonder Dimitri, Aline, Marit, Inge, Tirsa en Thomas bedankt voor jullie aanzienlijke bijdrage bij het opstarten en uitvoeren van de PETPET studie! Ook PET kernlaboranten Evelien, Erik, Aline, Dimitri, Bianca en Diane, bedankt voor jullie bereidheid om mee te denken hoe we alle nieuwe mogelijkheden die onze PET scanners bieden zo goed en makkelijk mogelijk kunnen implementeren in de praktijk.

Beste collega's van de administratie, Birgul, Natascha, Willy, Angela, Marieke, Jonathan en Anne-lien, bedankt voor jullie hulp en flexibiliteit bij het inplannen van de PETPET studiepatiënten en andere studiegerelateerde werkzaamheden, jullie zijn onmisbaar!

Beste applicatiebeheerders, in het bijzonder Gerard, Susanne, Having en Arina, ik weet dat ik regelmatig langskwam met onmogelijke vragen en wensen. Jullie waren altijd bereid om mee te denken en te zoeken naar een oplossing en daar zijn we samen steeds weer goed in geslaagd, bedankt!

Ook het RVE bestuur en de MZE managers van de afdeling wil ik graag bedanken. Coen, Carolina, Siert, Corné, Wim, Egbert en Edwin, bedankt voor de kans om dit promotieonderzoek uit te voeren in Isala, de mogelijkheid om het onderzoek te gaan combineren met een functie als kwaliteitsadviseur en de ruimte om mezelf verder te ontwikkelen. Ik heb zoveel van jullie geleerd! Ook alle andere collega's, waaronder stafleden, OL'ers en kwaliteitspecialisten, bedankt voor de prettige samenwerking en de leerzame tijd. In het bijzonder Saskia bedankt voor de fijne samenwerking als team-kwaliteit en bedankt voor jouw flexibiliteit, het was heel fijn dat we onze taken zo konden verdelen dat ik in de drukke periodes toch ook voldoende tijd kon besteden aan m'n onderzoek!

Beste medisch specialisten in Isala, in het bijzonder Anne Brecht Francken en Jos Stigt, bedankt voor jullie klinische bijdrage in onze studies naar de invloed van nieuwe PET technologie en de mogelijkheid die onze studenten en ik kregen om meer klinische ervaring op te doen! Ook Gijs Patijn bedankt voor jouw enthousiasme en betrokkenheid, het is ontzettend mooi om te zien hoe mijn onderzoek naar nieuwe PET technologie nu leidt tot nieuwe studieplannen met als ultiem doel de allerbeste en meest patiëntgerichte behandeling bij allerlei soorten kanker.
Dear Philips team, Maryam, Piotr, Dennis, Pedro and Sofie, your support as our research partner on new PET technologies was very important for the realisation of this thesis. Thank you for all interesting meetings and discussions over the past six years!

Lieve studiegenootjes, in het bijzonder Marleen, Marit, Marij en Colien, hoewel we inmiddels verspreid zijn over het hele land zaten we allemaal in hetzelfde TG/PhD schuitje. Het was fijn om ervaringen te kunnen delen, bedankt voor jullie steun en gezelligheid en laten we onze reunies vooral blijven organiseren :). Marit en Marij, veel succes met de afronding van jullie promotietraject!

Beste atletiekvrienden, in het bijzonder oud-Kronauten, Daventrianen, WOC-leden van Daventria en de WTO groep van de FBK Games, bedankt voor alle mooie atletiekwedstrijden die we de afgelopen jaren hebben georganiseerd en bijgewoond. Dit gaf altijd plezierige afleiding naast m'n onderzoek! Viktor in het bijzonder bedankt voor de gezelligheid bij de internationale toernooien die we de afgelopen jaren bezocht hebben, wanneer gaan we weer?! Ook andere vrienden en oud-klasgenootjes, bedankt voor de gezellige uitjes, feestjes en etentjes de afgelopen jaren!

Lieve familie, opa's en oma's (in herinnering), ooms en tantes, neven en nichten, en lieve schoonfamilie, bedankt voor jullie steun en interesse in mijn werk de afgelopen jaren, en bedankt voor de altijd gezellige familiefeestjes. Sven in het bijzonder bedankt, ik vind het mooi om te zien hoe je je plek hebt gevonden in Hengelo en top dat je nu zelfs werkt bij een bedrijf in medische technologie ;)!

Lieve pap en mam, bedankt voor jullie onvoorwaardelijke vertrouwen, steun en hulp om zorgeloos te kunnen studeren en m'n promotieonderzoek uit te voeren, dit was en is ontzettend belangrijk voor me!

Lieve Ronald, tijdens het hele promotietraject was jij mijn grootste steun en toeverlaat. Bedankt voor je heerlijke relativeringsvermogen en je hulp op zoveel fronten. Ook ben ik heel blij dat je vandaag mijn paranimf wil zijn. We hebben een heerlijk leven samen en ik kijk uit naar een mooie toekomst!

Over de auteur

Daniëlle Koopman (20 januari 1990) uit Hengelo is Technisch Geneeskundige en atletiekliefhebber. In haar jeugd kwam ze door sportblessures meermaals op de spoedeisende hulp terecht en zo ontstond haar interesse in de medische wereld.

Na het behalen van haar VWO diploma (2008, Bataafse Kamp, Hengelo) startte ze met de studie *Technische Geneeskunde* (Universiteit Twente, Enschede). Haar bachelordiploma behaalde ze in 2011. Aansluitend volgde ze de master *Technical Medicine* (specialisatie *Robotics and Imaging*) en liep ze stages op de nucleaire geneeskunde (Isala, Zwolle), interventieradiologie (Radboud UMC, Nijmegen), radiotherapie (RISO, Deventer) en reumatologie (ZGT, Almelo/Hengelo).

Daarna voerde ze haar afstudeerproject uit op de afdeling nucleaire geneeskunde (Isala, Zwolle) onder begeleiding van dr. Piet Jager, dr. Jorn van Dalen en prof. dr. ir. Kees Slump. Dit onderzoek rondde ze in oktober 2014 af met een 9 als eindcijfer. Het onderzoek werd voortgezet in een promotietraject, resulterend in dit proefschrift. Sinds 2016 is ze ook kwaliteitsadviseur voor de afdelingen radiologie en nucleaire geneeskunde in Isala.

Haar vrije tijd besteed Daniëlle het liefst aan haar hobby atletiek. Als atleet, vrijwilliger en atletiekfan bezoekt ze regelmatig (inter)nationale atletiekwedstrijden. Ze is wedstrijdsecretaris bij AV Daventria 1906 (Deventer) en jurycoördinator bij de internationale FBK Games (Hengelo). Daniëlle woont samen met Ronald in Deventer.